天津大学博士学位论文

基于桁架方法的空间过约束机构分析与可变多面体设计

Truss Method for Kinematic Analysis of 3D Overconstrained Linkages and Design of Transformable Polyhedrons

学科专业：机械工程专业

研 究 生：杨富富

指导教师：陈焱 教授

天津大学机械工程学院

2017 年 12 月

中文摘要

连杆机构是机械系统组成中一类由连杆构件用低副联接组成的构件系统。它的主要功能是可用来传递运动和力。连杆机构由于具有一些特定的优势，如构件和铰链形式均较为简单、承载能力强、可靠性好、可实现多样化空间复杂运动等，在机械、汽车、仪器等领域中得到了广泛应用。而桁架是一种由杆件彼此在两端用铰链连接而成的平面或空间结构，它一般是由稳定的三角形或四面体单元组成。桁架的主要功能是通过杆件在轴向受拉或受压来承受结点处的外载荷。由于结构简单、成本低、以较小的自重提供较大刚度等优点，桁架结构广泛应用于工程结构、建筑材料等各个领域。

虽然机构和结构的主要功能有所不同，但它们并不是两个完全不相关的概念。一方面，当锁定机构的所有的输入参数时，机构可以被看作是具有一定承载能力的结构。另一方面，工程中也存在一些力静定或静不定的可运动的结构,在机构学中，这两种结构分别看作是一般机构和过约束机构。结构侧重于对稳定性和力学特征的分析，而机构则倾向于对自由度和运动特性的研究。

经历着近 200 年的发展，现代机构运动学已经形成了一些较为成熟的研究理论和方法，如矩阵方法、旋量理论、李群李代数等。但是，这些理论和方法难以有效地解决复杂的空间机构的运动学问题。如空间过约束机构由于具有复杂的几何关系，其自由度计算常常需要进行特殊修正。同时，空间多环路机构的复杂拓扑环路关系使运动学分析更为困难。特别是空间多环路机构的运动轨迹解析分析仍是当前机构学的难点之一。

桁架结构可以被认为是由杆件通过球副连接而成的多环路结构。在结构中，通常采用包含了几何和拓扑信息的平衡矩阵来分析桁架的结构特性。因为这个过程无需单独考虑桁架的具体拓扑环路关系，该方法有潜力应用于空间复杂机构的运动学分析。

因此，本文的研究目的是将三维空间机构转换为与其等价的桁架形式，通过桁架理论与方法对复杂空间过约束机构的运动学特性进行分析，并以此为工具设计具有折展功能的可变多面体结构。

本文首先提出一套将连杆机构转换为与其等价桁架形式的通用方法，并验证该方法的有效性；其次，采用该方法识别并去除空间过约束机构中冗余约束，得到过约束机构的非过约束形式；最后，应用桁架转换方法中的自由度计算、运动轨迹预测以及分叉点的判断等方法，得到了三组可单自由度变换的多面体。具体工作包括如下五个部分：

- **桁架方法**

本文**第二章**提出了一种将空间连杆机构转换为与其等价的桁架结构的方法。基于该方法，可将桁架中关于运动分析的理论和方法引入到机构运动特性的分析中。该方法为具有复杂拓扑关系机构的运动学分析开辟了一条新途径。

将直线视为杆件、结点视为球副，一个转动副即可用一条直线两端分别连接一个结点进行表达。因为直线、三角形和四面体是一维、二维和三维空间中最简单稳定的刚体，而桁架是由刚性杆通过结点连接而成，所以，一个转动副连接两个构件所实现的相对转动可由两个三角形，或两个四面体，或一个三角形与一个四面体，通过一条公共边连接而成的桁架来实现。同时，两端均为球副的构件可表示为两端均为结点的一条直线。两端分别为球副和转动副的构件可表示为一个三角形（其中一个顶点对应球副位置，该顶点的对边对应转动副位置）。两端均为转动副的构件通常可表示为一个三角形（两转动副共面相交）或者一个四面体（两转动副空间异面）。当该构件所连接的两转动副轴线相互平行时，采用上述等价方式得到的 6 条边将处于同一平面内。通过对其力学分析发现，该等价后的桁架含一个瞬时自由度。为避免等价转换后机构的运动特性发生变化且避免引入冗余杆，需在该平面外确定一辅助结点，将该结点与四边形的 4 个顶点分别相连，并去除原四边形中两条对角线中的一根杆，可得到其桁架形式。因此，采用该转换方法，可将含转动副和球副的连杆机构等价转换为它们对应的桁架形式。

本文以一个三重旋转对称的 Bricard 连杆机构为例，首先将其转换为对应的桁架形式，对其平衡矩阵进行分析，验证了其单自由度的特性；再利用对平衡矩阵进行奇异值分解的数值算法生成了其运动轨迹；最后以平衡矩阵的奇异值为依据确定了该机构的两个分叉点位置。所得到的结果与已有结论完全一致，从而验证了该方法的有效性。

以平面四杆和球面四杆两个机构为例，验证了机构运动雅可比矩阵和力平衡矩阵对于运动分析具有等效性的结论。最后，推导了空间桁架中结点线速度与角速度之间的关系。这可将机构学中的铰链角位移问题转换为相应桁架中结点线位移问题。

- **过约束机构的非过约束形式**

空间过约束机构由于以最少杆件可提供较好刚性而在工程领域有着广泛的应用前景。而复杂的几何条件对其构件的制造精度以及机构的装配精度提出了极为苛刻的要求。因此，这在很大程度上制约了过约束机构的进一步应用。为了解决该问题，就需要寻找过约束机构的等价非过约束形式。

本文**第三章**以桁架方法为依据，介绍了一种在空间过约束机构等价桁架形式中识别并去除冗余杆的通用方法，从而得到过约束机构的非过约束形式。

首先将过约束机构等价转换为对应的桁架结构。再根据麦克斯韦准则，计算出桁架结构中冗余杆的数目，并根据桁架中各杆件之间的相对位置关系，确定去除冗余杆的所有可能方案。通过建立合适的空间直角坐标系，求得所有去除冗余杆件后桁架结构的平衡矩阵并准确地计算出自由度数。相对于原桁架结构，删除杆件后的平衡矩阵若未出现降秩现象，则得到了过约束机构的非过约束简化形式。

以 Bennett 机构和 Myard 5*R* 机构为例，详细描述了该方法的具体实施过程。通过对 Bennett 机构和与其有着相同参数的 *RSSR* 机构的输入输出规律进行分析研究，发现它们的运动规律保持一致。采用旋量方法对 *RSSR* 机构进行分析，发现其中的这两个球副在运动过程中均与转动副等价。基于以上两点分析，可以证明 *RSSR* 机构确实为 Bennet 机构的非过约束形式。同时，为了验证该方法的通用性，本文还研究了 Myard 5*R* 机构的非过约束形式，即为空间 *RRSRR* 机构。

理论上，制造误差很容易使空间过约束机构出现卡死而失去自由度。然而，制造误差通常并不会改变非过约束形式的自由度，同时对其运动规律也有着较小的影响。通过对输出角关于制造误差的灵敏度分析，发现非过约束形式对制造误差具有更好的协调性。最后，设计出了一类特殊运动副，该运动副即可用于非过约束机构形式，还在提升制造误差协调性的同时，保留了过约束机构所具有的刚性的特点。这些工作为过约束机构的进一步工程应用打下了坚实的基础。

- **立方八面体与正八面体之间的单自由度变换**

在几何中，有两类都是由正多边形组成且具有较好对称性的凸多面体，它们分别为柏拉图多面体和阿基米德多面体。其中，柏拉图多面体是由一种正多边形围成的凸多面体，它包含以下 5 种：正四面体、立方体、正八面体、正十二面体和正二十面体。阿基米德多面体则是由两种或两种以上正多边形围成的凸多面体，它包含 13 种。

在几何中，经典的截角，截半，交错，扭棱等方式可实现阿基米德多面体和柏拉图多面体之间的变换。但这些变换都是通过截短多面体的边长来实现的，因此，它们均无法由连杆机构来实现。

在工程领域，最经典的多面体变换是由 Fuller 提出的立方八面体与正八面体之间变换的 Jitterbug。该变换是通过“旋转+平移”的方式来实现的。运动学上，可认为 Jitterbug 中的 8 个三角形面都通过圆柱副与机架连接，且多面体的各顶点均设置为球副。虽然它可单自由度完成变换，但这些圆柱副的存在增加了机构的复杂度、破坏了多面体内部的整体可用区域且降低了有效的体积折展比。

自 Fuller 提出 Jitterbug 后，已有大量学者对多面体变换以及多面体机构的运动性进行了研究。但这些变换通常要么在改变杆长的情况下改变多面体的大小而不改变其形状，要么不能被单自由度实现，要么不能在两个多面体之间进行。

因此，我们的目标是设计简单的机构实现多面体之间的单自由度变换。具体地，在多面体每个顶点处仅设置一个转动副或球副，运用机构运动学理论对多面体展开和折叠构型进行分析，确定各顶点的运动副类型以及转动副的方位，从而得到多面体之间的单自由度变换。

本文**第四章**，采用桁架转换方法，得到了一种空间多环路连杆结构。该机构可实现含6个镂空四边形面和8个刚性三角形面的立方八面体和正八面体之间的变换，其体积折展比为5。

将立方八面体中一个四边形设置为一个 Bennett 机构可将立方八面体中的 4 个三角形单自由度地折叠为正八面体中共定点的 4 个三角形，通过分析这些三角形在初始和终止构型下的几何位置关系求得了转动轴的具体方位。类似地，剩下的 4 个三角形也由参数完全相同的 Bennett 机构来实现折叠运动。最后，通过 4 个球副将这两个 Bennett 机构进行连接，得到了所需的多面体机构。

通过桁架方法求得该机构的自由度为 1。在此基础上，运用基于奇异值分解的数值算法，得到了该多面体变换的运动轨迹。通过记录运动过程中奇异值的变化，分析了变换过程中的分叉情况。结果显示该机构可实现立方八面体和正八面体之间的单自由度变换，且不会出现运动分叉情况。

同时，通过分析各三角形面中心的运动轨迹，对比了所得到的多面体变换与基于“旋转+平移”方式的多面体变换在运动特性和对称性上的差别。此外，对于该机构中 4 个球副的运动情况也进行了分析。结果显示，这些球副并不能进一步替换为转动副。

该可展结构含有 8 个转动副和 4 个球副，其中 8 个转动副构成 2 个 Bennett 机构。这 2 个 Bennett 机构通过 4 个球副连接形成 4 个 *RSRS* 机构。这样 8 个三角形构件通过 2 个 Bennett 机构和 4 个 *RSRS* 机构的并联网格连接成立方八面体。随着这 6 个机构的折展运动，立方八面体被折叠成由 8 个三角形拼接而成的正八面体。在工程中，由于球副的设计和制作均较困难，故将该多面体机构中的球副用 3 个转动副所构成的折纸结构进行代替。最后设计并制作了只有转动副的多面体实物模型。该模型进一步验证了计算和设计结果的正确性。

- **截角八面体与立方体之间的单自由度变换**

本文**第五章**，研究了一种可实现 11.3 倍体积折展比的截角八面体和立方体之间的变换，该变可换由另一个空间单自由度多环路连杆机构实现。

将截角八面体中 8 个镂空六边形面折叠起来，可得到由 6 个正方形面拼成的立方体。将截角八面体的所有边均视为直杆，并将所有顶点设置为球副，通过桁架方法，求得所形成的多面体机构的自由度为 18。因此，为了得到单自由度的多面体变换，需要在此基础上引入约束来降低自由度数。通常，将一个球副替换

为一个转动副可增加 2 个约束、减少 2 个自由度数。然而，由于多面体中存在着复杂的拓扑环路，故不能通过简单数数的方式确定需要引入转动副的数目。

截角八面体中的一个镂空正六边形对应的折叠状态是立方体中具有公共顶点的 3 条相互垂直的边。因其展开和和折叠状态均具有三重旋转对称性，故选取了同样具有三重旋转对称的 Bricard 机构来实现它们之间的变换。该机构是一种经典的由 6 个转动副连接而成的单自由度六杆机构。通过分析变换前后各正方形的几何方位关系，运用机构运动学方法，求得了各个顶点处转动副的具体轴线方位。

类似地，将由剩下的 3 个正方形面和对应的 3 条边所围成的六边形也设置成了具有相同参数的 Bricard 机构。通过桁架方法，对引入 2 个 Bricard 机构后的多面体机构进行分析，求得其自由度数为 2。为了获得单自由度变换的目标，仍需将剩余的 12 个球副中的某一个替换为转动副。

研究发现，将这 12 个球副分别单独替换为在特定方位平面内的转动副均可获得单自由度变换。考虑折叠和展开过程的完整性以及运动过程的物理干涉情况，通过对运动路径的模拟以及对平衡矩阵奇异值的记录，确定了转动副在对应平面内的方位范围。

最后，通过 3D 打印，制作了一个边长为 20cm 的截角八面体和立方体之间变换的验证模型。

- **截角四面体与正四面体之间的单自由度变换**

本文**第六章**，通过一个由 1 个 Bricard 机构和 3 个 *RSRRSR*（或者 3 个 *RRSSRR*）机构构建的多环路机构，实现了截角四面体和正四面体之间的单自由度变换，它们的体积比为 23。

截角四面体是一类由 4 个正六边形和 4 个正三角形组成的阿基米德多面体。其中，镂空的正六边形是由 3 个三角形面和 3 条边围成，呈三重旋转对称分布。类似于前一个多面体变换，该正六边形也可由三重旋转对称的 Bricard 连杆机构单自由度折叠为正四面体中有公共顶点的 3 条边。将其余 6 个顶点均设置为球副，通过桁架方法，求得所得到的多面体机构的自由度为 4。为获得单自由度的多面体变换，仍需将部分球副替换为具有特定转轴方向的转动副。

考虑结构的对称特性，该机构存在两类仍被设置为球副的顶点位置，即（1）Bricard 机构所连接的 3 个三角形中未被设置成转动副的顶点，（2）第四个三角形的 3 个顶点。研究发现，分别将其中一类顶点上的球副单独替换为转轴在特定平面内的转动副均可实现单自由度的多面体变换。

通过桁架方法联合基于奇异值分解的数值模拟方法，分别求得了这两类替换方案的机构运动轨迹。结果显示，后确定的转动副轴线在对应平面内的某些范围

内，可完整地实现预期的截角四面体与正四面体之间的单自由度变换，同时这些变换过程也不会出现物理干涉。

最后，基于折纸技术制作了一个实现该多面体变换的实物模型，验证了设计结果的正确性。

- **结论与展望**

本文着眼于机构学与结构力学的交叉学科，提出了一种将连杆机构等价转换为桁架形式方法。这为研究复杂连杆机构的运动特性开拓了一种新的研究思路。同时，得到的非过约束形式获取方法和求解多面体之间单自由度变换的方法以及所有设计结果均具有一定理论和工程实用价值。

此外，本文研究工作还可以从如下几个方面进行进一步深入研究：

（1）机构的雅可比矩阵与桁架的平衡矩阵之间的本质关系仍有待进一步探索和论证。基于该关系，机构的动力学问题也可通过对其等价桁架的平衡矩阵进行分析来解决。由于平衡矩阵的建立过程较雅可比矩阵的建立过程要更加容易、更加便捷，故这可大大简化复杂机构的动力学分析过程。

（2）为获取过约束机构的非过约束形式，本文在等价桁架形式中选取待去除的冗余杆时，制定了一些选取规则。放开其中部分或者全部规则，可能会获得更多的非过约束形式。而所得到的非过约束形式与原机构的运动学关系仍需要进一步研究。

（3）本文采用了 Bennett 四杆和 Bricard 六杆机构实现了 3 组多面体之间的变换。这两种机构均是经典的空间单自由度机构。而有些多面体变换需要引入八杆或更多杆机构，如可利用空间八杆机构将截角立方体中的镂空正八边形面进行折叠可获得正八面体。因此，以多自由度的单环路连杆机构为单元，能否得到多面体之间单自由度变换需要进一步深入研究。同时，为采用最简单的空间多环路机构来实现多面体之间的变换，在多面体的每个顶点处仅允许设置一个转动副或一个球副。因此，如果释放此限制条件，如在某些顶点处设置两个自由度的 U 副，也可能会得到更多多面体之间的单自由度变换。更进一步，由于部分多面体变换的展开和折叠构型都具有可三维阵列的特点，因此，以这些少自由度变换的多面体机构为单元，有希望构建出少自由度的可变多面体阵列。这将为模块化设计可展卫星群等航天器提供可能的方案。

（4）本文采用结构中的桁架的方法解决了机构运动学中的部分难题。而结构力学中是否还有其它理论亦可用来解决机构运动学问题，仍需要进一步探索。另一方面，机构学中的理论能否解决结构中的一些难题，也有待于进一步探讨。

关键词：桁架方法，过约束机构，非过约束形式，Bennett 机构，Bricard 机构，

多面体变换

ABSTRACT

To overcome the problem that it is very difficult to analysis or design complicated 3D overconstrained linkages and their assemblies with conventional kinematic tools, this dissertation has proposed a novel *truss method* by applying structural theory to the truss form of 3D linkages to study their kinematic behaviours with the consideration of both the topology and geometry conditions. The method has also been adopted to analyse 3D overconstrained linkages and to design deployable polyhedrons. The major research findings are as follows.

First, the new *truss method* was developed, which converts 3D linkages to their corresponding truss forms while maintaining the kinematic behaviours. Under this method, mobility of complex linkages can be analysed by counting states of independent displacements with Maxwell's rule. Besides that, their motion paths are able to be generated by the displacement updated algorithm based on singular value decomposition (SVD) of equilibrium matrix, and bifurcation position can hence be detected by recording singular values of equilibrium matrix during the motion process. The proposed method has been validated with planar 4*R* linkage, spherical 4*R* linkage, and threefold-symmetric Bricard linkage as examples.

Next, to eliminate strict overconstrained geometric conditions of linkages so that the tolerance of their fabrication error can be improved, the 3D overconstrained linkages are transformed into their corresponding truss forms. According to Maxwell's rule and rank of the equilibrium matrix, the redundant bars in the truss form of the overconstrained linkage can be detected and removed to obtain a *non-overconstrained linkage*, while its kinematic equivalence is well kept. Adopting this method, the non-overconstrained forms of Bennett linkage and Myard 5*R* linkage have been found as *RSSR* linkage and *RRSRR* linkages, respectively. Furthermore, discussion on fabrication errors has been carried out to demonstrate the tolerance on the mobility and input-output curve of the non-overconstrained form.

And, *polyhedral transformation* has been realised by a kind of multi-loop linkages with complex topology, which enables large volumetric change amongst Platonic and Archimedean solids. Here, three sets of transformations have been proposed with their corresponding spatial linkages, namely truncated octahedron and cube, truncated tetrahedron and tetrahedron, as well as cuboctahedron and octahedron. Their constructions process and kinematic analysis were investigated in details by using the proposed truss method. Finally, motion analysis indicates that transformation paths are unique without singularity, which are further demonstrated with physical validation models. We envisage that our method could be extended to other paired polyhedrons.

Therefore, the truss method opens up a new way to analyse kinematics of 3D linkages. Meanwhile, the resultant non-overconstrained forms of overconstrained linkages and polyhedral transformations with one DOF are of great potential in engineering applications.

KEY WORDS: Truss method, overconstrained linkage, non-overconstrained form, Bennett linkage, Bricard linkage, polyhedral transformation

Contents

List of Figures

List of Table

Notation

Parameters

a	Link length of a Bennett linkage, or of other linkages
a_1, a_2, a_3, a_4	Link lengths of a four-bar linkage
a_{ij}	Link length of link ij between joints i and j
b	Number of bars in truss
c, d	Distance between joint of the original linkage and that of the alternative form of the original linkage along the axis of joint
$\boldsymbol{d}$	Vector of displacements of joints
$\boldsymbol{d}_{\mathrm{c}}$	A set of correcting displacements on all vertices during the generation of motion path
$\boldsymbol{d}_i$	Vector of displacements of joint i
$\boldsymbol{d}_i'$	Projection of $\boldsymbol{d}_i$ to plane $\mathrm{P}_{i-1}\mathrm{P}_i\mathrm{P}_{i+1}$
${}^j\boldsymbol{d}_i'$	Projection of $\boldsymbol{d}_i$ to plane $\mathrm{P}_{j-1}\mathrm{P}_j\mathrm{P}_{j+1}$
$\boldsymbol{e}$	Vector of elongation along bars
$\boldsymbol{f}$	Vector of external forces on joints
f_i	Number of degrees of freedom of the relative movement allowed by the i-th kinematic pair in mechanism
g	Number of joints in linkage
h	Pitch of a screw
j	Number of joints in truss
$l_{(i-1)i(i+1)}$	The module of $\boldsymbol{P}_i\boldsymbol{P}_{i-1} \times \boldsymbol{P}_i\boldsymbol{P}_{i+1}$
m	Mobility of mechanism or truss
n	Number of links in linkage
$\boldsymbol{n}_i$	Normal vector of plane $\mathrm{P}_{i-1}\mathrm{P}_i\mathrm{P}_{i+1}$ at joint i
p^{nom}	Nominal value of variable p
r	Rank of equilibrium matrix of truss
$\boldsymbol{r}$	Position vector of any point on the rotation axis of a screw
s	State of self-stress of mechanism or truss
$\boldsymbol{s}_i$	Revolute axis or translating direction vector on joint i
$\boldsymbol{s}_i'$	Instantaneous revolute axis to equal spherical joint i
$\boldsymbol{t}$	Vector of inner forces along bars in truss
w_i	Velocity of joint i

x_i, y_i, z_i	x, y, z coordinate of system i
$\boldsymbol{C}$	Compatibility matrix of truss
$\boldsymbol{C}'$	Compatibility matrix without fixed bars and joints
$\boldsymbol{H}$	Equilibrium matrix of truss
$\boldsymbol{H}'$	Equilibrium matrix without fixed bars and joints
$\boldsymbol{I}_i$	The identity matrix of order i
$\boldsymbol{J}$	Jacobian matrix of linkage
${}^i\boldsymbol{P}$	Coordinate of P in the ith system
$\boldsymbol{P}^{\mathrm{c}}$	Coordinate of point P in cube
$\boldsymbol{P}^{\mathrm{co}}$	Coordinate of point P in cuboctahedron
$\boldsymbol{P}^{\mathrm{f}}$	Coordinate of point P in the final configuration
$\boldsymbol{P}^{\mathrm{o}}$	Coordinate of point P in octahedron
$\boldsymbol{P}^{\mathrm{t}}$	Coordinate of point P in tetrahedron
$\boldsymbol{P}^{\mathrm{to}}$	Coordinate of point P in truncated octahedron
$\boldsymbol{P}^{\mathrm{tt}}$	Coordinate of point P in truncated tetrahedron
$\boldsymbol{PQ}$	Vector directing from point P to point Q
R^i	The ith configuration of linkage
R_i	Offset on joint i
$Rot(\boldsymbol{s}, \theta)$	Transformation matrix of rotating θ around axis $\boldsymbol{s}$
$\boldsymbol{S}_i$	Screw of $\boldsymbol{s}_i$
$\boldsymbol{S}_i^r$	Reciprocity of screw $\boldsymbol{S}_i$
$\boldsymbol{T}_{ij}$	Transformation matrix from system i to system j
$\boldsymbol{U}$	Matrix consisting of left singular vectors in SVD
$\boldsymbol{V}$	Diagonal matrix of singular values in SVD
$\boldsymbol{W}$	Matrix consisting of right singular vectors in SVD

Symbolic Variables

α_{ij}	Twist angle of link ij between joints i and j
α, β	Twist angles of a Bennett linkage, or of other linkages
γ, γ_1, γ_2	Axis angles between revolute axis and its adjacent edges in polyhedrons
δ, ρ	Folding angles of polyhedral edges
$\zeta_{A3}, \zeta_{A4}, \zeta_{D3}, \zeta_{D4}$	Derivation angles for variable revolute joints

η	Step variable in the numerical algorithm for generating motion path
θ, ϕ	Kinematic angles of linkages
θ_{d}, ϕ_{d}	Kinematic angles at deployed configuration
θ_{f}, ϕ_{f}	Kinematic angles at folded configuration
λ_1	Folding angle BGK in the first construction scheme of transformation between truncated tetrahedron and tetrahedron.
λ_2	Folding angle GKM in the second construction scheme of transformation between truncated tetrahedron and tetrahedron.
μ	Dimension of the tangent space which contains all the relative displacements among arbitrary links of the linkage
χ_{PQ}	Angle between instantaneous revolute $\boldsymbol{s}'_{\mathrm{P}}$, to equal spherical joint i, and its connected edge PQ
$\Delta\theta$	Angular displacement of angle θ
$\Delta\theta_{i(i+1)}$	Angular displacement of link $i(i+1)$

Abbreviations

R joint	Revolute joint
S joint	Spherical joint
SVD	Singular Value Decomposition

Chapter 1 Introduction

1.1 Background and Significance

Two typical mechanical systems in engineering are rigid structures and mobile mechanisms. Without external forces, structures can be statically determinate or indeterminate depending on whether the equilibrium matrix is full ranked or not. As a subgroup of structures, truss is based on the geometric rigidity of triangle in plane and tetrahedron in space, composed of linear members whose ends are connected at joints referred to as nodes. A mechanism is a device that transforms input forces and movement into a desired set of output forces and movement. And linkages, as one of the most common mechanisms, are assemblies connecting rigid links with lower kinematic pairs, which contain planar, spherical and spatial linkages.

While the concerns of rigid structures are about stability and statics, the study of mechanisms focuses on mobility and kinematics. Yet, structures and mechanisms are not completely irrelevant. From the viewpoint of rigidity, a structure is obtained once the mobility of a mechanism is locked. The structure could be statically determinate when the corresponding mechanism is a normal one, or statically indeterminate when the corresponding mechanism is overconstrained.

Modern kinematics, treated as an independent science, began about two centuries ago, and a number of theories thereby have been developed, such as matrix method, screw theory, Lie group and Lie algebra, to deal with issues on this problem. However, there are still some obstacles for studying kinematic behaviours, including mobility, motion path, and bifurcation, of complicated linkages, in particular overconstrained linkages and multi-loop linkages. Meanwhile, the truss system can be considered as multi-loop system, where the bars and nodes are regarded as links and spherical joints (S joints) in kinematics. And there are a number of structure theories to deal with truss analysis on the structure determinacy, displacement, force equilibrium and so on.

Therefore, if a 3D linkage could be transformed to its corresponding truss form, it will be possible to study the kinematics of the 3D linkage with the theory and method in the field of truss or structure.

1.2 Review of Previous Works

1.2.1 Kinematic Theory in Mechanism

In mechanical engineering, kinematics deals with the characteristics of motion without regard for the effects of forces or mass, and it contains kinematics of mass points, kinematics of rigid bodies, and kinematic constraints.

Mobility, which is the number of independent coordinates needed to define the configuration of a kinematic chain or mechanism [1], is the main structural parameters

of a mechanism and also one of the most fundamental concepts in the kinematic and dynamic modelling of mechanisms [2]. Research work on mobility has lasted about 160 years. As early as the 19th century, mathematicians, including Chebychev [3], Sylvester [4], and Grubler [5, 6], proposed several formulas to calculate mobility of simple linkages. One classical form, proposed by Hunt [7], is

$$m = \mu\left(n - g - 1\right) + \sum_{i=1}^{g} f_i \tag{1-1}$$

where m is the number of degrees of freedom, μ is the dimension of the tangent space which contains all the relative displacements among arbitrary links of the linkage, n is the number of links of the linkage including the fixed link, g is the number of kinematic pairs of the linkage, f_i is the number of degrees of freedom of the relative movement allowed by the i-th kinematic pair. Whereas these formulas failed in acquiring right results for some complicated mechanisms such as overconstrained linkages. Meanwhile, this formula can not calculate correctly the mobility of some multi-loop linkages, called mixed linkages, whose geometry has nothing in particular. The reason is the existence of loops whose links have relative motions associated with different subgroups of the Euclidean group. Hence, it is not possible to use a unique value of μ in Eq. (1-1).

Thereby, a number of modified formulas were proposed, as summarised by Gogu [2], none of which is the universal solution to the mobility of all sorts of mechanism. To present the motion process, several mathematical methods have been adopted for descriptions of position and orientation, such as matrix method, screw theory, Lie group and Lie algebra, dual quaternions and so on.

Denavit and Hartenberg have established a procedure to standardlise the kinematic study of spatial linkage with four independent parameters which are called D-H notation [8]. It is still widely used in mechanism. As shown in Fig. 1-1, a coordinate system is attached to each joint in such a way that z_i is along the axis of revolute joint (R joint) i, and x_i is along the direction of the normal line between z_{i-1} and z_i, and y_i is determined by the right-had rule. Thus, the relative position between two adjacent joints can be determined by following parameters:

- Link length $a_{(i-1)i}$: the shortest distance between z_{i-1} and z_i;
- Twist $\alpha_{(i-1)i}$: the angle between z_{i-1} and z_i, measured in the plane with x_i as the normal;
- Offset R_i: z coordinate component of O_i in system $i-1$;
- Kinematic variable angle θ_i: the angle between x_{i-1} and x_i, measured in the plane perpendicular to z_{i-1}.

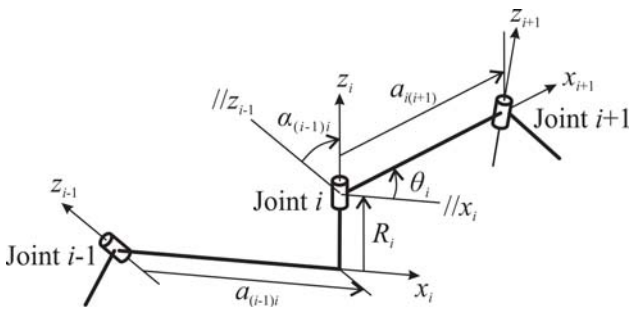

Fig. 1-1. D-H Parameters.

Then, these four parameters are assembled into a homogeneous transformation matrix for kinematic analysis, as shown in Eq. (1-2).

$$\boldsymbol{T}_{i(j)} = \begin{bmatrix} \cos\theta_i & -\sin\theta_i\cos\alpha_i & \sin\theta_i\sin\alpha_i & a_i\cos\theta_i \\ \sin\theta_i & \cos\theta_i\cos\alpha_i & -\cos\theta_i\sin\alpha_i & a_i\sin\theta_i \\ 0 & \sin\alpha_i & \cos\alpha_i & R_i \\ 0 & 0 & 0 & 1 \end{bmatrix} \tag{1-2}$$

The necessary condition for closed loop linkages of n links is that the successive product of the transformation matrices must be preserved as a unit matrix, i.e.,

$$\boldsymbol{T}_{12}\boldsymbol{T}_{23}\cdots\boldsymbol{T}_{(n-1)n}\boldsymbol{T}_{n1} = \boldsymbol{I}_4 \tag{1-3}$$

According to Chasles' theorem [9], a spatial displacement of a rigid body can be defined by a rotation about a line and a translation along the same line, called a screw displacement. In mechanism, screw theory, proposed by Ball [10] and developed by Hunt [7], is an efficient tool to solve not only kinematic but also dynamic problems. Dai extended this method to finite motion analysis [9], which revealed the relationship between finite and instantaneous screws through eigenscrew and derivative of the finite displacement screw matrix. Meanwhile, based on screw triangle linear decomposition [11], analytical solutions of kinematics can be derived for closure linkages with screw method [12, 13].

Screw can be used to represent velocity of joint, shown in Fig. 1-2, which is expressed as

$$\boldsymbol{S} = \begin{bmatrix} \boldsymbol{s} \\ \boldsymbol{s}\times\boldsymbol{r} + h\boldsymbol{r} \end{bmatrix}, \tag{1-4}$$

where $\boldsymbol{s}$, the primary part, is the unit vector of the rotation axis, $\boldsymbol{s}\times\boldsymbol{r}+h\boldsymbol{r}$ is the secondary part which can be decomposed into components parallel and perpendicular to $\boldsymbol{s}$, $\boldsymbol{r}$ is position vector of any point on the rotation axis, and h is called the pitch. For R joints, $h=0$, i.e.,

$$\boldsymbol{S} = \begin{bmatrix} \boldsymbol{s} \\ \boldsymbol{s}\times\boldsymbol{r} \end{bmatrix}, \tag{1-5}$$

and for translating joints, $h=\infty$, i.e.,

$$\boldsymbol{S}=\begin{bmatrix}0\\ \boldsymbol{s}\end{bmatrix}, \tag{1-6}$$

here $\boldsymbol{s}$ is the unit direction vector of the translating joint.

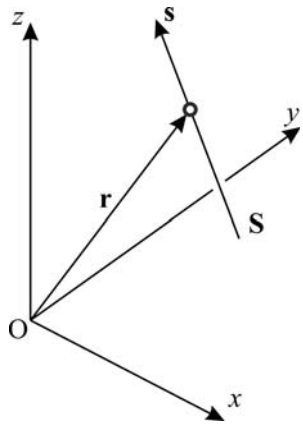

Fig. 1-2. Position and rotation axis of a screw.

For a serial linkage connected with *n* links, the velocity of its end-effector can be expressed by the combination of velocities of these *n* joints,

$$\begin{bmatrix}\boldsymbol{v}\\ \boldsymbol{\omega}\end{bmatrix}=\sum_{i=1}^{n} w_i \boldsymbol{S}_i\ , \tag{1-7}$$

where w_i is the velocity of joint *i*. Therefore, if the linkage forms a close loop,

$$\sum_{i=1}^{n} w_i \boldsymbol{S}_i=\boldsymbol{0}, \tag{1-8}$$

namely,

$$\begin{bmatrix}\boldsymbol{S}_1 & \boldsymbol{S}_2 & \cdots & \boldsymbol{S}_n\end{bmatrix}\begin{bmatrix}w_1\\ w_2\\ \vdots\\ w_n\end{bmatrix}=\boldsymbol{0}\ . \tag{1-9}$$

As dimension of the non-zero solution of w_i is the independent number of joint velocities, the rank of the coefficient matrix is related to the mobility of the linkage. Therefore, screw theory can be used to study mobility of linkages.

And to analyse kinematics of multi-loop linkages, equation like Eq. (1-9) should be established for each independent loop of the multi-loop linkage and then be assembled to a large matrix form. Thus, topology of the linkage should be considered in detail at first, which renders the analysis more complicated.

Lie group associated Lie algebra play a major role in modern physics, with the

Lie group typically playing the role of a symmetry of a physical system [14]. Murray et al. adopted Lie group theory as analytic tools to derive kinematics of robotic manipulators [15]. Hervé illustrated Lie group method to analyse the motion of parallel platform with some examples of 3-DOF robotic manipulators in detail [16].

In mathematics and physics, the set of dual quaternions is a Clifford algebra that can be used to represent spatial rigid body displacements [17]. Perez and McCarthy presented a dual quaternion formulation for the kinematic synthesis of constrained serial chains, where kinematics equations of the chain are transformed to successive screw displacements, which can be written in dual quaternion form [18]. Meanwhile, Leclercq, Lefèvre, and Blohm showed that dual quaternions are able to deal with 3D kinematics in neuroscience, including forward and inverse kinematics [19].

Recently, a new method, called Bond theory, was proposed from mathematics to study mobility of linkages by Hegedüs et al. [20, 21, 22, 23, 24], and they analysed kinematics of closed 5*R* linkage [20], Stewart-Gough platforms [23], closed 6*R* linkages [24].

Selig summarised geometric methods in robotics such as Lie group, Lie algebra, Screw theory, Line geometry and Clifford algebra [25]. These methods are normally efficient for corresponding linkages, however kinematics of some complicated linkages, such as overconstrained linkages and multi-loop linkages, are still challenging to be studied.

In the theory of mechanisms, many linkages are known whose instantaneous mobility in certain positions of the linkage is greater than mobility of other positions. The reason for this phenomenon is that the kinematic Jacobian matrix has a rank deficiency, i.e., it is at a singular configuration. If the extra mobility is finite rather than infinitesimal, it will appear another motion path at this configuration, i.e., motion bifurcation occurs. Even though bifurcation points may lead mechanisms to an unexpected motion branch, it could also be utilised for designing reconfigurable mechanisms. Therefore, it is significant to judge bifurcation situations during motion processes. Some research works on singularity analysis of single-loop linkages and parallel platforms were studied.

Gosselin and Angeles presented an analysis of different kinds of singularities encountered in closed-loop kinematic chains [26]. Based on the properties of Jacobian matrices of the chain, a general classification of these singularities in three main groups was obtained. Di Gregorio and Parenti-Castelli analysed the singularities of the 3-*UPU* translational platform [27]. They derived the conditions where the actuators cannot control the linear velocity of the moving platform, generally known as architecture singularities. Zlatanov, Bonev and Gosselin proposed the concept, constraint singularity, which is a phenomenon occurring in parallel mechanisms with reduced freedoms when the screw system, formed by the constraint wrenches in all

legs, loses rank [28]. Joshi and Tsai proposed a method for Jacobian analysis of limited DOF parallel manipulators, which is 6 by 6 Jacobian matrix providing information about both architecture and constraint singularities [29]. Grassman geometry is also a significant tool to analyse singularity. By this tool, Kanaan et al. analysed singularity of lower mobility parallel manipulators [30], Merlet found singular configuration of parallel manipulators [31], and the general Gough-Stewart platform was analysed and represented by St-Onge and Gosselin [32]. Chai and Li adopted geometric algebra to derive the analytical expression of the motion space of Bennett linkage [33]. Chen and Chai obtained the bifurcation points from motion paths of a special Bricard linkage with both line and plane symmetry after closure equations derivation of the linkage [34]. These approaches to judge bifurcation situations are based on establishing Jacobian matrix of linkages. Thus, as the complexity of the linkage increases, bifurcation detection becomes more and more complicated due to the complexity is determined by topological and geometric information of the linkages.

1.2.2 Truss Theory

Since an overconstrained mechanism is statically indeterminate, the Maxwell's rule in truss can be applied in the analysis. Maxwell defined a frame as 'a system of lines connecting a number of points', and defined a stiff frame as 'one in which the distance between any two points cannot be altered without altering the length of one or more of the connecting lines of the frame' [35]. A frame having j nodes in three dimensional space requires $3j-6$ bars to be rendered stiff in general, thus,

$$m = 3j - b - 6 . \tag{1-10}$$

However, similar to the Chebychev-Grübler-Kutzbach criteria [36], without detailed topological and geometrical information of the system, Maxwell's rule cannot determine the mobility of overconstrained mechanisms correctly.

Considering a spatial truss consisting of a total of j joints connected by b bars to each other, each joint can be acted upon by an arbitrary force in 3D space, then joints will hold $3j$ components of external forces, assembled in the vector $\boldsymbol{f}$, while the tension in each bar is denoted by a single number, so there are altogether b tensions, assembled in the vector $\boldsymbol{t}$. Similarly, the vector assembled with $3j$ displacements of joints is $\boldsymbol{d}$, and the elongation vector along bars, $\boldsymbol{e}$, is assembled with b components.

For establishing equations, it is convenient to use a tension coefficient instead of tension, defined as tension/length, and the corresponding elongation coefficient is defined as elongation*length. Terms tension and elongation to include these convenient variants were usually adopted.

For joint i connecting joints h and j with bars l and m, shown in Fig. 1-3, three equilibrium equations can be established

$$\begin{aligned}
&\left(x_i - x_h\right) t_l + \left(x_i - x_j\right) t_m = f_{ix} \\
&\left(y_i - y_h\right) t_l + \left(y_i - y_j\right) t_m = f_{iy} \\
&\left(z_i - z_h\right) t_l + \left(z_i - z_j\right) t_m = f_{iz}
\end{aligned} . \tag{1-11}$$

Here, x_i, y_i, z_i are the Cartesian coordinates of joint i, and f_{ix}, f_{iy}, f_{iz} are the components of external force.

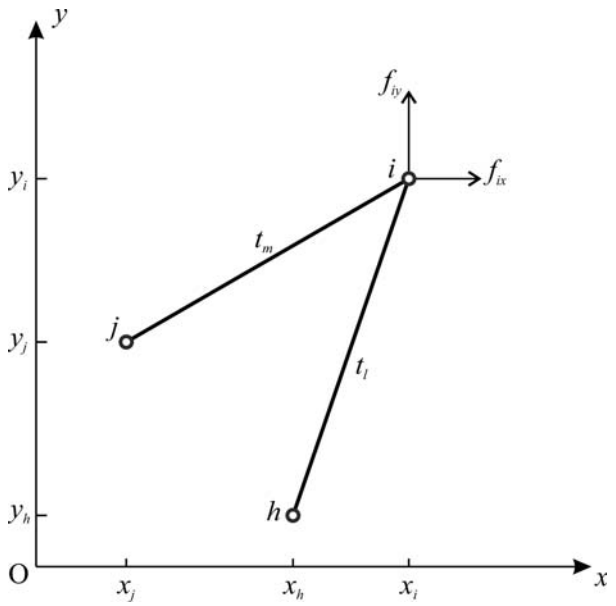

Fig. 1-3. View along Oz of a joint i which carries external forces and is connected by bars to joints h and j.

In this way the $3j$ equations of equilibrium in b unknowns can be written and assembled in a matrix form

$$\boldsymbol{Ht} = \boldsymbol{f} , \tag{1-12}$$

where

$$\boldsymbol{H} = \begin{bmatrix} & \vdots & & \vdots & \\ \cdots & x_i - x_h & \cdots & x_i - x_j & \cdots \\ \cdots & y_i - y_h & \cdots & y_i - y_j & \cdots \\ \cdots & z_i - z_h & \cdots & z_i - z_j & \cdots \\ & \vdots & & \vdots & \end{bmatrix}, \tag{1-13}$$

is the equilibrium matrix with dimensions $3j$ by b.

Meanwhile, the equations of kinematics of small displacements of the assembly can be set up.

$$\boldsymbol{Cd} = \boldsymbol{e}, \tag{1-14}$$

where $\boldsymbol{C}$ is the compatibility matrix with dimensions b by $3j$. By application of the principle of virtual work, the following relationship can be proven.

$$\boldsymbol{C} = \boldsymbol{H}^{\mathrm{T}}. \tag{1-15}$$

It should be noted that there is no elongation for all bars in mechanisms as all links are considered as rigid, namely

$$\boldsymbol{e} = \boldsymbol{0}. \tag{1-16}$$

Calladine further developed Maxwell's rule and used rank of the equilibrium matrix of the system to decide its static and kinematic determinacy [37]. As the equilibrium matrix contains both geometrical and topological information, this method is certainly valid in the analysis of overconstrained mechanisms. Tarnai presented a conjecture about how to decide whether kinematical indeterminacy takes the form of an infinitesimal or a finite mechanism [38]. Then, Pellegrino and Calladine proposed a matrix analysis method to answer Tarnai's conjecture [39]. Later Kuznetsov used kinematical constraint and virtual displacement to respond for Tarnai's conjecture as well [40]. In 2002, Tarnai himself used principle of virtual work to close this conjecture and got a unified form of previous two methods [41].

Besides, bifurcation was also studied in structural engineering. Tarnai presented an exact equation describing the finite displacements of assemblies consisting of rigid bars and pin joints, and a numerical procedure with linear approximation of this equation was presented to determine compatible states and motion of single- or multiple-DOF mechanisms consisting of rigid bars and pin joints [42].

Singular value decomposition (SVD) of a matrix can get a left singular matrix which can depict the left nullspace, a right singular matrix which can construct nullspace, and a diagonal matrix where the number of non-zero singular values is the rank of the original matrix. Meanwhile, the nullspace, left nullspace, and the rank of equilibrium matrix determine states of selfstress, states of mechanisms, and mobility, respectively. Therefore, SVD is potential to analyse motions of movable assemblies. An SVD method on the equilibrium matrix for movable structures was introduced by Kumar and Pellegrino to simulate its kinetic trajectory considering bifurcation points [43]. Gan and Pellegrino proposed a novel kind of deployable structures, which form closed loops. These structures can be folded into a bundle of bars using simple hinges. Its folding process was obtained by SVD of the transforming matrix of closure equations [44]. And Gan and Pellegrino also successfully used the SVD of equilibrium matrix to simulate the motion of closed linkages [45]. Chen and You presented an approach to analyse twofold-symmetric 6*R* foldable frame and its bifurcations by using SVD of the Jacobian matrix of closure equations [46].

There were some works on the intersection of linkage and truss as they both

concern kinematic behaviours. Tanaka introduced a truss-type mechanism from a statically determinate truss by making its joint bars adjustable [47]. Shai showed that, in general, the graph representations of mechanisms and trusses are mathematically dual [48, 49]. Furthermore, how to transform linkages into their equivalent truss forms to adopt structural methods to analyse kinematics of original linkages is a challenging business.

1.2.3 Overconstrained Linkages

Overconstrained linkage [50] is one kind of special linkage, which does not satisfy the classical Kutzbach mobility criterion [36]. As a 3D overconstrained mechanism is able to generate complicated 3D motion with least number of bars, it has attracted great interests in kinematic research. Many 3D overconstrained mechanisms have been proposed in the last 160 years by Sarrus [51], Bennett [52, 53], Delassus [54], Bricard [55, 56], Myard [57], Goldberg [58], Waldron [59, 60, 61], Wohlhart [62, 63, 64], Song and Chen [65], and so on.

Sarrus linkage [51], invented in 1853, is the first overconstrained linkage, which can convert a limited circular motion to a linear motion without any reference guide rail, with which morphing wings [66, 67] were realised.

Bennett linkage, as shown in Fig. 1-4, is the only one four-bar linkage to realise spatial motion with neither parallel nor intersected *R* joints [52, 53], which is an overconstrained linkage with the least number of bars.

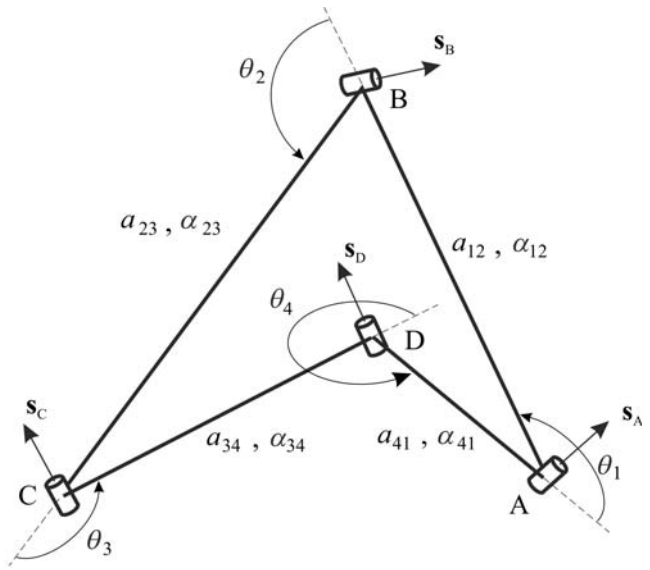

Fig. 1-4. The Bennett linkage.

The overconstrained geometric conditions of the Bennett linkage [52] are

$$a_{12} = a_{34} = a_1,\ a_{23} = a_{41} = a_2, \tag{1-17a}$$

$$\alpha_{12} = \alpha_{34} = \alpha,\ \alpha_{23} = \alpha_{41} = \beta, \tag{1-17b}$$

$$\frac{\sin\alpha}{a_1} = \frac{\sin\beta}{a_2}, \tag{1-17c}$$

$$R_i = 0\ (i = 1, 2, 3, 4). \tag{1-17d}$$

and its closure equations are

$$\theta_1 + \theta_3 = 2\pi,\ \theta_2 + \theta_4 = 2\pi, \tag{1-18a}$$

$$\tan\frac{\theta_1}{2}\tan\frac{\theta_2}{2} = \frac{\sin\frac{1}{2}(\beta+\alpha)}{\sin\frac{1}{2}(\beta-\alpha)}. \tag{1-18b}$$

All these parameters are defined according to D-H notation [8].

Baker derived its input-output equation and demonstrated the mobility is one [68], and also found that the four *R* joints in a Bennett linkage are related to the J-hyperboloid defined by its joint axes and its four links are also related to another hyperboloid called the L-hyperboloid defined by its links [69, 70].

The Goldberg 5*R* linkage [58] is obtained by combining a pair of Bennett linkages in such a way that a link common to both is removed and a pair of adjacent links is rigidly attached to each other. The techniques he developed can be summarised as the summation of two loops to produce another linkage, or the subtraction of a primary composite loop from another chain to form a new linkage. Similar to this method, a 6*R* linkage was generated by merging two Goldberg 5*R* linkages [63]. Another two double-Goldberg 6*R* linkages [71] were created by summation of Goldberg 5*R* linkages. Then a complete family of double-Goldberg 6*R* linkages was proposed [65] by combining a subtractive Goldberg 5*R* linkage and a Goldberg 5*R* linkage through the common link-pair or common Bennett-linkage method.

The Myard 5*R* linkage [57], proposed in 1931, is combined by two rectangular Bennett linkages with one pair of twist angles as $\frac{\pi}{2}$ [68], which can be classified as a special case of Goldberg 5*R* linkage. As shown in Fig. 1-5, Bennett linkages ABCD and ADCE are disposed as mirror images to each other. Combining them in the symmetric plane, the common *R* joint D and common links AD and CD are removed. Its geometric conditions are

$$
\begin{aligned}
&a_{34}=0,\, a_{12}=a_{51},\, a_{23}=a_{45};\\
&\alpha_{23}=\alpha_{45}=\frac{\pi}{2},\, \alpha_{51}=\pi-\alpha_{12},\, \alpha_{34}=\pi-2\alpha_{12};\\
&R_i=0\left(i=1,2,\cdots,5\right);\text{ and}\\
&a_{12}=a_{23}\sin\alpha_{12}.
\end{aligned}
\tag{1-19}
$$

And the closure equations are

$$
\begin{aligned}
&\theta_1+\theta_3+\theta_4=2\pi,\ \ \theta_2+\theta_5=2\pi,\\
&\tan\frac{\theta_4}{2}\tan\frac{\theta_5}{2}=\frac{\sin\frac{1}{2}\left(\frac{\pi}{2}+\alpha_{12}\right)}{\sin\frac{1}{2}\left(\frac{\pi}{2}-\alpha_{12}\right)},\\
&\tan\frac{\theta_2}{2}=\frac{\sin\frac{1}{2}\left(\frac{\pi}{2}+\alpha_{12}\right)}{\sin\frac{1}{2}\left(\frac{\pi}{2}-\alpha_{12}\right)}\tan\frac{\theta_3}{2}.
\end{aligned}
\tag{1-20}
$$

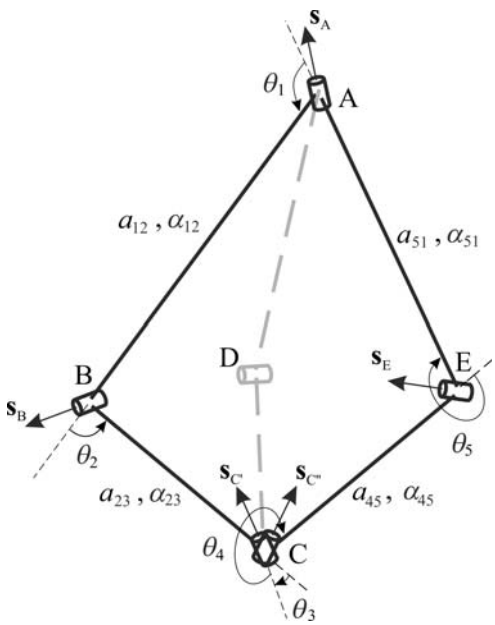

Fig. 1-5. The Myard 5*R* linkage.

The extended Myard 5*R* linkage [72] was obtained by combining two complementary Bennett linkages, where the twist is not necessary to be 90°.

Bricard proposed six types of mobile 6*R* linkage [55, 56], which are summarised as the general line-symmetric, the general plane-symmetric, the trihedral, the line-symmetric octahedral, the plane-symmetric octahedral, and the doubly collapsible octahedral cases as shown in Fig. 1-6. Their geometric conditions were summarised as follows [73]:

(a) The general line-symmetric case

$$\begin{aligned} &a_{12}=a_{45},\, a_{23}=a_{56},\, a_{34}=a_{61} \\ &\alpha_{12}=\alpha_{45},\, \alpha_{23}=\alpha_{56},\, \alpha_{34}=\alpha_{61} \\ &R_1=R_4,\, R_2=R_5,\, R_3=R_6 \end{aligned} \tag{1-21}$$

(b) The general plane-symmetric case

$$\begin{aligned} &a_{12}=a_{61},\, a_{23}=a_{56},\, a_{34}=a_{45} \\ &\alpha_{12}+\alpha_{61}=\pi,\, \alpha_{23}+\alpha_{56}=\pi,\, \alpha_{34}+\alpha_{45}=\pi \\ &R_1=R_4=0,\, R_2=R_6,\, R_3=R_5 \end{aligned} \tag{1-22}$$

(c) The trihedral case

$$\begin{aligned} &a_{12}^2+a_{34}^2+a_{56}^2=a_{23}^2+a_{45}^2+a_{61}^2 \\ &\alpha_{12}=\alpha_{34}=\alpha_{56}=\frac{\pi}{2},\, \alpha_{23}=\alpha_{45}=\alpha_{61}=\frac{\pi}{2} \\ &R_i=0\ (i=1,2,\cdots,6) \end{aligned} \tag{1-23}$$

(d) The line-symmetric octahedral case

$$\begin{aligned} &a_{12}=a_{23}=a_{34}=a_{45}=a_{56}=a_{61}=0 \\ &R_1+R_4=R_2+R_5=R_3+R_6=0 \end{aligned} \tag{1-24}$$

(e) The plane-symmetric octahedral case

$$\begin{aligned} &a_{12}=a_{23}=a_{34}=a_{45}=a_{56}=a_{61}=0 \\ &R_4=-R_1,\, R_2=-R_1\frac{\sin\alpha_{34}}{\sin(\alpha_{12}+\alpha_{34})},\, R_5=-R_1\frac{\sin\alpha_{61}}{\sin(\alpha_{45}+\alpha_{61})} \\ &R_3=-R_1\frac{\sin\alpha_{12}}{\sin(\alpha_{12}+\alpha_{34})},\, R_6=-R_1\frac{\sin\alpha_{45}}{\sin(\alpha_{45}+\alpha_{61})} \end{aligned} \tag{1-25}$$

(f) The doubly collapsible octahedral case

$$\begin{aligned} &a_{12}=a_{23}=a_{34}=a_{45}=a_{56}=a_{61}=0 \\ &R_1R_3R_5+R_2R_4R_6=0 \end{aligned} \tag{1-26}$$

Baker studied all these linkages, delineating them by appropriate sets of independent closure equations [74]. Wohlhart focused on the orthogonal Bricard linkage, and found that there are two distinct types [64]. The five input-output equations as explicit functions of the input angle were derived for both types of linkages. Chen and You studied a particular Bricard linkage with threefold symmetric [75], as shown in Fig. 1-7. Its geometric conditions are

$$\begin{aligned} &a_{12}=a_{23}=a_{34}=a_{45}=a_{56}=a_{61}=a \\ &\alpha_{12}=\alpha_{34}=\alpha_{56}=\alpha,\, \alpha_{23}=\alpha_{45}=\alpha_{61}=360^\circ-\alpha \\ &R_i=0\ (i=1,2,\cdots,6) \end{aligned} \tag{1-27}$$

Features of kinematic bifurcation were analysed in detail after deriving its closure equation.

Meanwhile, adopting its alternative forms, the linkage has some significant configurations with large deployable/packaging ratio, such as a deployed configuration as a hexagon and a folded configuration as a bundle.

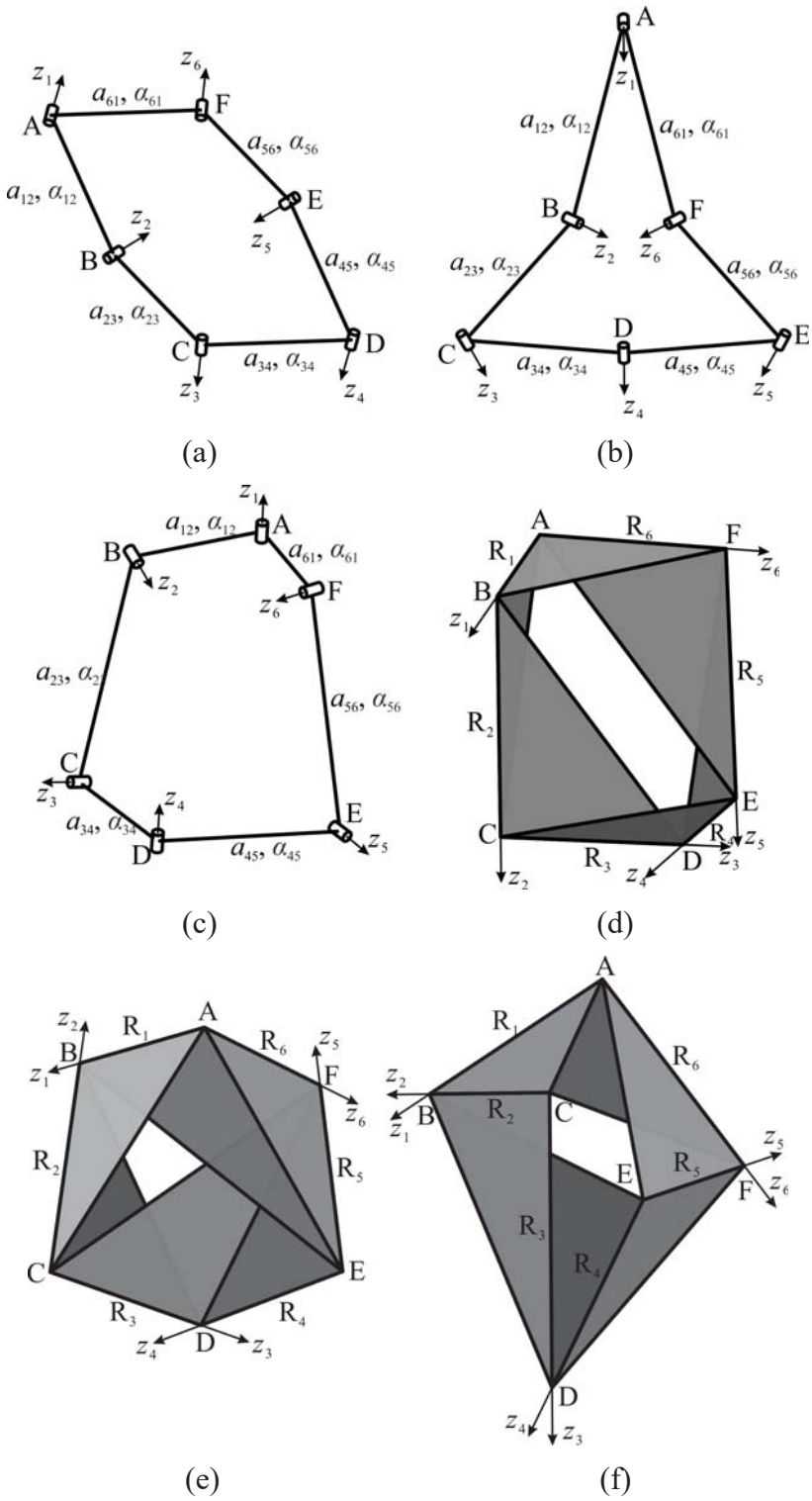

Fig. 1-6. Bricard 6*R* linkages. (a) The general line-symmetric case; (b) the general plane-symmetric case; (c) the trihedral case;(d) the line-symmetric octahedral case; (e) the plane-symmetric octahedral case; (f) the doubly collapsible octahedral case.

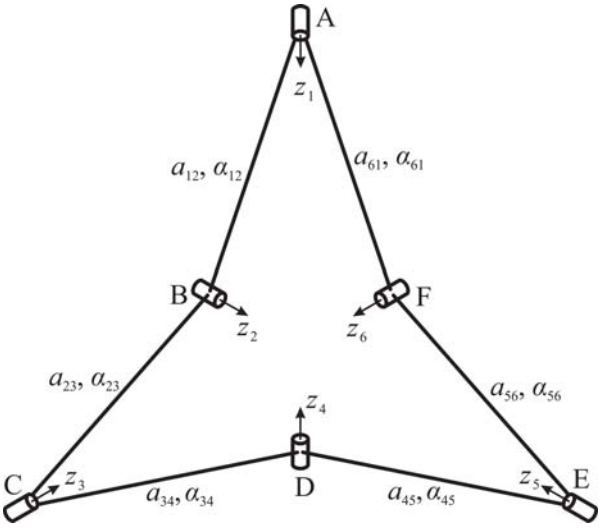

Fig. 1-7. Threefold-symmetric Bricard 6*R* linkage.

1.2.4 Engineering Applications of Overconstrained Linkages

Shang et al. presented a deployable robot based on this threefold-symmetric Bricard linkage, and the robot realises a large-scale transformation with a deployable area ratio of 39.3 [76]. Moreover, it is capable of moving through limited space easily by changing its configuration from folded to deployed, and vice versa. Kinematics of some other Bricard linkages were also researched in detail, such as kinematics and bifurcation situations of line-symmetric octahedral Bricard linkage [77], a special line and plane symmetric Bricard linkage [34], the original and revised general line-symmetric Bricard linkage [78]. Feng et al. derived the input-output formula analytically for the general plane-symmetric Bricard linkage, and its bifurcation cases were studied in detail [79].

Being with great rigidity and one DOF, overconstrained single-loop linkages are always adopted as elements to construct large deployable structures, which are capable of varying their shapes from a compact, folded configuration to an expanded, deployed configuration [80].

Analogising to Kempe's linkages [81], Baker and Yu presented some guidelines to construct multi-loop ensembles but only to an exploratory depth, and some candidates of possible mobile assemblies were proposed [82]. Then, according to these guidelines, Baker and Hu studied one particular assembly in detail and attempted to connect two Bennett linkages, but they obtained a rigid one with instantaneous mobility [83]. Chen summarised the methods to build network with Bennett linkages by three general ways [73], including single-loop network of Bennett linkages, multi-loop network of Bennett linkages, and connectivity of Bennett linkages [84, 85]. Chen and Baker used a Bennett linkage as a connector between other Bennett loops [86]. The alternative form of Bennett linkage to achieve compact

folding was studied in [87, 88]. Based on the alternative form of the Bennett linkage and square cross-section bars, Yu, Luo and Li developed a deployable membrane structure [89]. Guo and You built a deployable mast using the Bennett linkages as the basic element [90]. Baker obtained a collapsible network of similar pairs of nested Bennett linkages [91]. Yang et al. constructed a saddle-like surface with identical Bennett linkages [92], in which the deployment is driven by one DOF. Unlike other assemblies, configurations of elements in the obtained framework at general instantaneous movement are not the same to each other and grading varying. Lu, Zlatanov and Ding constructed a one-DOF network of Bennett linkages which can be deployed to approximate a cylindrical surface [93].

Besides of constructing deployable structures with Bennett linkages, other single-loop overconstrained linkages were also tried to construct large assemblies. Liu and Chen created a number of deployable blocks based on the Myard linkage. With these blocks, large deployable assemblies can be built [94]. These assemblies can transform between a deployed planar configuration and a folded compact bundle. Qi et al. built a quadrangular deployable module composed of four plane symmetric Bricard linkages [95], where the vertical links of the adjacent units are shared to be assembled. Huang et al. proposed some single DOF deployable networks using the threefold-symmetric Bricard mechanisms [96]. Song et al. proposed a large-scale modular deployable mechanical network constructed by networking Altmann linkages [97]. Then, Korkmaz and Kiper constructed alternatives of network with several identical single-loop Altmann linkages [98], which have both fully deployed and folded configurations.

Being capable to generate large deployable structures with low DOF and high rigidity, overconstrained linkages and their large networks have great potential application in various areas, such as civil engineering, aerospace, medicine. However, their engineering applications are very limited except 'Turbula' from Schatz linkage [99] and deployable structures from Bennett linkage [52, 53], Myard linkage [57], and Bricard linkage [56]. This is due to the fact that the strict overconstrained geometric conditions require very high precision in the manufacture, which is very difficult and costly to achieve in mass production. Thus, there is a conflict between the desired 3D motion and undesired overconstrained conditions. To overcome this problem, Milenkovic and Brown substituted an *S* joint for one of the *R* joints to reduce the degree of overconstraint in Bennett linkage, and reduced the closure relationship to two equations [100]. Lee and Hervé used oblique circular torus to find a *RRRS* linkage kinematically equivalent to the Bennett linkage [101]. However, the resultant linkages are still overconstrained. Therefore, it is a challenge to find the non-overconstrained forms of overconstrained linkages.

1.2.5 Polyhedral Linkages

On the other hand, polyhedral linkages are the most typically multi-loop. In geometry, two important classes of convex polyhedrons consisting of regular polygonal faces with highly symmetrical geometry are the Platonic solids and Archimedean solids [102]. The Platonic solids have only one type of regular polygonal faces, which include five polyhedrons: tetrahedron, cube, octahedron, dodecahedron, and icosahedron [103], whereas the Archimedean solids are composed of more than one types of regular polygonal faces, which have thirteen polyhedrons excluding the prisms and antiprisms [104].

Meanwhile, some transformations between Platonic and Archimedean solids can be achieved in numerous ways. Classical transformations such as truncation, cantellation, snub, and omnitruncation, are much studied and well understood geometrical operators [105].

In engineering, transformation of polyhedrons was first proposed by Buckminster Fuller [106], which was called Jitterbug as its transformation process is like the classical dance. A comprehensive list was provided by Clinton [107]. Such transformation involves rotation and translation of rigid facets. This, however, makes the transformation of little practical use as the space enclosed by the faces is taken up by the physical joints. If the axes of the cylindrical joints were not physically fixed together, the system would have six DOFs, as demonstrated by Buckminster Fuller's own model [108], making it impossible to complete the transformation in an orderly way.

The above example demonstrates that it is extremely challenging to accomplish the transformation of polyhedrons mechanically. To date two engineering approaches have been proposed. A modified Buckminster Fuller's Jitterbug capable of performing a symmetrical transformation between a regular octahedron and a cuboctahedron was fabricated at the Heureka Exposition, shown in Fig. 1-8, in Zurich in 1991 [109, 110] in which the cylindrical joints at the centres of the triangular faces were eliminated, and the *S* joints at vertices were replaced by universal joints.

Yet this approach cannot be extended to other paired polyhedrons as the numbers of DOFs would remain high (e.g., the truncated octahedron would end up with 18 DOFs). Verheyen fabricated some Jitterbug-like polyhedrons where each triangular faces were made into two layers joined by an *R* joint (hinge joint), whereas the *S* joints at vertices remained [111, 112]. The resulted double layered structures were far too complex and rather unstable during the transformation due to the existence of motion bifurcations.

Fig. 1-8. The Heureka [110].

Apart from the above attempts, other transformable polyhedron models were also produced where no shape transformation between a Platonic solid and an Archimedean solid exists. For instance, Agrawal et al. constructed a 1-DOF expanding polyhedron by installing telescopic bars on each side of a polyhedron [113]. The polyhedron preserved its shape when volumetric change took place. A toy known as the Switch Pitch [114] was generated using a centrally geared expanding mechanism within the central void. Wohlhart [115], Kiper [116], and Roschel [117, 118] used gussets and *R* joints, Li, Yao and Kong [119] used multi-layer extended paralledlogram linkages to construct shape-unchanged expandable polyhedrons. Wohlhart [120, 121, 122], Gosselin and Gagnon-Lachance [123], Laliberté and Gosselin [124], as well as Wei and Dai [125, 126, 127] proposed a number of expandable polyhedrons, but expansion ended up with irregular polyhedral shapes. Kiper and Söylemez [128, 129] introduced the overconstrained Bennett linkage to regular polyhedrons, resulted in structures with a rather small expansion ratio. Shim et al., [130] suggested synchronising the transformation by applying a uniformly distributed pressure. This approach, however, works only for polyhedrons made from relative soft materials, and because of that, their behaviour becomes both material and loading dependent.

Although polyhedral transformation undergone a rather long period of study, solutions for practical applications are still lacked. Not only are transformable polyhedrons mathematically interesting, but they also have many potential applications, e.g., they form perfect habitats for space travel which have growth capability [131], and they may be used to package a CubeSat to a small volume for

launch which then expand to a considerably large structure once it reaches the orbit. The rigid facets are ideal for mounting electronic devices such as solar panels [132]. Therefore, a mechanical transformable polyhedron requires, first of all, the number of DOF to be low so that the transformation can be easily controlled, and secondly, the central void must not be taken up by complex joints or control systems. The limitations of existing concepts prompt us to devise an effective method to transform polyhedrons amongst paired Platonic and Archimedean solids with one DOF. This objective is achieved by the introduction of spatial linkages.

We can match polyhedrons between two kinds of solids based on the same number of identical polygons. For example, tetrahedron and truncated tetrahedron both have four triangles. Take the triangle as rigid piece and hexagon as hollow one formed by six links connected by moving joints. If we can move the triangles in the truncated tetrahedron into the position as tetrahedron and vanish four hexagons in the truncated tetrahedron, the transformation between them can be realised. Following this rule, all the possible transformations are listed in Table 1-1. Totally, there are eight matches between Platonic and Archimedes solids numbered as 1-5 and 9-11, among which No. 5 is the transformation between rhombicuboctahedron and octahedron via or not via cub-octahedron, and No. 11 is between rhombicosidodecahedron and icosidodecahedron, both belonging to Archimedes solids.

We have found that the transformations are actually realised by folding motions of those hollowed polygons, which are connected as multi-loops. Therefore, multi-loop linkages are potential to realise polyhedral transformations, whose designs and kinematic analysis can be performed by employing the truss method.

1.3 Aim and Scope

Studying in the interdiscipnary area of kinematics and structure, the aim of this dissertation is to develop a truss method by converting 3D linkages to their equivalent truss forms, and employing methods in structural engineering to analyse complicated 3D overconstrained linkages and design new transformable linkages with deployable functions.

In this process, we first expound how to convert 3D linkages to their truss forms and compare the relationship between the truss method and the conventional kinematic method. Then based on the truss method, overconstrained linkages are analysed, and an approach to seek non-overconstrained forms of overconstrained linkages is studied. Finally, we look into the design of three pairs of transformable polyhedrons.

Table 1-1. All possible transformations between Platonic and Archimedean polyhedrons

No.	Archimedean polyhedrons				Platonic polyhedrons	
1	 Truncated tetrahedron	4 triangles 4 hexagons			 Tetrahedron	4 triangles
2	 Cuboctahedron	8 triangles 6 squares			 Octahedron	8 triangles
3	 Truncated cube	8 triangles 6 octagons			 Octahedron	8 triangles
4	 Truncated octahedron	6 squares 8 hexagons			 Cube	6 squares
5	 Rhombicuboctahedron	8 triangles 18 squares	 Cuboctahedron	8 triangles 6 squares	 Octahedron	8 triangles
6	 Truncated cuboctahedron	12 squares 8 hexagons 6 octagons			--	
7	 Snub cube (cuboctahedron)	32 triangles 6 squares			--	
8	 icosidodecahedron	20 triangles 12 pentagons			--	
9	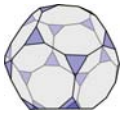 Truncated dodecahedron	20 triangles 12 decagons			 Icosahedron	20 triangles
10	 Truncated icosahedron	12 pentagons 20 hexagons			 Dodecahedron	12 pentagons

Table 1-1. All possible transformations between Platonic and Archimedean polyhedrons (Continued)

No.	Archimedean polyhedrons				Platonic polyhedrons
11	 Rhombicosidodecahedron	20 triangles 30 squares 12 pentagons	 Icosido-decahedron	20 triangles 12 pentagons	--
12	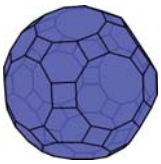 Truncated icosidodecahedron	30 squares 20 hexagons 12 decagons			--
13	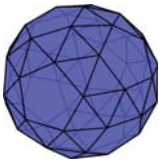 Snub dodecahedron	80 triangles 12 pentagons			--

1.4 Outline of Dissertation

This dissertation consists of seven chapters, which are outlined as follows.

Chapter 2 presents a method to transform 3D linkages to their equivalent truss forms, and then mobility calculation, motion path generation, and bifurcation detection can be performed by studying their equilibrium matrices. Its validity is verified by a threefold-symmetric Bricard 6*R* linkage. The discussion on the relationship between kinematic Jacobian matrix of linkages and equilibrium matrix of the truss form and conclusions end this chapter.

Chapter 3 deals with the technique to seek non-overconstrained forms of overconstrained linkages. It is achieved by detecting and removing redundant bars from truss forms of original linkages, whose generality is proven by taking Bennett 4*R* linkage and Myard 5*R* linkage as examples. Output errors, which are produced by fabrication errors on link length and twist, and sensitivities of these factors are analysed to show the advantage of non-overconstrained forms. This chapter is ended with the conclusions.

Chapter 4 is to construct a deployable 3D solid with Bennett linkage. A spatial multi-loop linkage, constructed with 2 Bennett linkages and 4 *RSRS* linkages, is obtained to realise the transformation between cuboctahedron and octahedron with one DOF, where each vertex is set with one *R* joint or *S* joint. Joint arrangement and directions are determined by geometrical analysis. A metal prototype demonstrates the

validity of the designed result. Finally, kinematics study and conclusions end this chapter.

Chapter 5 is devoted to construct a polyhedral transformation between truncated octahedron and cube with one DOF. The first step is to consider a threefold-symmetric Bricard 6*R* linkage to realise the folding of one hollowed hexagonal face as compositions of all hexagonal faces are all threefold-symmetric. Introducing more constraints, its one-DOF solution is obtained after setting two Bricard linkages with the same parameters, where mobility is calculated by the proposed truss method. Then, a 3D printed prototype validates the transformation process. The last section is the discussion on parameter study and conclusion.

Chapter 6 focuses on the pair of polyhedrons, the truncated tetrahedron and tetrahedron. One-DOF transformation of them is achieved with two schemes of spatial linkages constructed with 1 threefold-symmetric Bricard 6*R* linkage and 3 *RSRRSR* linkages (or 3 *RRSSRR* linkages), where the expansion/packing ratio in volume is up to 23. The prototype is fabricated by equaling an *S* joint to three folding creases with the origami folding technique. For both constructions, possible ranges to realise the transformation without physical interference has been found through the discussion on the folding performance under different joint directions.

The main achievements of the research are summarised in Chapter 7, together with suggestions for future works, which concludes this dissertation.

Chapter 2 Truss Method by Analogying 3D Linkages to Trusses

2.1 Introduction

In this chapter, we proposed a method for transforming 3D linkages into their truss forms, then kinematics, including mobility calculation, motion path generation and bifurcation detection, can be studied based on analysing equilibrium matrix of truss forms.

The layout of this chapter is as follows. Section 2.2 expounds how to transform linkages into their truss forms, based on which mobility and degrees of overconstraint can be obtained in Section 2.3. Section 2.4 shows a numerical approach to simulate motion paths of linkages based on the truss analogy. The relationship between Jacobian matrix in mechanism and equilibrium matrix in truss is derived in Section 2.5. Discussion and conclusions in Section 2.6 end this chapter.

2.2 Truss analogy

As truss is formed by straight bars connected by nodes, a rigid body in space can be represented by a straight bar or a tetrahedron with six bars connected by four nodes, see Fig. 2-1(a). From the kinematic point of view, a straight bar is a link and a node is an *S* joint. Then an *R* joint can be represented by a straight bar with one node (*S* joint) at each end, see Fig. 2-1(b), so that the links connected to it can generate revolute motion about the axis along the straight bar, or the line passing through two *S* joints, as shown in Fig. 2-1(c).

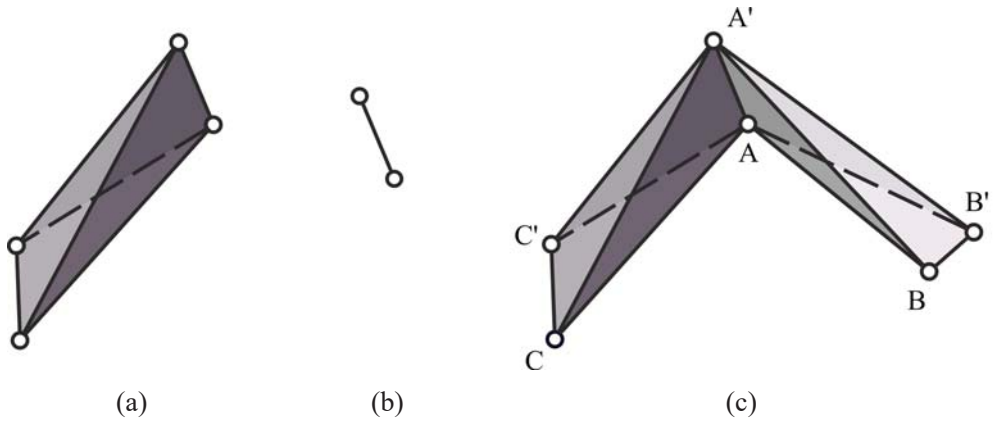

Fig. 2-1. Truss equivalence. (a) A tetrahedron as a rigid body; (b) two *S* joints connected by one straight bar as an *R* joint; (c) two rigid bodies connected by one *R* joint.

In general, a link connected with two *R* joints is equivalent to a truss tetrahedron taking AA', CC' as *R* joint axes, see Fig. 2-2(a). Thus, AA', CC' are called

joint bars. AC, AC', $A'C$, and $A'C'$ are called *body bars*. In kinematics, link is usually the shortest distance between two *R* joints. Here, AC is the shortest link in Fig. 2-2(a), i.e., $AC \perp AA'$ and $AC \perp CC'$. AC', $A'C$ and $A'C'$ can be considered as alternative links [87] between *R* joints AA' and CC'. When the two *R* joint axes intersect, a tetrahedron degenerates into a triangle, see Fig. 2-2(b). And for the parallel axes, all bars in the tetrahedron are in a plane, see Fig. 2-2(c), which has one instantaneous mobility. To avoid it, an arbitrary point out of the plane, P, is introduced, see Fig. 2-2(d), to generate the truss form for the link with two parallel axes.

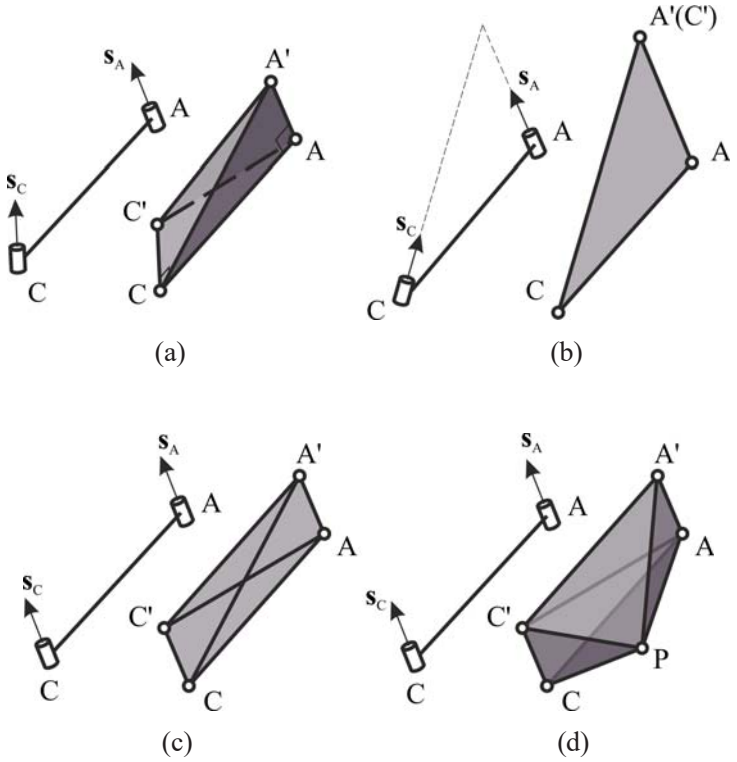

Fig. 2-2. One link with two *R* joints. (a) common situation; (b) two intersecting revolute axes; (c) two parallel revolute axes with an instantaneous mobility; (d) two parallel revolute axes.

In such a way, 3D linkages with *R* joints and *S* joints can be transformed into their truss forms. For example, a threefold-symmetric Bricard linkage [79] in Fig. 2-3(a) is transformed to its truss form as shown in Fig. 2-3(b), where black thick lines and black points are original bars and positions of joints, thick gray lines are along corresponding *R* joints, thin gray lines and gray points are to form bars with *R* joints.

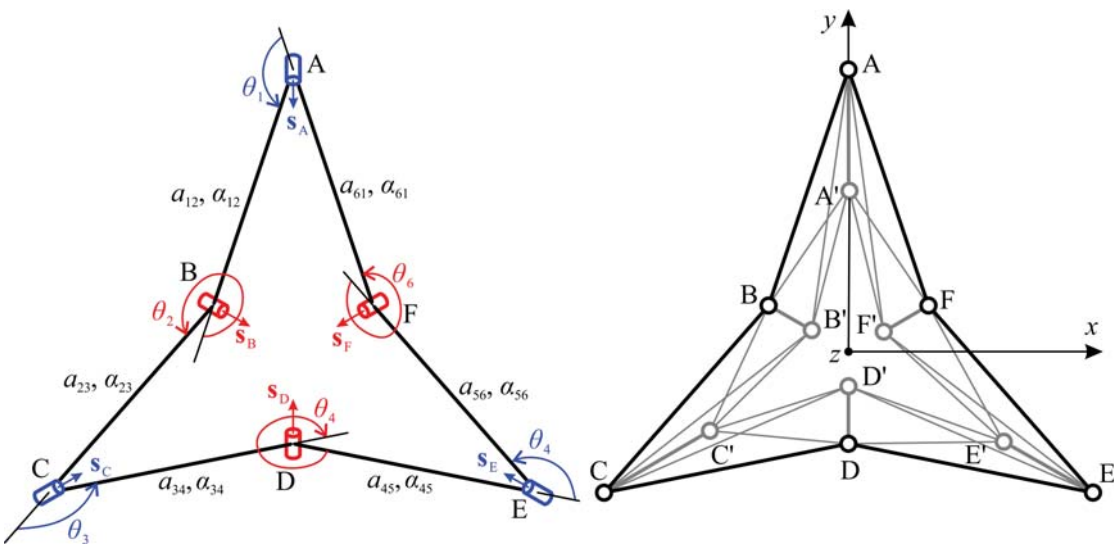

(a) (b)

Fig. 2-3. Kinematic analysis of a threefold-symmetric Bricard linkage by transforming (a) its original form to (b) its truss form.

2.3 Kinematic Analysis with Equilibrium Equation of Truss Form

After the truss analogy, a 3D linkage could be transformed to its truss form with j nodes and b bars. According to Maxwell's rule, when $3j-6-b=0$, the truss is stiff without self-stress, e.g., the tetrahedron in Fig. 2-1(a) with $j=4$, $b=6$. When $3j-6-b>0$, the truss has mobility, $m=3j-6-b$, e.g., the system in Fig. 2-1(c) with $j=6$, $b=11$, and $m=1$. When $3j-6-b<0$, the truss should be stiff and statically indeterminate.

For the threefold-symmetric Bricard linkage in Fig. 2-3(a), a well-known spatial 6*R* linkage with mobility one, its truss form in Fig. 2-3(b) has $j=12$ nodes, $b=30$ bars, and $3j-6-b=0$. Thus it is statically indeterminate, i.e., overconstrained. In this case, the equilibrium equation has to be considered [133, 134].

$$\boldsymbol{Ht}=\boldsymbol{f}, \tag{2-1}$$

in which $\boldsymbol{t}$ is a $b\times 1$ vector of bar axial forces per unit length, $\boldsymbol{f}$ is a $3j\times 1$ vector of node forces, and $\boldsymbol{H}$ is a $3j\times b$ equilibrium matrix which might not be full ranked. Here we only consider the truss without external forces, i.e., $\boldsymbol{f}=\boldsymbol{0}$. Then Eq. (2-1) becomes a set of homogenous linear equations

$$\boldsymbol{Ht}=\boldsymbol{0}. \tag{2-2}$$

Take r as the rank of equilibrium matrix $\boldsymbol{H}$. Analysing the homogenous equilibrium equation, Eq. (2-2), gives the number of self-stresses,

$$s = b - r\,. \tag{2-3}$$

Meanwhile, the following compatibility equations should be satisfied according to structure mechanics,

$$\boldsymbol{Cd} = \boldsymbol{e}\,, \tag{2-4}$$

where **d** is the vector of node displacements, **e** is the vector of bar elongations, **C** is the compatibility matrix. As links in linkages are always assumed to be rigid, there is no elongation of any bars, i.e., $\boldsymbol{e} = \mathbf{0}$. Then, Eq. (2-4) becomes a set of homogenous linear equations

$$\boldsymbol{Cd} = \mathbf{0}\,. \tag{2-5}$$

According to the principle of virtual work, the compatibility matrix is the transposition of the equilibrium matrix [39],

$$\boldsymbol{C} = \boldsymbol{H}^{\mathrm{T}}\,. \tag{2-6}$$

Therefore, the number of inextensional mechanisms (mobility) is

$$m = 3j - 6 - r\,. \tag{2-7}$$

Hereto, m and s, degrees of freedom and overconstraint of the 3D linkage, respectively, can be obtained by the truss method at the same time.

Then, the threefold-symmetric Bricard linkage, shown in Fig. 2-3(a), with detailed parameters is taken as the example to verify its mobility by this method, whose design parameters are

$$a_{12} = a_{23} = a_{34} = a_{45} = a_{56} = a_{61} = 1 \tag{2-8}$$

and

$$\begin{aligned} \alpha_{12} = \alpha_{34} = \alpha_{56} &= \frac{2\pi}{3} \\ \alpha_{23} = \alpha_{45} = \alpha_{61} &= \frac{\pi}{3} \end{aligned}\,. \tag{2-9}$$

A configuration of this linkage is placed in a Cartesian coordinate system on the centre of triangle BDF, and coordinate of vertices are

$$\begin{aligned} \boldsymbol{A} &= [0, 1.1372, 0.1569]^{\mathrm{T}} \\ \boldsymbol{B} &= [-0.4280, 0.2471, 0]^{\mathrm{T}} \\ \boldsymbol{C} &= [-0.9848, -0.5686, 0.1569]^{\mathrm{T}} \\ \boldsymbol{D} &= [0, -0.4943, 0]^{\mathrm{T}} \\ \boldsymbol{E} &= [0.9848, -0.5686, 0.1569]^{\mathrm{T}} \\ \boldsymbol{F} &= [0.4281, 0.2471, 0]^{\mathrm{T}} \end{aligned}\,. \tag{2-10}$$

After the truss analogy, six more nodes are added along corresponding axes in in its truss form

$$\begin{aligned}
\boldsymbol{A}' &= [0, 1.1198, 0.2554]^{\mathrm{T}} \\
\boldsymbol{B}' &= [-0.3498, 0.2019, 0.0428]^{\mathrm{T}} \\
\boldsymbol{C}' &= [-0.9698, -0.5599, 0.2554]^{\mathrm{T}} \\
\boldsymbol{D}' &= [0, -0.4039, 0.0428]^{\mathrm{T}} \\
\boldsymbol{E}' &= [0.9698, -0.5599, 0.2554]^{\mathrm{T}} \\
\boldsymbol{F}' &= [0.3498, 0.2019, 0.0428]^{\mathrm{T}}
\end{aligned} . \tag{2-11}$$

It is easy to verify that Eqs. (2-8) and (2-9) are satisfied by calculating link lengths and twist angles, i.e., it is indeed one configuration of threefold-symmetric Bricard linkage.

Then, its equilibrium matrix can be established according to [39]. The mobility can be obtained according to Eq. (2-7) after calculating the rank of the above matrix, $m = 3j - 6 - r = 1$.

2.4 Motion Path and Bifurcation Detection

Although analytical solution of kinematics is always the best desired result in mechanism, there are still a lot of linkages without analytical solutions or their solutions are rather difficult to solve, such as kinematics of multi-loop linkages with complex topology. To deal with this problem, a numerical approach was proposed by Kumar and Pellegrino [43]. It is called predictor-corrector algorithm, and it can detect bifurcation points with singular values of equilibrium matrices.

Being transformed to the truss form, equilibrium equation can be established. Then filtering ground joints and bars, for an equilibrium matrix $\boldsymbol{H}'$ with dimensions $3j \times b$ and rank *r*, there exist: a $3j \times 3j$ orthogonal matrix $\boldsymbol{U} = [\boldsymbol{u}_1, \cdots, \boldsymbol{u}_{3j}]$; a $b \times b$ orthogonal matrix $\boldsymbol{W} = [\boldsymbol{w}_1, \cdots \boldsymbol{w}_b]$; and a $b \times b$ matrix **V** with *r* positive elements v_i (i = 1, … , r) on the leading diagonal, such that

$$\boldsymbol{H}' = \boldsymbol{U}\boldsymbol{V}\boldsymbol{W}^{\mathrm{T}} . \tag{2-12}$$

It is the SVD of the equilibrium matrix **H'**. According to Eq. (2-7), the left singular vectors **U**, the set of right singular vectors **W** and the set of non-zero singular values **V** are

$$\boldsymbol{U} = [\boldsymbol{u}_1, \cdots, \boldsymbol{u}_r, \boldsymbol{u}_{r+1}, \cdots, \boldsymbol{u}_{r+m}], \tag{2-13}$$

$$\boldsymbol{W} = [\boldsymbol{w}_1, \cdots, \boldsymbol{w}_r, \boldsymbol{w}_{r+1}, \cdots, \boldsymbol{w}_{r+s}], \tag{2-14}$$

$$\boldsymbol{V} = \begin{bmatrix} \mathrm{diag}(v_1, \cdots, v_r) & \mathbf{0} \\ \mathbf{0} & \mathbf{0} \end{bmatrix} . \tag{2-15}$$

As each linkage obtained by our method is always with one DOF, the left

singular vectors **U** becomes

$$\boldsymbol{U} = [\boldsymbol{u}_1, \cdots, \boldsymbol{u}_r, \boldsymbol{u}_{r+1}], \tag{2-16}$$

and it moves along a determined kinematic path generally. According to [39], the left nullspace of $\boldsymbol{H}'$, $\boldsymbol{u}_{r+1}$, is precisely the space spanned by the m independent inextensional mechanisms of the assembly. Assume the current configuration is $\boldsymbol{R}^i$, then the next configuration of the linkage is predicted as

$$\boldsymbol{R}^{i'} = \boldsymbol{R}^i + \boldsymbol{u}_{r+1}^i \eta , \tag{2-17}$$

η is used to control the motion direction and the transformation speed. As the configuration $\boldsymbol{R}^{i'}$ is not an exact one in the motion path, bars of the truss form of the linkage undergone extensions $\boldsymbol{e}$. A set of correcting displacements $\boldsymbol{d}_{\mathrm{c}}$ on all vertices was adopted to eliminate those extensions to correct the configuration [134],

$$\boldsymbol{d}_{\mathrm{c}} = -\sum_{i=1}^{r} \frac{\boldsymbol{w}_i^{\mathrm{T}} \boldsymbol{e}}{v_i} \boldsymbol{u}_i . \tag{2-18}$$

Thus, the configuration $\boldsymbol{R}^{i+1} = \boldsymbol{R}^{i'} + \boldsymbol{d}_{\mathrm{c}}$ is the strain-free configuration nearest to $\boldsymbol{R}^i$, and Fig. 2-4 shows operations of one step in the iteration process. This corrector step can be repeated a number of times until a desired convergence accuracy is achieved.

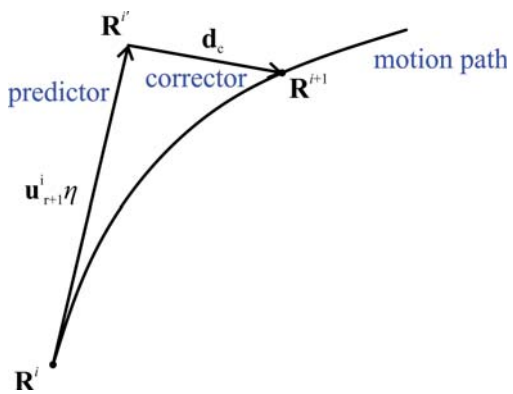

Fig. 2-4. Predictor-corrector algorithm in each iteration step of the numerical method proposed by Kumar and Pellegrino [43].

As the rank of equilibrium matrix, $\boldsymbol{H}$, is related with the number of non-zero singular values in $\boldsymbol{V}$, thus instantaneous mobility equals to the number of zero-valued singular values in $\boldsymbol{V}$. Therefore, bifurcation positions can be detected by singular values of $\boldsymbol{V}$ during motion process. Figure 2-5(a) shows kinematic curves between kinematic angles θ and ϕ.

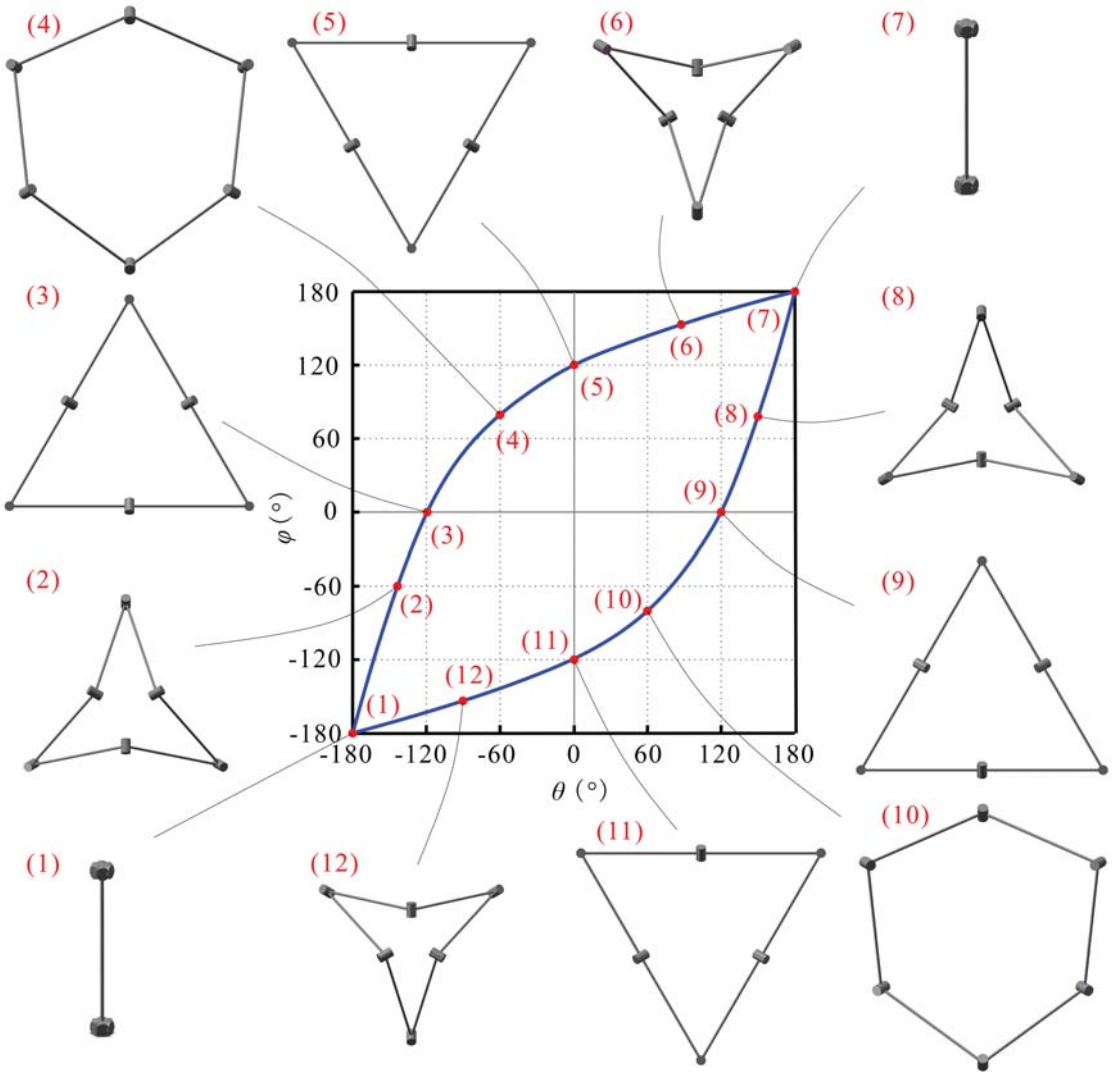

(a)

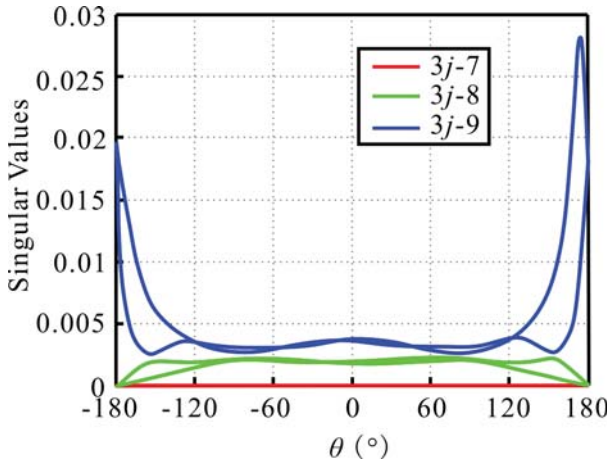

(b)

Fig. 2-5. Kinematic behaviour of the threefold-symmetric Bricard linkage. (a) Curves among folding angles at all joints, and (b) singular values recorded by the numerical algorithm after the truss analogy.

And singular values were recorded at the same time as shown in Fig. 2-5(b). The smallest value keeps equaling zero, and second last singular value, 3*j*-8, is generally far from zero except two configurations, i.e., $\theta = -180°$ and $\theta = 180°$. Therefore, the linkage is always movable, and there are two bifurcation positions at two folded configurations, i.e., six bars being folded as a bundle. Meanwhile, according to kinematic curves, we can find that there are two motion paths. The result matches well to the conclusion from [73], which shows that this numerical algorithm based on the truss method is credible.

2.5 Relationship between Jacobian Matrix of Mechanism and Equilibrium Matrix of Truss

Chen and Chai shown that kinematic behaviours, including motion path and bifurcation detection, of 3D linkages can be realised by a numerical algorithm based on SVD of kinematic Jacobian matrix [34]. While, those kinematic behaviours can also be obtained by the approach, described in section 2.4, based on SVD of equilibrium matrix of the truss form of the 3D linkage. Therefore, there must be some relationship between the kinematic Jacobian matrix and the equilibrium matrix.

In the following parts, planar 4*R* linkage and spherical 4*R* linkages are taken as examples to show the relationship between those two matrices.

2.5.1 Planar 4*R* Linkage

For a planar 4*R* linkage, see Fig. 2-6, a Cartesian coordinate system is established, where A is the origin, *x* axis directs from D to A, *y* axis directs upward, and *z* axis is determined by the right-hand rule. Obviously, it can also be viewed as its truss form in the plane.

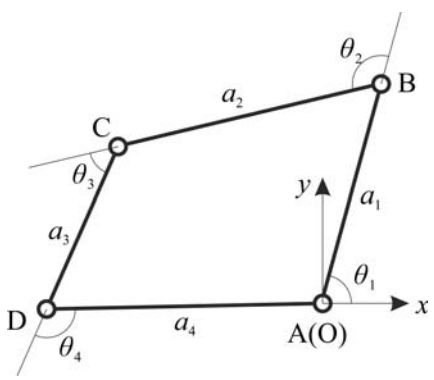

Fig. 2-6. Kinematics of planar 4*R* linkage.

Denoting joint kinematic angles at A, B, C, D as θ_1, θ_2, θ_3, θ_4 respectively. Therefore, coordinates of all vertices are

$$\boldsymbol{B} = \left[a_1 \cos\theta_1, a_1 \sin\theta_1\right]^{\mathrm{T}}, \tag{2-19}$$

$$\boldsymbol{C} = \left[a_1 \cos\theta_1 + a_2 \cos(\theta_1+\theta_2), a_1 \sin\theta_1 + a_2 \sin(\theta_1+\theta_2)\right]^{\mathrm{T}}, \tag{2-20}$$

$$\boldsymbol{D} = \begin{bmatrix} a_1 \cos\theta_1 + a_2 \cos(\theta_1+\theta_2) + a_3 \cos(\theta_1+\theta_2+\theta_3) \\ a_1 \sin\theta_1 + a_2 \sin(\theta_1+\theta_2) + a_3 \sin(\theta_1+\theta_2+\theta_3) \end{bmatrix}, \tag{2-21}$$

$$\boldsymbol{A} = \begin{bmatrix} a_1 \cos\theta_1 + a_2 \cos(\theta_1+\theta_2) + a_3 \cos(\theta_1+\theta_2+\theta_3) + a_4 \cos(\theta_1+\theta_2+\theta_3+\theta_4) \\ a_1 \sin\theta_1 + a_2 \sin(\theta_1+\theta_2) + a_3 \sin(\theta_1+\theta_2+\theta_3) + a_4 \sin(\theta_1+\theta_2+\theta_3+\theta_4) \end{bmatrix}. \tag{2-22}$$

Thus the velocity of vertex A is

$$\begin{bmatrix} v_{\mathrm{Ax}} \\ v_{\mathrm{Ay}} \\ w_{\mathrm{Az}} \end{bmatrix} = \boldsymbol{J} \begin{bmatrix} \dot{\theta}_1 \\ \dot{\theta}_2 \\ \dot{\theta}_3 \\ \dot{\theta}_4 \end{bmatrix} = \begin{bmatrix} 0 \\ 0 \\ 0 \end{bmatrix}, \tag{2-23}$$

where

$$\boldsymbol{J} = \begin{bmatrix} J_{11} & J_{12} & J_{13} & J_{14} \\ J_{21} & J_{22} & J_{23} & J_{24} \\ 1 & 1 & 1 & 1 \end{bmatrix}. \tag{2-24}$$

And each element is

$$J_{11} = -y_{\mathrm{A}} = 0,\ J_{12} = -y_{\mathrm{A}} + y_{\mathrm{B}},\ J_{13} = -y_{\mathrm{A}} + y_{\mathrm{C}},\ J_{14} = -y_{\mathrm{A}} + y_{\mathrm{D}}, \tag{2-25}$$

$$J_{21} = -x_{\mathrm{A}} = 0,\ J_{22} = -x_{\mathrm{A}} + x_{\mathrm{B}},\ J_{23} = -x_{\mathrm{A}} + x_{\mathrm{C}},\ J_{24} = -x_{\mathrm{A}} + x_{\mathrm{D}}. \tag{2-26}$$

$\boldsymbol{J}$ is the Jacobian matrix. By some column transformations, $c_1 - c_2$, $c_2 - c_3$, $c_3 - c_4$, it becomes

$$\boldsymbol{J}_1 = \begin{bmatrix} y_{\mathrm{A}} - y_{\mathrm{B}} & y_{\mathrm{B}} - y_{\mathrm{C}} & y_{\mathrm{C}} - y_{\mathrm{D}} & y_{\mathrm{D}} - y_{\mathrm{A}} \\ x_{\mathrm{B}} - x_{\mathrm{A}} & x_{\mathrm{C}} - x_{\mathrm{B}} & x_{\mathrm{D}} - x_{\mathrm{C}} & x_{\mathrm{A}} - x_{\mathrm{D}} \\ 0 & 0 & 0 & 1 \end{bmatrix}, \tag{2-27}$$

where $c_{\mathrm{i}} - c_{\mathrm{j}}$ represents the ith column is subtracted by the jth column.

This linkage can be viewed as a planar truss with four joints and four bars, its equilibrium matrix is

$$\boldsymbol{H}=\begin{bmatrix} x_A-x_B & & & x_A-x_D \\ y_A-y_B & & & y_A-y_D \\ x_B-x_A & x_B-x_C & & \\ y_B-y_A & y_B-y_C & & \\ & x_C-x_B & x_C-x_D & \\ & y_C-y_B & y_C-y_D & \\ & & x_D-x_C & x_D-x_A \\ & & y_D-y_C & y_D-y_A \end{bmatrix}. \tag{2-28}$$

By some row transformations, r_1+r_5, r_2+r_6, r_3+r_7, r_4+r_8, $\boldsymbol{H}$ becomes

$$\boldsymbol{H}_1=\begin{bmatrix} x_A-x_B & x_C-x_B & x_C-x_D & x_A-x_D \\ y_A-y_B & y_C-y_B & y_C-y_D & y_A-y_D \\ x_B-x_A & x_B-x_C & x_D-x_C & x_D-x_A \\ y_B-y_A & y_B-y_C & y_D-y_C & y_D-y_A \\ & x_C-x_B & x_C-x_D & \\ & y_C-y_B & y_C-y_D & \\ & & x_D-x_C & x_D-x_A \\ & & y_D-y_C & y_D-y_A \end{bmatrix}, \tag{2-29}$$

where r_i+r_j represents the ith row is added by the jth row. A serial of transformations are followed, r_1+r_3, r_2+r_4, r_5+r_7, r_6+r_8, then the matrix becomes

$$\boldsymbol{H}_2=\begin{bmatrix} 0 & 0 & 0 & 0 \\ 0 & 0 & 0 & 0 \\ x_B-x_A & x_B-x_C & x_D-x_C & x_D-x_A \\ y_B-y_A & y_B-y_C & y_D-y_C & y_D-y_A \\ & x_C-x_B & x_C-x_D & \\ & y_C-y_B & y_C-y_D & \\ & & x_D-x_C & x_D-x_A \\ & & y_D-y_C & y_D-y_A \end{bmatrix}. \tag{2-30}$$

Then, after exchanging the 3rd row and the 4th row,

$$\boldsymbol{H}_3=\begin{bmatrix} 0 & 0 & 0 & 0 \\ 0 & 0 & 0 & 0 \\ y_A-y_B & y_B-y_C & y_C-y_D & y_D-y_A \\ x_B-x_A & x_C-x_B & x_D-x_C & x_A-x_D \\ & x_B-x_C & x_C-x_D & \\ & y_B-y_C & y_C-y_D & \\ & & x_D-x_C & x_A-x_D \\ & & y_D-y_C & y_A-y_D \end{bmatrix}. \tag{2-31}$$

The matrix is briefly denoted as

$$\boldsymbol{H}_3 = \begin{bmatrix} \boldsymbol{0} \\ \boldsymbol{0} \\ \boldsymbol{M} \\ \boldsymbol{N}_2 \end{bmatrix}, \tag{2-32}$$

where

$$\boldsymbol{M} = \begin{bmatrix} y_A - y_B & y_B - y_C & y_C - y_D & y_D - y_A \\ x_B - x_A & x_C - x_B & x_D - x_C & x_A - x_D \end{bmatrix}, \tag{2-33}$$

$$\boldsymbol{N}_2 = \begin{bmatrix} 0 & x_B - x_C & x_C - x_D & 0 \\ 0 & y_B - y_C & y_C - y_D & 0 \\ 0 & 0 & x_D - x_C & x_A - x_D \\ 0 & 0 & y_D - y_C & y_A - y_D \end{bmatrix}. \tag{2-34}$$

$\boldsymbol{J}_1$ in Eq. (2-27) can also be denoted as

$$\boldsymbol{J}_1 = \begin{bmatrix} \boldsymbol{M} \\ \boldsymbol{N}_1 \end{bmatrix}, \tag{2-35}$$

where

$$\boldsymbol{N}_1 = \begin{bmatrix} 0 & 0 & 0 & 1 \end{bmatrix}. \tag{2-36}$$

Obviously,

$$rank(\boldsymbol{N}_1) = 1, \tag{2-37}$$

$$rank(\boldsymbol{N}_2) = 3. \tag{2-38}$$

Therefore, Jacobian matrix and equilibrium matrix are both related with the variable matrix M. Meanwhile, mobility can be calculated from equilibrium,

$$m = 2j - 3 - r = 5 - rank(\boldsymbol{H}_3) = 2 - rank(\boldsymbol{M}). \tag{2-39}$$

And, mobility calculated from Jacobian matrix is

$$m = 3 - rank(\boldsymbol{J}) = 2 - rank(\boldsymbol{M}). \tag{2-40}$$

Therefore, considering Eqs. (2-35), (2-37), mobility, calculated by the mechanical method and the truss method, is the same with $2 - rank(\boldsymbol{M})$.

By linear transformations according to Eqs. (2-29, 30, 31), the matrix $\boldsymbol{M}$ can be generated from the equilibrium matrix. Then, the matrix $\boldsymbol{J}_1$ can be constructed by $\boldsymbol{M}$ and constant matrix $\boldsymbol{N}$, shown in Eq. (2-35). Finally, Jacobian matrix $\boldsymbol{J}$ can be obtained from $\boldsymbol{J}_1$ by the inverse operation of Eq. (2-27). On the other hand, equilibrium matrix $\boldsymbol{H}$ can also be obtained from Jacobian matrix $\boldsymbol{J}$ from Eqs. (2-29, 30, 31, 33, 34). Therefore, these two matrices are equivalent to each other.

2.5.2 Spherical 4*R* Linkage

For a spherical 4*R* linkage, see Fig. 2-7(a), a Cartesian coordinate system is established at A. E is the spherical centre of the linkage. Its truss form is obtained by the approach described in section 2.2. Denote joint kinematic angles at A, B, C, D as θ_1, θ_2, θ_3, θ_4 respectively. Therefore, revolute axes at A, B, C, and D are

$$\boldsymbol{s}_{\mathrm{A}} = \boldsymbol{AE}, \quad \boldsymbol{s}_{\mathrm{B}} = \boldsymbol{BE}, \quad \boldsymbol{s}_{\mathrm{C}} = \boldsymbol{CE}, \quad \boldsymbol{s}_{\mathrm{D}} = \boldsymbol{DE}. \tag{2-41}$$

Then, the Jacobian matrix is

$$\begin{aligned} \boldsymbol{J} &= \begin{bmatrix} \boldsymbol{s}_{\mathrm{A}} \times \boldsymbol{OA} & \boldsymbol{s}_{\mathrm{B}} \times \boldsymbol{BA} & \boldsymbol{s}_{\mathrm{C}} \times \boldsymbol{CA} & \boldsymbol{s}_{\mathrm{D}} \times \boldsymbol{DA} \\ \boldsymbol{s}_{\mathrm{A}} & \boldsymbol{s}_{\mathrm{B}} & \boldsymbol{s}_{\mathrm{C}} & \boldsymbol{s}_{\mathrm{D}} \end{bmatrix} \\ &= \begin{bmatrix} \boldsymbol{AE} \times \boldsymbol{OA} & \boldsymbol{BE} \times \boldsymbol{BA} & \boldsymbol{CE} \times \boldsymbol{CA} & \boldsymbol{DE} \times \boldsymbol{DA} \\ \boldsymbol{AE} & \boldsymbol{BE} & \boldsymbol{CE} & \boldsymbol{DE} \end{bmatrix} \end{aligned} \tag{2-42}$$

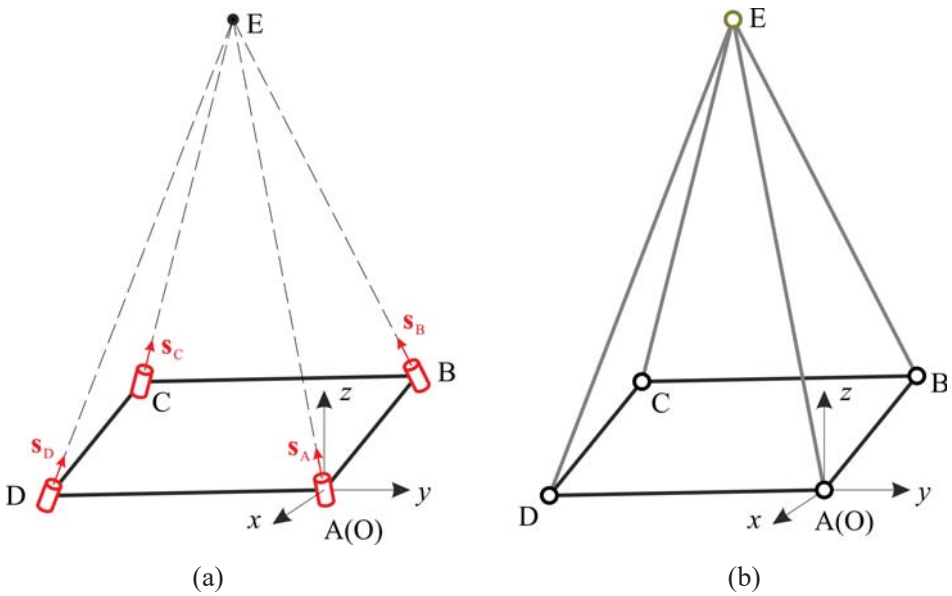

Fig. 2-7. Kinematics of (a) spherical 4*R* linkage, by transforming it to (b) truss form.

Eq. (2-42) can be expanded as

$$\boldsymbol{J} = \begin{bmatrix} (y_{\mathrm{E}} - y_{\mathrm{A}})z_{\mathrm{A}} - (z_{\mathrm{E}} - z_{\mathrm{A}})y_{\mathrm{A}} & (y_{\mathrm{E}} - y_{\mathrm{B}})(z_{\mathrm{B}} - z_{\mathrm{A}}) - (z_{\mathrm{E}} - z_{\mathrm{B}})(y_{\mathrm{B}} - y_{\mathrm{A}}) \\ (z_{\mathrm{E}} - z_{\mathrm{A}})x_{\mathrm{A}} - (x_{\mathrm{E}} - x_{\mathrm{A}})z_{\mathrm{A}} & (z_{\mathrm{E}} - z_{\mathrm{B}})(x_{\mathrm{B}} - x_{\mathrm{A}}) - (x_{\mathrm{E}} - x_{\mathrm{B}})(z_{\mathrm{B}} - z_{\mathrm{A}}) \\ (x_{\mathrm{E}} - x_{\mathrm{A}})y_{\mathrm{A}} - (y_{\mathrm{E}} - y_{\mathrm{A}})x_{\mathrm{A}} & (x_{\mathrm{E}} - x_{\mathrm{B}})(y_{\mathrm{B}} - y_{\mathrm{A}}) - (y_{\mathrm{E}} - y_{\mathrm{B}})(x_{\mathrm{B}} - x_{\mathrm{A}}) \\ x_{\mathrm{E}} - x_{\mathrm{A}} & x_{\mathrm{E}} - x_{\mathrm{B}} \\ y_{\mathrm{E}} - y_{\mathrm{A}} & y_{\mathrm{E}} - y_{\mathrm{B}} \\ z_{\mathrm{E}} - z_{\mathrm{A}} & z_{\mathrm{E}} - z_{\mathrm{B}} \end{bmatrix}$$

$$
\begin{matrix}
(y_E - y_C)(z_C - z_A) - (z_E - z_C)(y_C - y_A) & (y_E - y_D)(z_D - z_A) - (z_E - z_D)(y_D - y_A) \\
(z_E - z_C)(x_C - x_A) - (x_E - x_C)(z_C - z_A) & (z_E - z_D)(x_D - x_A) - (x_E - x_D)(z_D - z_A) \\
(x_E - x_C)(y_C - y_A) - (y_E - y_C)(x_C - x_A) & (x_E - x_D)(y_D - y_A) - (y_E - y_D)(x_D - x_A) \\
x_E - x_C & x_E - x_D \\
y_E - y_C & y_E - y_D \\
z_E - z_C & z_E - z_D
\end{matrix}
\Bigg]
\tag{2-43}
$$

It can be briefly denoted as

$$
\boldsymbol{J} = \begin{bmatrix} \boldsymbol{J}_U \\ \boldsymbol{J}_D \end{bmatrix}, \tag{2-44}
$$

in which $\boldsymbol{J}_U$ is the upper three rows and $\boldsymbol{J}_D$ is the bottom three rows.

Obviously, the linkage can be seen as a truss with five joints and eight bars, its equilibrium equation is

$$
\boldsymbol{Ht} = \boldsymbol{f}, \tag{2-45}
$$

where $\boldsymbol{H}$ is the equilibrium matrix

$$
\boldsymbol{H} = \begin{bmatrix}
x_A - x_B & & & x_A - x_D & x_A - x_E & & & \\
y_A - y_B & & & y_A - y_D & y_A - y_E & & & \\
z_A - z_B & & & z_A - z_D & z_A - z_E & & & \\
x_B - x_A & x_B - x_C & & & & x_B - x_E & & \\
y_B - y_A & y_B - y_C & & & & y_B - y_E & & \\
z_B - z_A & z_B - z_C & & & & z_B - z_E & & \\
 & x_C - x_B & x_C - x_D & & & & x_C - x_E & \\
 & y_C - y_B & y_C - y_D & & & & y_C - y_E & \\
 & z_C - z_B & z_C - z_D & & & & z_C - z_E & \\
 & & x_D - x_C & x_D - x_A & & & & x_D - x_E \\
 & & y_D - y_C & y_D - y_A & & & & y_D - y_E \\
 & & z_D - z_C & z_D - z_A & & & & z_D - z_E \\
 & & & & x_E - x_A & x_E - x_B & x_E - x_C & x_E - x_D \\
 & & & & y_E - y_A & y_E - y_B & y_E - y_C & y_E - y_D \\
 & & & & z_E - z_A & z_E - z_B & z_E - z_C & z_E - z_D
\end{bmatrix}.
\tag{2-46}
$$

It is briefly denoted as

$$
\boldsymbol{H} = \begin{bmatrix} \boldsymbol{H}_U \\ \boldsymbol{0} \quad \boldsymbol{J}_D \end{bmatrix}, \tag{2-47}
$$

where $\boldsymbol{H}_U$ is the upper 12 rows, and $\boldsymbol{J}_D$ is the submatrix with dimensions three by

four in the lower right corner of $\boldsymbol{H}$.

By some row transformations, $r_1+r_4+r_7+r_{10}+r_{13}$, $r_2+r_5+r_8+r_{11}+r_{14}$, $r_3+r_6+r_9+r_{12}+r_{15}$, $\boldsymbol{H}$ becomes

$$\boldsymbol{H}'=\begin{bmatrix} 0 & 0 & 0 & 0 & 0 & 0 & 0 & 0 \\ 0 & 0 & 0 & 0 & 0 & 0 & 0 & 0 \\ 0 & 0 & 0 & 0 & 0 & 0 & 0 & 0 \\ x_B-x_A & x_B-x_C & & & & x_B-x_E & & \\ y_B-y_A & y_B-y_C & & & & y_B-y_E & & \\ z_B-z_A & z_B-z_C & & & & z_B-z_E & & \\ & x_C-x_B & x_C-x_D & & & & x_C-x_E & \\ & y_C-y_B & y_C-y_D & & & & y_C-y_E & \\ & z_C-z_B & z_C-z_D & & & & z_C-z_E & \\ & & x_D-x_C & x_D-x_A & & & & x_D-x_E \\ & & y_D-y_C & y_D-y_A & & & & y_D-y_E \\ & & z_D-z_C & z_D-z_A & & & & z_D-z_E \\ & & & & x_E-x_A & x_E-x_B & x_E-x_C & x_E-x_D \\ & & & & y_E-y_A & y_E-y_B & y_E-y_C & y_E-y_D \\ & & & & z_E-z_A & z_E-z_B & z_E-z_C & z_E-z_D \end{bmatrix}. \tag{2-48}$$

It is briefly denoted as

$$\boldsymbol{H}'=\begin{bmatrix} \boldsymbol{0} \\ \boldsymbol{H}_{\mathrm{UD}} \\ \boldsymbol{0} \quad \boldsymbol{J}_{\mathrm{D}} \end{bmatrix}. \tag{2-49}$$

Then, a new matrix $\boldsymbol{H}_1$, where its rank equals to that of $\boldsymbol{H}$, is constructed as

$$\boldsymbol{H}_1=\begin{bmatrix} \boldsymbol{H} \\ \boldsymbol{0} \\ \boldsymbol{0} \\ \boldsymbol{0} \end{bmatrix}. \tag{2-50}$$

By some row transformations, $r_{16}+r_2(-z_A)+r_3*y_A+r_5(z_A-z_B)+r_6(y_B-y_A)+r_8(z_A-z_C)+r_9(y_C-y_A)+r_{11}(z_A-z_D)+r_{12}(y_D-y_A)$, $r_{17}+r_3(-x_A)+r_1*z_A+r_6(x_A-x_B)+r_4(z_B-z_A)+r_9(x_A-x_C)+r_7(z_C-z_A)+r_{12}(x_A-x_D)+r_{10}(z_D-z_A)$, $r_{18}+r_1(-y_A)+r_2*x_A+r_4(y_A-y_B)+r_5(x_B-x_A)+r_7(y_A-y_C)+r_8(x_C-x_A)+r_{10}(y_A-y_D)+r_{11}(x_D-x_A)$, $\boldsymbol{H}_1$ is similar with

$$\boldsymbol{H}_1\sim\begin{bmatrix} \boldsymbol{H} \\ \boldsymbol{0} \quad \boldsymbol{J}_{\mathrm{U}} \end{bmatrix}. \tag{2-51}$$

Considering Eq. (2-47),

$$\boldsymbol{H}_1 \sim \begin{bmatrix} \boldsymbol{H} & \\ \boldsymbol{0} & \boldsymbol{J}_{\mathrm{U}} \end{bmatrix} = \begin{bmatrix} \boldsymbol{H}_{\mathrm{U}} & \\ \boldsymbol{0} & \boldsymbol{J}_{\mathrm{D}} \\ \boldsymbol{0} & \boldsymbol{J}_{\mathrm{U}} \end{bmatrix} \sim \begin{bmatrix} \boldsymbol{H}_{\mathrm{U}} & \\ \boldsymbol{0} & \boldsymbol{J}_{\mathrm{U}} \\ \boldsymbol{0} & \boldsymbol{J}_{\mathrm{D}} \end{bmatrix} = \begin{bmatrix} \boldsymbol{0} & \\ \boldsymbol{H}_{\mathrm{UD}} & \\ 0 & \boldsymbol{J} \end{bmatrix}. \tag{2-52}$$

It is the relationship between these two matrices. Meanwhile, as

$$rank(\boldsymbol{H}_{\mathrm{UD}}) = 7\,. \tag{2-53}$$

Then mobility, calculated by the truss method and the mechanical method, is both related to the rank of $\boldsymbol{J}$.

Obviously, the Jacobian matrix $\boldsymbol{J}$, as one part of the final matrix in Eq. (2-52), can be obtained by a series of operations in Eqs. (2-47, 48, 49, 50, 51, 52) from the equilibrium matrix $\boldsymbol{H}$. Similarly, the equilibrium matrix $\boldsymbol{H}$ can be constructed with the Jacobian matrix $\boldsymbol{J}$ as shown in Eq. (2-52). Therefore, we can say that these two matrices are equivalent to each other.

2.6 Discussion and Conclusions

In the work of Chen and Chai [34], the motion path of the Bricard linkage was obtained by SVD of the kinematic Jacobian matrix of the linkage and the iteration of angular displacements of mechanical joints. While, in the work of Kumar and Pellegrino [43], the motion path was generated by SVD of the equilibrium matrix of the truss and the iteration of linear displacements of joints. Obviously, there must be some relationships between linear and angular displacements of any assembly which possesses the determined motion, as they are both the properties of the assembly.

In the view of mechanism, a joint connecting two bars in a truss is regarded as an *S* joint connecting two links, see joint P_i connecting bars $\mathrm{P}_i\mathrm{P}_{i-1}$ and $\mathrm{P}_i\mathrm{P}_{i+1}$ in Fig. 2-8.

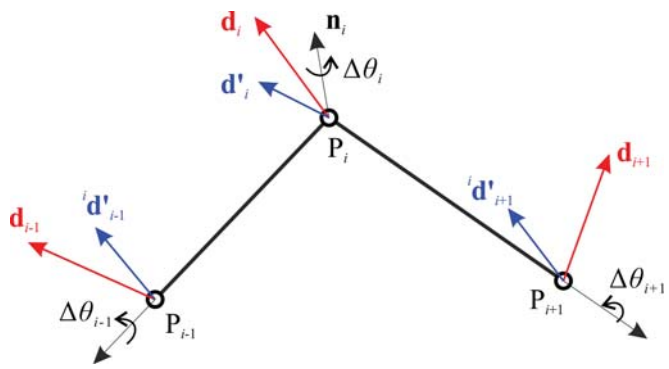

Fig. 2-8. The relationship between angular and linear displacements.

Generally, this S joints can be dealt with three rotations around three R joints, e.g., linear displacements $\boldsymbol{d}_{i-1}$, $\boldsymbol{d}_i$, and $\boldsymbol{d}_{i+1}$ on joints P_{i-1}, P_i, and P_{i+1}, respectively, will generate angular displacements $\Delta\theta_{i(i-1)}$, $\Delta\theta_{i(i+1)}$, and $\Delta\theta_i$ around $\boldsymbol{P}_i\boldsymbol{P}_{i-1}$, $\boldsymbol{P}_i\boldsymbol{P}_{i+1}$, and $\boldsymbol{n}_i$ which is perpendicular to both $\boldsymbol{P}_i\boldsymbol{P}_{i-1}$ and $\boldsymbol{P}_i\boldsymbol{P}_{i+1}$.

As $\Delta\theta_i$ is angular displacement in plane $\mathrm{P}_{i-1}\mathrm{P}_i\mathrm{P}_{i+1}$, thus, linear displacements beyond this plane have no contribution to this angular displacement. Thus, all linear displacements are projected to this plane as ${}^i\boldsymbol{d}'_{i-1}$, $\boldsymbol{d}'_i$, and ${}^i\boldsymbol{d}'_{i+1}$.

For $\boldsymbol{d}_i$,

$$\boldsymbol{d}_i = \boldsymbol{d}'_i + q_i\boldsymbol{n}_i, \tag{2-54}$$

where q_i is the component along $\boldsymbol{n}_i$. Both sides dot product $\boldsymbol{n}_i$,

$$\boldsymbol{d}_i \cdot \boldsymbol{n}_i = \left(\boldsymbol{d}'_i + q_i\boldsymbol{n}_i\right)\cdot \boldsymbol{n}_i, \tag{2-55}$$

Then,

$$q_i = \boldsymbol{d}_i \cdot \boldsymbol{n}_i. \tag{2-56}$$

Thus,

$$\boldsymbol{d}'_i = \boldsymbol{d}_i - \left(\boldsymbol{d}_i \cdot \boldsymbol{n}_i\right)\boldsymbol{n}_i. \tag{2-57}$$

Then,

$$\boldsymbol{d}'_i = \boldsymbol{d}_i - \left(\boldsymbol{n}_i^{\mathrm{T}}\boldsymbol{d}_i\right)\boldsymbol{n}_i, \tag{2-58a}$$

$$\boldsymbol{d}'_i = \boldsymbol{d}_i - \boldsymbol{n}_i\boldsymbol{n}_i^{\mathrm{T}}\boldsymbol{d}_i. \tag{2-58b}$$

Thus,

$$\boldsymbol{d}'_i = \left(\boldsymbol{I}_4 - \boldsymbol{n}_i\boldsymbol{n}_i^{\mathrm{T}}\right)\boldsymbol{d}_i. \tag{2-59}$$

Similarly,

$${}^i\boldsymbol{d}'_{i-1} = \left(\boldsymbol{I}_4 - \boldsymbol{n}_i\boldsymbol{n}_i^{\mathrm{T}}\right)\boldsymbol{d}_{i-1}, \tag{2-60a}$$

$${}^i\boldsymbol{d}'_{i+1} = \left(\boldsymbol{I}_4 - \boldsymbol{n}_i\boldsymbol{n}_i^{\mathrm{T}}\right)\boldsymbol{d}_{i+1}. \tag{2-60b}$$

It should be noted that ${}^i\boldsymbol{d}'_{i-1}$ and ${}^i\boldsymbol{d}'_{i+1}$ are distinguished with $\boldsymbol{d}'_{i-1}$ and $\boldsymbol{d}'_{i+1}$, which represent component of $\boldsymbol{d}_{i-1}$ and $\boldsymbol{d}_{i+1}$ in planes $\mathrm{P}_{i-2}\mathrm{P}_{i-1}\mathrm{P}_i$ and $\mathrm{P}_i\mathrm{P}_{i+1}\mathrm{P}_{i+2}$, respectively.

Meanwhile, angular displacement of links $\mathrm{P}_i\mathrm{P}_{i-1}$ and $\mathrm{P}_i\mathrm{P}_{i+1}$ are

$$\Delta\theta_{i(i-1)} = \frac{1}{l_{i(i-1)}^2}\left(\boldsymbol{n}_i \times \boldsymbol{P}_i\boldsymbol{P}_{i-1}\right)\cdot\left({}^i\boldsymbol{d}'_{i-1} - \boldsymbol{d}'_i\right), \tag{2-61a}$$

$$\Delta\theta_{i(i+1)} = \frac{1}{l_{i(i+1)}^2}\left(\boldsymbol{n}_i \times \boldsymbol{P}_i\boldsymbol{P}_{i+1}\right)\cdot\left({}^i\boldsymbol{d}'_{i+1} - \boldsymbol{d}'_i\right), \tag{2-61b}$$

respectively. Then

$$\Delta\theta_i = \Delta\theta_{i(i+1)} - \Delta\theta_{i(i-1)} = \frac{1}{l_{i(i+1)}^2}\left(\boldsymbol{n}_i \times \boldsymbol{P}_i\boldsymbol{P}_{i+1}\right)\cdot\left({}^i\boldsymbol{d}'_{i+1} - \boldsymbol{d}'_i\right) - \frac{1}{l_{i(i-1)}^2}\left(\boldsymbol{n}_i \times \boldsymbol{P}_i\boldsymbol{P}_{i-1}\right)\cdot\left({}^i\boldsymbol{d}'_{i-1} - \boldsymbol{d}'_i\right), \tag{2-62}$$

It can be expressed by the matrix form

$$\Delta\theta_i = \boldsymbol{K}_i\left[{}^i\boldsymbol{d}'_{i-1} \quad {}^i\boldsymbol{d}'_i \quad {}^i\boldsymbol{d}'_{i+1}\right]^{\mathrm{T}}, \tag{2-63}$$

where

$$\boldsymbol{K}_i = \left[-\frac{\boldsymbol{n}_i \times \boldsymbol{P}_i\boldsymbol{P}_{i+1}}{l_{i(i-1)}^2} \quad \frac{\boldsymbol{n}_i \times \boldsymbol{P}_i\boldsymbol{P}_{i-1}}{l_{i(i-1)}^2} - \frac{\boldsymbol{n}_i \times \boldsymbol{P}_i\boldsymbol{P}_{i+1}}{l_{i(i+1)}^2} \quad \frac{\boldsymbol{n}_i \times \boldsymbol{P}_i\boldsymbol{P}_{i-1}}{l_{i(i+1)}^2}\right]. \tag{2-64}$$

Considering Eqs. (2-59) and (2-60),

$$\Delta\theta_i = \boldsymbol{K}_i\boldsymbol{M}_i\left[\boldsymbol{d}_{i-1} \quad \boldsymbol{d}_i \quad \boldsymbol{d}_{i+1}\right]^{\mathrm{T}}, \tag{2-65}$$

where

$$\boldsymbol{M}_i = \begin{bmatrix} \boldsymbol{I}_4 - \boldsymbol{n}_i\boldsymbol{n}_i^{\mathrm{T}} & & \\ & \boldsymbol{I}_4 - \boldsymbol{n}_i\boldsymbol{n}_i^{\mathrm{T}} & \\ & & \boldsymbol{I}_4 - \boldsymbol{n}_i\boldsymbol{n}_i^{\mathrm{T}} \end{bmatrix}. \tag{2-66}$$

For the angular displacements $\Delta\theta_{i(i-1)}$,

$$\Delta\theta_{i(i-1)}\frac{\boldsymbol{P}_i\boldsymbol{P}_{i-1}}{l_{i(i-1)}} \times \boldsymbol{P}_i\boldsymbol{P}_{i+1} = \left(\boldsymbol{d}_{i+1}\cdot\boldsymbol{n}_i\right)\boldsymbol{n}_i - \left(\boldsymbol{d}_i\cdot\boldsymbol{n}_i\right)\boldsymbol{n}_i. \tag{2-67}$$

Then,

$$\Delta\theta_{i(i-1)}\frac{\boldsymbol{P}_i\boldsymbol{P}_{i-1}}{l_{i(i-1)}} \times \boldsymbol{P}_i\boldsymbol{P}_{i+1} = \left(\boldsymbol{d}_{i+1}\cdot\boldsymbol{n}_i - \boldsymbol{d}_i\cdot\boldsymbol{n}_i\right)\boldsymbol{n}_i. \tag{2-68}$$

As

$$\boldsymbol{P}_i\boldsymbol{P}_{i-1} \times \boldsymbol{P}_i\boldsymbol{P}_{i+1} = l_{(i-1)i(i+1)}\boldsymbol{n}_i, \tag{2-69}$$

where $l_{(i-1)i(i+1)}$ is the module of $\boldsymbol{P}_i\boldsymbol{P}_{i-1} \times \boldsymbol{P}_i\boldsymbol{P}_{i+1}$. Thus,

$$\Delta\theta_{i(i-1)}\frac{l_{(i-1)i(i+1)}}{l_{i(i-1)}} = \boldsymbol{d}_{i+1}\cdot\boldsymbol{n}_i - \boldsymbol{d}_i\cdot\boldsymbol{n}_i = \left(\boldsymbol{d}_{i+1} - \boldsymbol{d}_i\right)\cdot\boldsymbol{n}_i = \boldsymbol{n}_i^{\mathrm{T}}\left(\boldsymbol{d}_{i+1} - \boldsymbol{d}_i\right). \tag{2-70}$$

Namely,

$$\Delta\theta_{i(i-1)} = \frac{l_{i(i-1)}}{l_{(i-1)i(i+1)}}\boldsymbol{n}_i^{\mathrm{T}}\left(\boldsymbol{d}_{i+1} - \boldsymbol{d}_i\right). \tag{2-71}$$

Similarly,

$$\Delta\theta_{i(i+1)} = \frac{-l_{i(i+1)}}{l_{(i-1)i(i+1)}}\boldsymbol{n}_i^{\mathrm{T}}\left(\boldsymbol{d}_{i-1} - \boldsymbol{d}_i\right). \tag{2-72}$$

Hereto, the relationships between angular and linear displacements are obtained as shown in Eqs. (2-65), (2-71) and (2-72).

As the topology of spatial truss is not fixed and is determined according to detailed configurations, it is difficult to establish a unified formula for the relationship between vectors of angular and linear displacements. However, the obtained relationships can be adopted for detailed linkages.

In this chapter, we proposed an approach to transform 3D linkages to their equivalent truss forms, then truss methods were employed to analyse kinematic behaviour of linkages, including mobility, motion path and bifurcation situations. An example of a threefold-symmetric Bricard linkage shows the validity of this approach. The relationship between truss methods and mechanical methods were studied by seeking the relationship between Jacobian matrix of linkages and equilibrium matrix of their truss and discussing the relationship between angular and linear displacements.

As Jacobian matrix is effective not only for kinematics but also dynamics, while the establishing process is rather complicated especially to complicated linkages. Therefore, equilibrium matrix may also be feasible for simplifying the dynamic analysis process.

Chapter 3 Non-overconstrained Forms of Overconstrained Linkages

3.1 Introduction

3D overconstrained linkages exhibite excellent kinematic behaviours for spatial motion and deployable property. Yet, their strict overconstrained geometric conditions request very high fabrication accuracy, which makes them have an expensive cost in application. In order to solve this conjugation, we use truss as an intermedium to transform overconstrained linkages with *R* joints into their non-overconstrained forms with kinematic equivalence.

The layout of this chapter is as follows. Section 3.2 expounds the transformation method from linkage to truss structure. The non-overconstrained form of Bennett linkage is obtained in Section 3.3 with the proof of the kinematic equivalence between the non-overconstrained form and its original linkage. Myard 5*R* linkage as another case study is dealt with in Section 3.4 to show the generality of the proposed method. Output errors, which are produced by fabrication errors on link length and twist, and sensitivities of these factors are analysed in Section 3.5. Conclusions in Section 3.6 end the chapter.

3.2 The Truss Form of Linkage

According to the truss method illustrated in Chapter 2, Bennett linkage [52, 53] in Fig. 1-4, a well-known spatial 4*R* linkage with mobility one, is transformed to its truss form, in Fig. 3-1, which has $j=8$ nodes, $b=20$ bars, and $3j-6-b=-2$. Thus it is statically indeterminate, i.e., overconstrained. In this case, the equilibrium equation has to be considered [133, 134]. Numbers of mobility *m* and self-stress *s* can be calculated by Eqs. (2-7) and (2-3), respectively.

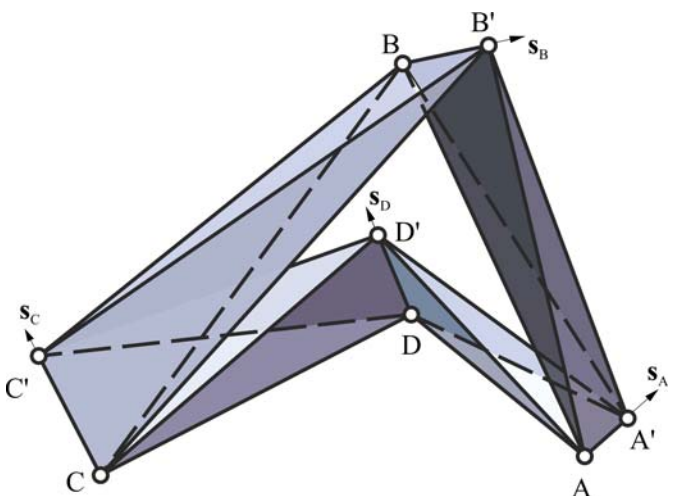

Fig. 3-1. The equivalent truss form of Bennett linkage.

A structural assembly without external forces and bar elongations can be classified into four types based on the values of m and s [135].

(1) $m=0, s=0$: Statically determinate and kinematically determinate, referred as to a normal structure;

(2) $m>0, s=0$: Statically determinate and kinematically indeterminate, referred as to a normal mechanism (non-overconstrained mechanism);

(3) $m=0, s>0$: Statically indeterminate and kinematically determinate, referred as to a statically indeterminate structure; and

(4) $m>0, s>0$: Statically indeterminate and kinematically indeterminate, referred as to an overconstrained mechanism.

Our focus is on the fourth type, $m>0$, $s>0$, namely the overconstrained linkage. To obtain its non-overconstrained form, the system should become statically determinate while keeping the kinematic indeterminacy, i.e., reducing s to zero without changing m. Considering Eqs. (2-7) and (2-3), when the number of nodes j and rank of equilibrium matrix r of a truss are unchanged, the mobility will not be changed. And $s>0$ means that there are $b-r$ bars redundant. To make $s=0$, we have to remove the $b-r$ redundant bars from the truss system. Then the non-overconstrained form can be obtained.

In the following sections, the Bennett linkage and Myard linkage are taken as examples to demonstrate how to obtain the non-overconstrained form of an overconstrained linkage through truss analogy.

3.3 Non-overconstrained Form of the Bennett Linkage

The truss form of the Bennett linkage with mobility one, see Fig. 3-1, is composed of four rigid bodies $\mathrm{AA'B'B}$, $\mathrm{B'BCC'}$, $\mathrm{CC'D'D}$ and $\mathrm{D'DAA'}$, which are connected by joint bars $\mathrm{BB'}$, $\mathrm{CC'}$, $\mathrm{DD'}$, and $\mathrm{AA'}$, successively. Here, AB, BC, CD, and DA are the shortest links. For this overconstrained linkage, we cannot calculate the mobility simply from Maxwell's rule.

In the truss form of a Bennett linkage, see Fig. 3-2, set $\overline{\mathrm{AC}}=2v$, $\overline{\mathrm{BD}}=2w$, $\overline{\mathrm{MN}}=u$, and the angle between AC and BD as γ. The coordinate system is set up as Huang et al. [136] presented, and then the equilibrium matrix of the truss form with symbols is

$\boldsymbol{H}_{24\times20}$=

[-$v$sinγ, -u, -u-$w$sinγ, -u, $w$sinγ-u, 0, 0, 0, 0, 0, 0, 0, 0, 0, 0, 0, 0, 0, 0, 0, 0;

-$u$sinγ, v-$w$cosγ, v-$w$cosγ, v+$w$cosγ, v+$w$cosγ, 0, 0, 0, 0, 0, 0, 0, 0, 0, 0, 0, 0, 0, 0, 0;

-$u$cosγ, $w$sinγ, $w$sinγ-u, -$w$sinγ, -u-$w$sinγ, 0, 0, 0, 0, 0, 0, 0, 0, 0, 0, 0, 0, 0, 0, 0;

$$
\begin{aligned}
&0, u, 0, 0, 0, -w\sin\gamma, u-v\sin\gamma, u, u+v\sin\gamma, 0, 0, 0, 0, 0, 0, 0, 0, 0, 0, 0;\\
&0, -v+w\cos\gamma, 0, 0, 0, 0, w\cos\gamma-v-u\sin\gamma, v+w\cos\gamma, w\cos\gamma+v-u\sin\gamma, 0, 0, 0, 0, 0, 0, 0, 0, 0, 0, 0;\\
&0, -w\sin\gamma, 0, 0, 0, -u, -w\sin\gamma-u\cos\gamma, -w\sin\gamma, -w\sin\gamma-u\cos\gamma, 0, 0, 0, 0, 0, 0, 0, 0, 0, 0, 0;\\
&0, 0, 0, 0, 0, 0, 0, -u, 0, -u-w\sin\gamma, v\sin\gamma, -u, w\sin\gamma-u, 0, 0, 0, 0, 0, 0, 0, 0;\\
&0, 0, 0, 0, 0, 0, 0, -v-w\cos\gamma, 0, -v-w\cos\gamma, -u\sin\gamma, -v+w\cos\gamma, -v+w\cos\gamma, 0, 0, 0, 0, 0, 0, 0;\\
&0, 0, 0, 0, 0, 0, 0, w\sin\gamma, 0, w\sin\gamma-u, -u\cos\gamma, -w\sin\gamma, -u-w\sin\gamma, 0, 0, 0, 0, 0, 0, 0;\\
&0, 0, 0, u, 0, 0, 0, 0, 0, 0, 0, u, 0, u+v\sin\gamma, u-v\sin\gamma, w\sin\gamma, 0, 0, 0, 0;\\
&0, 0, 0, -v-w\cos\gamma, 0, 0, 0, 0, 0, 0, 0, v-w\cos\gamma, 0, -w\cos\gamma+v-u\sin\gamma, -w\cos\gamma-v-u\sin\gamma, 0, 0, 0, 0, 0;\\
&0, 0, 0, w\sin\gamma, 0, 0, 0, 0, 0, 0, 0, w\sin\gamma, 0, w\sin\gamma-u\cos\gamma, w\sin\gamma-u\cos\gamma, -u, 0, 0, 0, 0;\\
&v\sin\gamma, 0, 0, 0, 0, 0, -u+v\sin\gamma, 0, 0, 0, 0, 0, 0, 0, -u+v\sin\gamma, 0, v\sin\gamma-u-w\sin\gamma, v\sin\gamma+w\sin\gamma-u, 0, 0;\\
&u\sin\gamma, 0, 0, 0, 0, 0, v+u\sin\gamma-w\cos\gamma, 0, 0, 0, 0, 0, 0, 0, v+u\sin\gamma+w\cos\gamma, 0, v+u\sin\gamma-w\cos\gamma, v+u\sin\gamma+w\cos\gamma, 0, 0;\\
&u\cos\gamma, 0, 0, 0, 0, 0, w\sin\gamma+u\cos\gamma, 0, 0, 0, 0, 0, 0, 0, -w\sin\gamma+u\cos\gamma, 0, u\cos\gamma+w\sin\gamma-u, u\cos\gamma-u-w\sin\gamma, 0, 0;\\
&0, 0, u+w\sin\gamma, 0, 0, w\sin\gamma, 0, 0, 0, u+w\sin\gamma, 0, 0, 0, 0, 0, 0, -v\sin\gamma+u+w\sin\gamma, 0, u+w\sin\gamma+v\sin\gamma, 0;\\
&0, 0, -v+w\cos\gamma, 0, 0, 0, 0, 0, 0, v+w\cos\gamma, 0, 0, 0, 0, 0, 0, w\cos\gamma-v-u\sin\gamma, 0, w\cos\gamma+v-u\sin\gamma, 0;\\
&0, 0, -w\sin\gamma+u, 0, 0, u, 0, 0, 0, -w\sin\gamma+u, 0, 0, 0, 0, 0, 0, -w\sin\gamma+u-u\cos\gamma, 0, -w\sin\gamma+u-u\cos\gamma, 0;\\
&0, 0, 0, 0, 0, 0, 0, 0, -u-v\sin\gamma, 0, -v\sin\gamma, 0, 0, -u-v\sin\gamma, 0, 0, 0, 0, -u-w\sin\gamma-v\sin\gamma, -v\sin\gamma+w\sin\gamma-u;\\
&0, 0, 0, 0, 0, 0, 0, 0, -w\cos\gamma-v+u\sin\gamma, 0, u\sin\gamma, 0, 0, -v+u\sin\gamma+w\cos\gamma, 0, 0, 0, 0, -w\cos\gamma-v+u\sin\gamma, -v+u\sin\gamma+w\cos\gamma;\\
&0, 0, 0, 0, 0, 0, 0, 0, w\sin\gamma+u\cos\gamma, 0, u\cos\gamma, 0, 0, -w\sin\gamma+u\cos\gamma, 0, 0, 0, 0, u\cos\gamma+w\sin\gamma-u, u\cos\gamma-u-w\sin\gamma;\\
&0, 0, 0, 0, -w\sin\gamma+u, 0, 0, 0, 0, 0, 0, 0, -w\sin\gamma+u, 0, 0, -w\sin\gamma, 0, -v\sin\gamma-w\sin\gamma+u, 0, v\sin\gamma-w\sin\gamma+u;\\
&0, 0, 0, 0, -v-w\cos\gamma, 0, 0, 0, 0, 0, 0, 0, v-w\cos\gamma, 0, 0, 0, 0, -w\cos\gamma-v-u\sin\gamma, 0, -w\cos\gamma+v-u\sin\gamma;\\
&0, 0, 0, 0, u+w\sin\gamma, 0, 0, 0, 0, 0, 0, 0, u+w\sin\gamma, 0, 0, u, 0, -u\cos\gamma+u+w\sin\gamma, 0, -u\cos\gamma+u+w\sin\gamma].
\end{aligned}
\tag{3-1}
$$

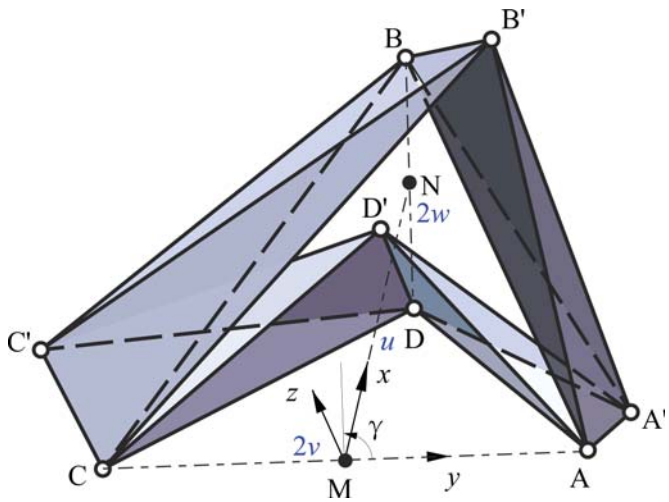

Fig. 3-2. Coordinate system for establishing the equilibrium matrix for Bennett linkage in its truss form.

The rank of the equilibrium matrix of this truss is $r = 17$, then $m = 3j - 6 - r = 18 - r = 1$, which is correct. Thus, there are $b - r = 20 - 17 = 3$ bars redundant. Rigorously, there are $C_{20}^{3} = 1140$ (combination of choosing 3 bars from 20 bars) possibilities to remove these three redundant bars from the truss form. However,

our aim is to find the non-overconstrained form of the linkage, i.e., the truss form without redundant bars, which should have the same kinematic characteristics as the original overconstrained linkage. Thus, the joint bars AA', BB', CC', and DD', working as revolute axes, should not be removed from the truss form. Otherwise, we could end up with a multi-loop linkage, see Fig. 3-3(a). So we have to remove three redundant bars among the body bars through three schemes, (a) all three bars are from three different rigid bodies; (b) two bars are from one rigid body and the 3rd one from another rigid body; and (c) all three bars are from the same rigid body.

If we remove only one body bar AB' from link $AA'BB'$, see Fig. 3-3(b), this link will become two bodies connected by an *R* joint $A'B$. This process increases the number of rigid bodies in the mechanism, which will not lead to a kinematically equivalent mechanism. Therefore neither removing schemes (a) nor (b) can be applied to Bennett linkage.

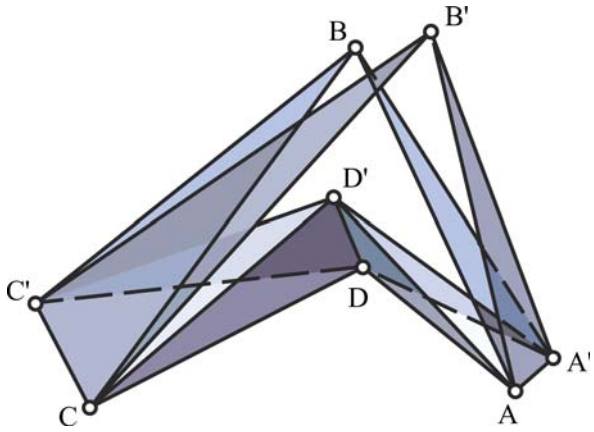

(a)

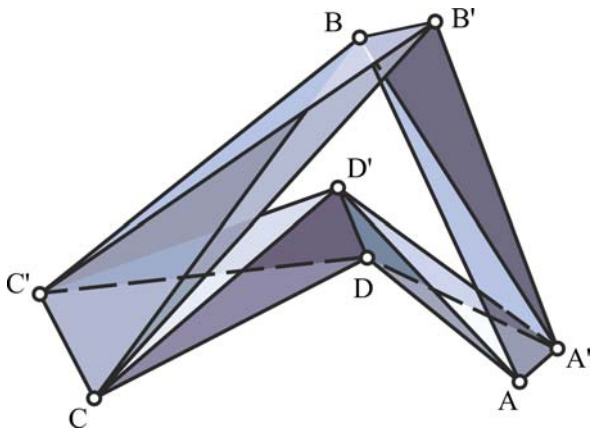

(b)

Fig. 3-3. Two redundant-bar removing schemes. (a) removing bar BB', (b) removing bar AB'.

Then we have to remove all three bars from a single rigid body. Due to the topological similarity among four bars of the Bennett linkage, we can take any one link, say $CC'DD'$, as an example. Removing three body bars CD', $C'D$, and $C'D'$ will leave bar CD as the link connecting to link $BB'CC'$ at node C and to link $DD'AA'$ at node D, see Fig. 3-4(a). In this case, nodes C and D work as *S* joints. Here, bar CD is kept because it is the shortest link so that it can be used directly in the following kinematic analysis. Now, bar CC' does not work as an *R* joint. Hence, CC' together with bars BC' and $B'C'$ can be removed without changing the kinematics of the resultant linkage. The same applies to link $AA'DD'$. Hence the non-overconstrained truss form of the Bennett linkage is shown in Fig. 3-4(b), which composes $b=11$ bars and $j=6$ nodes. And the mobility is $m=3j-6-b=1$. Then there is $b-(3j-6-m)=0$ bar redundant. Using kinematic joints to present the truss form, the *RSSR* linkage in Fig 3-4(c) can be obtained as the non-overconstrained form of the Bennett linkage.

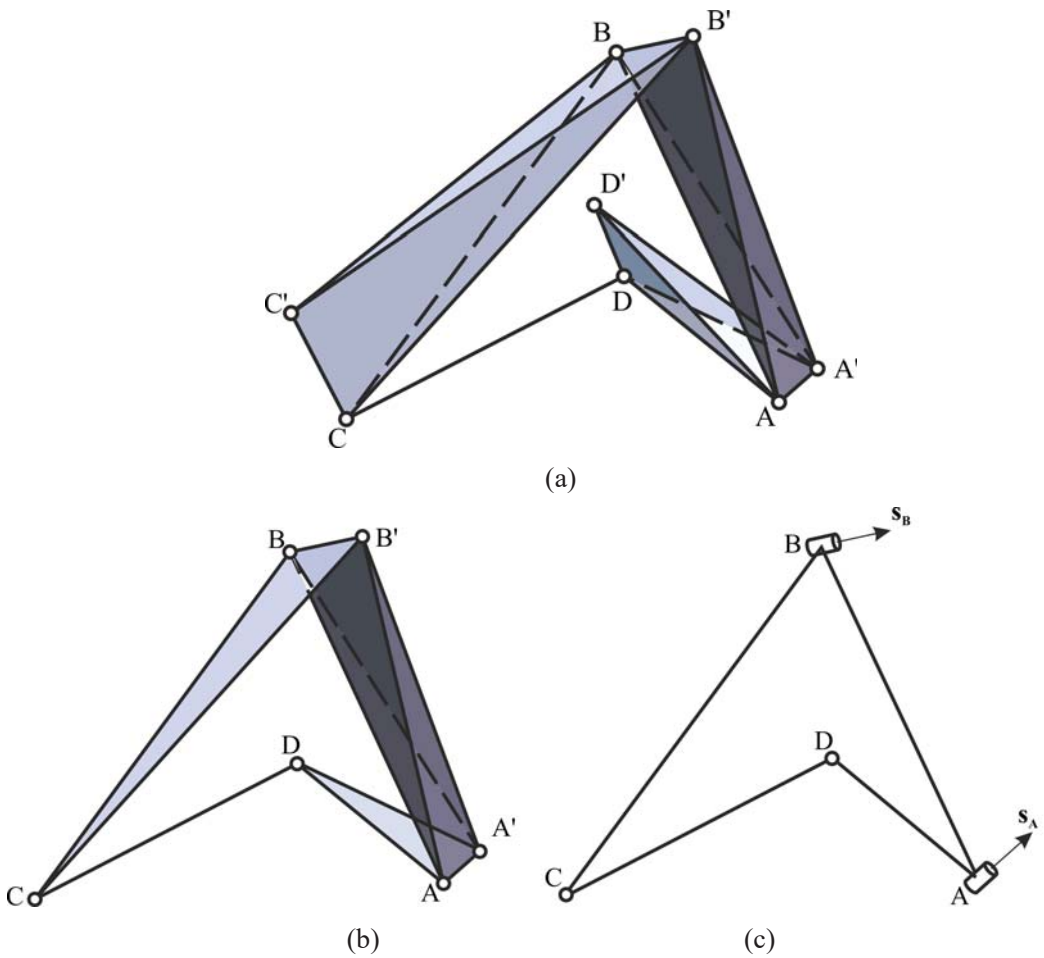

Fig. 3-4. The removing scheme of redundant bars. (a) removing three body bars in a rigid body; (b) the result after simplification; (c) the resultant mechanism.

Next, we are going to verify that the *RSSR* linkage as the non-overconstrained form and the original Bennett linkage have identical kinematic behaviours.

When joints A and B are chosen as the input and output joints of the *RSSR* linkage, respectively, adopting the same notation as the Bennett linkage, see Fig. 1-4 and Eq. (1-17), the input-output equation of the general *RSSR* linkage can be written as [137],

$$\left(-\cos\alpha_{12}\sin\theta_1+\frac{R_1\sin\alpha_{12}}{a_{41}}\right)\sin\theta_2+\left(\frac{a_{12}}{a_{41}}+\cos\theta_1\right)\cos\theta_2$$
$$+\frac{a_{23}^2-a_{34}^2+a_{41}^2+a_{12}^2+R_1^2+R_2^2+2R_1R_2\cos\alpha_{12}}{2a_{23}a_{41}}+\frac{a_{12}}{a_{23}}\cos\theta_1+\frac{R_2\sin\alpha_{12}}{a_{23}}\sin\theta_1=0. \tag{3-2}$$

As the equivalent linkage of the Bennett linkage, the analysed *RSSR* linkage should satisfy the geometric equations, Eq. (1-17). Then the input-output equation becomes,

$$a\left(\cos\theta_1+\cos\theta_2\right)+b\left(\cos\theta_1\cos\theta_2+1-\cos\alpha\sin\theta_1\sin\theta_2\right)=0, \tag{3-3}$$

which can be derived as

$$A\cdot\sin\theta_2+B\cdot\cos\theta_2-C=0. \tag{3-4}$$

where $A=\cos\alpha\sin\theta_1$, $B=-\cos\theta_1-\frac{a}{b}$, $C=1+\frac{a}{b}\cos\theta_1$. With trigonometric transformation, θ_2 in Eq. (3-4) can be solved as

$$\theta_2=2\arctan\left[\frac{A\pm\sqrt{A^2+B^2-C^2}}{B+C}\right]. \tag{3-5}$$

When $\sin\theta_1\cos\beta>0$, taking the '+' sign gives

$$\theta_2=2\arctan\left\{\frac{\sin\left[(\beta+\alpha)/2\right]}{\sin\left[(\beta-\alpha)/2\right]}\cdot\frac{1}{\tan(\theta_1/2)}\right\}, \tag{3-6a}$$

and when $\sin\theta_1\cos\beta<0$, taking the '-' sign yields

$$\theta_2=2\arctan\left\{\frac{\cos\left[(\beta-\alpha)/2\right]}{\cos\left[(\beta+\alpha)/2\right]}\cdot\frac{1}{\tan(\theta_1/2)}\right\}. \tag{3-6b}$$

It can be found that one of the solutions, Eq. (3-6a), equivalent to the closure equation of the Bennett linkage, Eq. (1-18). Whilst, Eq. (3-6b) is another form of the closure equation by taking the opposite axial directions on joints A and B. These two solutions are physically identical. As the input-output equations of the *RSSR* linkage and the Bennett linkage are identical, each *S* joint in the *RSSR* linkage ought to work as an *R* joint, which is demonstrated in details with screw theory as follows.

As an *S* joint is equivalent to three *R* joints, *S* joint C can be considered as three *R* joints, the common normal line of BC and CD as one revolute axis, CD as another revolute axis, and the third revolute axis is determined by the right-hand rule. And the same procedure can be applied to *S* joint D, see Fig. 3-5. To establish a coordinate system, $\boldsymbol{s}_{\mathrm{A}}$ and $\boldsymbol{s}_{\mathrm{B}}$ are axis vectors, where $\boldsymbol{s}_{\mathrm{A}} \perp \mathrm{AB}$ and $\boldsymbol{s}_{\mathrm{A}} \perp \mathrm{AD}$, $\boldsymbol{s}_{\mathrm{B}} \perp \mathrm{AB}$ and $\boldsymbol{s}_{\mathrm{B}} \perp \mathrm{BC}$. $\boldsymbol{s}_{\mathrm{A}} = \boldsymbol{AB} \times \boldsymbol{AD}$, $\boldsymbol{s}_{\mathrm{B}} = \boldsymbol{BA} \times \boldsymbol{BC}$, $\boldsymbol{s}_{\mathrm{Cz}} = \boldsymbol{CB} \times \boldsymbol{CD}$, $\boldsymbol{s}_{\mathrm{Dz}} = \boldsymbol{DC} \times \boldsymbol{DA}$. The coordinate system is set up as the one in Fig. 3.2. The coordinate vectors of all the points in the truss can be determined as

$$\boldsymbol{A} = [0, v, 0]^{\mathrm{T}}, \quad \boldsymbol{B} = [u, w\cos\gamma, -w\sin\gamma]^{\mathrm{T}}, \tag{3-7a}$$

$$\boldsymbol{C} = [0, -v, 0]^{\mathrm{T}}, \quad \boldsymbol{D} = [u, -w\cos\gamma, w\sin\gamma]^{\mathrm{T}}. \tag{3-7b}$$

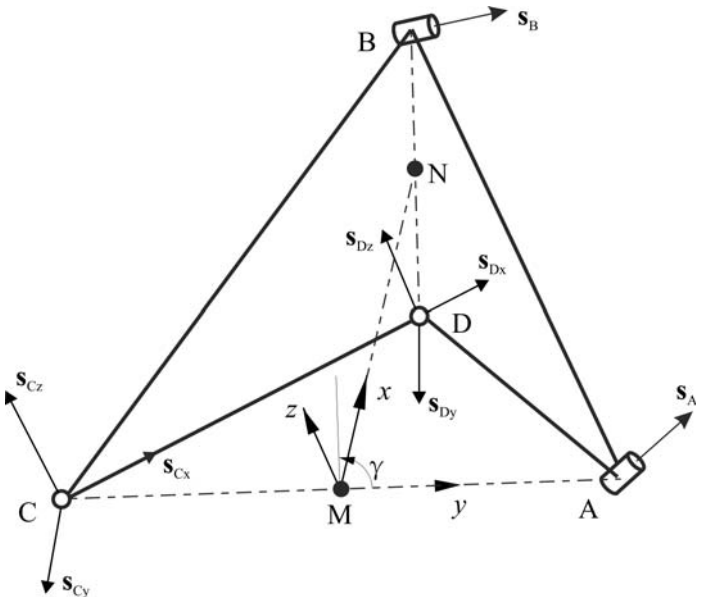

Fig. 3-5. Coordinate system for equivalence verification of Bennett linkage and its non-overconstrained form, *RSSR* linkage.

And all the screws of *R* joints and *S* joints can be written as

$$\boldsymbol{S}_{\mathrm{A}} = \left(-v\sin\gamma, -u\sin\gamma, -u\cos\gamma, uv\cos\gamma, 0, -v^2\sin\gamma\right)^{\mathrm{T}}. \tag{3-8}$$

$$\boldsymbol{S}_{\mathrm{B}} = \left(-w\sin\gamma, 0, -u, uw\cos\gamma, -u^2 - w^2\sin^2\gamma, -w^2\cos\gamma\sin\gamma\right)^{\mathrm{T}}, \tag{3-9}$$

$$\boldsymbol{S}_{\mathrm{C}x} = \left(-u, -v + w\cos\gamma, -w\sin\gamma, -vw\sin\gamma, 0, uv\right)^{\mathrm{T}}, \tag{3-10}$$

$$\begin{aligned}\boldsymbol{S}_{\mathrm{C}y} = \big(&uv\cos\gamma - uw, -u^2\cos\gamma - vw\sin^2\gamma, (u^2+v^2)\sin\gamma - vw\cos\gamma\sin\gamma,\\ &vu^2\sin\gamma + v^2(v - w\cos\gamma)\sin\gamma, 0, -uv^2\cos\gamma + uvw\big)^{\mathrm{T}},\end{aligned} \tag{3-11}$$

$$\boldsymbol{S}_{\mathrm{C}z}=\left(v\sin\gamma,-u\sin\gamma,-u\cos\gamma,-uv\cos\gamma,0,-v^2\sin\gamma\right)^{\mathrm{T}},\tag{3-12}$$

$$\boldsymbol{S}_{\mathrm{D}x}=\left(-u,-v+w\cos\gamma,-w\sin\gamma,-wv\sin\gamma,0,uv\right)^{\mathrm{T}},\tag{3-13}$$

$$\begin{aligned}\boldsymbol{S}_{\mathrm{D}y}=\Big(&u(v-w\cos\gamma),-u^2-w^2\sin^2\gamma,w(v-w\cos\gamma)\sin\gamma,\\&w\sin\gamma(wv\cos\gamma-w^2-u^2),0,-uvw\cos\gamma+u^3+uw^2\Big)^{\mathrm{T}},\end{aligned}\tag{3-14}$$

$$\boldsymbol{S}_{\mathrm{D}z}=\left(w\sin\gamma,0,-u,-uw\cos\gamma,-u^2-w^2\sin^2\gamma,-w^2\cos\gamma\sin\gamma\right)^{\mathrm{T}}.\tag{3-15}$$

The motions of bar CD can be expressed by two branches CB and DA if AB is taken as the reference link. Taking reciprocal of the motion screws, these two constraint screw systems are

$$\boldsymbol{S}^r{}_{11}=\left(1,\frac{u(v+w\cos\gamma)}{u^2+w^2\sin^2\gamma},0,0,0,-v\right)^{\mathrm{T}},\tag{3-16a}$$

$$\boldsymbol{S}^r{}_{12}=\left(0,-\frac{w\sin\gamma(v+w\cos\gamma)}{u^2+w^2\sin^2\gamma},1,v,0,0\right)^{\mathrm{T}},\tag{3-16b}$$

And

$$\boldsymbol{S}^r{}_{21}=\left(1,-\frac{v+w\cos\gamma}{u},\frac{w\sin\gamma}{u},-\frac{vw\sin\gamma}{u},0,v\right)^{\mathrm{T}},\tag{3-17a}$$

$$\begin{aligned}\boldsymbol{S}^r{}_{22}=\Bigg(&0,\frac{(u^2+v^2+vw\cos\gamma)\sin\gamma}{u(u^2\cos\gamma-vw\sin^2\gamma)},\frac{1}{u},\\&\frac{w(u^2+v^2-v^2\cos^2\gamma)}{u(u^2\cos\gamma-vw\sin^2\gamma)},1,-\frac{(u^2+v^2+vw\cos\gamma)\sin\gamma}{u^2\cos\gamma-vw\sin^2\gamma}\Bigg)^{\mathrm{T}}.\end{aligned}\tag{3-17b}$$

As the dual relationship between constraints and motions, the motions of bar CD could be obtained as

$$\boldsymbol{S}_1=\left(0,\frac{uw\sin\gamma}{v(u^2+w^2\sin^2\gamma)},\frac{u(v+w\cos\gamma)}{v(u^2+w^2\sin^2\gamma)},0,1,\frac{w(v+w\cos\gamma)\sin\gamma}{u^2+w^2\sin^2\gamma}\right)^{\mathrm{T}},\tag{3-18a}$$

$$\boldsymbol{S}_2=\left(1,\frac{v-w\cos\gamma}{u},\frac{w\sin\gamma}{u},\frac{vw\sin\gamma}{u},0,-v\right)^{\mathrm{T}}.\tag{3-18b}$$

These two independent motions of bar CD should be satisfied by these two branches, then for kinetic branch CB, ω_{Cx1}, ω_{Cy1}, ω_{Cz1}, ω_{B1} and ω_{Cx2}, ω_{Cy2}, ω_{Cz2}, ω_{B2} must satisfy

$$\begin{aligned}\boldsymbol{S}_1&=\omega_{\mathrm{Cx1}}\boldsymbol{S}_{\mathrm{Cx}}+\omega_{\mathrm{Cy1}}\boldsymbol{S}_{\mathrm{Cy}}+\omega_{\mathrm{Cz1}}\boldsymbol{S}_{\mathrm{Cz}}+\omega_{\mathrm{B1}}\boldsymbol{S}_{\mathrm{B}},\\\boldsymbol{S}_2&=\omega_{\mathrm{Cx2}}\boldsymbol{S}_{\mathrm{Cx}}+\omega_{\mathrm{Cy2}}\boldsymbol{S}_{\mathrm{Cy}}+\omega_{\mathrm{Cz2}}\boldsymbol{S}_{\mathrm{Cz}}+\omega_{\mathrm{B2}}\boldsymbol{S}_{\mathrm{B}}.\end{aligned}\tag{3-19}$$

For kinetic branch DA, ω_{Dx1}, ω_{Dy1}, ω_{Dz1}, ω_{A1} and ω_{Dx2}, ω_{Dy2}, ω_{Dz2}, ω_{A2} must

satisfy

$$\begin{aligned} \boldsymbol{S}_1 &= \omega_{\mathrm{Dx1}}\boldsymbol{S}_{\mathrm{Dx}} + \omega_{\mathrm{Dy1}}\boldsymbol{S}_{\mathrm{Dy}} + \omega_{\mathrm{Dz1}}\boldsymbol{S}_{\mathrm{Dz}} + \omega_{\mathrm{A1}}\boldsymbol{S}_{\mathrm{A}}, \\ \boldsymbol{S}_2 &= \omega_{\mathrm{Dx2}}\boldsymbol{S}_{\mathrm{Dx}} + \omega_{\mathrm{Dy2}}\boldsymbol{S}_{\mathrm{Dy}} + \omega_{\mathrm{Dz2}}\boldsymbol{S}_{\mathrm{Dz}} + \omega_{\mathrm{A2}}\boldsymbol{S}_{\mathrm{A}}. \end{aligned} \tag{3-20}$$

The coefficients are solved as follows.

$$\begin{aligned} &\omega_{\mathrm{Cx1}} = \omega_{\mathrm{Cy1}} = 0, \\ &\omega_{\mathrm{Cz1}} = -\frac{w}{v(u^2 + w^2\sin^2\gamma)}, \\ &\omega_{\mathrm{B1}} = -\frac{1}{u^2 + w^2\sin^2\gamma}, \end{aligned} \tag{3-21}$$

$$\begin{aligned} &\omega_{\mathrm{Cx2}} = -\frac{1}{u}, \\ &\omega_{\mathrm{Cy2}} = \omega_{\mathrm{Cz2}} = \omega_{\mathrm{B2}} = 0. \end{aligned} \tag{3-22}$$

And

$$\begin{aligned} &\omega_{\mathrm{Dx1}} = \omega_{\mathrm{Dy1}} = 0, \\ &\omega_{\mathrm{Dz1}} = -\frac{1}{u^2 + w^2\sin^2\gamma}, \\ &\omega_{\mathrm{A1}} = -\frac{w}{v(u^2 + w^2\sin^2\gamma)}, \end{aligned} \tag{3-23}$$

$$\begin{aligned} &\omega_{\mathrm{Dx2}} = -\frac{1}{u}, \\ &\omega_{\mathrm{Dy2}} = \omega_{\mathrm{Dz2}} = \omega_{\mathrm{A2}} = 0. \end{aligned} \tag{3-24}$$

In Eqs. (3-21) and (3-23), $\omega_{\mathrm{Cx1}} = \omega_{\mathrm{Cy1}} = \omega_{\mathrm{Dx1}} = \omega_{\mathrm{Dy1}} = 0$, and therefore there is no motion around axes $\boldsymbol{S}_{\mathrm{Cx}}$, $\boldsymbol{S}_{\mathrm{Cy}}$ on *S* joint C and axes $\boldsymbol{S}_{\mathrm{Dx}}$, $\boldsymbol{S}_{\mathrm{Dy}}$ on *S* joint D. So joint C works as an *R* joint about axis $\boldsymbol{S}_{\mathrm{Cz}}$ and joint D as an *R* joint about axis $\boldsymbol{S}_{\mathrm{Dz}}$. And the lengths of the four bars in this *RSSR* linkage are identical to those in the original Bennett linkage. Thus, $\boldsymbol{S}_1$ is just the motion of a Bennett 4*R* linkage. And according to Eqs. (3-22) and (3-24), $\boldsymbol{S}_2$ only contains motions around axes $\boldsymbol{S}_{\mathrm{Cx}}$ and $\boldsymbol{S}_{\mathrm{Dx}}$, and these axes are collinear. Thus, $\boldsymbol{S}_2$ is in fact the independent self-rotation along CD, which forms the passive DOF in all *RSSR* linkages expressed by Hunt [7]. Therefore, the *RSSR* linkage obtained from the truss method is equivalent to the original Bennett linkage with two *S* joints working as *R* joints along the corresponding axes in the Bennett linkage. This calculation process has been done through the symbolic manipulations in Mathematica, and the programming diagram is shown in Fig. 3-6.

3.4 Non-overconstrained Forms of the Myard 5*R* Linkage

The truss form of a Myard 5*R* linkage, see Fig. 3-7, possesses $b = 22$ bars and $j = 9$ nodes. As the real mobility of this linkage is one, i.e., $m = 3j - 6 - r = 21 - r = 1$, the rank of the equilibrium matrix of this truss should be 20. Thus there are $b - r = 22 - 20 = 2$ bars redundant, which have to be removed in order to get the non-overconstrained form.

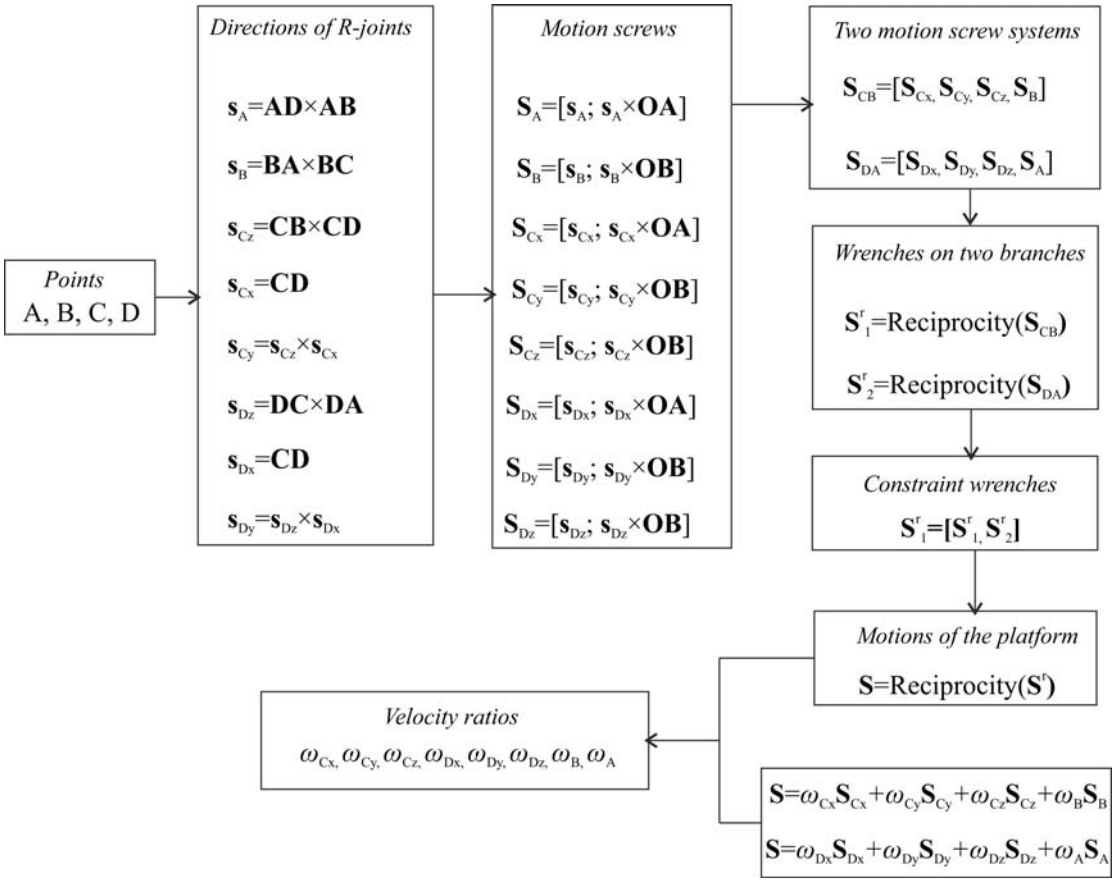

Fig. 3-6. The diagram for the calculation.

Firstly, joint bars AA', BB', CC', CC", and EE' should not be removed. At the same time, bar C'C", which is the only body bar in the rigid body CC'C", should not be removed. Secondly, to avoid bringing in extra joint, as shown in Fig. 3-3(b), two redundant bars must be selected on the same link. Since there are four body bars connected by four nodes on one rigid link, two of them can have a common node or none.

In the case of no common node, taking link AA'BB' as an example, AB' and A'B are removed, see Fig. 3-8(a). Then a kinetic sub-loop ABB'A' is formed, which is not desired. Hence two redundant bars must be removed from the same node on the same link. Because of the symmetry of the Myard 5*R* linkage, we can only consider

nodes A', B', and C' as the common nodes. Here, nodes A, B, C are not considered as bars AB and BC are the shortest distance between the *R* joints of the Myard linkage, which are kept for the convenience of further kinematic analysis. When A' is chosen as the common joint, BA' and $B'A'$ are removed, see Fig. 3-8(b). Then node A' just belongs to one rigid body $AA'EE'$, which could be removed with bars AA', $A'E'$, and $A'E$, as shown in Fig. 3-9(a). And node A becomes an *S* joint. The resultant truss owns $b=17$ bars and $j=8$ nodes with mobility $m=3j-6-b=1$, which is non-overconstrained. Its linkage form is an *RRSRR*, see Fig. 3-9(b).

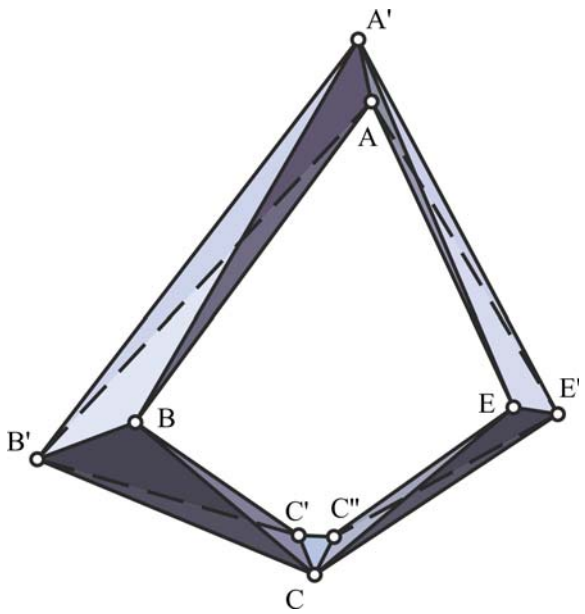

Fig. 3-7. The truss form of Myard linkage.

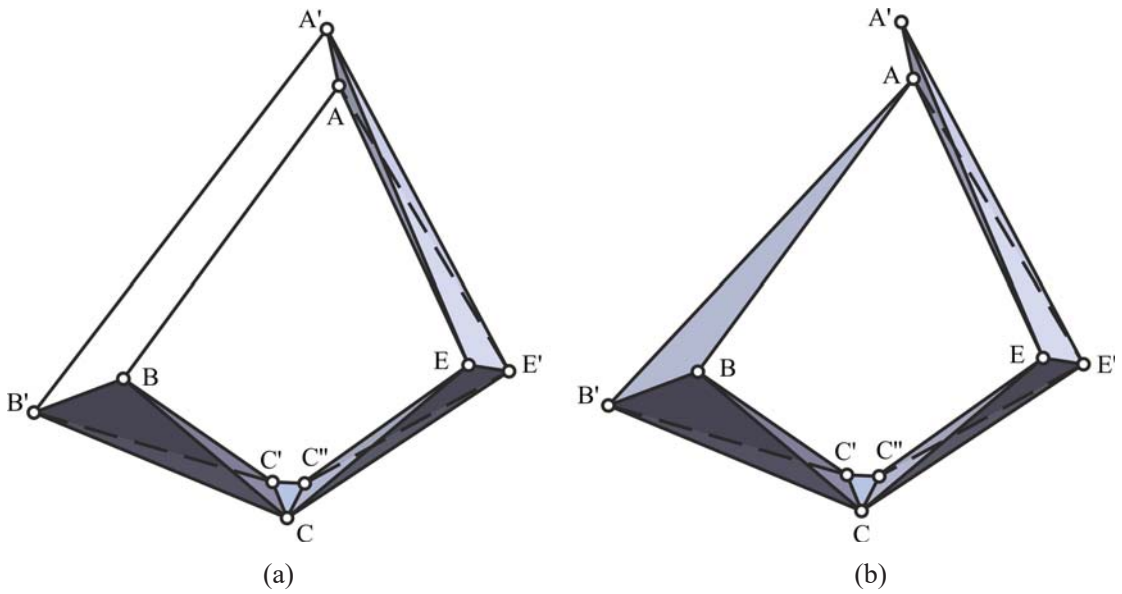

Fig. 3-8. Removing two redundant body bars from the Myard linkage. (a) bars AB' and A'B are removed; (b) bars A'B and A'B' are removed.

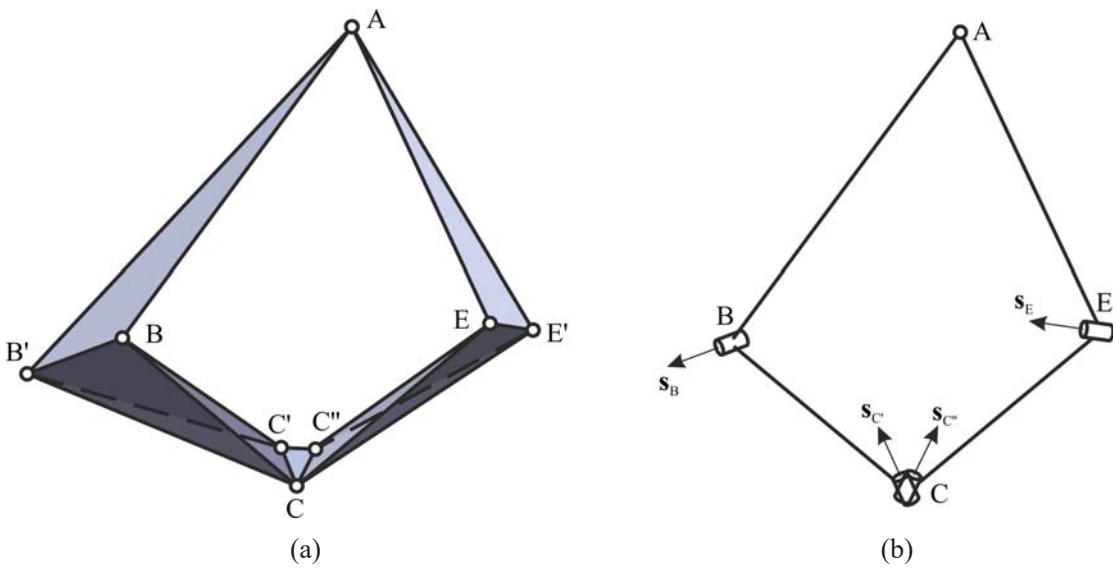

Fig. 3-9. Non-overconstrained forms (a) the final simplified truss; (b) the final linkage.

Similarly, node B can be changed into an *S* joint after removing redundant bars, which gives an *RSRRR* linkage in Fig. 3-10(a). But changing node C into an *S* joint gives an *RRSR* linkage in Fig. 3-10(b), which is neither a non-overconstrained one nor a five-bar linkage. Yet, if we consider the link bar which is not the shortest link, an *RRSRR* linkage can be formed with node C' as the *S* joint, see Fig. 3-10(c). It can be verified with screw theory that the three linkages in Figs. 3-9(b), 3-10(a), and 3-10(c) are the non-overconstrained forms of the Myard 5*R* linkage, one of which is shown in the following.

Taking the linkage in Fig. 3-9(a) as an example, *S* joint A can be regarded as three *R* joints, the common normal line of BA and AE as one revolute axis, *y* axis as another revolute axis, and the third revolute axis is determined by the right-hand rule. Adopting the same setup and notions as in the previous analysis, the coordinate system of the Myard 5*R* linkage is setup on the Bennett linkage ABCD which is shown in Fig. 3-11, and all the geometry coordinates are

$$\boldsymbol{A}=\left[0,\frac{u^2\cos\gamma}{w\sin^2\gamma},0\right]^{\mathrm{T}},\quad \boldsymbol{B}=\left[u,w\cos\gamma,-w\sin\gamma\right]^{\mathrm{T}},\tag{3-25a}$$

$$\boldsymbol{C}=\left[0,-\frac{u^2\cos\gamma}{w\sin^2\gamma},0\right]^{\mathrm{T}},\quad \boldsymbol{D}=\left[u,-w\cos\gamma,w\sin\gamma\right]^{\mathrm{T}},\tag{3-25b}$$

$$\boldsymbol{E}=\left[u-\frac{4w^2u\sin^2\gamma}{u^2+w^2\sin^2\gamma},w\cos\gamma,-w\sin\gamma+\frac{4wu^2\sin\gamma}{u^2+w^2\sin^2\gamma}\right]^{\mathrm{T}},\tag{3-25c}$$

$$\boldsymbol{B}'=\left[u+w\sin\gamma,w\cos\gamma,-w\sin\gamma+u\right]^{\mathrm{T}},\tag{3-25d}$$

$$\boldsymbol{C}' = \left[-\frac{u^2 \cos\gamma}{w \sin\gamma}, -\frac{u^2 \cos\gamma}{w \sin^2\gamma} + u \sin\gamma, u \cos\gamma \right]^{\mathrm{T}}, \tag{3-25e}$$

$$\boldsymbol{C}'' = \left[-\frac{u^2 \cos\gamma}{w \sin\gamma} + \frac{4u^2 w \cos\gamma \sin\gamma}{u^2 + w^2 \sin^2\gamma}, -\frac{u^2 \cos\gamma}{w \sin^2\gamma} + u \sin\gamma, u \cos\gamma - \frac{4u^3 \cos\gamma}{u^2 + w^2 \sin^2\gamma} \right]^{\mathrm{T}}, \tag{3-25f}$$

$$\boldsymbol{E}' = \left[u - \frac{4w^2 u \sin^2\gamma + 2w^3 \sin^3\gamma - 2u^2 w \sin\gamma}{u^2 + w^2 \sin^2\gamma} + w \sin\gamma, w \cos\gamma, \right. \\ \left. -w \sin\gamma + \frac{4wu^2 \sin\gamma + 2w^2 u \sin^2\gamma - 2u^3}{u^2 + w^2 \sin^2\gamma} + u \right]^{\mathrm{T}}. \tag{3-25g}$$

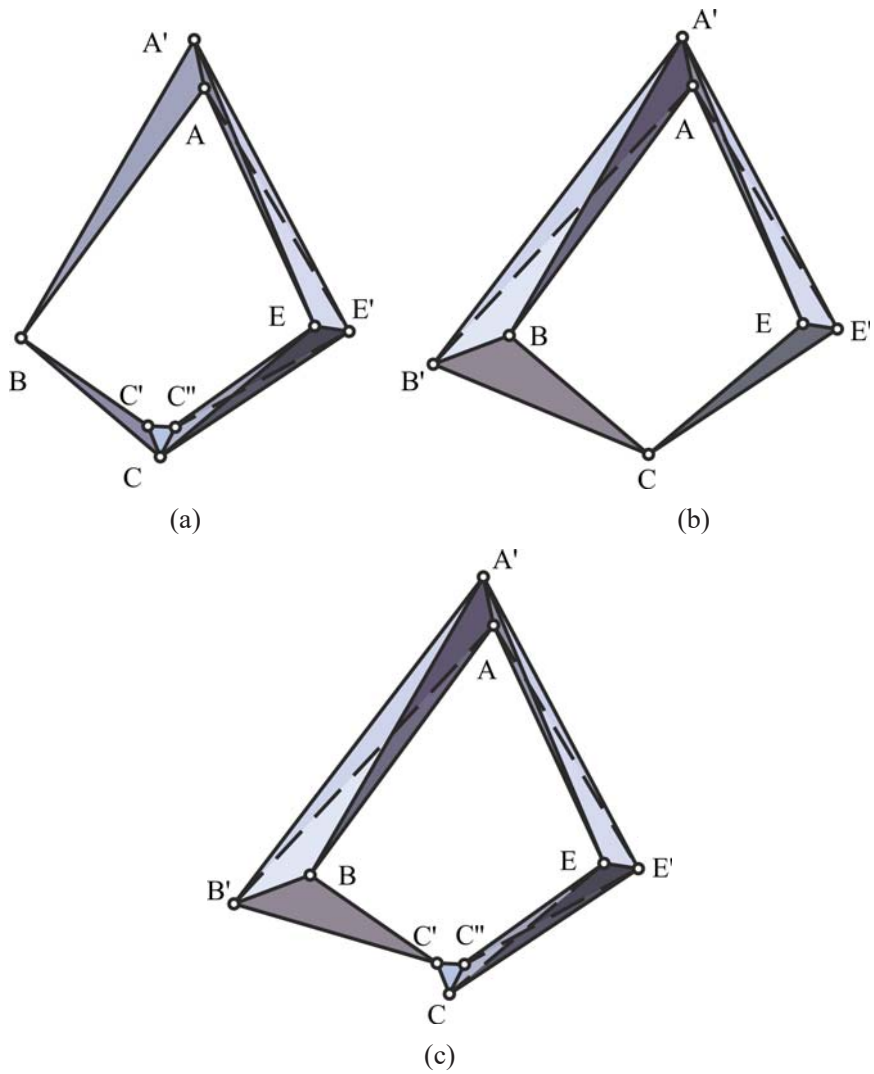

Fig. 3-10. The three possibilities of removing two body bars in a rigid body with a common joint from the Myard linkage. (a) B' as the common joint; (b) C' as the common joint; (c) C as the common joint.

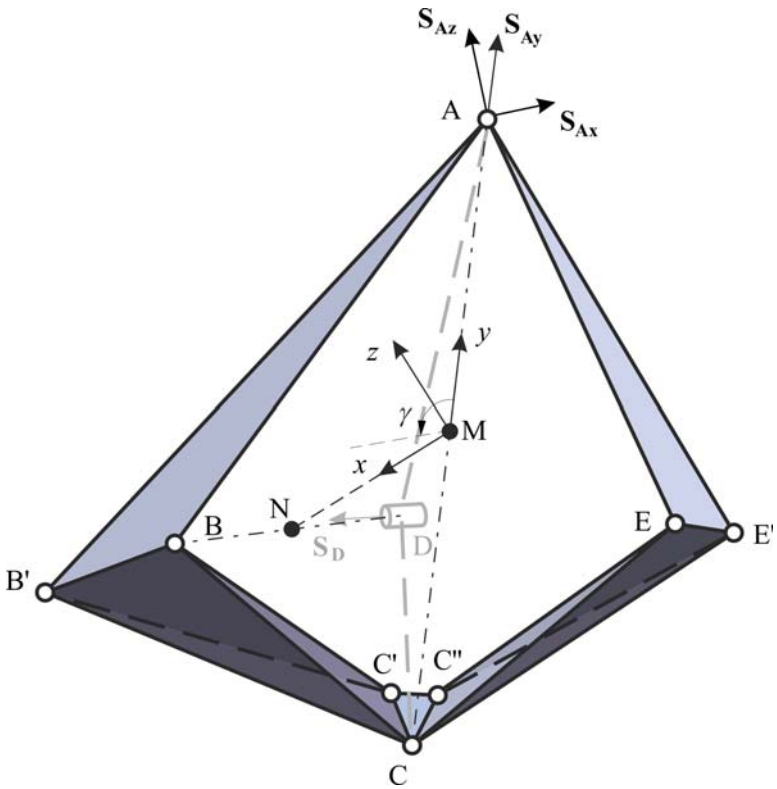

Fig. 3-11. Coordinate system for equivalence verification of Myard 5*R* linkage and its non-overconstrained form *RRSRR* linkage.

And all the kinetic screws can be written as

$$\boldsymbol{S}_{\mathrm{A}x}=\left(-w\sin\gamma,0,u,-\frac{u^3\cos\gamma}{w\sin^2\gamma},0,-\frac{u^2\cos\gamma}{\sin\gamma}\right)^{\mathrm{T}},\tag{3-26}$$

$$\boldsymbol{S}_{\mathrm{A}y}=\left(0,\frac{u^2\cos\gamma}{w\sin^2\gamma},0,0,0,0\right)^{\mathrm{T}},\tag{3-27}$$

$$\boldsymbol{S}_{\mathrm{A}z}=\left(\frac{u^2\cos\gamma}{w\sin\gamma},u\sin\gamma,u\cos\gamma,-\frac{u^3\cos^2\gamma}{w\sin^2\gamma},0,\frac{u^4\cos^2\gamma}{w^2\sin^3\gamma}\right)^{\mathrm{T}},\tag{3-28}$$

$$\boldsymbol{S}_{\mathrm{B}}=\left(w\sin\gamma,0,u,-uw\cos\gamma,u^2+w^2\sin^2\gamma,w^2\sin\gamma\cos\gamma\right)^{\mathrm{T}},\tag{3-29}$$

$$\boldsymbol{S}_{\mathrm{C'}}=\left(-\frac{u^2\cos\gamma}{w\sin\gamma},u\sin\gamma,u\cos\gamma,\frac{u^3\cos^2\gamma}{w\sin^2\gamma},0,\frac{u^4\cos^2\gamma}{w^2\sin^3\gamma}\right)^{\mathrm{T}},\tag{3-30}$$

$$\begin{aligned}\boldsymbol{S}_{\mathrm{C''}}=\Bigg(&-\frac{u^2\cos\gamma}{w\sin\gamma}+\frac{4u^2w\sin\gamma\cos\gamma}{u^2+w^2\sin^2\gamma},u\sin\gamma,u\cos\gamma-\frac{4u^3\cos\gamma}{u^2+w^2\sin^2\gamma},\\&\frac{\left(w^2\sin^2\gamma-3u^2\right)u^2\cos^2\gamma}{\left(u^2+w^2\sin^2\gamma\right)w\sin^2\gamma},0,-\left(-\frac{u^2\cos\gamma}{w\sin\gamma}+\frac{4u^2w\sin\gamma\cos\gamma}{u^2+w^2\sin^2\gamma}\right)\frac{u^2\cos\gamma}{w\sin^2\gamma}\Bigg)^{\mathrm{T}},\end{aligned}\tag{3-31}$$

$$\boldsymbol{S}_{\mathrm{E}}=\left(w\sin\gamma-2w\sin\gamma\frac{w^2\sin^2\gamma-u^2}{u^2+w^2\sin^2\gamma},0,u+2u\frac{w^2\sin^2\gamma-u^2}{u^2+w^2\sin^2\gamma},\right.$$
$$\left.-(u+2u\frac{w^2\sin^2\gamma-u^2}{u^2+w^2\sin^2\gamma})w\cos\gamma,-w^2\sin^2\gamma-u^2,\frac{w^2\sin 2\gamma(3u^2-w^2\sin^2\gamma)}{2(u^2+w^2\sin^2\gamma)}\right)^{\mathrm{T}}. \tag{3-32}$$

The motion of bar AE can be expressed by two branches C'BA and C"E when C'C" is taken as the reference link. Taking reciprocal of the motion screws, these two constraint screw systems are

$$\boldsymbol{S}^r{}_{11}=\left(\frac{w\sin^2\gamma}{u^2\cos\gamma},-\frac{u^2-w^2\sin^2\gamma}{u^3},-\frac{w^2\sin^3\gamma}{u^3\cos\gamma},\frac{w\sin\gamma}{u},0,1\right)^{\mathrm{T}}, \tag{3-33}$$

and

$$\boldsymbol{S}^r{}_{21}=\left(0,-\frac{w^4\left(3u^2-w^2\sin^2\gamma\right)\sin^5\gamma}{\left(u^2-3w^2\sin^2\gamma\right)u^3\cos\gamma\left(u^2+w^2\sin^2\gamma\right)},-\frac{w^2\sin^4\gamma\left(u^2+w^2\sin^2\gamma\right)}{\left(u^2-3w^2\sin^2\gamma\right)u^3\cos^2\gamma},0,1,0\right)^{\mathrm{T}}, \tag{3-34a}$$

$$\boldsymbol{S}^r{}_{22}=\left(0,-\frac{u^6-7u^4w^2\sin^2\gamma+7u^2w^4\sin^4\gamma-w^6\sin^6\gamma}{\left(u^2-3w^2\sin^2\gamma\right)u^3\left(u^2+w^2\sin^2\gamma\right)},\frac{w^2\sin^3\gamma\left(3u^2-w^2\sin^2\gamma\right)}{\left(u^2-3w^2\sin^2\gamma\right)u^3\cos\gamma},0,0,1\right)^{\mathrm{T}}, \tag{3-34b}$$

$$\boldsymbol{S}^r{}_{23}=\left(0,\frac{w\left(3u^2-w^2\sin^2\gamma\right)\sin\gamma}{u^2\left(u^2+w^2\sin^2\gamma\right)},\frac{w\sin^2\gamma}{u^2\cos\gamma},1,0,0\right)^{\mathrm{T}}, \tag{3-34c}$$

$$\boldsymbol{S}^r{}_{24}=\left(1,\frac{\left(u^2+w^2\sin^2\gamma\right)w\cos\gamma}{u\left(u^2-3w^2\sin^2\gamma\right)},\frac{\left(3u^2-w^2\sin^2\gamma\right)w\sin\gamma}{u\left(u^2-3w^2\sin^2\gamma\right)},0,0,0\right)^{\mathrm{T}}. \tag{3-34d}$$

As the dual relationship between constraints and motions, the motion of bar AE could be obtained as

$$\boldsymbol{S}=\begin{pmatrix}\frac{2u\cos\gamma}{w\sin^2\gamma},1,-\cos\gamma\frac{u^2-w^2\sin^2\gamma}{w^2\sin^3\gamma},-\frac{2u^2\cos^2\gamma}{w\sin^3\gamma},\\ u\cos\gamma\frac{u^2+w^2\sin^2\gamma}{w^2\sin^3\gamma},u\cos^2\gamma\frac{u^2-w^2\sin^2\gamma}{w^2\sin^4\gamma}\end{pmatrix}^{\mathrm{T}}. \tag{3-35}$$

And this motion could be expressed by each branch. Considering branch C'BA, coefficients ω_{Ax}, ω_{Ay}, ω_{Az}, ω_{B}, and $\omega_{\mathrm{C'}}$ must satisfy

$$\boldsymbol{S}=\omega_{\mathrm{Ax}}\boldsymbol{S}_{\mathrm{Ax}}+\omega_{\mathrm{Ay}}\boldsymbol{S}_{\mathrm{Ay}}+\omega_{\mathrm{Az}}\boldsymbol{S}_{\mathrm{Az}}+\omega_{\mathrm{B}}\boldsymbol{S}_{\mathrm{B}}+\omega_{\mathrm{C'}}\boldsymbol{S}_{\mathrm{C'}}, \tag{3-36}$$

which are solved as

$$\omega_{\mathrm{Ax}}=\omega_{\mathrm{Ay}}=0, \tag{3-37a}$$

$$\omega_{\mathrm{Az}} = \frac{2}{u\sin\gamma}, \tag{3-37b}$$

$$\omega_{\mathrm{B}} = -\frac{u\cos\gamma}{w^2\sin^3\gamma}, \tag{3-37c}$$

$$\omega_{\mathrm{C'}} = -\frac{1}{u\sin\gamma}. \tag{3-37d}$$

There is no motion around axes $\boldsymbol{S}_{\mathrm{Ax}}$ and $\boldsymbol{S}_{\mathrm{Ay}}$, and therefore the constraint on *S* joint A has been degenerated to an *R* joint, with axis along $\boldsymbol{S}_{\mathrm{A}z}$ which is the same as the Myard 5*R* linkage. Hence, this *RRSRR* mechanism and its original Myard 5*R* linkage have the same motion properties.

The extended Myard 5*R* linkage was obtained by combining two complementary Bennett linkages [72], where the twist α_{23} is not necessary to be $\frac{\pi}{2}$. From the above analysis, it can be assured that the *RRSRR* linkage with the corresponding geometric conditions is also the non-overconstrained form of the extended Myard 5*R* linkage.

3.5 Discussion on the Fabrication Errors

The non-overconstrained forms of overconstrained spatial linkages will expand their practical application as the manufacturing accuracy and subsequent cost can be greatly reduced. For most of 3D overconstrained linkages, the overconstrained geometric conditions are rigorous. In theory, fabrication errors could easily make the linkage lose its mobility if the clearance on joints is not considered. Yet for the non-overconstrained form, fabrication errors on the overconstrained geometric condition will only slightly affect the input-out relationship of the linkage without changing its mobility, which will be demonstrated through the following fabrication-error sensitivity analysis.

Considering the non-overconstrained form of the Bennett linkage, the *RSSR* linkage, the geometric parameters a_1, a_2, α and the kinematic variable θ_2 in Eq. (3-3) are denoted as a_{1R}, a_{2R}, α_R and θ_{2R}, respectively. The parameters of the Bennett linkage are the corresponding nominal variables, i.e.,

$$\left(\frac{a_{1R}}{a_{2R}}\right)^{nom} = \frac{\sin\alpha}{\sin\beta},\ a_{1R}^{nom} = a_1,\ a_{2R}^{nom} = a_2,\ \alpha_R^{nom} = \alpha\ . \tag{3-38}$$

Meanwhile the general output can be written as,

$$\theta_{2R} = f\left(x_1, x_2\right), \tag{3-39}$$

in which $x_1 = \alpha_R$ and $x_2 = \frac{a_{1R}}{a_{2R}}$. Expanding this function in Taylor-series around the

nominal values $x_1^{nom} = \alpha$ and $x_2^{nom} = \dfrac{a_1}{a_2}$ gives

$$\theta_{2R} = \theta_{2R}^{nom} + \sum_{i=1}^{2} \left.\frac{\partial f}{\partial x_i}\right|_{nom} \Delta x_i + \frac{1}{2!}\sum_{i=1}^{2} \left.\frac{\partial^2 f}{\partial x_i^2}\right|_{nom} \Delta x_i^{\,2} + \left.\frac{\partial^2 f}{\partial x_1 \partial x_2}\right|_{nom} \Delta x_1 \Delta x_2 + \cdots, \quad (3\text{-}40)$$

where $\Delta x_i = x_i - x_i^{nom}$. For small, independent variations about the nominal configuration, a linear approximation can be made. Thereby the above equation renders the output error of the *RSSR* linkage from the nominal configuration as

$$\Delta\theta_{2R} = \theta_{2R} - \theta_{2R}^{nom} \approx \sum_{i=1}^{2} \left.\frac{\partial f}{\partial x_i}\right|_{nom} \Delta x_i = \left.\frac{\partial f}{\partial \boldsymbol{X}}\right|_{nom} \Delta \boldsymbol{X}, \quad (3\text{-}41)$$

where $\Delta \boldsymbol{X} = \left[\Delta x_1, \Delta x_2\right]^{\mathrm{T}}$. $\left.\dfrac{\partial f}{\partial \boldsymbol{X}}\right|_{nom}$ is known as the sensitivity Jacobian of the mechanism [138], evaluated at the nominal configuration. Deriving from Eqs. (3-5) and (3-39),

$$\frac{\partial f}{\partial x_i} = \frac{\left(A' \pm \dfrac{AA' + BB' - CC'}{\sqrt{A^2 + B^2 - C^2}}\right)(B + C) - \left(A \pm \sqrt{A^2 + B^2 - C^2}\right)(B' + C')}{A^2 + B^2 + BC \pm A\sqrt{A^2 + B^2 - C^2}}, \quad (3\text{-}42)$$

where $A' = \dfrac{\partial A}{\partial x_i}$, $B' = \dfrac{\partial B}{\partial x_i}$, and $C' = \dfrac{\partial C}{\partial x_i}$, while $\dfrac{\partial A}{\partial x_1} = -\sin\alpha_R \sin\theta_1$, $\dfrac{\partial B}{\partial x_1} = 0$, $\dfrac{\partial C}{\partial x_1} = 0$, $\dfrac{\partial A}{\partial x_2} = 0$, $\dfrac{\partial B}{\partial x_2} = -1$, and $\dfrac{\partial C}{\partial x_2} = \cos\theta_1$. Obviously, the sign ‘ ± ’ in Eq. (3-42) should be chosen as the one in the condition of Eq. (3-6a). The output error is related to the components variability linearly.

Take a Bennett linkage and its equivalent *RSSR* linkage with twists $\alpha_R^{nom} = 45°$ and link lengths $a_{1R}^{nom} = 100\text{mm}$ and $a_{2R}^{nom} = 70.72\text{mm}$ as an example. Denote the deviations of the angular and linear dimensions as $\Delta\alpha$ and Δl , respectively. Based on the ISO standard about tolerances [139], for the very coarse class,

$$\Delta\alpha = 1^{\circ} \text{ and } \Delta l = 1.5\,\text{mm}. \quad (3\text{-}43)$$

A scale factor $k \in [-1,1]$ is introduced, i.e.,

$$\Delta x_1 = \alpha_R - \alpha = k\Delta\alpha, \quad \Delta x_2 = \frac{a_1 + k\Delta l}{a_2 - k\Delta l} - \frac{a_1}{a_2}. \quad (3\text{-}44)$$

Then, the sensitivity Jacobian $\left.\dfrac{\partial f}{\partial \boldsymbol{X}}\right|_{nom}$ can be estimated from Eq. (3-43). And the output error

$$\Delta\theta_{2R} \approx \left[\frac{\partial f}{\partial x_1} \quad \frac{\partial f}{\partial x_2}\right]\Bigg|_{nom} \left[k\Delta\alpha \quad \frac{a_1 + k\Delta l}{a_2 - k\Delta l} - \frac{a_1}{a_2}\right]^{\mathrm{T}}. \tag{3-45}$$

Figure 3-12(a) shows the effect of each fabrication error on the output error. The magnitude of the output error due to link length errors is always greater than that from twist angle errors. The maximum is reached when the input angle θ_1 is around 180°. For the 'coarse' tolerance with twist error 1°, the maximum deviation of the output is 0.58°.

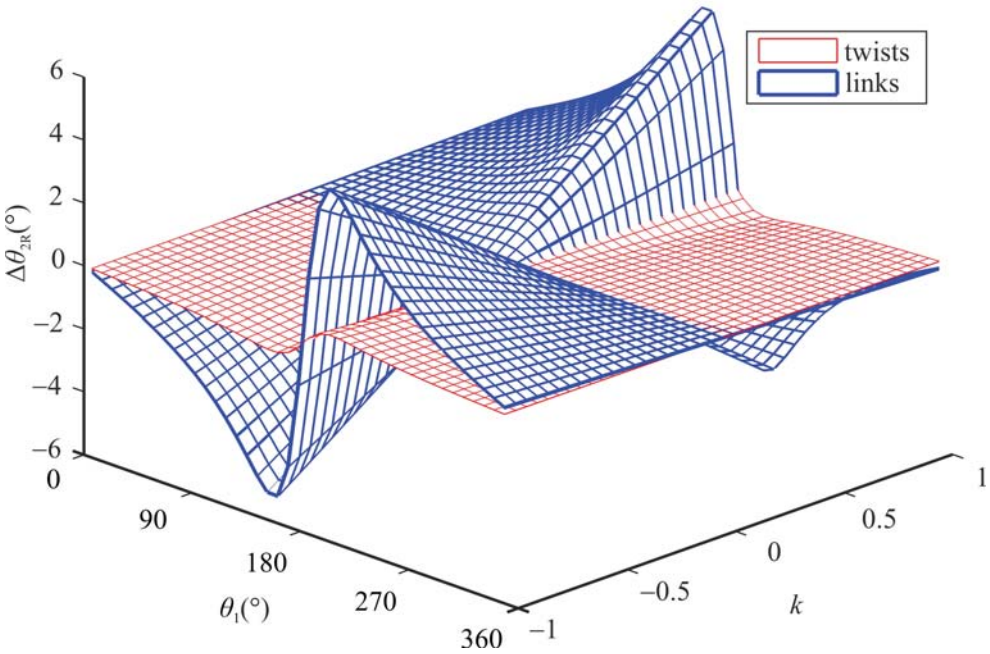

(a)

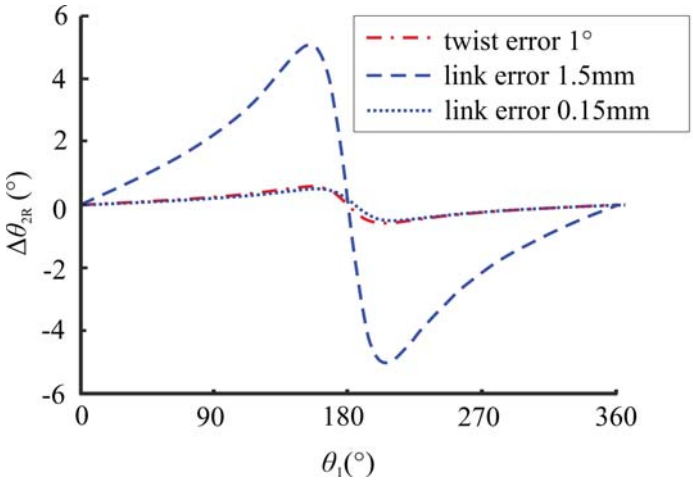

(b)

Fig. 3-12. Output deviations generated by twist angle error and link length error.

And with link length error 1.5mm, the maximum $\Delta\theta_2$ is 5.06°, which is much larger than the former one, see Fig. 3-12(b). Therefore, more attention needs to be paid to the link length accuracy to keep the output deviation small. In practice, link length accuracy is easier to be improved than angular accuracy. Figure 3-13 also shows the output deviation caused by the 'fine' link length accuracy with a link length error of 0.15mm, in which the maximum $\Delta\theta_2$ is 0.53°. For other design parameters of *RSSR* linkage, the tolerances can also be taken from [139] and the output errors can be calculated with Eqs. (3-41), (3-43) and (3-44).

Once there are fabrication errors on the link length and joint twist, the *RSSR* linkage will not work as the Bennett linkage, i.e., the two *S* joints do no work as *R* joints, but also rotate on the other two orthogonal directions. To calculate the waggle angles about other rotation axes, the coordinate systems on A, B are established by D-H notation, and the coordinate system on D is fixed with bar AD whose *z* axis is along the axis of this joint in its original Bennett linkage, *x* axis is along the direction of DA, and *y* axis is set by the right-hand rule, as shown in Fig. 3-13. Therefore, the motion of point C in the coordinate system on joint D reflects the motion which is provided by joint D. As C is expressed in system B as

$$\boldsymbol{C}_{\mathrm{B}} = [a_{2R}\cos\theta_{2R}, a_{2R}\sin\theta_{2R}, 0, 1]^{\mathrm{T}}, \tag{3-46}$$

and transformations matrices are

$$\boldsymbol{T}_{\mathrm{B(A)}} = \begin{bmatrix} \cos\theta_1 & -\sin\theta_1\cos\alpha_R & \sin\theta_1\sin\alpha_R & a_{1R}\cos\theta_1 \\ \sin\theta_1 & \cos\theta_1\cos\alpha_R & -\cos\theta_1\sin\alpha_R & a_{1R}\sin\theta_1 \\ 0 & \sin\alpha_R & \cos\alpha_R & 0 \\ 0 & 0 & 0 & 1 \end{bmatrix}, \tag{3-47a}$$

$$\boldsymbol{T}_{\mathrm{A(D)}} = \begin{bmatrix} 1 & 0 & 0 & a_{2R} \\ 0 & \cos\beta & -\sin\beta & 0 \\ 0 & \sin\beta & \cos\beta & 0 \\ 0 & 0 & 0 & 1 \end{bmatrix}, \tag{3-47b}$$

then,

$$\begin{aligned} \boldsymbol{C}_{\mathrm{D}} &= \boldsymbol{T}_{\mathrm{A(D)}}\boldsymbol{T}_{\mathrm{B(A)}}\boldsymbol{C}_{\mathrm{B}} \\ &= [a_{2R} + a_{1R}\cos\theta_1 + a_{2R}\cos\theta_1\cos\theta_{2R} - a_{2R}\cos\alpha_R\sin\theta_1\sin\theta_{2R}; \\ &\quad a_{1R}\cos\beta\sin\theta_1 - a_{2R}\sin\theta_{2R}(\sin\alpha_R\sin\beta - \cos\alpha_R\cos\beta\cos\theta_1) + a_{2R}\cos\beta\cos\theta_{2R}\sin\theta_1; \\ &\quad a_{1R}\sin\beta\sin\theta_1 + a_{2R}\sin\theta_{2R}(\sin\alpha_R\cos\beta + \cos\alpha_R\sin\beta\cos\theta_1) + a_{2R}\sin\beta\cos\theta_{2R}\sin\theta_1; \\ &\quad 1] \end{aligned} \tag{3-48}$$

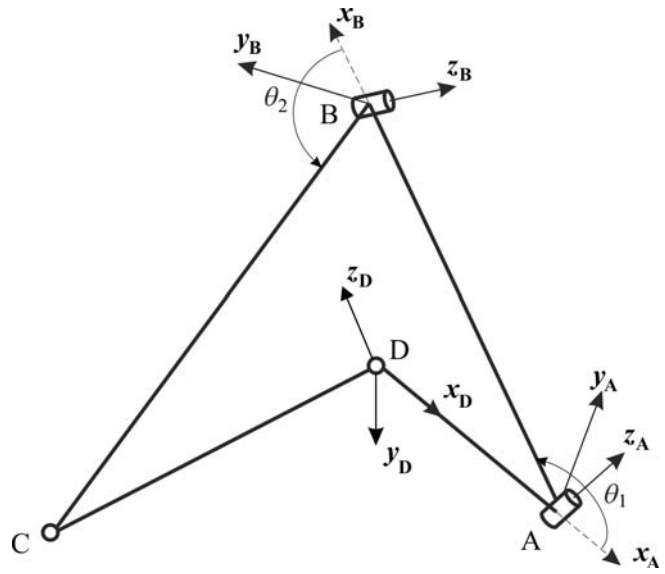

Fig. 3-13. Coordinate systems for the calculation of deviations on the *RSSR* linkage.

If there are no fabrication errors, *S* joint D works as an *R* joint, namely, bar CD is always perpendicular to z_{D}. With fabrication errors, the angle between CD and z_{D} is

$$\gamma_{D_Z} = \arccos \frac{\boldsymbol{CD}_{\mathrm{D}} \cdot \boldsymbol{k}}{\overline{\mathrm{CD}}}, \tag{3-49}$$

where $\boldsymbol{k} = [0, 0, 1]^{\mathrm{T}}$, and $\overline{\mathrm{CD}} = a_{2R}$, and then

$$\begin{aligned} \gamma_{D_z} = \arccos\Big[&\sin\theta_{2R}(\sin\alpha_R\cos\beta + \cos\alpha_R\sin\beta\cos\theta_1) + \\ &\sin\beta\cos\theta_{2R}\sin\theta_1 + \frac{a_{1R}}{a_{2R}}\sin\beta\sin\theta_1\Big]. \end{aligned} \tag{3-50}$$

Figure 3-14 shows the deviation angles from the right angle. With the errors given in Eq. (3-42), the largest deviation generated by angular errors $\Delta\alpha = -1^{\circ}$ is 0.58°, and the largest deviation generated by linear errors is 1.22° when $\Delta a_1 = -1.5mm$ and $\Delta a_2 = 1.5mm$. It demonstrates that the *S* joint actually provides a main revolution at the *R* joint direction of its original Bennett linkage and a small waggle at the other two orthogonal directions.

Therefore, reasonable fabrication errors on the *RSSR* linkage will keep the mobility and offer good accuracy in replacing the Bennett linkage for engineering applications. And a particular *S* joint is designed to provide the main revolution and allow small waggle to compensate fabrication errors, see Fig. 3-15, C and D are set with these particular *S* joints, and the allowing deviation, θ_e, in Fig. 3-15(c).

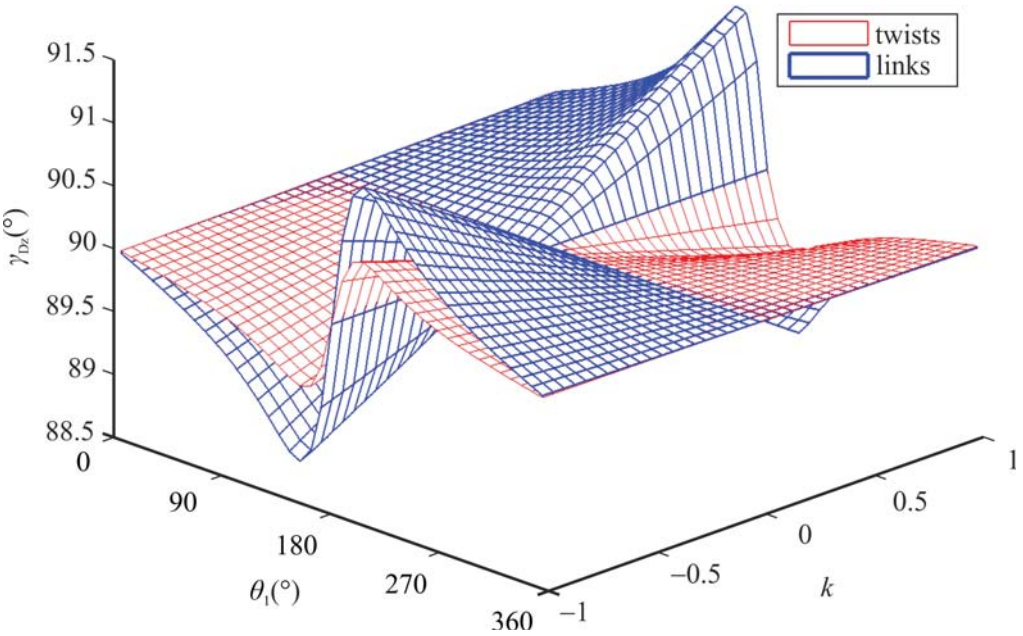

Fig. 3-14. Deviations on the main rotation direction due to fabrication errors.

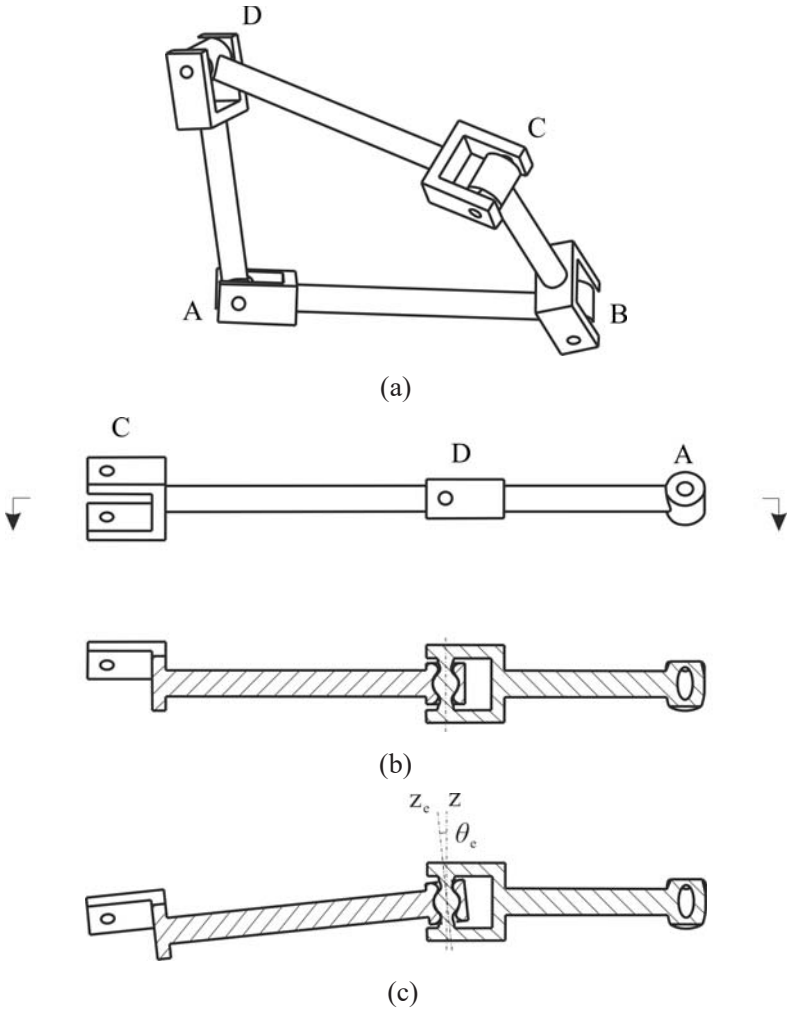

Fig. 3-15. The particular *S* joints on C and D in the *RSSR* linkage. (a) the whole linkage; (b) a particular *S* joint; (c) the waggling angle of the revolute axis.

3.6 Conclusions

In this chapter, we proposed a procedure to obtain the non-overconstrained forms of overconstrained linkages by the truss method. First, the truss forms of the overconstrained linkages are obtained. Second, the redundant bars in the truss forms are determined by Maxwell's rule and equilibrium matrices. Finally, non-overconstrained forms are obtained after removing those redundant bars from the truss forms. The Bennett linkage and Myard 5*R* linkage have been taken as two case studies. Their non-overconstrained forms are *RSSR* linkage and *RRSRR* linkages, respectively. Furthermore their kinematic equivalences have also been illustrated with the input-output equation by screw theory. The discussion of output deviations caused by fabrication errors has shown that the non-overconstrained forms can keep the kinematic characteristics of the original overconstrained linkages with great fault-tolerance capability.

Chapter 4 Transformation between Cuboctahedron and Octahedron

4.1 Introduction

Cuboctahedron is a semi-regular polyhedron with six square faces and eight triangular faces, which owns 12 identical vertices, with two triangles and two squares meeting at each, and 24 identical edges, each separating a triangle from a square [102]. Meanwhile, a regular octahedron is a Platonic solid composed of eight equilateral triangles, four of which meet at each vertex [102]. Intuitively, both containing eight equilateral regular triangle faces, a cuboctahedron and a regular octahedron may be transformed to each other by deploying and folding the six square faces.

In this chapter, we propose a polyhedral transformation between them with one DOF kinematic motion. The layout of the chapter is as follows. Section 4.2 expounds the construction of the deployable polyhedron. Section 4.3 presents kinematics of this transformation done by geometric analysis and a numerical method based on the truss method. And, conclusions are given in Section 4.4.

4.2 Construction of Transformable Polyhedron between Cuboctahedron and Octahedron

Figure 4-1 shows the object of this chapter, a cuboctahedron and an octahedron with unit-length edges. All square faces are hollow, while triangle faces are rigid. By setting one movable joint at each vertex, the cuboctahedron can be folded into the octahedron along a determined motion trend, such as pairs of vertices A and I, B and D, C and K, E and F, G and H, J and L trend to meet respectively, see Fig. 4-1(b). As a result, all of the six square hollows will vanish after the transformation. If only *S* joints are used at all of the vertices, the cuboctahedron would have 18 DOFs according to the truss method. Hence, extra constraints must be imposed to reduce the number of DOFs. One way was first proposed by Buckminster Fuller [106]. Each triangular face is allowed to rotate and translate about its normal at the centre, and its connections with the neighbouring triangles are always maintained. This is kinematically equivalent to a system where each of eight triangles in cuboctahedron has its own cylindrical joint whose axis passes through both the centres of the triangles and that of the polyhedrons, and the triangles are connected by *S* joints (ball joints) at the polyhedral vertices. The system has one degree of freedom (DOF) provided that the axes of all cylindrical joints are fastened together at the centre of the polyhedron. This, however, makes the transformation of little practical use as the space enclosed by the faces is taken up by the physical joints. If the axes of the cylindrical joints were not physically fixed together, the system would have six DOFs, as demonstrated by Buckminster Fuller's own model [108], making it impossible to

complete the transformation in an orderly way. The other way is to replace the 3-DOF *S* joint with 1-DOF *R* joint. Each such replacement will reduce two DOFs in general according to the Kutzbach criterion [36]. In fact, to vanish square faces, four-bar linkages should be employed. Meanwhile, Bennett linkage is the only four-bar linkage to realise non-spherical and non-planar motion. When all the vertices are *R* joints, the cuboctahedron becomes an assembly of six Bennett linkages in space to form a multi-loop linkage. Yet, previous research on Bennett mobile assemblies [85] shows no readily solution with such topology. Meanwhile, this cuboctahedron can also be considered as the connection of Bennett linkage ABCD on the bottom and linkage IJKL on the top by four *R* joints in the middle vertices E, F, G, and H. And Baker already proved that the connection of two Bennett linkages with *R* joints could not obtain a mobile network [83]. But two Bennett linkages can be inter-connected by *S* joints to form a mobile assembly, whose mobility is one calculated by the truss method [140]. Therefore, we can make vertices on the top and bottom into *R* joints and keep the middle ones as *S* joints.

A coordinate system is set up on the body centre of the cuboctahedron by the right-hand rule where *z* axis directs upward passing through the centre of square IJLK, and axes *x*, *y* direct to centres of two adjacent squares in the side, respectively, as shown in Fig. 4-1(a). Then vertices of the cuboctahedron are

$$\boldsymbol{A}^{\mathrm{co}} = (\frac{\sqrt{2}}{2}, 0, -\frac{\sqrt{2}}{2})^{\mathrm{T}}, \quad \boldsymbol{B}^{\mathrm{co}} = (0, -\frac{\sqrt{2}}{2}, -\frac{\sqrt{2}}{2})^{\mathrm{T}}, \tag{4-1a}$$

$$\boldsymbol{C}^{\mathrm{co}} = (-\frac{\sqrt{2}}{2}, 0, -\frac{\sqrt{2}}{2})^{\mathrm{T}}, \quad \boldsymbol{D}^{\mathrm{co}} = (0, \frac{\sqrt{2}}{2}, -\frac{\sqrt{2}}{2})^{\mathrm{T}}, \tag{4-1b}$$

$$\boldsymbol{E}^{\mathrm{co}} = (\frac{\sqrt{2}}{2}, -\frac{\sqrt{2}}{2}, 0)^{\mathrm{T}}, \quad \boldsymbol{F}^{\mathrm{co}} = (-\frac{\sqrt{2}}{2}, -\frac{\sqrt{2}}{2}, 0)^{\mathrm{T}}, \tag{4-1c}$$

$$\boldsymbol{G}^{\mathrm{co}} = (-\frac{\sqrt{2}}{2}, \frac{\sqrt{2}}{2}, 0)^{\mathrm{T}}, \quad \boldsymbol{H}^{\mathrm{co}} = (\frac{\sqrt{2}}{2}, \frac{\sqrt{2}}{2}, 0)^{\mathrm{T}}, \tag{4-1d}$$

$$\boldsymbol{G}^{\mathrm{co}} = (-\frac{\sqrt{2}}{2}, \frac{\sqrt{2}}{2}, 0)^{\mathrm{T}}, \quad \boldsymbol{J}^{\mathrm{co}} = (0, -\frac{\sqrt{2}}{2}, \frac{\sqrt{2}}{2})^{\mathrm{T}}, \tag{4-1e}$$

$$\boldsymbol{K}^{\mathrm{co}} = (-\frac{\sqrt{2}}{2}, 0, \frac{\sqrt{2}}{2})^{\mathrm{T}}, \quad \boldsymbol{L}^{\mathrm{co}} = (0, \frac{\sqrt{2}}{2}, \frac{\sqrt{2}}{2})^{\mathrm{T}}, \tag{4-1f}$$

where superscript "co" represents cuboctahedron.

For the octahedron, the coordinate system is set where *z* axis directs upward, *x* axis directs to A and *y* axis directs to G, as shown in Fig. 4-1(b). Then vertices are

$$\boldsymbol{A}^{\mathrm{o}} = \boldsymbol{I}^{\mathrm{o}} = (\frac{\sqrt{2}}{2}, 0, 0)^{\mathrm{T}}, \quad \boldsymbol{B}^{\mathrm{o}} = \boldsymbol{D}^{\mathrm{o}} = (0, 0, -\frac{\sqrt{2}}{2})^{\mathrm{T}}, \tag{4-2a}$$

$$\boldsymbol{C}^{\mathrm{o}} = \boldsymbol{K}^{\mathrm{o}} = (-\frac{\sqrt{2}}{2}, 0, 0)^{\mathrm{T}}, \boldsymbol{E}^{\mathrm{o}} = \boldsymbol{F}^{\mathrm{o}} = (0, -\frac{\sqrt{2}}{2}, 0)^{\mathrm{T}}, \tag{4-2b}$$

$$\boldsymbol{G}^{\mathrm{o}} = \boldsymbol{H}^{\mathrm{o}} = (0, \frac{\sqrt{2}}{2}, 0)^{\mathrm{T}}, \quad \boldsymbol{J}^{\mathrm{o}} = \boldsymbol{L}^{\mathrm{o}} = (0, 0, \frac{\sqrt{2}}{2})^{\mathrm{T}}, \tag{4-2c}$$

where superscript "o" represents Octahedron.

To vanish the square face, a Bennett linkage ABCD will be folded into the edge ABC on octahedron in Fig. 4-1(b). So, the next work is to determin joint directions of *R* joints A, B, C, D to make the linkage move between desired initial and final configurations.

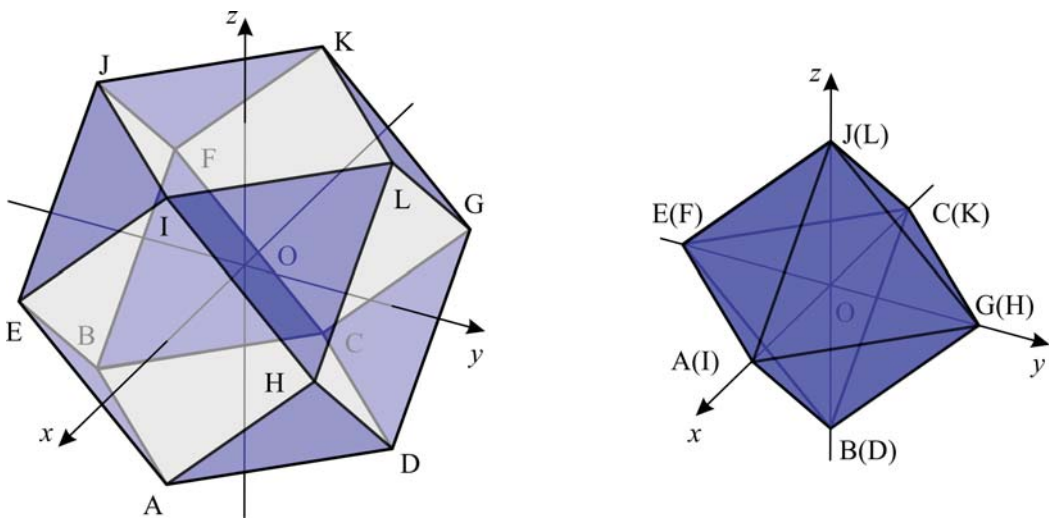

(a) (b)

Fig. 4-1. Transformation between (a) cuboctahedron and (b) octahedron illustrated in the coordinate system fixed on their body centres.

Triangle BCF is assumed to be fixed in the coordinate system, triangle CDG could rotate around the *R* joint $\boldsymbol{s}_{\mathrm{C}}$ a certain angle to its final position CBG^{f}, as shown in Fig. 4-2. As dihedral angle of each pair of adjacent triangles in octhedron is $\arccos(-\frac{1}{3})$, G^{f} can be obtained by roation of F around $\boldsymbol{BC}$ by the angle, the transformation matrix is

$$\boldsymbol{T} = \begin{bmatrix} \frac{1}{3} & -\frac{2}{3} & \frac{2}{3} \\ -\frac{2}{3} & \frac{1}{3} & \frac{2}{3} \\ -\frac{2}{3} & -\frac{2}{3} & -\frac{1}{3} \end{bmatrix}, \tag{4-3}$$

and then

$$\boldsymbol{G}^{\mathrm{f}} = \boldsymbol{T}\boldsymbol{F}^{\mathrm{co}} = (\frac{\sqrt{2}}{6}, \frac{\sqrt{2}}{6}, -\frac{\sqrt{2}}{3})^{\mathrm{T}}. \tag{4-4}$$

Meanwhile, axis of R joint on C, $\boldsymbol{s}_{\mathrm{C}}$, must be in both bisecting planes of angle DCB and angle GCG^{f}, thus

$$\boldsymbol{s}_{\mathrm{C}} \perp \boldsymbol{D}^{\mathrm{co}}\boldsymbol{B}^{\mathrm{co}} \quad \text{and} \quad \boldsymbol{s}_{\mathrm{C}} \perp \boldsymbol{G}^{\mathrm{co}}\boldsymbol{G}^{\mathrm{f}}, \tag{4-5}$$

then

$$\boldsymbol{s}_{\mathrm{C}} = \boldsymbol{D}^{\mathrm{co}}\boldsymbol{B}^{\mathrm{co}} \times \boldsymbol{G}^{\mathrm{co}}\boldsymbol{G}^{\mathrm{f}} = (\frac{2}{3}, 0, \frac{4}{3})^{\mathrm{T}}. \tag{4-6}$$

γ_1 and γ_2 are pairs of two axis angles on C, which are angles between the revolute axis and its connected edges,

$$\angle \mathrm{BCC'} = \angle \mathrm{DCC'} = \gamma_1 = \arcsin(\frac{\boldsymbol{s}_{\mathrm{C}} \times \boldsymbol{C}^{\mathrm{co}}\boldsymbol{B}^{\mathrm{co}}}{|\boldsymbol{s}_{\mathrm{C}}|}) = 71.57°, \tag{4-7a}$$

$$\angle \mathrm{FCC'} = \angle \mathrm{GCC'} = \gamma_2 = \arcsin(\frac{\boldsymbol{s}_{\mathrm{C}} \times \boldsymbol{C}^{\mathrm{co}}\boldsymbol{F}^{\mathrm{co}}}{|\boldsymbol{s}_{\mathrm{C}}|}) = 50.77°. \tag{4-7b}$$

Other revolute axes in this Bennett linkage can be determined similarly,

$$\boldsymbol{s}_{\mathrm{A}} = (-\frac{2}{3}, 0, \frac{4}{3})^{\mathrm{T}}, \quad \boldsymbol{s}_{\mathrm{B}} = (0, \frac{4}{3}, \frac{2}{3})^{\mathrm{T}}, \quad \boldsymbol{s}_{\mathrm{D}} = (0, -\frac{4}{3}, \frac{2}{3})^{\mathrm{T}}. \tag{4-8}$$

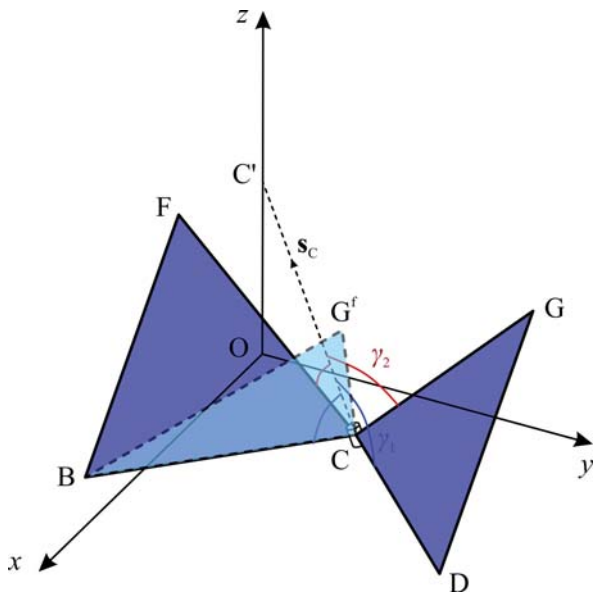

Fig. 4-2. One pair of adjacent triangles BCF and CDG is chosen to show the determination of the revolute axis.

Similarly, other four triangular faces, surrounding a hollowed square IJKL, could be set with the same Bennett linkage shown in Fig. 4-3(a). Rotation axes on the second Bennett linkage can be calculated by symmetric rotations of Euler-Rodrigues

formula [141],

$$\boldsymbol{s}_{\mathrm{I}} = \boldsymbol{s}_{\mathrm{C}} \cdot Rot(y,\pi) = (-\frac{2}{3}, 0, -\frac{4}{3})^{\mathrm{T}}, \tag{4-9a}$$

$$\boldsymbol{s}_{\mathrm{J}} = \boldsymbol{s}_{\mathrm{B}} \cdot Rot(y,\pi) = (0, \frac{4}{3}, -\frac{2}{3})^{\mathrm{T}}, \tag{4-9b}$$

$$\boldsymbol{s}_{\mathrm{K}} = \boldsymbol{s}_{\mathrm{A}} \cdot Rot(y,\pi) = (\frac{2}{3}, 0, -\frac{4}{3})^{\mathrm{T}}, \tag{4-9c}$$

$$\boldsymbol{s}_{\mathrm{L}} = \boldsymbol{s}_{\mathrm{D}} \cdot Rot(y,\pi) = (0, -\frac{4}{3}, -\frac{2}{3})^{\mathrm{T}}, \tag{4-9d}$$

where $Rot(y,\pi)$ is the matrix for rotating around y axis by π.

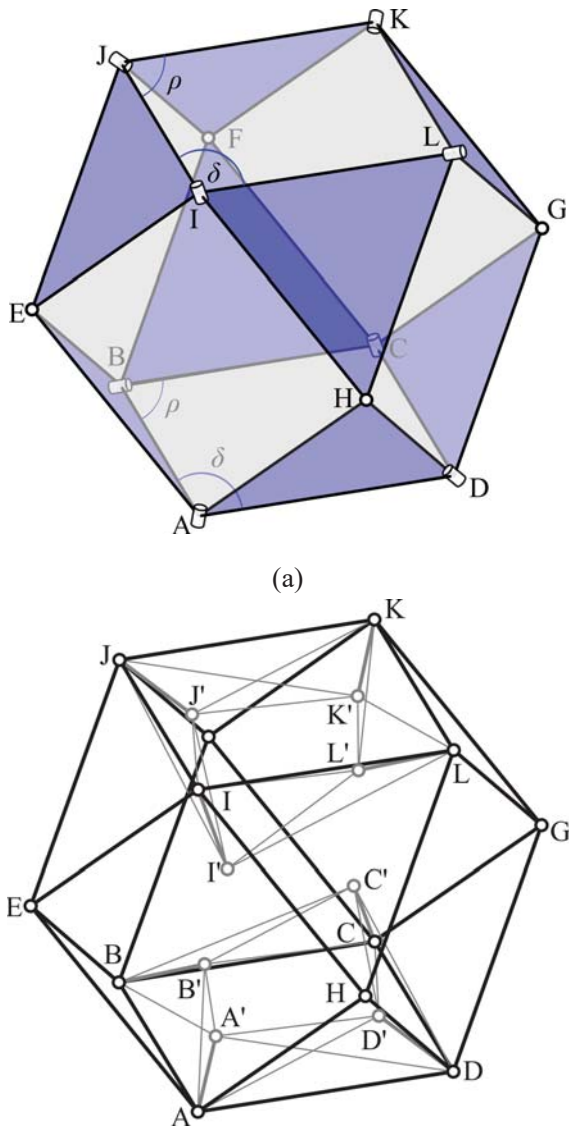

Fig. 4-3. Transforming (a) the polyhedral linkage constructed with two Bennett linkages to (b) its truss form.

Hereto, the polyhedral linkage is constructed with two Bennett linkages, whose links are all triangle, and these two linkages are connected with four *S* joints. The truss analogy of this polyhedral linkage, shown in Fig. 4-3(b), yields $j = 20$ joints, $b = 64$ bars, and the rank of its equilibrium matrix $r = 53$, thus, an overall DOF is $m = 3j - r - 6 = 1$ according to the Maxwell's rule. No further replacement of *S* joints is needed.

4.3 Kinematics of the Transformable Polyhedron

Let us consider the kinematic behavior of Bennett linkage ABCD. Its deployed configuration is the square in cuboctahedron and the folded one is along two edges of octahedron while joint axes A, C and B, D intersect in two pairs. As revolute axes are not perpendicular to their connecting links, linkage ABCD is in fact an alternative form of Bennett linkage [87, 88]. Its corresponding original form can be found by extending the joint axes and connecting the shortest distance between the adjacent joints, see Fig. 4-4 for the geometric relationship between the alternative form and its original Bennett linkage of quadrilateral ABCD, in which $\mathrm{A_bB_b}$, $\mathrm{B_bC_b}$, $\mathrm{C_bD_b}$, and $\mathrm{D_bA_b}$ are bars of its original Bennett linkage as $\boldsymbol{s}_\mathrm{A} \perp \boldsymbol{D}_\mathrm{b}\boldsymbol{A}_\mathrm{b}$, $\boldsymbol{s}_\mathrm{A} \perp \boldsymbol{A}_\mathrm{b}\boldsymbol{B}_\mathrm{b}$, $\boldsymbol{s}_\mathrm{B} \perp \boldsymbol{A}_\mathrm{b}\boldsymbol{B}_\mathrm{b}$, $\boldsymbol{s}_\mathrm{B} \perp \boldsymbol{B}_\mathrm{b}\boldsymbol{C}_\mathrm{b}$, $\boldsymbol{s}_\mathrm{C} \perp \boldsymbol{B}_\mathrm{b}\boldsymbol{C}_\mathrm{b}$, $\boldsymbol{s}_\mathrm{C} \perp \boldsymbol{C}_\mathrm{b}\boldsymbol{D}_\mathrm{b}$, $\boldsymbol{s}_\mathrm{D} \perp \boldsymbol{C}_\mathrm{b}\boldsymbol{D}_\mathrm{b}$, and $\boldsymbol{s}_\mathrm{D} \perp \boldsymbol{D}_\mathrm{b}\boldsymbol{A}_\mathrm{b}$. Meanwhile, $\boldsymbol{s}_\mathrm{A}$ and $\boldsymbol{s}_\mathrm{C}$ meet at M, $\boldsymbol{s}_\mathrm{B}$ and $\boldsymbol{s}_\mathrm{D}$ meet at N, both on $\boldsymbol{z}$ axis, which is the rotation axis of the linkage as it crosses the midpoint of $\mathrm{A_bC_b}$, Q, and the midpoint of $\mathrm{B_bD_b}$, P. Axis orientation angles γ_1 and γ_2, Eq. (4-7), are depicted at vertices A and B, respectively. Denote the length of original linkage, which is shortest distance between adjacent revolute axes, as a, the extensions $\mathrm{AA_b}$ and $\mathrm{BB_b}$ on $\mathrm{A_b}$ and $\mathrm{B_b}$ in its alternative form as c and d, respectively, and the twist angle of link $\mathrm{A_bB_b}$ as α. Then we have

$$\overline{\mathrm{AB}} = \overline{\mathrm{BC}} = \overline{\mathrm{CD}} = \overline{\mathrm{DA}} = \sqrt{a^2 + c^2 + d^2 - 2cd\cos\alpha} = 1 \cdot \tag{4-10}$$

Denote kinematic angles at joints $\mathrm{A_b}$ and $\mathrm{B_b}$ as θ and ϕ, respectively, and the closure equation, Eq. (1-18), must be satisfied. Then,

$$\overline{\mathrm{A_bC_b}}^2 = 2a^2(1+\cos\phi), \tag{4-11a}$$

$$\overline{\mathrm{B_bD_b}}^2 = 2a^2(1+\cos\theta), \tag{4-11b}$$

In $\Delta\mathrm{A_bB_bP}$,

$$\overline{\mathrm{A_bP}}^2 = \overline{\mathrm{A_bB_b}}^2 - \overline{\mathrm{B_bP}}^2 = \frac{1}{2}a^2(1-\cos\theta). \tag{4-12}$$

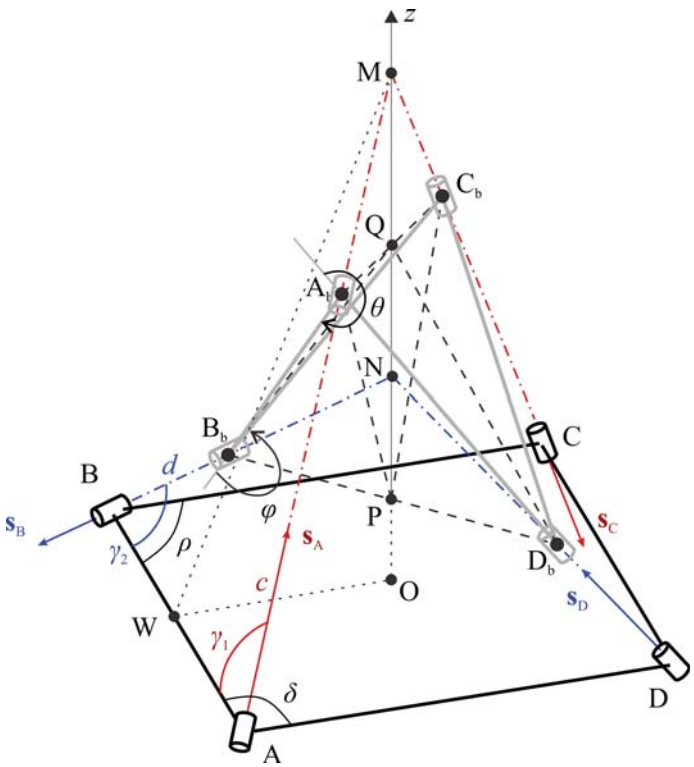

Fig. 4-4. The geometric relationship between original form of Bennett linkage, $A_bB_bC_bD_b$, and its alternative form, ABCD which is a square in the cuboctahedron.

Then,

$$\cos\angle A_bPC_b = \frac{2\overline{A_bP}^2 - \overline{A_bC_b}^2}{2\overline{A_bP}^2} = 1 - 2\frac{1+\cos\phi}{1-\cos\theta}. \tag{4-13}$$

From quadrilateral A_bMC_bP,

$$\cos\angle A_bMC_b = -\cos\angle A_bPC_b = 2\frac{1+\cos\phi}{1-\cos\theta} - 1. \tag{4-14}$$

In ΔA_bMC_b,

$$\overline{A_bC_b}^2 = 2\overline{A_bM}^2(1-\cos\angle A_bMC_b) = 4\overline{A_bM}^2\frac{-\cos\theta-\cos\phi}{1-\cos\theta}, \tag{4-15}$$

Comparing Eqs. (4-11) and (4-15),

$$\overline{A_bM}^2 = \frac{a^2(1+\cos\phi)(1-\cos\theta)}{-2(\cos\theta+\cos\phi)}. \tag{4-16}$$

Similarly,

$$\cos\angle B_bND_b = 2\frac{1+\cos\theta}{1-\cos\phi} - 1. \tag{4-17}$$

$$\overline{\mathrm{B_bN}}^2 = \frac{a^2(1+\cos\theta)(1-\cos\phi)}{-2(\cos\theta+\cos\phi)}. \tag{4-18}$$

In $\Delta\mathrm{AMC}$,

$$\overline{\mathrm{AC}}^2 = 2\overline{\mathrm{AM}}^2(1-\cos\angle\mathrm{A_bMC_b}) = 2\left(\overline{\mathrm{A_bM}}+c\right)^2\left(1-\cos\angle\mathrm{A_bMC_b}\right). \tag{4-19}$$

Similarly,

$$\overline{\mathrm{BD}}^2 = 2\overline{\mathrm{BN}}^2(1-\cos\angle\mathrm{B_bND_b}) = 2\left(-\overline{\mathrm{B_bN}}+d\right)^2\left(1-\cos\angle\mathrm{B_bND_b}\right). \tag{4-20}$$

In the deployed configuration, O is the centre of square ABCD, W is the midpoint of AB, then

$$\overline{\mathrm{MW}} = \overline{\mathrm{AM}}\sin\gamma_1, \tag{4-21a}$$

$$\overline{\mathrm{OW}} = \overline{\mathrm{AW}} = \overline{\mathrm{AM}}\cos\gamma_1, \tag{4-21b}$$

$$\overline{\mathrm{OM}} = \overline{\mathrm{AM}}\cos\frac{1}{2}\angle\mathrm{A_bMC_b}, \tag{4-21c}$$

In $\Delta\mathrm{OMW}$,

$$\overline{\mathrm{OW}}^2 + \overline{\mathrm{OM}}^2 = \overline{\mathrm{AM}}^2\cos^2\gamma_1 + \overline{\mathrm{AM}}^2\cos^2\frac{1}{2}\angle\mathrm{A_bMC_b} = \overline{\mathrm{MW}}^2 = \overline{\mathrm{AM}}^2\sin^2\gamma_1, \tag{4-22}$$

then considering Eq. (4-14),

$$\cos 2\gamma_1 = \frac{\cos\phi_d + 1}{\cos\theta_d - 1}, \tag{4-23}$$

similarly,

$$\cos 2\gamma_2 = \frac{\cos\theta_d + 1}{\cos\phi_d - 1}. \tag{4-24}$$

Combining Eqs. (4-10), (4-23, 4-24),

$$\alpha = \arccos\left(\sqrt{\cos 2\gamma_1 \cos 2\gamma_2}\right) = \arccos\left(0.4\right). \tag{4-25}$$

With trigonometric transformations, Eqs. (4-23) and (4-24) become

$$\cos 2\gamma_1 = \frac{1+\tan^2\frac{\theta_\mathrm{d}}{2}}{-\tan^2\frac{\theta_\mathrm{d}}{2}\left(1+\tan^2\frac{\phi_\mathrm{d}}{2}\right)}, \tag{4-26}$$

$$\cos 2\gamma_2 = \frac{1+\tan^2\frac{\phi_\mathrm{d}}{2}}{-\tan^2\frac{\phi_\mathrm{d}}{2}\left(1+\tan^2\frac{\theta_\mathrm{d}}{2}\right)}, \tag{4-27}$$

and considering Eq. (1-18)

$$\tan\frac{\theta_{\mathrm{d}}}{2} = -\frac{\sqrt{-\cos^2\alpha - \cos 2\gamma_1}}{\sqrt{2}\cos\gamma_1\cos\alpha} = -2\sqrt{5}\,,$$

$$\tan\frac{\phi_{\mathrm{d}}}{2} = \frac{\sqrt{2}\cos\gamma_1}{\sqrt{-\cos^2\alpha - \cos 2\gamma_1}} = -\frac{\sqrt{5}}{4}\,, \tag{4-28}$$

then

$$\theta_{\mathrm{d}} = 2\arctan(-2\sqrt{5}) = -154.79^\circ \quad \text{and} \quad \varphi_{\mathrm{d}} = 2\arctan(-\frac{\sqrt{5}}{4}) = -58.41^\circ\,. \tag{4-29}$$

Denoting

$$t_3 = \sqrt{\frac{(1+\cos\varphi_d)(1-\cos\theta_d)}{-2(\cos\theta_d + \cos\varphi_d)}} \quad \text{and} \quad t_4 = \sqrt{\frac{(1+\cos\theta_d)(1-\cos\varphi_d)}{-2(\cos\theta_d + \cos\varphi_d)}}\,, \tag{4-30}$$

and as $\overline{\mathrm{AC}}^2 = 2$ and $\overline{\mathrm{BD}}^2 = 2$ at the deployed configuration, Eq. (4-30) is substituted into Eqs. (4-19) and (4-20),

$$c = \frac{1}{2\cos\gamma_1} - t_3 a\,, \tag{4-31a}$$

$$d = \frac{1}{2\cos\gamma_2} + t_4 a\,, \tag{4-31b}$$

then consider Eq. (4-10)

$$a = \frac{-TermB + \sqrt{TermB^2 - 4TermATermC}}{2TermA} = 0.46\,, \tag{4-32}$$

where

$$TermA = 1 + t_3{}^2 + t_4{}^2 + 2t_3t_4\cos\alpha\,, \tag{4-33a}$$

$$TermB = -\frac{t_3}{\cos\gamma_1} + \frac{t_4}{\cos\gamma_2} + \frac{t_3}{\cos\gamma_2}\cos\alpha - \frac{t_4}{\cos\gamma_1}\cos\alpha\,, \tag{4-33b}$$

$$TermC = \frac{1}{4\cos^2\gamma_1} + \frac{1}{4\cos^2\gamma_2} - \frac{\cos\alpha}{2\cos\gamma_1\cos\gamma_2} - 1\,. \tag{4-33c}$$

Therefore c and d can be determined from Eq. (4-31)

$$c = 0.68 \quad \text{and} \quad d = 0.90\,. \tag{4-34}$$

As the meet of B and D, quadrilateral ABCD becomes two perpendicular lines in the folded configuration as shown in Fig. 4-5 with a half part of the octahedron. Revolute axes on A and C, $\boldsymbol{s}_{\mathrm{A}}$ and $\boldsymbol{s}_{\mathrm{C}}$, must be in plane ABC, while revolute axes on B and D, $\boldsymbol{s}_{\mathrm{B}}$ and $\boldsymbol{s}_{\mathrm{D}}$, must be in plane EDG due to the symmetric property of Bennett linkage. Meanwhile, these two planes are perpendicular to each other

according the property of octahedron. Then,

$$\cos\gamma_2 = \frac{\frac{1}{2}\overline{\mathrm{AG}}}{\overline{\mathrm{AM}}} = \frac{1}{2\overline{\mathrm{AM}}} \tag{4-35}$$

$$\sin\frac{1}{2}\angle \mathrm{A_b M C_b} = \frac{\frac{1}{2}\overline{\mathrm{AC}}}{\overline{\mathrm{AM}}} = \frac{\sqrt{2}}{2\overline{\mathrm{AM}}} \tag{4-36}$$

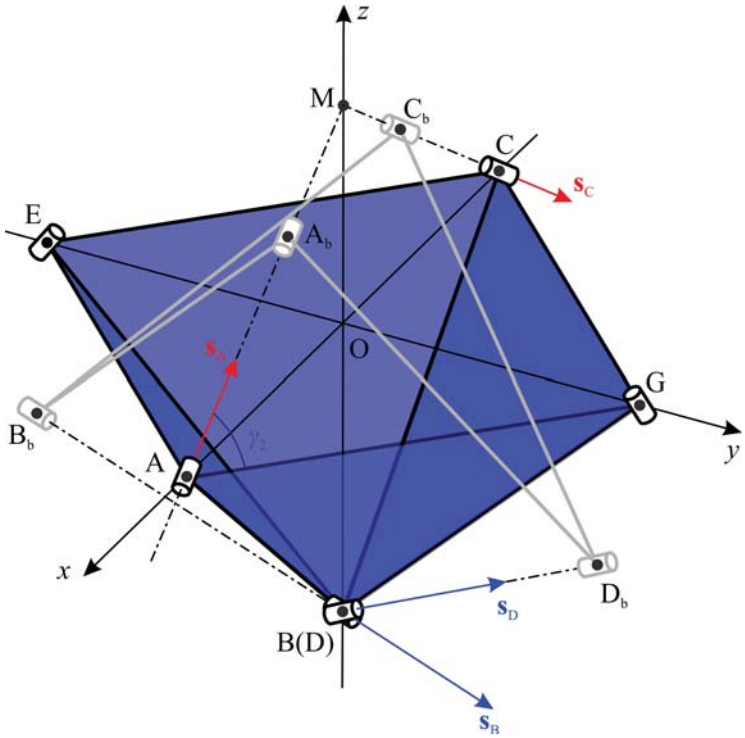

Fig. 4-5. Half of the octahedron for illustrating kinematic variables at the folded configuration.

Thus, the relationship between axis angle, γ_2, and $\angle \mathrm{A_b M C_b}$ are

$$\cos\gamma_2 = \frac{\sqrt{2}}{2}\sin\frac{1}{2}\angle \mathrm{A_b M C_b}\,. \tag{4-37}$$

According to Eq. (4-14),

$$\cos\gamma_2 = \frac{\sqrt{2}}{2}\sqrt{\frac{-\cos\phi_\mathrm{f} - \cos\theta_\mathrm{f}}{1-\cos\phi_\mathrm{f}}}\,, \tag{4-38}$$

namely,

$$\cos\gamma_2 = \frac{\sqrt{2}}{2}\sqrt{-\frac{\dfrac{1-\tan^2\dfrac{\theta_\mathrm{f}}{2}}{1+\tan^2\dfrac{\theta_\mathrm{f}}{2}}+\dfrac{1-\tan^2\dfrac{\phi_\mathrm{f}}{2}}{1+\tan^2\dfrac{\phi_\mathrm{f}}{2}}}{1-\dfrac{1-\tan^2\dfrac{\theta_\mathrm{f}}{2}}{1+\tan^2\dfrac{\theta_\mathrm{f}}{2}}}}\,. \tag{4-39}$$

Considering Eq. (1-18),

$$\cos\gamma_2 = \frac{\sqrt{2}}{2}\sqrt{\frac{1+\cos^2\alpha\tan^2\dfrac{\theta_\mathrm{f}}{2}}{1+\tan^2\dfrac{\theta_\mathrm{f}}{2}}}\,. \tag{4-40}$$

Then, considering Eq. (4-7), kinematic angle at folded configuration can be solved,

$$\tan\frac{\theta_\mathrm{f}}{2} = -2\sqrt{5}\,. \tag{4-41}$$

Compared with Eq. (4-29)

$$\theta_\mathrm{f} = -58.41^\circ = \phi_\mathrm{d}\,, \tag{4-42a}$$

$$\phi_\mathrm{f} = -154.79^\circ = \theta_\mathrm{d}\,. \tag{4-42b}$$

Hereto, kinematical analysis can be done with the relationship between variables of the mechanism and geometric parameters.

Here, we start to evaluate the performance of the obtained polyhedral linkage. Considering the symmetric property, there are three sets of quadrilateral linkages in the polyhedral linkage, ABCD and IJKL, AEIH and CGKF, DHLG and BFJE. Its motion path is generated with the numerical method after the truss analogy of the obtained linkage, illustrated in Section 2.4. Two diagonal lengths in each set of these linkages are depicted in Fig. 4-6(a) as the increase of the input angle θ. The result shows that at the folded configuration pairs of vertices B and D, A and I, E and F meet, respectively, and distances of A and C, E and H, B and J become $\sqrt{2}$. All of these are properties of the octahedron. Therefore, the obtained linkage can realise the transformation from cuboctahedron to octahedron.

Meanwhile, singular values of equilibrium matrix of the truss form were recorded in Fig. 4-6(b) during the transformation process. The smallest value keeps zero all the time and other values never reach to zero, which demonstrate that the obtained linkage is always with one DOF and without any bifurcation situation. Thus, the expected linkage is obtained.

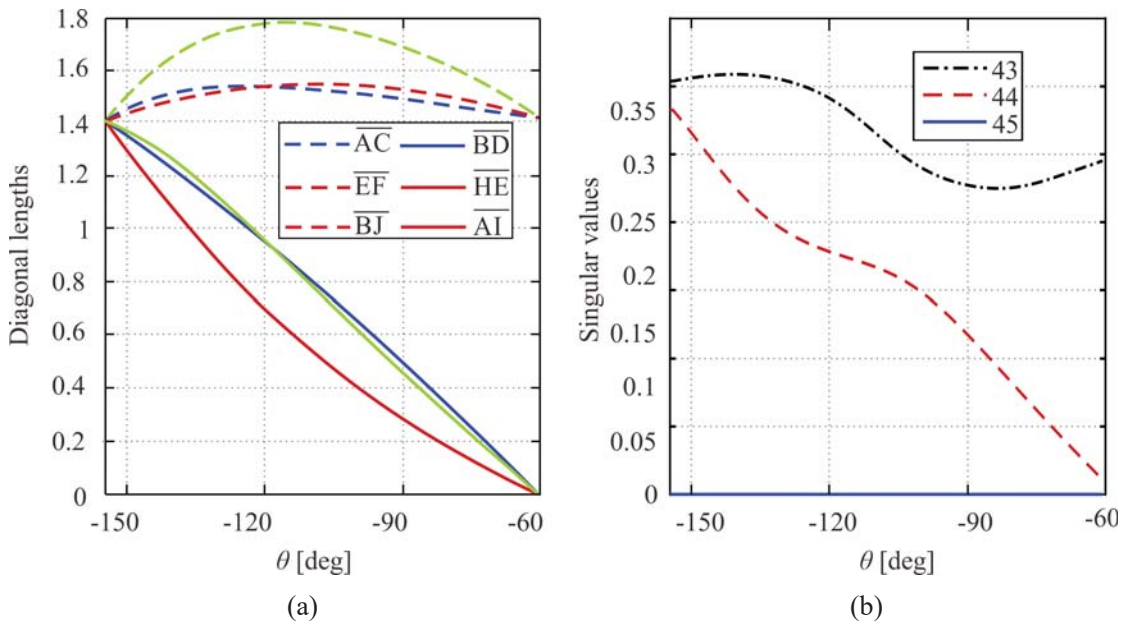

Fig. 4-6. Folding behaviours depicted by (a) diagonal lengths between B and D, A and I, E and F, as well as A and C, E and H, B and J in three quadrilaterals; and (b) bifurcation analysis with the relationship between singular values and the input angle.

The basic frame of the obtained linkage, the cuboctahedron and the octahedron, are both octahedral linkage, $\boldsymbol{O}_{\mathrm{h}}$, which is a full symmetric one. While, the linkage with the particular joint arrangement is just $\boldsymbol{C}_{2\mathrm{h}}$ composed of one rotational and one reflect symmetries. Therefore, it is interesting to study motions supplied by different kind of joints which are on symmetric positions in those polyhedrons, such as motions supplied by *S* joints on E, F, G, H and those supplied by *R* joints on other vertices.

According to Euler's rotation theorem [141], any *S* joint works as an equivalent *R* joint instantaneously whose axis is unfixed in its connected links. Here, *S* joint at vertex E is taken as an example, as shown in Fig. 4-7(a), where $\boldsymbol{s}'_{\mathrm{E}}$ represents the instantaneous revolute axis. Figure 4-7(b) depicts angles between the axis of its instantaneous rotation of the *S* joint and its connecting links, χ_{EA}, χ_{EB}, χ_{EI}, and χ_{EJ}. All these angles are not constant, therefore, it demonstrates that E can not be set with *R* joint. Similarly, other *S* joints can not be set with *R* joints too.

Meanwhile, the motion of the Bennett linkage ABCD can be described by the relationship between two folding angles ρ and δ, which are marked in Fig. 4-3(a). In Fig. 4-4,

$$\cos\rho = \frac{\overline{\mathrm{AB}}^2 + \overline{\mathrm{BC}}^2 - \overline{\mathrm{AC}}^2}{2\overline{\mathrm{AB}}\cdot\overline{\mathrm{BC}}} = 1 - \frac{1}{2}\overline{\mathrm{AC}}^2, \tag{4-43a}$$

$$\cos\delta = \frac{\overline{\mathrm{AB}}^2 + \overline{\mathrm{AD}}^2 - \overline{\mathrm{BD}}^2}{2\overline{\mathrm{AB}}\cdot\overline{\mathrm{AD}}} = 1 - \frac{1}{2}\overline{\mathrm{BD}}^2. \tag{4-43b}$$

Considering Eqs. (4-19) and (4-20), the relationship between folding angles and kinematic angles can be obtained. The nature of mirror symmetry connotes that both Bennett linkages ABCD and IJKL always take the same configuration during the transformation, whose motion paths in terms of the folding angles are shown in Fig. 4-8(a). Figure 4-8(b) depicts motion paths of the triangular face centres and their normal directions with face ABE chosen as the driven element. It indicates that the octahedral symmetry is also broken during the transformation but the three orthogonal plane symmetries are maintained, see Fig. 4-9(a). A prototype has been made with rigid metal faces and hinge joints, whose transformation sequence is shown in Fig. 4-9(b).

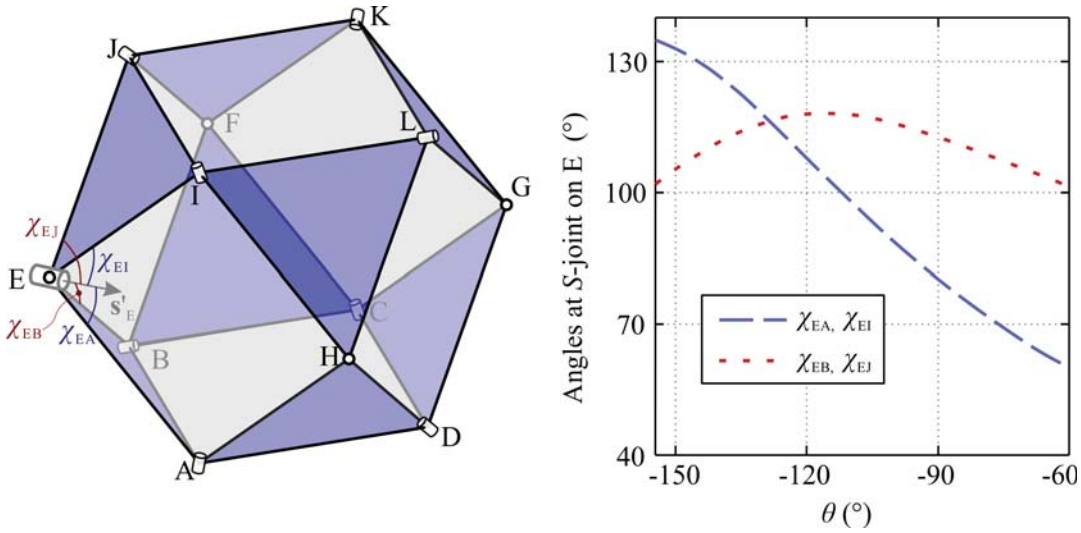

(a) (b)

Fig. 4-7. Motion of the *S* joint on E (a) equaling to the instantaneous *R* joint $\mathbf{s}'_E$, and (b) angles between the revolute axis and its connecting bars EA, EB, EI, EJ show the *S* joint can not be replaced with *R* joint.

4.4 Conclusions

In this chapter, we proposed a solution to realise the transformation between cuboctahedron and octahedron by a spatial multi-loop linkage with one DOF. Two opposite square faces are set with Bennett linkages, and other four square faces are connected with *RSRS* linkages, thus deploying processes of those six square faces are not the same, i.e., the transformation broke some symmetric properties of original polyhedrons. An analysis of the singular values of the equilibrium matrix of each polyhedron in its truss form has shown that the minimum always remains zero whereas the rest never deduce to zero, which indicates that motion can take place without any bifurcation.

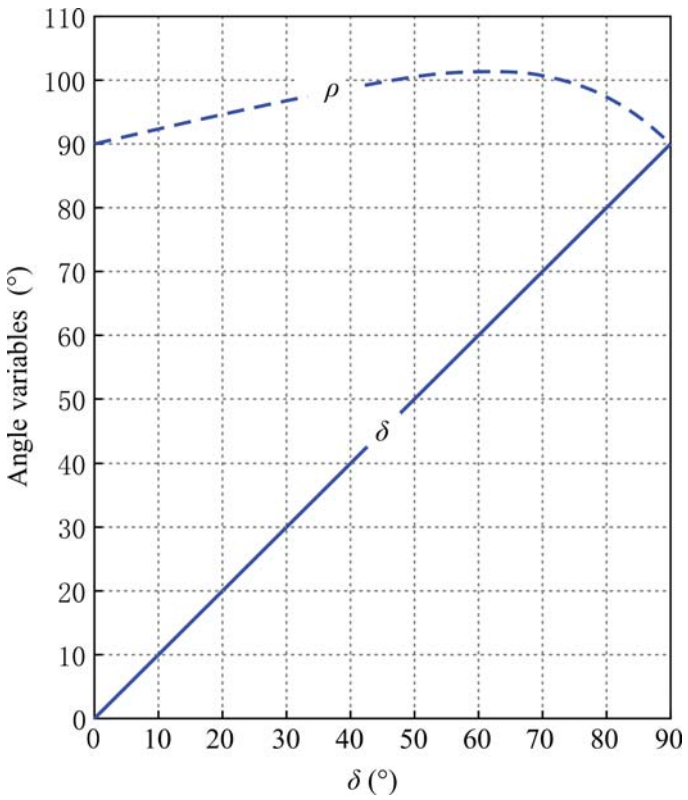

(a)

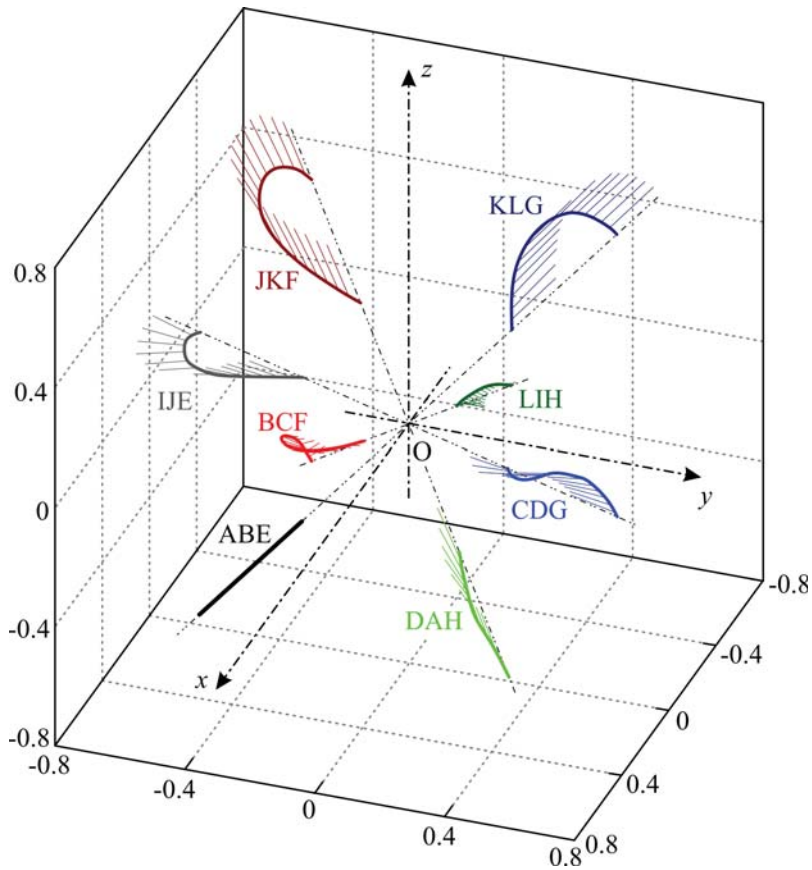

(b)

Fig. 4-8. Folding process of the linkage illustrated by (a) the relationships amongst folding angles; and (b) motion paths of the triangular face centres and their normals.

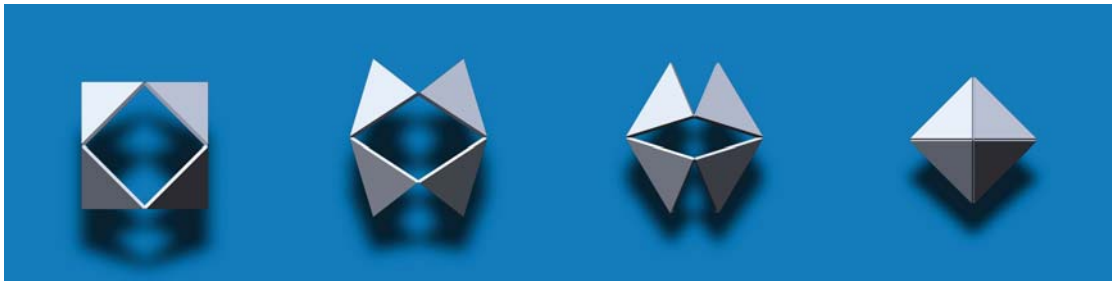

(a)

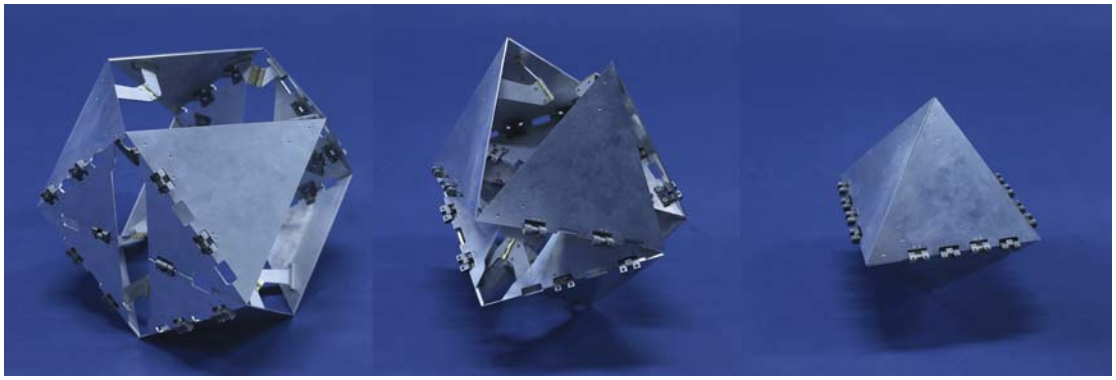

(b)

Fig. 4-9. Folding sequences of the polyhedral transformation of (a) a CAD model from symmetric view; (b) a prototype where the rigid triangular faces are made of metal sheet and the *R* joints are made of common door hinges.

Chapter 5 Transformation between Truncated Octahedron and Cube

5.1 Introduction

In truncated octahedron, each hexagonal face is surrounded with three square faces and three connecting bars, which present threefold-symmetric. Folding all these hexagonal faces, the remained six square faces will form a cube. Therefore, in this chapter, we are going to construct the transformation between these two polyhedrons with a multi-loop linkage from a threefold-symmetric Bircard linkage.

The layout of the chapter is as follows. Section 5.2 expounds the construction of the deployable polyhedron with two DOFs, and it is reduced to one in Section 5.3. Section 5.4 presents kinematics of this transformation. Parameter study to determine the feasible range of one design parameter is performed in Section 5.5. Finally, a conclusion is given in Section 5.6.

5.2 Construction of a 2-DOF System

Figures 5-1(a) and 5-1(b) show the object of this chapter, a truncated octahedron and a cube with unit-length edges. Such a vertex-motion arrangement is unique if no interference occurs during the transformation. As a result, all of the eight hexagonal hollows will vanish after the transformation. If only *S* joints are used at all of the vertices, the truncated octahedron would have 18 DOFs, thus some of these *S* joints are expected to be replaced with 1-DOF *R* joints to reduce the number of DOFs.

The transformation between truncated octahedron and cube is better illustrated by the positions of the vertices using the Cartesian coordinate system shown in Fig. 5-1(a) and 5-1(b). When each side of the polyhedrons has unit length, the positions of the vertices of the truncated octahedron are

$$\boldsymbol{A}_1^{\mathrm{to}} = (\sqrt{2}, \frac{\sqrt{2}}{2}, 0)^{\mathrm{T}}, \quad \boldsymbol{A}_2^{\mathrm{to}} = (\sqrt{2}, 0, \frac{\sqrt{2}}{2})^{\mathrm{T}}, \tag{5-1a}$$

$$\boldsymbol{A}_3^{\mathrm{to}} = (\sqrt{2}, -\frac{\sqrt{2}}{2}, 0)^{\mathrm{T}}, \quad \boldsymbol{A}_4^{\mathrm{to}} = (\sqrt{2}, 0, -\frac{\sqrt{2}}{2})^{\mathrm{T}}, \tag{5-1b}$$

$$\boldsymbol{B}_1^{\mathrm{to}} = (0, \sqrt{2}, \frac{\sqrt{2}}{2})^{\mathrm{T}}, \quad \boldsymbol{B}_2^{\mathrm{to}} = (\frac{\sqrt{2}}{2}, \sqrt{2}, 0)^{\mathrm{T}}, \tag{5-1c}$$

$$\boldsymbol{B}_3^{\mathrm{to}} = (0, \sqrt{2}, -\frac{\sqrt{2}}{2})^{\mathrm{T}}, \quad \boldsymbol{B}_4^{\mathrm{to}} = (-\frac{\sqrt{2}}{2}, \sqrt{2}, 0)^{\mathrm{T}}, \tag{5-1d}$$

$$\boldsymbol{C}_1^{\mathrm{to}} = (\frac{\sqrt{2}}{2}, 0, \sqrt{2})^{\mathrm{T}}, \quad \boldsymbol{C}_2^{\mathrm{to}} = (0, \frac{\sqrt{2}}{2}, \sqrt{2})^{\mathrm{T}}, \tag{5-1e}$$

$$\boldsymbol{C}_3^{\mathrm{to}} = (-\frac{\sqrt{2}}{2}, 0, \sqrt{2})^{\mathrm{T}}, \quad \boldsymbol{C}_4^{\mathrm{to}} = (0, -\frac{\sqrt{2}}{2}, \sqrt{2})^{\mathrm{T}}, \tag{5-1f}$$

$$\boldsymbol{D}_1^{\mathrm{to}} = (-\sqrt{2}, 0, -\frac{\sqrt{2}}{2})^{\mathrm{T}}, \quad \boldsymbol{D}_2^{\mathrm{to}} = (-\sqrt{2}, -\frac{\sqrt{2}}{2}, 0)^{\mathrm{T}}, \tag{5-1g}$$

$$\boldsymbol{D}_3^{\mathrm{to}} = (-\sqrt{2}, 0, \frac{\sqrt{2}}{2})^{\mathrm{T}}, \quad \boldsymbol{D}_4^{\mathrm{to}} = (-\sqrt{2}, \frac{\sqrt{2}}{2}, 0)^{\mathrm{T}}, \tag{5-1h}$$

$$\boldsymbol{E}_1^{\mathrm{to}} = (-\frac{\sqrt{2}}{2}, -\sqrt{2}, 0)^{\mathrm{T}}, \quad \boldsymbol{E}_2^{\mathrm{to}} = (0, -\sqrt{2}, -\frac{\sqrt{2}}{2})^{\mathrm{T}}, \tag{5-1i}$$

$$\boldsymbol{E}_3^{\mathrm{to}} = (\frac{\sqrt{2}}{2}, -\sqrt{2}, 0)^{\mathrm{T}}, \quad \boldsymbol{E}_4^{\mathrm{to}} = (0, -\sqrt{2}, \frac{\sqrt{2}}{2})^{\mathrm{T}}, \tag{5-1j}$$

$$\boldsymbol{F}_1^{\mathrm{to}} = (0, -\frac{\sqrt{2}}{2}, -\sqrt{2})^{\mathrm{T}}, \quad \boldsymbol{F}_2^{\mathrm{to}} = (-\frac{\sqrt{2}}{2}, 0, -\sqrt{2})^{\mathrm{T}}, \tag{5-1k}$$

$$\boldsymbol{F}_3^{\mathrm{to}} = (0, \frac{\sqrt{2}}{2}, -\sqrt{2})^{\mathrm{T}}, \quad \boldsymbol{F}_4^{\mathrm{to}} = (\frac{\sqrt{2}}{2}, 0, -\sqrt{2})^{\mathrm{T}}. \tag{5-1l}$$

where superscript “to” is for the truncated octahedron. For the cube, the vertices positions are

$$\boldsymbol{A}_1^{\mathrm{c}} = \boldsymbol{B}_1^{\mathrm{c}} = \boldsymbol{C}_1^{\mathrm{c}} = (\frac{1}{2}, \frac{1}{2}, \frac{1}{2})^{\mathrm{T}}, \quad \boldsymbol{B}_4^{\mathrm{c}} = \boldsymbol{C}_2^{\mathrm{c}} = \boldsymbol{D}_3^{\mathrm{c}} = (-\frac{1}{2}, \frac{1}{2}, \frac{1}{2})^{\mathrm{T}}, \tag{5-2a}$$

$$\boldsymbol{C}_3^{\mathrm{c}} = \boldsymbol{D}_2^{\mathrm{c}} = \boldsymbol{E}_4^{\mathrm{c}} = (-\frac{1}{2}, -\frac{1}{2}, \frac{1}{2})^{\mathrm{T}}, \quad \boldsymbol{A}_2^{\mathrm{c}} = \boldsymbol{C}_4^{\mathrm{c}} = \boldsymbol{E}_3^{\mathrm{c}} = (\frac{1}{2}, -\frac{1}{2}, \frac{1}{2})^{\mathrm{T}}, \tag{5-2b}$$

$$\boldsymbol{A}_4^{\mathrm{c}} = \boldsymbol{B}_2^{\mathrm{c}} = \boldsymbol{F}_3^{\mathrm{c}} = (\frac{1}{2}, \frac{1}{2}, -\frac{1}{2})^{\mathrm{T}}, \quad \boldsymbol{B}_3^{\mathrm{c}} = \boldsymbol{D}_4^{\mathrm{c}} = \boldsymbol{F}_2^{\mathrm{c}} = (-\frac{1}{2}, \frac{1}{2}, -\frac{1}{2})^{\mathrm{T}}, \tag{5-2c}$$

$$\boldsymbol{D}_1^{\mathrm{c}} = \boldsymbol{E}_1^{\mathrm{c}} = \boldsymbol{F}_1^{\mathrm{c}} = (-\frac{1}{2}, -\frac{1}{2}, -\frac{1}{2})^{\mathrm{T}}, \quad \boldsymbol{A}_3^{\mathrm{c}} = \boldsymbol{E}_2^{\mathrm{c}} = \boldsymbol{F}_4^{\mathrm{c}} = (\frac{1}{2}, -\frac{1}{2}, -\frac{1}{2})^{\mathrm{T}}, \tag{5-2d}$$

in which superscript “c” represents the cube.

First of all, let us examine a single hollow, $A_1A_2C_1C_2B_1B_2$, Fig. 5-1(a), whose initial configuration is a regular hexagon. After transformation, vertices A_1, C_1 and B_1 converge to a single vertex on the cube, whilst A_2, C_2 and B_2 end up at the adjacent vertices of the cube, Fig. 5-1(b), and so do the vertices on the neighbouring hollows.

Hence, the motion of hollow $A_1A_2C_1C_2B_1B_2$ will have threefold-symmetry. We decide to use 1-DOF *R* joint at those vertices, and to enable the motion, the hollow must be a threefold-symmetric Bricard 6*R* linkage, which is made of six links connected by six *R* joints (hence 6*R*) forming a loop [75].

The Bricard linkage is an overconstrained linkage which has mobility only under strict geometrical conditions [75]. These conditions are met by adjusting the orientation of each 1-DOF *R* joint.

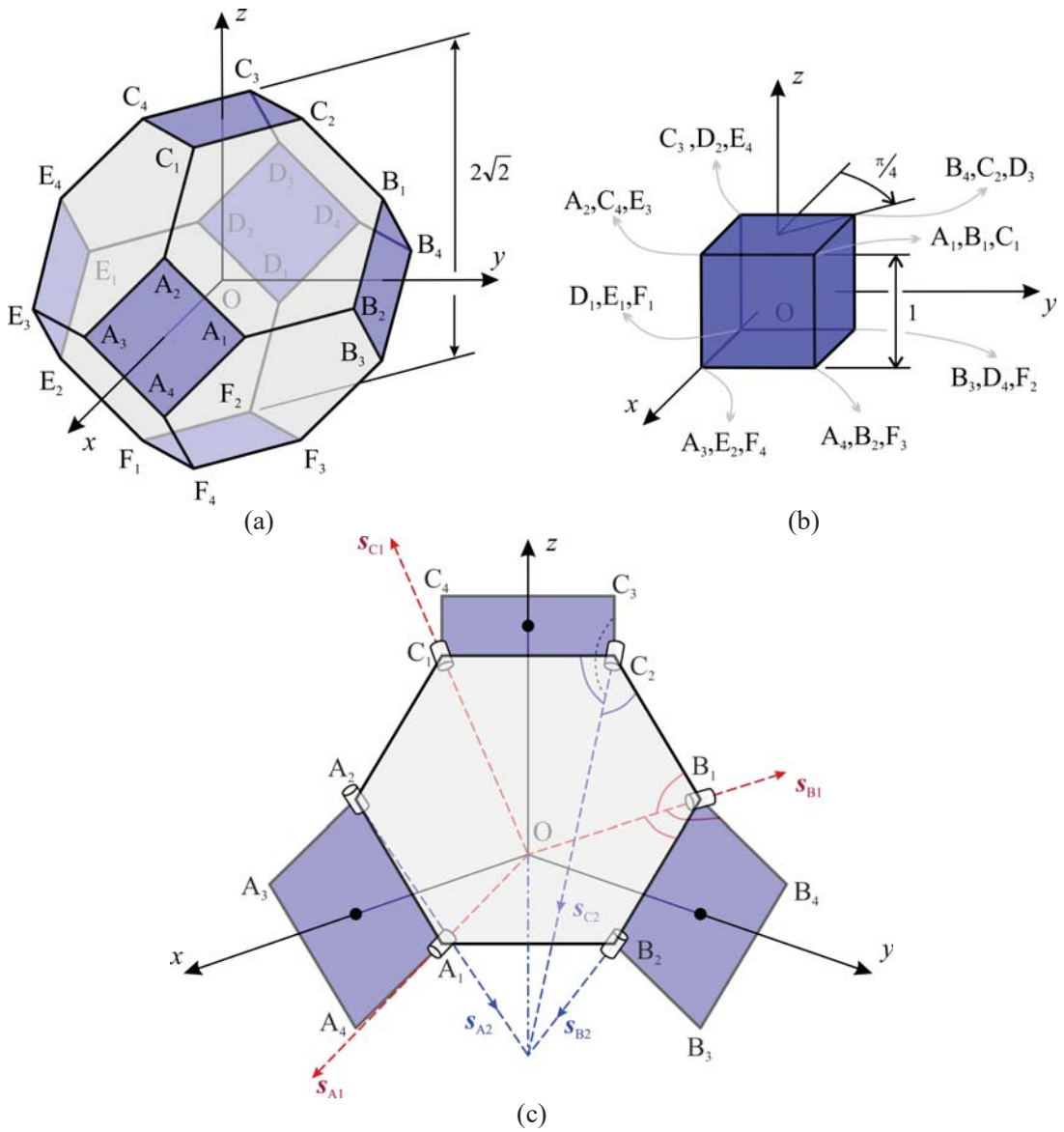

Fig. 5-1. Joint replacement and joint positions in the truncated octahedron and cube. (a) The truncated octahedron and the Cartesian coordinate system; (b) positions of the vertices when the truncated octahedron shrinks to a cube; (c) a threefold-symmetric Bricard 6*R* linkage is introduced to realise the transformation of three squares A, B, C.

The rotational axes of the *R* joints of the threefold-symmetric Bricard linkage $A_1A_2C_1C_2B_1B_2$ can be determined based on the initial and final configurations on the paired polyhedrons, which is illustrated in Fig. 5-1(c). After transforming into cube, sides B_1C_2 and B_1B_4 must be collinear, which demands the *R* joint axis at B_1 be on the plane bisecting angle $\angle C_2B_1B_4$. Meanwhile, because of the threefold-symmetry of the linkage, the same axis must be on the plane containing B_1, O and A_2. Thus, the direction of the *R* joint axis at B_1 is

$$\boldsymbol{s}_{\mathrm{B1}} = \boldsymbol{OB}_1^{\mathrm{to}} = (\frac{\sqrt{2}}{2}, \sqrt{2}, 0)^{\mathrm{T}} . \tag{5-3}$$

Then, axis angles on B_1 which are angles between the revolute axis $\boldsymbol{s}_{B1}$ and its connected edges B_1B_2, B_1B_4, B_1C_2 can be calculated. These angles are the same as the axis directs to the body centre.

$$\gamma = \arccos(\frac{\boldsymbol{s}_{B1} \cdot \boldsymbol{C}_2^{to} \boldsymbol{B}_1^{to}}{|\boldsymbol{s}_{B1}|}) = \arccos(\frac{\sqrt{10}}{10}) = 71.57° . \tag{5-4}$$

Similarly, the revolute axes at A_1 and C_1 can be set as

$$\boldsymbol{s}_{A1} = (\sqrt{2}, \frac{\sqrt{2}}{2}, 0)^T , \tag{5-5}$$

$$\boldsymbol{s}_{C1} = (\frac{\sqrt{2}}{2}, 0, \sqrt{2})^T . \tag{5-6}$$

These axes all point towards the centres of both polyhedrons.

Figure 5-2 shows squares B and C of the truncated octahedron and their final positions with dashed edges when bar B_1C_2 is fixed in the coordinate system, where superscript f represents final positions. As square B rotates around the *R* joint on B_1, vertex B_4 goes to C_2, $\boldsymbol{B}_4^f = \boldsymbol{C}_2^{to}$. Similarly, $\boldsymbol{B}_1^f = \boldsymbol{B}_1^{to}$. Then the transformation matrix is obtained,

$$\boldsymbol{T} = \begin{bmatrix} -\frac{2}{3} & -\frac{1}{3} & \frac{2}{3} \\ \frac{1}{3} & \frac{2}{3} & \frac{2}{3} \\ -\frac{2}{3} & \frac{2}{3} & -\frac{1}{3} \end{bmatrix} . \tag{5-7}$$

Thus, final positions of B_2 and B_3 are

$$\boldsymbol{B}_2^f = \boldsymbol{T}\boldsymbol{B}_2^{to} = (-\frac{2\sqrt{2}}{3}, \frac{5\sqrt{2}}{6}, \frac{\sqrt{2}}{3})^T , \tag{5-8}$$

$$\boldsymbol{B}_3^f = \boldsymbol{T}\boldsymbol{B}_3^{to} = (-\frac{2\sqrt{2}}{3}, \frac{\sqrt{2}}{3}, \frac{5\sqrt{2}}{6})^T . \tag{5-9}$$

As squares B and C in the final position form two perpendicular faces of the cube,

$$\boldsymbol{C}_1^f \boldsymbol{C}_4^f \perp \boldsymbol{C}_1^f \boldsymbol{C}_2^f , \ \boldsymbol{C}_1^f \boldsymbol{C}_4^f \perp \boldsymbol{B}_1^f \boldsymbol{B}_2^f , \tag{5-10}$$

where $\boldsymbol{C}_1^f = \boldsymbol{B}_1^{to}$, $\boldsymbol{C}_2^f = \boldsymbol{C}_2^{to}$, then,

$$\boldsymbol{B}_1^{to} \boldsymbol{C}_4^f = \boldsymbol{B}_1^{to} \boldsymbol{C}_2^{to} \times \boldsymbol{B}_1^{to} \boldsymbol{B}_2^f , \tag{5-11}$$

thus

$$\boldsymbol{C}_4^f = (\frac{1}{3}, \frac{\sqrt{2}}{2} - \frac{2}{3}, \sqrt{2} - \frac{2}{3})^T . \tag{5-12}$$

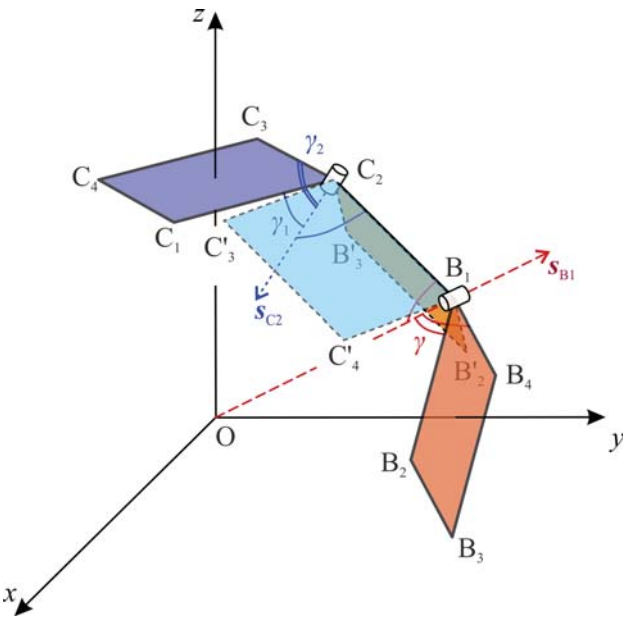

Fig. 5-2. Directions of the rotational axes of the *R* joints at B_1 and C_2.

So, the direction of the axis on C_2 is

$$\boldsymbol{s}_{C2} = \boldsymbol{C}_1^{to}\boldsymbol{B}_1^{to} \times \boldsymbol{C}_4^{to}\boldsymbol{C}_1^{f} = (\frac{1-2\sqrt{2}}{2}, -\frac{\sqrt{2}+1}{2}, -\frac{3}{2})^{T}. \tag{5-13}$$

Axis angles on C_2 between the revolute axis and its connected edges C_2B_1, C_2C_1 and C_2C_3, in which the first two angles are equal due to the meet of C_1 and B_1 after folding, are

$$\gamma_1 = \arccos(\frac{\boldsymbol{C}_2^{to}\boldsymbol{C}_1^{to} \cdot \boldsymbol{s}_{C2}}{|\boldsymbol{s}_{C2}|}) = 84.42°, \tag{5-14}$$

and

$$\gamma_2 = \arccos(\frac{\boldsymbol{C}_2^{to}\boldsymbol{C}_3^{to} \cdot \boldsymbol{s}_{C2}}{|\boldsymbol{s}_{C2}|}) = 45.27°, \tag{5-15}$$

respectively, as shown in Fig. 5-2. Other axes can be determined by symmetric rotations.

$$\boldsymbol{s}_{A2} = (-\frac{3}{2}, -\frac{\sqrt{2}+1}{2}, \frac{1-2\sqrt{2}}{2})^{T}, \tag{5-16}$$

$$\boldsymbol{s}_{B2} = (\frac{1-2\sqrt{2}}{2}, -\frac{3}{2}, -\frac{\sqrt{2}+1}{2})^{T}. \tag{5-17}$$

As hexagon $D_1D_2E_1E_2F_1F_2$ is not connected with $A_1A_2C_1C_2B_1B_2$ directly, and structures of these two hexagons are the same, then hexagonal linkage $D_1D_2E_1E_2F_1F_2$ is set with the same Bricard linkage, then axes of its joints are

$$\boldsymbol{s}_{D1} = (-\sqrt{2}, 0, -\frac{\sqrt{2}}{2})^{T}, \quad \boldsymbol{s}_{E1} = (-\frac{\sqrt{2}}{2}, -\sqrt{2}, 0)^{T}, \tag{5-18}$$

$$\boldsymbol{s}_{\mathrm{F1}} = (0, -\frac{\sqrt{2}}{2}, -\sqrt{2})^{\mathrm{T}}, \quad \boldsymbol{s}_{\mathrm{D2}} = (\frac{3}{2}, -\frac{1-2\sqrt{2}}{2}, \frac{\sqrt{2}+1}{2})^{\mathrm{T}}, \tag{5-19}$$

$$\boldsymbol{s}_{\mathrm{E2}} = (\frac{\sqrt{2}+1}{2}, \frac{3}{2}, -\frac{1-2\sqrt{2}}{2})^{\mathrm{T}}, \quad \boldsymbol{s}_{\mathrm{F2}} = (-\frac{1-2\sqrt{2}}{2}, \frac{\sqrt{2}+1}{2}, \frac{3}{2})^{\mathrm{T}}, \tag{5-20}$$

So far, the polyhedral linkage is constructed with two of the same threefold-symmetric Bricard linkages, as shown in Fig. 5-3. A total of 12 vertices are converted to 1-DOF *R* joints.

Adopting the truss analogy, the *R* joint on A_1 in Fig. 5-4(a) equals to *S* joints A_1 and a_1 on $\boldsymbol{s}_{\mathrm{A1}}$ and transforming each rigid part to a line, triangle or tetrahedron, such as bar B_1C_2 equals to tetrahedron $B_1b_1C_2c_2$. According to this idea, a threefold-symmetric Bricard linkage [75] formed by three rigid squares and three rigid bars, in Fig. 5-4(a), could be transformed to its truss form, in Fig. 5-4(b).

If the truncated octahedron is treated as a truss with the truss analogy [140], the total number of DOF, *m*, is 2 according to the Maxwell's rule as the Kutzbach criterion cannot give the correct DOF for the overconstrained linkage [2].

The polyhedron will have threefold-symmetry during the transformation, instead of octahedral symmetry, due to the introduction of the Bricard linkages. In addition, the mirror symmetry can be retained, then both Bricard linkages can be driven simultaneously, Fig. 5-5(a).

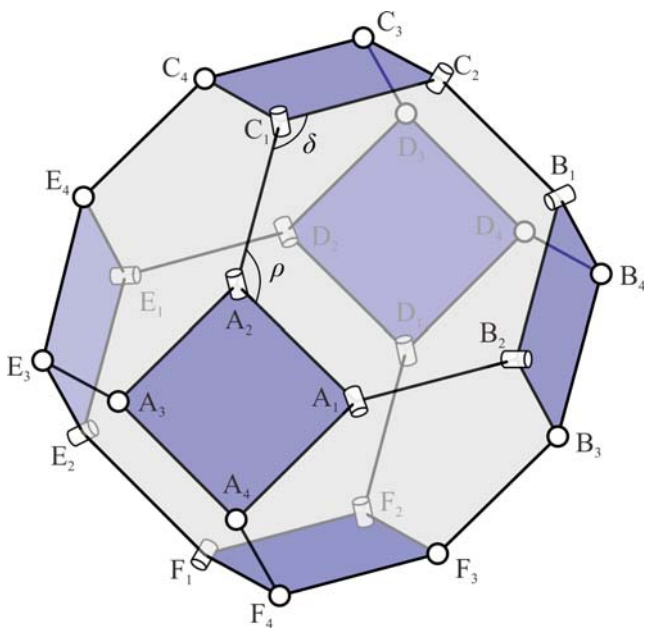

Fig. 5-3. A 2-DOF system obtained after introducing two threefold-symmetric Bricard 6*R* linkages $A_1A_2C_1C_2B_1B_2$ and $D_1D_2E_1E_2F_1F_2$.

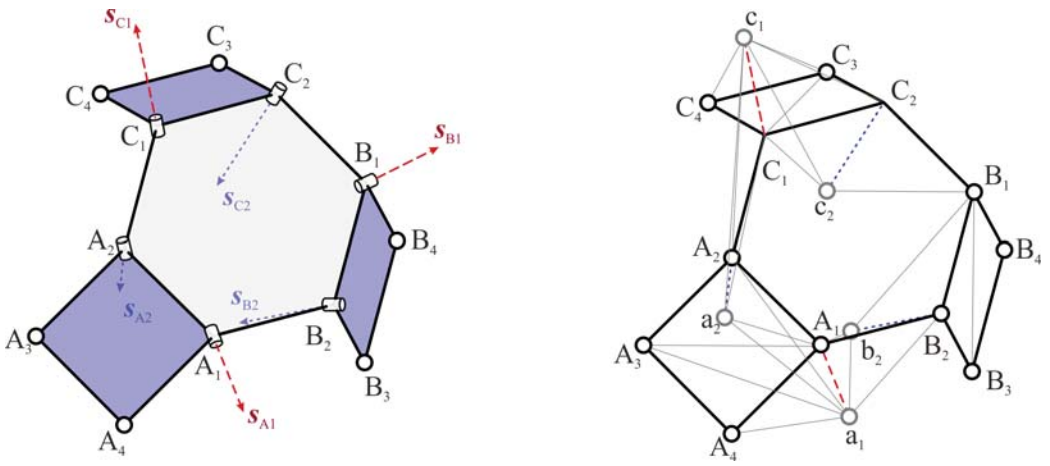

(a) (b)

Fig. 5-4. Truss method illustrated by (a) a threefold-symmetric Bricard linkage equaling to (b) its truss form kinematically, where points on each revolute axis differing to original vertices.

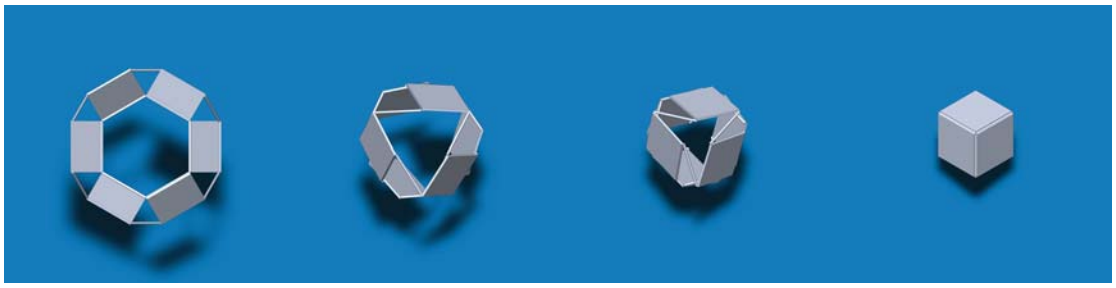

(a)

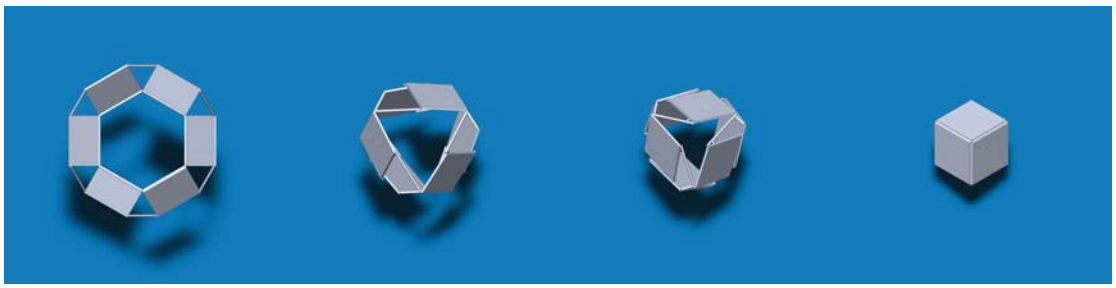

(b)

Fig. 5-5. Deployment sequences of a computer model showing the polyhedral transformation with (a) 2 DOFs and (b) 1 DOF.

5.3 One-DOF Transformable Polyhedron between Truncated Octahedron and Cube

To reduce the overall number of the DOF further, one more *S* joint at a vertex needs to be changed to a joint of other form. We choose to replace one *S* joint with one *R* joint. However, doing so generally cuts the mobility of mechanism to zero because an *R* joint has only one DOF. Since we have already used the overconstrained Bricard linkages, we speculate that the mobility could be retained by placing the *R* joint along a particular direction.

We pick vertex A_3, marked in red in Fig. 5-6(a), as the location for the *R* joint replacement. Since vertex E_3 will move towards A_2 during transformation, the rotational axis of the *R* joint at A_3 must be in the plane bisecting angle $\angle A_2A_3E_3$. Now the assembly has 13 *R* joints and 11 *S* joints. Using the truss analogy, it has 130 bars and 43 joints. The rank of the equilibrium matrix is 122, which gives a total DOF $m = 1$ according to Eq. (2-7).

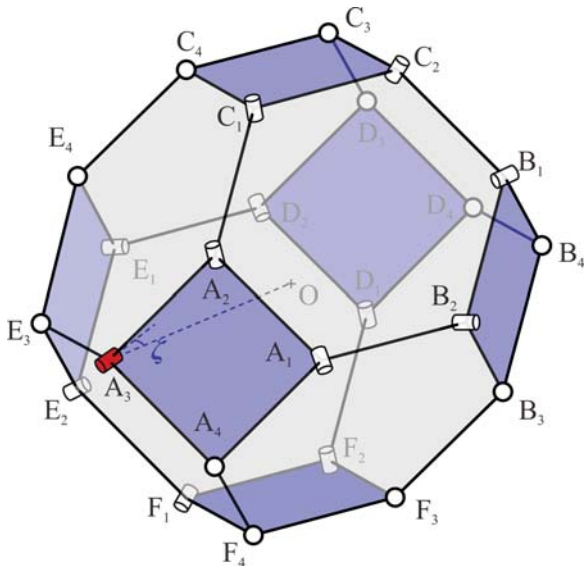

(a)

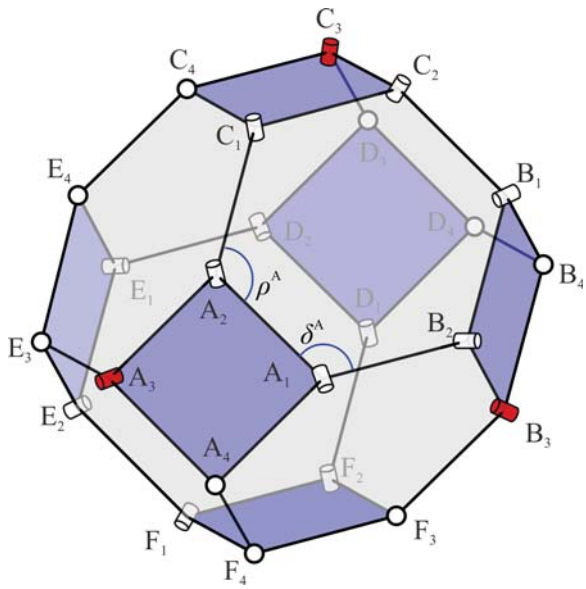

(b)

Fig. 5-6. One-DOF polyhedral transformation. (a) *S* joint at vertex A_3 is replaced with an *R* joint (shown in red) to obtain a 1-DOF system; (b) the same replacement takes place at vertices B_3 and C_3 whilst the system remains one DOF.

Note that making the rotational axis of the *R* joint at A_3 in the plane bisecting angle $\angle A_2A_3E_3$ does not completely define the direction of the axis. Angle ζ, which is the deviation angle of the rotational axis from the line linking A_3 to the centre of the polyhedron as shown in Fig. 5-6(a), is used to determine the precise direction of the rotation axis of the *R* joint. The angle's positive direction is defined by the right-hand rule with the thumb pointing along a line parallel to E_3A_2, which is actually the normal of the plane bisecting angle $\angle A_2A_3E_3$. It can be shown that ζ can take any value without changing the overall *m*. For convenience, we choose $\zeta = 0$, i.e., the *R* joint axis at A_3 pointing towards the body centre of the polyhedron.

Considering symmetric nature of the polyhedron, both *S* joints at B_3 and C_3 can also be replaced with *R* joints as well without altering the value of *m*, Fig. 5-6(b). The computer simulation on the deployment of the resulted assembly, given in Fig. 5-3(b), reveals that the transformation has only 1 DOF.

Similarly, the *S* joints at D_3, E_3 and F_3 can also be replaced with *R* joints to get a 1-DOF system, but it should be noted that the replacement can only take place at either vertices A_3, B_3 and C_3, or D_3, E_3 and F_3, not concurrently. This can be proven in two ways. The first is to calculate *m*, which turns out to be 0 if a total of six *R* joints are placed. Second, we can also use the relationships amongst the angle variables of the polyhedron to illustrate why only three *R* joints can be used, which is explained in detail next.

5.4 Kinematics of the Transformable Polyhedron

Now, we start to investigate the kinematics of the obtained linkage to observe its folding performance.

5.4.1 Relationship between Geometric Parameters and Kinematic Variables

In the kinematic analysis, the geometry of a Bricard 6*R* linkage is commonly described by its link lengths and twist angles [142]. The link lengths defined as the shortest distances between the axes of two adjacent *R* joints. Its motion is described by the kinematic variables θ and ϕ.

Consider the threefold-symmetric Bricard 6*R* linkage shown in Fig. 5-7(a), which loops three rigid faces together. These link lengths and kinematic variables are displayed in Fig. 5-7(b). The positions of the points giving the link lengths are denoted by A_{b1}, B_{b1}, ..., etc.. OP is the symmetric axis of the linkage. At each point, a coordinate system (denoted by x_1 and z_1, x_2 and z_2, ..., etc., respectively) is established based on the D-H notation [8]. The link lengths are

$$\overline{C_1^bC_2^b} = \overline{C_2^bB_1^b} = \overline{B_1^bB_2^b} = \overline{B_2^bA_1^b} = \overline{A_1^bA_2^b} = \overline{A_2^bC_1^b} = a, \tag{5-21}$$

and the other distances are

$$\overline{A_1^bA_1} = \overline{B_1^bB_1} = \overline{C_1^bC_1} = c\,, \tag{5-22}$$

$$\overline{A_2^bA_2} = \overline{B_2^bB_2} = \overline{C_2^bC_2} = d\,, \tag{5-23}$$

because of threefold-symmetry.

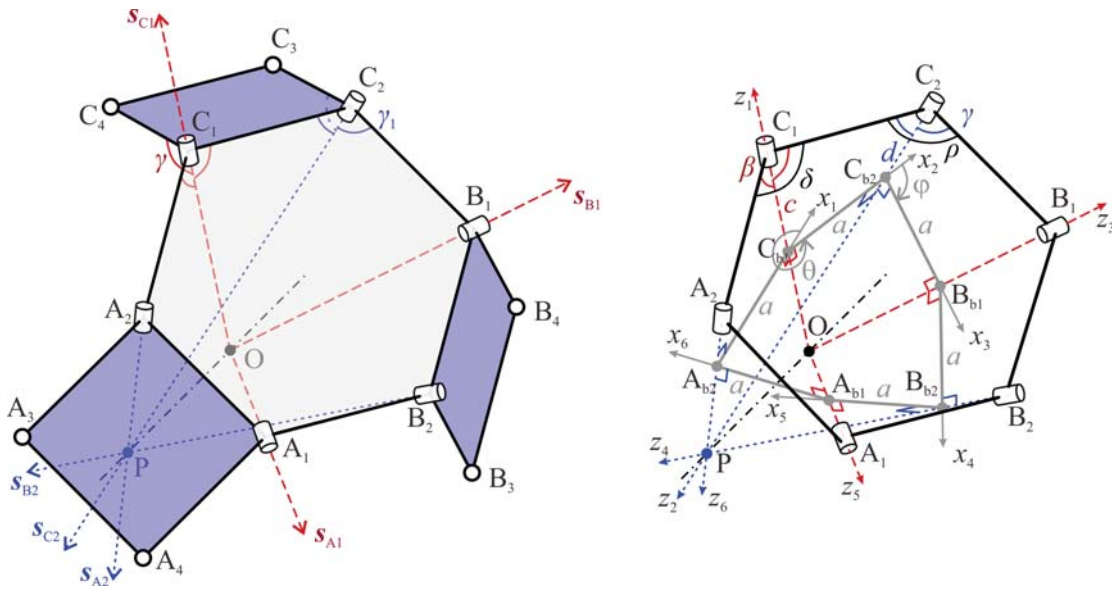

(a) (b)

Fig. 5-7. Kinematics of a threefold-symmetric Bricard linkage. (a) The hexagonal hollow $A_1A_2C_1C_2B_1B_2$; (b) the kinematic model of the linkage illustrated with thick gray lines.

On the other hand, denote by α and $360° - \alpha$ the twist angles between z_6 and z_1 (also between z_2 and z_3, z_4 and z_5) and between z_1 and z_2 (also between z_3 and z_4, z_5 and z_6), respectively. For the revolute axes given in Eqs. (5-5), (5-17),

$$\alpha = 2\pi - \arccos\left(\frac{\boldsymbol{s}_{B2}\cdot\boldsymbol{s}_{A1}}{|\boldsymbol{s}_{B2}||\boldsymbol{s}_{A1}|}\right) = 2\pi - \arccos\left(-\frac{5\sqrt{5}+2\sqrt{10}}{5\sqrt{21-2\sqrt{2}}}\right) = 214.79°\,. \tag{5-24}$$

Similar to the calculation in the alternative form of Bennett linkage,

$$a = \sqrt{1 - c^2 - d^2 - 2cd\cos\alpha}\,\cdot \tag{5-25}$$

In triangle $C_1^bC_2^bC_2$,

$$a^2 + d^2 = c^2 + 1 - 2c\cos\gamma\,, \tag{5-26}$$

and in triangle $C_1^bC_2^bC_1$,

$$a^2 + c^2 = d^2 + 1 - 2d\cos\gamma_1\,. \tag{5-27}$$

Eqs. (5-26), (5-27) are simplified as

$$c = d\cos\alpha + \cos\gamma\,, \tag{5-28}$$

$$d = c\cos\alpha + \cos\gamma_1\,. \tag{5-29}$$

Then, offsets can be calculated,

$$c = \frac{\cos\gamma - \cos\alpha\cos\gamma_1}{\sin^2\alpha} = 1.22\,, \tag{5-30}$$

$$d = \frac{\cos\gamma_1 - \cos\alpha\cos\gamma}{\sin^2\alpha} = 1.10\,. \tag{5-31}$$

Substitute Eqs. (5-30) and (5-31) into Eq. (5-24),

$$a = \sqrt{\frac{\sin^2\alpha - \cos^2\gamma - \cos^2\gamma_1 + 2\cos\alpha\cos\gamma\cos\gamma_1}{\sin^2\alpha}} = 0.71\,. \tag{5-32}$$

In coordinate system 2,

$$\boldsymbol{C}_{2\mathrm{b}} = (0, 0, 0)^{\mathrm{T}}\,,\ \ \boldsymbol{C}_2 = (0, 0, -d)^{\mathrm{T}}\,, \tag{5-33}$$

$$\boldsymbol{B}_{1\mathrm{b}} = (a\cos\phi, a\sin\phi, 0)^{\mathrm{T}}\,, \tag{5-34}$$

$$\boldsymbol{B}_1 = (a\cos\phi - c\sin\alpha\sin\phi, a\sin\phi + c\sin\alpha\cos\phi, c\cos\alpha)^{\mathrm{T}}\,, \tag{5-35}$$

$$\boldsymbol{C}_{1\mathrm{b}} = (-a, 0, 0)^{\mathrm{T}}\,, \tag{5-36}$$

$$\boldsymbol{C}_1 = (-a, c\sin\alpha, c\cos\alpha)^{\mathrm{T}}\,. \tag{5-37}$$

Then,

$$\boldsymbol{B}_1\boldsymbol{C}_1 = (-a\cos\phi + c\sin\alpha\sin\phi - a, c\sin\alpha - a\sin\phi - c\sin\alpha\cos\phi, 0)^{\mathrm{T}}\,, \tag{5-38}$$

and its norm can be calculated in triangle $B_1C_1C_2$,

$$\overline{\mathrm{B_1C_1}} = 2\sin\left(\delta_2/2\right). \tag{5-39}$$

Combine Eqs. (5-38) and (5-39), the relationship between joint kinematic angle ϕ and folding angle δ_2 is

$$\cos\delta_2 = 1 - [a^2(1+\cos\phi) + c^2\sin^2\alpha(1-\cos\phi) - 2ac\sin\alpha\sin\phi]\,. \tag{5-40}$$

Similarly, the relationship between joint kinematic angle θ and folding angle δ_1 is

$$\cos\delta_1 = 1 - [a^2(1+\cos\theta) + d^2\sin^2\alpha(1-\cos\theta) - 2ad\sin\alpha\sin\theta]\,. \tag{5-41}$$

Then, relationships between folding angles and joint kinematic angles are depicted in Fig. 5-8. Since the closure equation for the of the Bricard 6*R* linkage is given by

$$\cos^2\alpha + \sin^2\alpha(\cos\theta + \cos\phi) + (1+\cos^2\alpha)\cos\theta\cos\phi - 2\cos\alpha\sin\theta\sin\phi = 0 \tag{5-42}$$

in terms of the kinematic variables of the linkage. Using Eqs. (5-40) and (5-41), Eq. (5-42) can be converted to a relationship between ρ and δ. During the folding

process, δ_2 decreases from $\frac{2\pi}{3}$ to 0 while δ_1 increases from $\frac{2\pi}{3}$ at first, and then decreases to $\frac{\pi}{2}$. At the deployed configuration,

$$\delta_1 = \delta_2 = \frac{2\pi}{3}, \tag{5-43}$$

according to Eqs. (5-40) and (5-41), joint kinematic angles are

$$\theta_{\mathrm{d}} = 34.8°, \quad \phi_{\mathrm{d}} = 147.49°. \tag{5-44}$$

And at the folded configuration,

$$\delta_1 = \frac{\pi}{2}, \quad \delta_2 = 0, \tag{5-45}$$

according to Eqs. (5-40) and (5-41), joint kinematic angles are

$$\theta_{\mathrm{f}} = 166.12°, \quad \phi_{\mathrm{f}} = 268.0°. \tag{5-46}$$

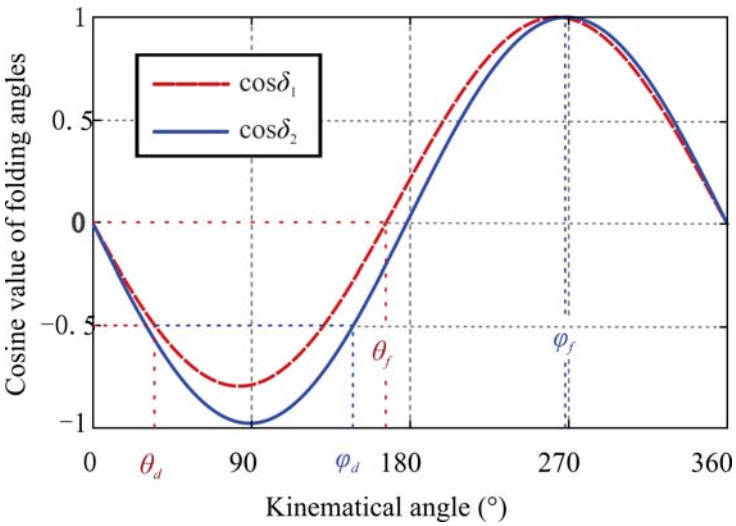

Fig. 5-8. The relationship between folding angles and joint kinematic angles.

5.4.2 Kinematics of the Polyhedral Transformation

After the truss analogy, motion path is generated by the numerical algorithm, described in section 2.4. Considering the symmetric property, there are four following sets of hexagons, $\{A_1A_2C_1C_2B_1B_2\}$, $\{A_1B_2B_3F_3F_4A_4$, $B_1C_2C_3D_3D_4B_4$, $C_1A_2A_3E_3E_4C_4\}$, $\{D_1F_2F_3B_3B_4D_4$, $E_1D_2D_3C_3C_4E_4$, $F_1E_2E_3A_3A_4F_4\}$, and $\{D_1D_2E_1E_2F_1F_2\}$. And configurations in each set keep the same as they can be obtained from others by symmetric rotations. Thus, one pair of vertices, which trends to meet, is chosen from each set of these hexagons, A_1B_1, A_2E_3, C_3D_2 and D_1E_1, to inspect the transformation process, and they are shown in Fig. 5-9(a). All of them equal $\sqrt{3}$ at the deployed configuration and become to zero at the folded

configuration, which shows that the obtained polyhedral linkage completes the transformation from the truncated octahedron to the cube.

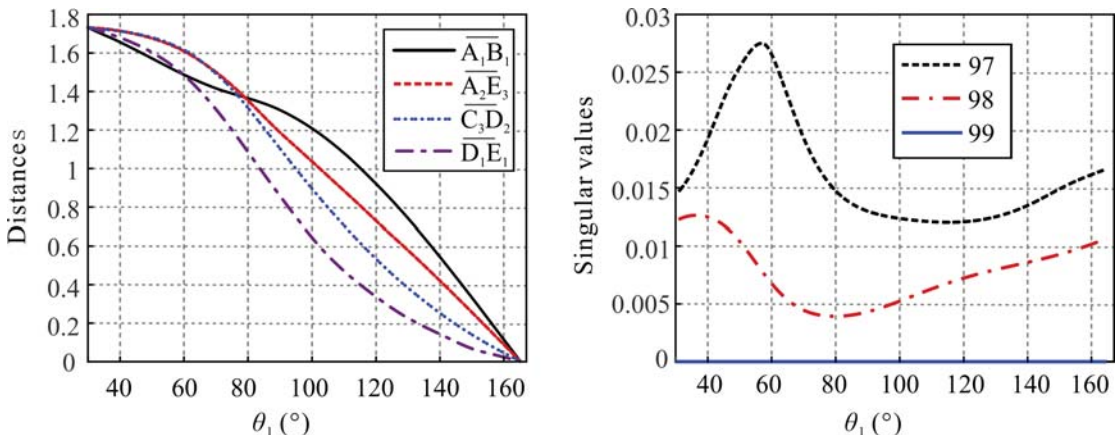

(a) (b)

Fig. 5-9. Kinematics of the transformation between truncated octahedron and cube illustrated by (a) distances between four pairs of vertices and (b) singular values during the transformation process.

Meanwhile, singular values of the equilibrium matrix are recorded in Fig. 5-9(b) which show the linkage is always movable as the minimum value keeps equaling to zero, and there is no bifurcation situation during the process as other values never deduce to zero.

Furthermore, in the obtained linkage, joints arrangement broke the symmetric property from octahedral symmetry O_h to threefold-symmetry C_3. It is interesting to study motions supplied by these *S* joints to see why they can not be set with *R* joints. It easy to find that there are three sets of *S* joints, {D_4, E_4, F_4}, {D_3, E_3, F_3} and {A_4, B_4, C_4}, and joints in each set can be obtained from others by symmetric rotations. Here, one joint in each set, i.e., *S* joints at E_4, E_3 and A_4, is analysed.

According to Euler's rotation theorem [141], any *S* joint works as an equivalent *R* joint whose axis is unfixed in its connected links. Figure 5-10 shows angles between axes of their equivalent *R* joints and their connecting links. As all of these angles are varying during the transformation, all of *S* joints do not work as *R* joints.

We can also use the relationships amongst the angle variables of the polyhedron to illustrate why only three *R* joints can be used. Consider the case shown in Fig. 5-6(a) with the rotational axes of *R* joints at A_3, B_3, C_3 pointing to centre of the polyhedron. Figure 5-5(b) shows that in the 1-DOF polyhedron, the two linkages do not move simultaneously as in the 2-DOF case in Fig. 5-5(a). Furthermore, Fig. 5-11(a) depicts δ^A vs. ρ^A, δ^D and ρ^D curves during the transformation, where δ^A and ρ^A, δ^D and ρ^D are folding angles of two adjacent joints in the Bricard

linkages $A_1A_2C_1C_2B_1B_2$ and $D_1D_2E_1E_2F_1F_2$, respectively. It is clear that generally $\delta^A \neq \delta^D$ and $\rho^A \neq \rho^D$ except at three configurations marked by red dots. Hence, the motion of these two Bricard linkages differs from each other in general during the transformation, which explains why the joint replacement cannot be done at A_3, B_3, C_3 and D_3, E_3, F_3 concurrently.

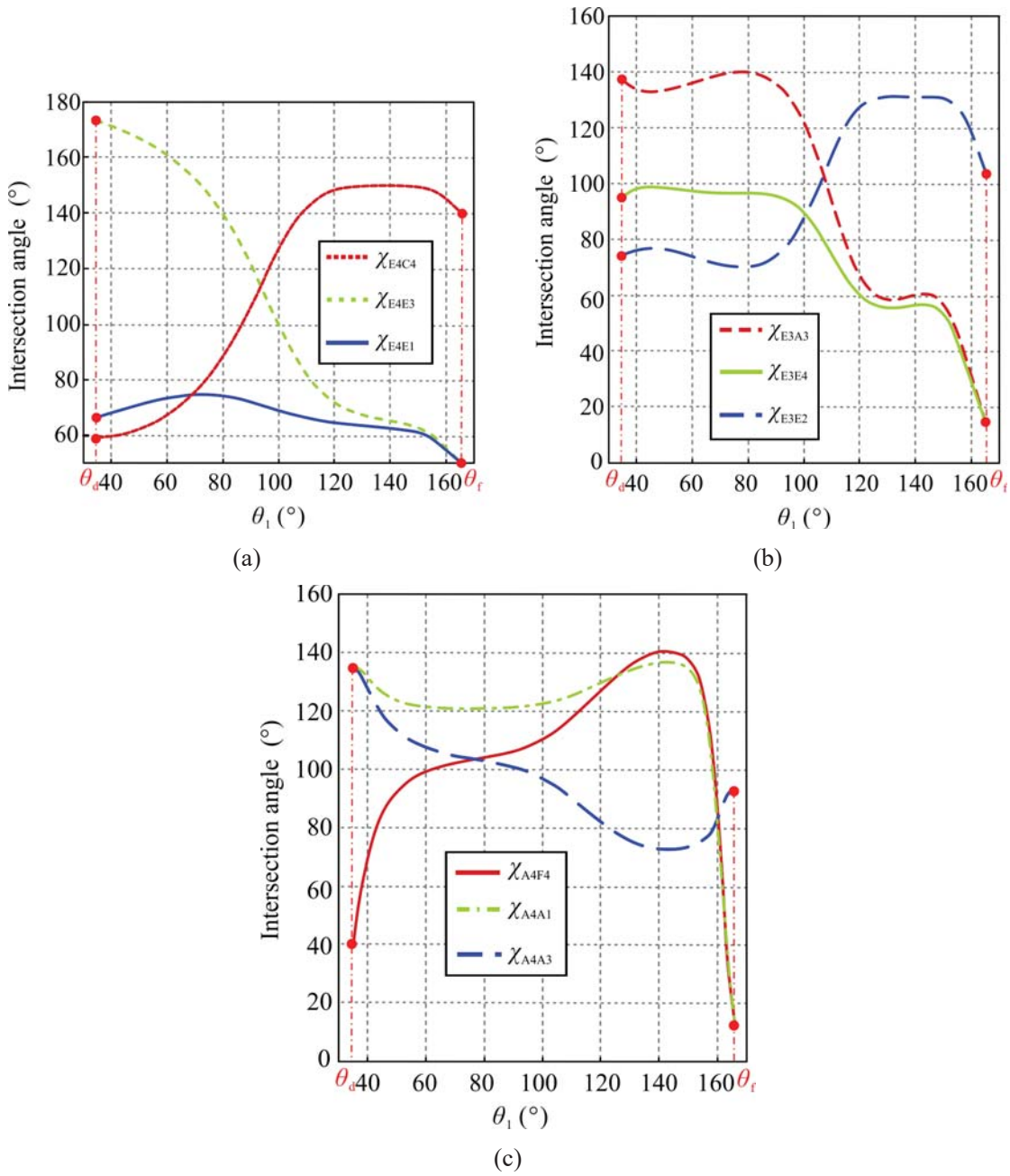

Fig. 5-10. Equivalent rotation axes of three *S* joints on (a) E_3, (b) E_4, (c) A_4 during the transformation depicted by angles between them and their connected links, respectively, where each letter pair in each legend represents the angle between the axis of the equivalent *R* joint and the corresponding edge.

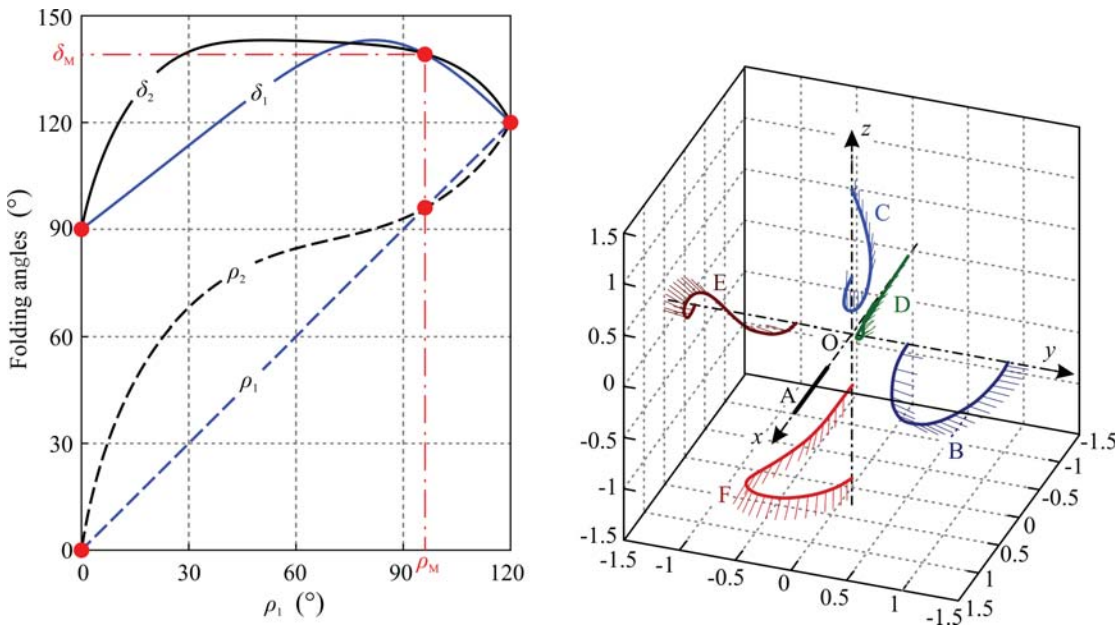

(a) (b)

Fig. 5-11. The folding process illustrated by (a) curves amongst folding angles of two threefold-symmetric Bricard 6*R* linkages $A_1A_2C_1C_2B_1B_2$ and $D_1D_2E_1E_2F_1F_2$; and (b) motion paths of the centres of the rigid square faces and their normals.

The introduction of additional *R* joints enables a 1-DOF transformation between a truncated octahedron and its paired octahedron at the cost that the octahedral symmetry is no longer preserved. In other words, the motion of each square is not the same as that in the face rotation-translation transformation. The motion paths of the eight square centres and their normal directions are plotted in Fig. 5-11(b) with square A being chosen as the driven one which moves along the path in the rotation-translation transformation. It is clear that the motion paths of other squares deviate from that of square A. However, once the transformation is completed, the truncated octahedron ends up being a cube, and the transformation is threefold-symmetric about the collinear symmetric axis of both Bricard linkages $A_1A_2C_1C_2B_1B_2$ and $D_1D_2E_1E_2F_1F_2$.

A 3D printed prototype, where $\zeta_{A3} = 0°$, vertices A_3, B_3, C_3 are all replaced with *R* joints directing to the body centre and other vertices A_4, B_4, C_4, D_3, E_3, F_3, D_4, E_4, F_4 are still set with *S* joints, has been made which has successfully verified the concept. The transformation sequence of this model is shown in Fig. 5-12.

5.5 Parameter Study

Note that the polyhedral linkage acquired in section 5-3 is not unique. There is one design parameter, angle ζ shown in Fig. 5-6(a), which has been set to zero previously in section 5-3.

Fig. 5-12. The transformation sequence of a prototype between a truncated octahedron (left) and a cube (right).

Here we investigate the folding performance with respect to this design parameter. Figure 5-13 shows curves of folding angles ρ_2 and δ_2 vs. input angle ρ_1 for a set of given ζ, which indicate configurations taken by two Bricard linkages $A_1A_2C_1C_2B_1B_2$ and $D_1D_2E_1E_2F_1F_2$, respectively. Though theoretically ζ can take any value without changing the mobility of the polyhedron, a close inspection of the curves reveals some choices can curtail the motions of both linkages. When $\zeta = -70°$, $\rho_1 < 0$ (blue curves shown in both Figs. 5-13(a) and 5-13(b)), which points to an interference of the linkages during the folding as all folding angles must be greater than and equal to zero. Moreover, δ_2 cannot reach fully folded angle $90°$. The negative ρ_1 appears when $\zeta < -60.9°$. On the other hand, when $\zeta = 30°$, $\rho_1 < 0$ again (orange curves shown in both Figs. 5-13(a) and 5-13(b)). In particular when $\zeta = 40°$, the both Bricard linkages cannot reach the folded configuration in which $\rho_1 = \rho_2 = 0$ and $\delta_2 = 90°$ (purple curves in Figs. 5-13(a) and 5-13(b)). The precise upper limit for ζ is $19.5°$.

Hence, the feasible range of ζ is between $-60.9°$ and $19.5°$. For a given ζ this range, it can be noticed from Fig. 5-13(a) that ρ_2 is not equal to ρ_1 in general from $\rho_1 = 120°$ (the truncated octahedron state) to $\rho_1 = 0$ (the cube state). This explains that the motions of both Bricard linkages are not the same, which further confirms our findings earlier that their motions are not in synchronization. However, if we choose $\zeta = -20°$, the ρ_2 vs. ρ_1 curve shown in green in Fig. 5-13(a) is closer to the red straight line where $\rho_2 = \rho_1$, and thus the motions of both Bricard linkages are more similar than those when other ζ values are selected.

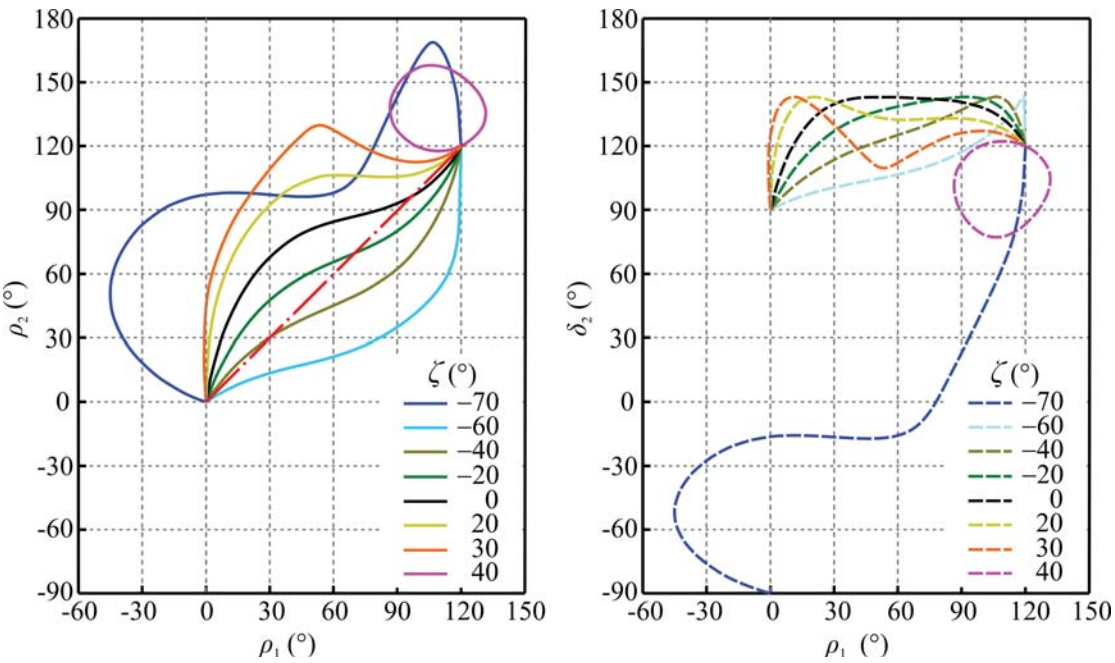

Fig. 5-13. Curves of (a) ρ_2 vs. ρ_1; and (b) δ_2 vs. ρ_1 for a set of given ζ.

5.6 Conclusions

In this chapter, we have proposed the kinematic method to accomplish 1-DOF shape transformation between paired Platonic solid and Archimedean solid using 6*R* spatial linkages. The method has successfully resulted in the truncated octahedron-cube transformation. The transformation always ends with the targeted polyhedral shapes though some symmetries of the original polyhedrons are broken during transformation. An analysis of the singular values of the equilibrium matrix of each polyhedron in its truss form has shown that the minimum always remains zero whereas the rest never deduce to zero, which indicates that motion can take place without any bifurcation. Parameter study on one design parameter ζ shows the feasible range of the parameter to get non-interrupted folding.

Chapter 6 Transformation between Truncated Tetrahedron and Tetrahedron

6.1 Introduction

Like the previous polyhedral transformation, a pair of polyhedrons, truncated tetrahedron and tetrahedron, may be transformed to each other by a multi-loop linkage constructed with four six-bar linkages as besides of four hexagonal faces in the truncated tetrahedron they both contain four triangular faces.

In the chapter, we create a transformation between these two polyhedrons with one degree of freedom by properly setting a movable joint at each vertex. Two schemes of joint arrangement are proposed, and their kinematic behaviors are respectively studied analytically and numerically, where mobility calculations are both based on the truss analogy. Finally, the transformation process adopting the first scheme is demonstrated to be valid through a cardboard prototype fabricated with the origami technique.

The layout of the chapter is as follows. Section 6.2 expounds the construction of the deployable polyhedron. Sections 6.3 and 6.4 present kinematics of two constructions, respectively. Discussion on the relationship between the folding performance and joint variables is described in Section 6.5. Conclusion in Section 6.6 ends the chapter.

6.2 Construction of Transformable Polyhedron between Truncated Tetrahedron and Tetrahedron

6.2.1 Geometry of Truncated Tetrahedron and Tetrahedron

Figure 6-1 shows a truncated tetrahedron and a tetrahedron with unit-length edges. All hexagonal faces are hollow, while the triangular faces and polyhedral edges are rigid. Setting one *S* joint at each vertex, the truncated tetrahedron can be folded into the tetrahedron with groups of vertices A, C, E and B, H, K and D, J, L as well as F, G, M trending to meet respectively, see Fig. 6-1 (c), via a middle configuration, see Fig. 6-1(b).

A Cartesian coordinate system is established in the truncated tetrahedron, the centre of face ABCDEF is chosen as the origin, the normal of the face at the centre is chosen as *z* axis, *x* axis directs from the centre to vertex F and *y* axis is determined by the right-hand rule. Then, coordinates of all vertices are

$$\boldsymbol{A}^{\mathrm{tt}} = \left[\frac{1}{2}, \frac{\sqrt{3}}{2}, 0\right]^{\mathrm{T}}, \quad \boldsymbol{B}^{\mathrm{tt}} = \left[-\frac{1}{2}, \frac{\sqrt{3}}{2}, 0\right]^{\mathrm{T}}, \quad \boldsymbol{C}^{\mathrm{tt}} = \left[-1, 0, 0\right]^{\mathrm{T}}, \tag{6-1a}$$

$$\boldsymbol{D}^{\mathrm{tt}}=\left[-\frac{1}{2},-\frac{\sqrt{3}}{2},0\right]^{\mathrm{T}},\ \boldsymbol{E}^{\mathrm{tt}}=\left[\frac{1}{2},-\frac{\sqrt{3}}{2},0\right]^{\mathrm{T}},\ \boldsymbol{F}^{\mathrm{tt}}=\left[1,0,0\right]^{\mathrm{T}},\tag{6-1b}$$

$$\boldsymbol{G}^{\mathrm{tt}}=\left[0,\frac{2\sqrt{3}}{3},\frac{\sqrt{6}}{3}\right]^{\mathrm{T}},\ \boldsymbol{H}^{\mathrm{tt}}=\left[-1,-\frac{\sqrt{3}}{3},\frac{\sqrt{6}}{3}\right]^{\mathrm{T}},\ \boldsymbol{J}^{\mathrm{tt}}=\left[1,-\frac{\sqrt{3}}{3},\frac{\sqrt{6}}{3}\right]^{\mathrm{T}},\tag{6-1c}$$

$$\boldsymbol{K}^{\mathrm{tt}}=\left[0,\frac{\sqrt{3}}{3},\frac{2\sqrt{6}}{3}\right]^{\mathrm{T}},\ \boldsymbol{L}^{\mathrm{tt}}=\left[-\frac{1}{2},-\frac{\sqrt{3}}{6},\frac{2\sqrt{6}}{3}\right]^{\mathrm{T}},\ \boldsymbol{M}^{\mathrm{tt}}=\left[\frac{1}{2},-\frac{\sqrt{3}}{6},\frac{2\sqrt{6}}{3}\right]^{\mathrm{T}}.\tag{6-1d}$$

in which the superscript "tt" represents the truncated tetrahedron. Thus, the body centre of the truncated tetrahedron is

$$\boldsymbol{Q}=\left[0,0,\frac{\sqrt{6}}{4}\right]^{\mathrm{T}}.\tag{6-2}$$

To realise the transformation, the truncated tetrahedron becomes the tetrahedron shown in Fig. 6-1(c) with vertices A, C, E meet at point O through a middle configuration shown in Fig. 6-1(b). The positions of the vertices of tetrahedron are

$$\boldsymbol{A}^{\mathrm{t}}=\boldsymbol{C}^{\mathrm{t}}=\boldsymbol{E}^{\mathrm{t}}=\left[0,0,0\right]^{\mathrm{T}},\ \boldsymbol{B}^{\mathrm{t}}=\boldsymbol{H}^{\mathrm{t}}=\boldsymbol{K}^{\mathrm{t}}=\left[-\frac{\sqrt{3}}{6},\frac{1}{2},\frac{\sqrt{6}}{3}\right]^{\mathrm{T}},\tag{6-3a}$$

$$\boldsymbol{D}^{\mathrm{t}}=\boldsymbol{J}^{\mathrm{t}}=\boldsymbol{L}^{\mathrm{t}}=\left[-\frac{\sqrt{3}}{6},-\frac{1}{2},\frac{\sqrt{6}}{3}\right]^{\mathrm{T}},\ \boldsymbol{F}^{\mathrm{t}}=\boldsymbol{G}^{\mathrm{t}}=\boldsymbol{M}^{\mathrm{t}}=\left[\frac{\sqrt{3}}{3},0,\frac{\sqrt{6}}{3}\right]^{\mathrm{T}}.\tag{6-3b}$$

where the superscript "t" represents the tetrahedron.

6.2.2 A Threefold-symmetric Bricard Linkage

Obviously, both polyhedrons are threefold rotational symmetric around the normal line of one triangle, such as *z* axis. Hence, a threefold-symmetric Bricard linkage is considered to realise the transformation of hollow hexagon ABCDEF with rigid links as triangles ABG, CDH, EFJ and bars BC, DE, FA. The next step is to determine joint directions in vertices A, B, C, D, E, F. In the coordinate system O-*xyz* in Fig. 6-2, bar AF is assumed to be fixed, triangle ABG will move to AB'F while triangle EFJ moves to AFJ' to form two adjacent faces of a tetrahedron. According to the property of threefold-symmetric Bricard linkage, each group of three alternate revolute axes intersects at one point. And two intersecting points must be both on the symmetric line, *z* axis. Meanwhile, according to the motion trend of vertices, see Fig. 6-1(b), G moves to F. So, the revolute axis at A has to also be in the plane bisecting angle FAG. Thus, it must pass the body centre $\boldsymbol{Q}$ with

$$\boldsymbol{s}_{\mathrm{A}}=\frac{\boldsymbol{A}-\boldsymbol{Q}}{\left|\boldsymbol{A}-\boldsymbol{Q}\right|}=\left[\frac{\sqrt{22}}{11},\frac{\sqrt{66}}{11},-\frac{\sqrt{33}}{11}\right]^{\mathrm{T}}.\tag{6-4}$$

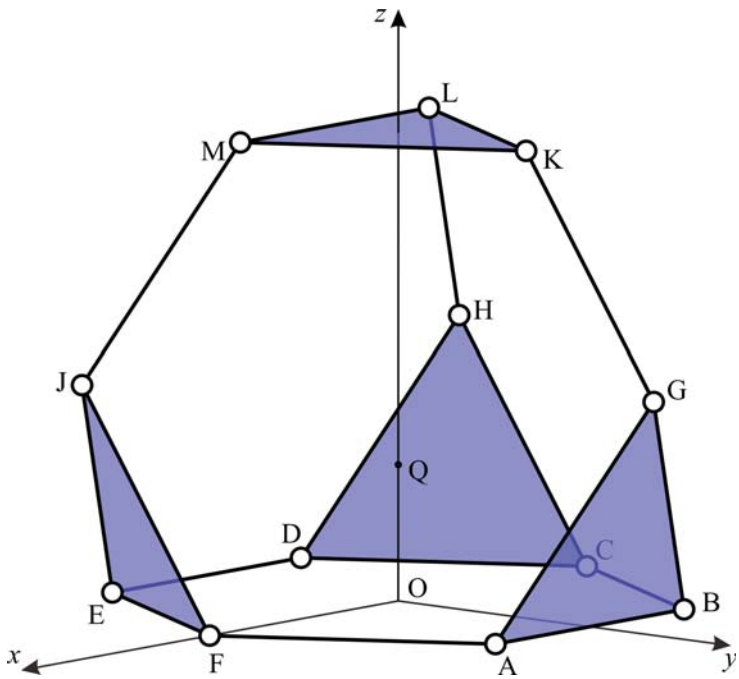

(a)

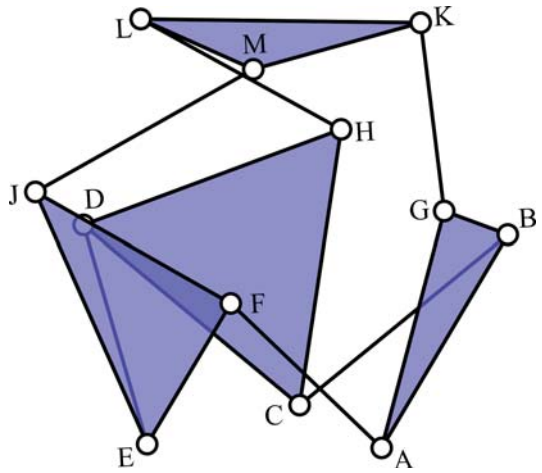

(b)

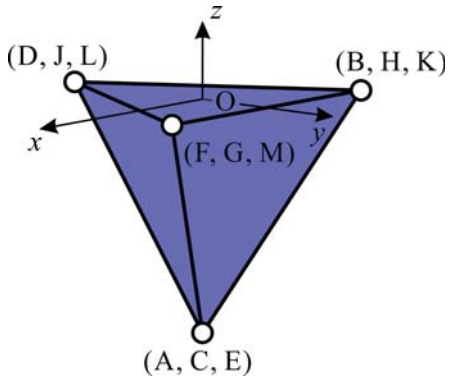

(c)

Fig. 6-1. Polyhedron transformed from (a) deployed configuration, truncated tetrahedron, via (b) a middle configuration, to (c) the tetrahedron.

Thus, the matrix for the transformation from ABG to AB'F is

$$\boldsymbol{T}_{\mathrm{A}}=\begin{bmatrix} -\frac{1}{2} & \frac{\sqrt{3}}{2} & 0 & 0 \\ \frac{\sqrt{3}}{6} & \frac{1}{6} & -\frac{2\sqrt{2}}{3} & \frac{\sqrt{3}}{3} \\ -\frac{\sqrt{6}}{3} & -\frac{\sqrt{2}}{3} & -\frac{1}{3} & \frac{\sqrt{6}}{3} \\ 0 & 0 & 0 & 1 \end{bmatrix}. \tag{6-5}$$

Then

$$\boldsymbol{B}'=\boldsymbol{T}_{\mathrm{A}}\boldsymbol{B}=\left[1,\frac{\sqrt{3}}{3},\frac{\sqrt{6}}{3}\right]^{\mathrm{T}}. \tag{6-6}$$

As triangles ABG and EFJ at their folded positions form two adjacent faces, their dihedral angle is $\arccos\left(1/3\right)$, then

$$\boldsymbol{J}'=Rot\left(\boldsymbol{AF},\arccos(\frac{1}{3})\right)\boldsymbol{B}'=\left[\frac{1}{6},\frac{\sqrt{3}}{18},\frac{2\sqrt{6}}{9}\right]^{\mathrm{T}}, \tag{6-7}$$

where $Rot\left(\boldsymbol{AF},\arccos(1/3)\right)$ is the matrix of transformation around $\boldsymbol{AF}$ by $\arccos(1/3)$. The matrix can be expressed by Rodrigues formula [141]. Assuming the matrix for the transformation from EFJ to AFJ' is $\boldsymbol{T}_{\mathrm{F}}$, then

$$\boldsymbol{A}=\boldsymbol{T}_{\mathrm{F}}\boldsymbol{E}, \tag{6-8a}$$

$$\boldsymbol{F}=\boldsymbol{T}_{\mathrm{F}}\boldsymbol{F}, \tag{6-8b}$$

$$\boldsymbol{J}'=\boldsymbol{T}_{\mathrm{F}}\boldsymbol{J}. \tag{6-8c}$$

Meanwhile, if an auxiliary point

$$\boldsymbol{U}=\boldsymbol{E}+\boldsymbol{EF}\times\boldsymbol{EJ}, \tag{6-9}$$

is fixed on triangle EFJ, its position on triangle AFJ' after the rigid motion must be

$$\boldsymbol{U}'=\boldsymbol{A}+\boldsymbol{AF}\times\boldsymbol{AJ}'. \tag{6-10}$$

Then,

$$\boldsymbol{U}'=\boldsymbol{T}_{\mathrm{F}}\boldsymbol{U}. \tag{6-11}$$

Therefore, the transformation matrix can be solved as

$$\boldsymbol{T}_{\mathrm{F}}=\begin{bmatrix}\boldsymbol{A} & \boldsymbol{F} & \boldsymbol{J}' & \boldsymbol{U}'\end{bmatrix}\begin{bmatrix}\boldsymbol{E} & \boldsymbol{F} & \boldsymbol{J} & \boldsymbol{U}\end{bmatrix}^{-1}=\begin{bmatrix} -\frac{7}{18} & \frac{25\sqrt{3}}{54} & -\frac{5\sqrt{6}}{27} & \frac{25}{18} \\ -\frac{25\sqrt{3}}{54} & -\frac{29}{54} & -\frac{5\sqrt{2}}{27} & \frac{25\sqrt{3}}{54} \\ -\frac{5\sqrt{6}}{27} & \frac{5\sqrt{2}}{27} & \frac{23}{27} & \frac{5\sqrt{6}}{27} \\ 0 & 0 & 0 & 1 \end{bmatrix}. \tag{6-12}$$

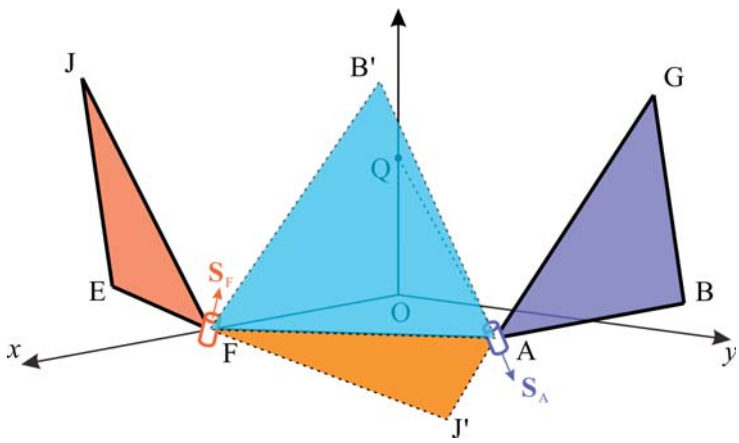

Fig. 6-2. Determination of revolute axes at A and F.

Then, the revolute axis at F can be determined

$$\boldsymbol{s}_{\mathrm{F}} = \left[-\frac{2\sqrt{166}}{83}, 0, \frac{5\sqrt{249}}{83} \right]^{\mathrm{T}}. \tag{6-13}$$

By symmetric operations, directions of other four revolute axes are

$$\boldsymbol{s}_{\mathrm{B}} = \left[\frac{\sqrt{166}}{83}, -\frac{\sqrt{498}}{83}, \frac{5\sqrt{249}}{83} \right]^{\mathrm{T}}, \quad \boldsymbol{s}_{\mathrm{C}} = \left[-\frac{2\sqrt{22}}{11}, 0, -\frac{\sqrt{33}}{11} \right]^{\mathrm{T}}, \tag{6-14a}$$

$$\boldsymbol{s}_{\mathrm{D}} = \left[\frac{\sqrt{166}}{83}, \frac{\sqrt{498}}{83}, \frac{5\sqrt{249}}{83} \right]^{\mathrm{T}}, \quad \boldsymbol{s}_{\mathrm{E}} = \left[\frac{\sqrt{22}}{11}, -\frac{\sqrt{66}}{11}, -\frac{\sqrt{33}}{11} \right]^{\mathrm{T}}. \tag{6-14b}$$

Hence, the threefold-symmetric Bricard linkage ABCDEF is formed.

According to D-H notation [8], its link length of original linkage, which is the shortest distance between two adjacent revolute axes $\boldsymbol{s}_{\mathrm{A}}$ and $\boldsymbol{s}_{\mathrm{F}}$, is

$$a = \frac{2\sqrt{69}}{23}, \tag{6-15}$$

and its twist angle, which is the angle between these two adjacent revolute axes, is

$$\alpha = \pi - \arccos\left(\frac{19\sqrt{913}}{913} \right). \tag{6-16}$$

6.2.3 Constructions of the Linkage

Hereto, those three bottom triangles in the truncated tetrahedron can be folded into three adjacent faces in the tetrahedron, while types of joints at G, H, J, K, L, and M are not determined yet. If these undetermined joints are still kept as with *S* joints, the mobility of the truncated tetrahedron is 4 calculated with the truss analogy method [140]. Thus, more constraints are required to obtain one DOF. One convenient way is replacing *S* joint into *R* joint. To maintain the threefold-symmetry, G, H, J and K, L, M are divided into two groups, which renders two construction schemes, I and II.

In scheme I, G, H, J are set with *R* joints and K, L, M are kept as *S* joints as shown in Fig. 6-3. According to the motion trend of vertices, B will meet K, see Fig. 6-1(b), revolute axis of joint G must be in the plane which bisects angle BGK. Here we can set it along the direction of QG as a special case and the other possible solutions are discussed in section 6.5. Joint axes at H and J can be obtained by symmetric operation. So

$$\boldsymbol{s}_{\mathrm{G}}=\left[0,\frac{\sqrt{6}}{3},\frac{\sqrt{3}}{3}\right]^{\mathrm{T}},\ \boldsymbol{s}_{\mathrm{H}}=\left[-\frac{\sqrt{2}}{2},-\frac{\sqrt{6}}{6},\frac{\sqrt{3}}{3}\right]^{\mathrm{T}},\ \boldsymbol{s}_{\mathrm{J}}=\left[\frac{\sqrt{2}}{2},-\frac{\sqrt{6}}{6},\frac{\sqrt{3}}{3}\right]^{\mathrm{T}},\tag{6-17}$$

Similarly, in scheme II, K, L, M are set with *R* joints and G, H, J are still *S* joints as shown in Fig. 6-5(a). According to the motion trend of vertices, G will meet M, see Fig. 6-1(b), revolute axis of joint K must be in the plane which bisects angle GKM, and joint axes at L and M can also be obtained by symmetric operation. One special case is

$$\boldsymbol{s}_{\mathrm{K}}=\left[0,\frac{2\sqrt{66}}{33},\frac{5\sqrt{33}}{33}\right]^{\mathrm{T}},\boldsymbol{s}_{\mathrm{L}}=\left[-\frac{\sqrt{22}}{11},-\frac{\sqrt{66}}{33},\frac{5\sqrt{33}}{33}\right]^{\mathrm{T}},\boldsymbol{s}_{\mathrm{M}}=\left[\frac{\sqrt{210}}{35},-\frac{2\sqrt{35}}{35},\frac{\sqrt{35}}{7}\right]^{\mathrm{T}},\tag{6-18}$$

when all three joints intersect at polyhedron's body centre Q. Calculating with the truss method, $m=1$ for both schemes. Their kinematics will be analysed in the following two parts, respectively.

6.3 Kinematics of Scheme I

6.3.1 Coordinates of Vertices during the Transformation Process

Figure 6-3 shows the construction of scheme I. As joint axis at each vertex is not perpendicular to its connected bars, hexagonal linkage ABCDEF is in fact an alternative form of Bricard linkage. The corresponding original linkage can be found by the shortest lines between the adjacent joints as links, illustrated by gray thick lines in Fig. 6-3. Thus, the geometric parameters of this 6*R* linkage are

$$\overline{\mathrm{A'B'}}=\overline{\mathrm{B'C'}}=\overline{\mathrm{C'D'}}=\overline{\mathrm{D'E'}}=\overline{\mathrm{E'F'}}=\overline{\mathrm{F'A'}}=a=\frac{2\sqrt{69}}{23},\tag{6-19}$$

and

$$\alpha_{\mathrm{AB}}=\alpha_{\mathrm{CD}}=\alpha_{\mathrm{EF}}=2\pi-\alpha=\pi+\arccos\left(\frac{19\sqrt{913}}{913}\right),\tag{6-20a}$$

$$\alpha_{\mathrm{BC}}=\alpha_{\mathrm{DE}}=\alpha_{\mathrm{FA}}=\alpha=\pi-\arccos\left(\frac{19\sqrt{913}}{913}\right),\tag{6-20b}$$

extensions at A, C, E and B, D, F are

$$\overline{AA'} = \overline{CC'} = \overline{EE'} = c = \frac{17\sqrt{22}}{92}, \tag{6-21}$$

$$\overline{BB'} = \overline{DD'} = \overline{FF'} = d = \frac{5\sqrt{166}}{92}, \tag{6-22}$$

respectively.

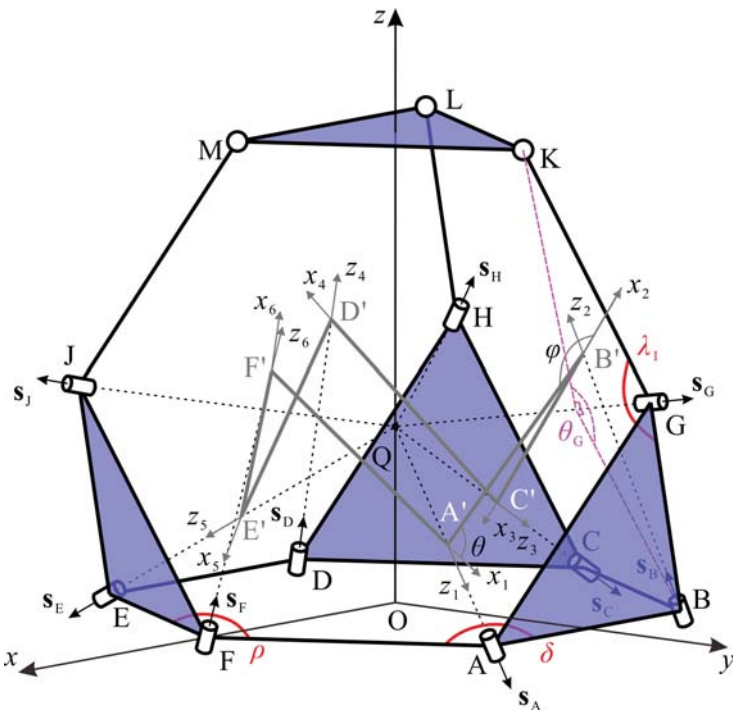

Fig. 6-3. Construction of Scheme I.

In order to analyse the motion of whole truncated tetrahedron, the global coordinate system is fixed as O-*xyz* in Fig. 6-3. Vertices B, D, F are kept on the plane *x*O*y* while F is fixed on the *x* axis and moves towards origin O during the transformation to tetrahedron while triangle KLM moves downwards along *z* axis. As the result, the Bricard linkage ABCDEF has no fixed link. In order to take the input of this linkage as the input of the whole polyhedron, the local coordinate systems 1-6 are set up on the original Bricard linkage. First, take the link 61 as reference, the motion of Bricard linkage can be described in the system 1. Second, transfer the joints G, H, J into global system to derive the motion of triangle KLM, then to obtain the motion of whole polyhedron. According to D-H notation, the local coordinate at each joint can be set up and the corresponding vertex coordinates are

$${}^{1}\boldsymbol{A} = {}^{3}\boldsymbol{C} = {}^{5}\boldsymbol{E} = \left[0, 0, c\right]^{\mathrm{T}}, \tag{6-23}$$

$${}^{2}\boldsymbol{B} = {}^{4}\boldsymbol{D} = {}^{6}\boldsymbol{F} = \left[0, 0, -d\right]^{\mathrm{T}}, \tag{6-24}$$

where superscript represents the corresponding local coordinate system. According to the property of threefold-symmetry, kinematic angles at *R* joints A, C, E are the same,

denoted by θ, and those at R joints B, D, F are the same, denoted by ϕ. Transformation matrices among coordinate systems are

$$\boldsymbol{T}_{2(1)}=\boldsymbol{T}_{4(3)}=\boldsymbol{T}_{6(5)}=\begin{bmatrix}\cos\theta & \frac{19}{913}\sqrt{913}\sin\theta & -\frac{2}{913}\sqrt{125994}\sin\theta & \frac{2}{23}\sqrt{69}\cos\theta\\ \sin\theta & -\frac{19}{913}\sqrt{913}\cos\theta & \frac{2}{913}\sqrt{125994}\cos\theta & \frac{2}{23}\sqrt{69}\sin\theta\\ 0 & -\frac{2}{913}\sqrt{125994} & -\frac{19}{913}\sqrt{913} & 0\\ 0 & 0 & 0 & 1\end{bmatrix}, \tag{6-25}$$

$$\boldsymbol{T}_{3(2)}=\boldsymbol{T}_{5(4)}=\boldsymbol{T}_{1(6)}=\begin{bmatrix}\cos\phi & \frac{19}{913}\sqrt{913}\sin\phi & \frac{2}{913}\sqrt{125994}\sin\phi & \frac{2}{23}\sqrt{69}\cos\phi\\ \sin\phi & -\frac{19}{913}\sqrt{913}\cos\phi & -\frac{2}{913}\sqrt{125994}\cos\phi & \frac{2}{23}\sqrt{69}\sin\phi\\ 0 & \frac{2}{913}\sqrt{125994} & -\frac{19}{913}\sqrt{913} & 0\\ 0 & 0 & 0 & 1\end{bmatrix} \tag{6-26}$$

Then vertices B, C, D, E, F can be expressed in coordinate system 1 as,

$$^{1}\boldsymbol{B}=\boldsymbol{T}_{2(1)}\,^{2}\boldsymbol{B}, \tag{6-27a}$$

$$^{1}\boldsymbol{C}=\boldsymbol{T}_{2(1)}\boldsymbol{T}_{3(2)}\,^{3}\boldsymbol{C}, \tag{6-27b}$$

$$^{1}\boldsymbol{D}=\boldsymbol{T}_{2(1)}\boldsymbol{T}_{3(2)}\boldsymbol{T}_{4(3)}\,^{4}\boldsymbol{D}, \tag{6-27c}$$

$$^{1}\boldsymbol{E}=\boldsymbol{T}_{2(1)}\boldsymbol{T}_{3(2)}\boldsymbol{T}_{4(3)}\boldsymbol{T}_{5(4)}\,^{5}\boldsymbol{E}, \tag{6-27d}$$

$$^{1}\boldsymbol{F}=\boldsymbol{T}_{2(1)}\boldsymbol{T}_{3(2)}\boldsymbol{T}_{4(3)}\boldsymbol{T}_{5(4)}\boldsymbol{T}_{6(5)}\,^{6}\boldsymbol{F}. \tag{6-27e}$$

Meanwhile, as G, H, J are fixed in bars 12, 34, 56, respectively. Thus,

$$^{2}\boldsymbol{G}=\,^{4}\boldsymbol{H}=\,^{6}\boldsymbol{J}=\left[\frac{\sqrt{69}}{138},-\frac{95\sqrt{5727}}{11454},\frac{45\sqrt{166}}{7636}\right]. \tag{6-28}$$

G, H, J can be expressed in coordinate system 1 as,

$$^{1}\boldsymbol{G}=\boldsymbol{T}_{2(1)}\,^{2}\boldsymbol{G},\ \ ^{1}\boldsymbol{H}=\boldsymbol{T}_{2(1)}\boldsymbol{T}_{3(2)}\boldsymbol{T}_{4(3)}\,^{4}\boldsymbol{H},\ \ ^{1}\boldsymbol{J}=\boldsymbol{T}_{2(1)}\boldsymbol{T}_{3(2)}\boldsymbol{T}_{4(3)}\boldsymbol{T}_{5(4)}\boldsymbol{T}_{6(5)}\,^{6}\boldsymbol{J}. \tag{6-29}$$

Then, during the transformation process, this linkage is set in the global frame O-*xyz*. The coordinate of the centre of B, D, F in system 1 is

$$^{1}\boldsymbol{O}=\frac{1}{3}\left(^{1}\boldsymbol{B}+\,^{1}\boldsymbol{D}+\,^{1}\boldsymbol{F}\right). \tag{6-30}$$

Thus, the transformation between system 1 and the global system, denoted by 0, is

$$\boldsymbol{T}_{1(0)} = \left[{}^{1}\boldsymbol{F} - {}^{1}\boldsymbol{O}, \frac{{}^{1}\boldsymbol{B}\,{}^{1}\boldsymbol{D} \times {}^{1}\boldsymbol{B}\,{}^{1}\boldsymbol{F}}{\left| {}^{1}\boldsymbol{B}\,{}^{1}\boldsymbol{D} \times {}^{1}\boldsymbol{B}\,{}^{1}\boldsymbol{F} \right|} \times \left({}^{1}\boldsymbol{F} - {}^{1}\boldsymbol{O} \right), \frac{{}^{1}\boldsymbol{B}\,{}^{1}\boldsymbol{D} \times {}^{1}\boldsymbol{B}\,{}^{1}\boldsymbol{F}}{\left| {}^{1}\boldsymbol{B}\,{}^{1}\boldsymbol{D} \times {}^{1}\boldsymbol{B}\,{}^{1}\boldsymbol{F} \right|}, {}^{1}\boldsymbol{O}; 0, 0, 0, 1 \right]. \tag{6-31}$$

Then,

$${}^{0}\boldsymbol{A} = \boldsymbol{T}_{1(0)}\,{}^{1}\boldsymbol{A}, \quad {}^{0}\boldsymbol{B} = \boldsymbol{T}_{1(0)}\,{}^{1}\boldsymbol{B}, \quad {}^{0}\boldsymbol{C} = \boldsymbol{T}_{1(0)}\,{}^{1}\boldsymbol{C}, \tag{6-32a}$$

$${}^{0}\boldsymbol{D} = \boldsymbol{T}_{1(0)}\,{}^{1}\boldsymbol{D}, \quad {}^{0}\boldsymbol{E} = \boldsymbol{T}_{1(0)}\,{}^{1}\boldsymbol{E}, \quad {}^{0}\boldsymbol{F} = \boldsymbol{T}_{1(0)}\,{}^{1}\boldsymbol{F}, \tag{6-32b}$$

$${}^{0}\boldsymbol{G} = \boldsymbol{T}_{1(0)}\,{}^{1}\boldsymbol{G}, \quad {}^{0}\boldsymbol{H} = \boldsymbol{T}_{1(0)}\,{}^{1}\boldsymbol{H}, \quad {}^{0}\boldsymbol{J} = \boldsymbol{T}_{1(0)}\,{}^{1}\boldsymbol{J}. \tag{6-32c}$$

As axis of R joint at G, $\boldsymbol{s}_{\mathrm{G}}$, passes to the body centre and is fixed in system 2, then

$${}^{2}\boldsymbol{s}_{\mathrm{G}} = \left[-\frac{\sqrt{1518}}{207}, \frac{217\sqrt{125994}}{188991}, \frac{27\sqrt{913}}{913} \right]. \tag{6-33}$$

Thus,

$${}^{0}\boldsymbol{s}_{\mathrm{G}} = \boldsymbol{T}_{1(0)}\boldsymbol{T}_{2(1)}\,{}^{2}\boldsymbol{s}_{\mathrm{G}}. \tag{6-34}$$

Denoting the kinematic angle at G by θ_{G}, see Fig. 6-3, then coordinate of K is

$${}^{0}\boldsymbol{K} = Rot({}^{0}\boldsymbol{s}_{\mathrm{G}}, \theta_{\mathrm{G}})\,{}^{0}\boldsymbol{B}, \tag{6-35}$$

where $Rot({}^{0}\boldsymbol{s}_{\mathrm{G}}, \theta_{\mathrm{G}})$ is the matrix of transformation around revolute axis ${}^{0}\boldsymbol{s}_{\mathrm{G}}$ by θ_{G}. The matrix can be expressed by Rodrigues formula [141]. Meanwhile, the centre of triangle KLM is always on z axis, thus the distance between K and z axis keeps constant. Then,

$${x_{\mathrm{K}}}^{2} + {y_{\mathrm{K}}}^{2} = \frac{1}{3}, \tag{6-36}$$

where x_{K} and y_{K} are x and y components of K, respectively. Combining Eqs. (6-35) and (6-36), θ_{G} can be solved, see the following part for details.

A rigid body rotates around axis $\boldsymbol{f} = [f_x, f_y, f_z]^{\mathrm{T}}$, which crosses point $\boldsymbol{N}$, by angle θ, then the transformation matrix can be expressed as

$$\boldsymbol{T}(\boldsymbol{Q}, \boldsymbol{f}, \theta) = \begin{bmatrix} \boldsymbol{R} & \boldsymbol{N} - \boldsymbol{R}\boldsymbol{N} \\ 0 & 1 \end{bmatrix}, \tag{6-37}$$

where

$$\boldsymbol{R} = \begin{bmatrix} f_x^{2}\mathrm{vers}\theta + \cos\theta & f_x f_y \mathrm{vers}\theta - f_z \sin\theta & f_x f_z \mathrm{vers}\theta + f_y \sin\theta \\ f_x f_y \mathrm{vers}\theta + f_z \sin\theta & f_y^{2}\mathrm{vers}\theta + \cos\theta & f_y f_z \mathrm{vers}\theta - f_x \sin\theta \\ f_x f_z \mathrm{vers}\theta - f_y \sin\theta & f_y f_z \mathrm{vers}\theta + f_x \sin\theta & f_z^{2}\mathrm{vers}\theta + \cos\theta \end{bmatrix}. \tag{6-38}$$

According to the definition of joint kinematic angle at G, $\boldsymbol{K}$ can be viewed as $\boldsymbol{B}$

being rotated around $\boldsymbol{s}_{\mathrm{G}}$ by θ_{G}. Therefore

$$\boldsymbol{K} = \boldsymbol{T}(\boldsymbol{G}, \boldsymbol{s}_{\mathrm{G}}, \theta_{\mathrm{G}})\boldsymbol{B}\,, \tag{6-39}$$

whose x and y components are

$$x_{\mathrm{K}} = TermA_1 + TermB_1 \cos\theta_{\mathrm{G}} + TermC_1 \sin\theta_{\mathrm{G}}\,, \tag{6-40}$$

$$y_{\mathrm{K}} = TermA_2 + TermB_2 \cos\theta_{\mathrm{G}} + TermC_2 \sin\theta_{\mathrm{G}}\,, \tag{6-41}$$

where

$$TermA_1 = f_x^{\,2} x_{\mathrm{B}} + f_x f_y y_{\mathrm{B}} + f_x f_z z_{\mathrm{B}}\,, \tag{6-42a}$$

$$TermB_1 = (1 - f_x^{\,2}) x_{\mathrm{B}} - f_x f_y y_{\mathrm{B}} - f_x f_z z_{\mathrm{B}}\,, \tag{6-42b}$$

$$TermC_1 = -f_z y_{\mathrm{B}} + f_z z_{\mathrm{B}}\,, \tag{6-42c}$$

$$TermA_2 = f_x f_y x_{\mathrm{B}} + f_y^{\,2} y_{\mathrm{B}} + f_x f_z z_{\mathrm{B}}\,, \tag{6-42d}$$

$$TermB_2 = -f_x f_y x_{\mathrm{B}} + (1 - f_y^{\,2}) x_{\mathrm{B}} - f_x f_z z_{\mathrm{B}}\,, \tag{6-42e}$$

$$TermC_2 = f_z x_{\mathrm{B}} - f_x z_{\mathrm{B}}\,. \tag{6-42f}$$

Denoting

$$\tan\frac{\theta_{\mathrm{G}}}{2} = t\,, \tag{6-43}$$

then

$$\sin\theta_{\mathrm{G}} = \frac{2t}{1+t^2} \quad \text{and} \quad \cos\theta_{\mathrm{G}} = \frac{1-t^2}{1+t^2}\,. \tag{6-44}$$

Considering Eq. (6-36), then

$$Term_4 \cdot t^4 + Term_3 \cdot t^3 + Term_2 \cdot t^2 + Term_1 \cdot t + Term_0 = 0\,, \tag{6-45}$$

where

$$Term_4 = 3(TermA_1^{\,2} + TermA_2^{\,2} + TermB_1^{\,2} + TermB_2^{\,2}) - 6(TermA_1 TermB_1 + TermA_2 TermB_2) - 1\,, \tag{6-46a}$$

$$Term_3 = 12(TermA_1 TermC_1 + TermA_2 TermC_2 - TermB_1 TermC_1 - TermB_2 TermC_2)\,, \tag{6-46b}$$

$$Term_2 = 6(TermA_1^{\,2} + TermA_2^{\,2} - TermB_1^{\,2} - TermB_2^{\,2} + 2TermC_1^{\,2} + 2TermC_2^{\,2}) - 2\,, \tag{6-46c}$$

$$Term_1 = 12(TermA_1 TermC_1 + TermA_2 TermC_2 + TermB_1 TermC_1 + TermB_2 TermC_2)\,, \tag{6-46d}$$

$$Term_0 = 3(TermA_1^{\,2} + TermA_2^{\,2} + TermB_1^{\,2} + TermB_2^{\,2}) + 6(TermA_1 TermB_1 + TermA_2 TermB_2) - 1\,. \tag{6-46e}$$

The quartic equation, Eq. (6-45), can be solved by the standard method or algorithm tools. Finally,

$$\theta_{\mathrm{G}} = 2\arctan t\,. \tag{6-47}$$

Then, all vertices are determined by one input variable θ or ϕ in the Bricard linkage ABCDEF.

6.3.2 Analysis of the Folding Process

According to [75], the input-output formula of threefold-symmetric Bricard linkage is

$$\cos^2\alpha + \sin^2\alpha(\cos\theta + \cos\phi) + (1+\cos^2\alpha)\cos\theta\cos\phi - 2\cos\alpha\sin\theta\sin\phi = 0\,. \tag{6-48}$$

Denoting

$$t_1 = \tan\frac{\theta}{2},\ \ t_2 = \tan\frac{\phi}{2}, \tag{6-49}$$

then

$$(4\cos^2\alpha - 1)t_1^{\,2}t_2^{\,2} - 8t_1t_2\cos\alpha - t_1^{\,2} - t_2^{\,2} + 3 = 0\,. \tag{6-50}$$

The solution is

$$t_2 = \frac{4\cos\alpha t_1 \pm \sqrt{(1+t_1^{\,2})(4\cos^2\alpha t_1^{\,2} - t_1^{\,2} + 3)}}{4\cos^2\alpha t_1^{\,2} - t_1^{\,2} - 1}\,. \tag{6-51}$$

Thus,

$$\phi = 2\arctan\left(\frac{4\cos\alpha\tan\frac{\theta}{2} \pm \sqrt{(1+\tan^2\frac{\theta}{2})(4\cos^2\alpha\tan^2\frac{\theta}{2} - \tan^2\frac{\theta}{2} + 3)}}{4\cos^2\alpha\tan^2\frac{\theta}{2} - \tan^2\frac{\theta}{2} - 1}\right). \tag{6-52}$$

Considering the deployed configuration, '−' of '±' in the above equation is adopted. Figure 6-4(a) shows kinematic curves among kinematic angles θ, ϕ and θ_{G}. ϕ increases from $\phi_{\mathrm{d}} = 143.55°$ to $\phi_{\mathrm{f}} = 266.03°$ while θ increases from $\theta_{\mathrm{d}} = 40.46°$ to $\theta_{\mathrm{f}} = 186.90°$. θ_{G} decreases from 146.44° to 0° during this movement, thus, distances between B and K, D and L, F and M decrease.

To describe the folding process more intuitively, folding angles, which are angles between adjacent edges, are employed. Folding angles AFE, BAF, BGK are denoted by ρ, δ, λ_1, respectively, see Fig. 6-3. Figure 6-4(b) shows the relationship among these folding angles. During the folding process, ρ decreases from $\rho_{\mathrm{d}} = 120°$ to $\rho_{\mathrm{f}} = 0°$, δ increases at first and then also decreases to 60°, while λ_1 decreases strictly from 120° to 0°. This means that the polyhedron completes the transformation from the deployed truncated tetrahedron to the folded tetrahedron.

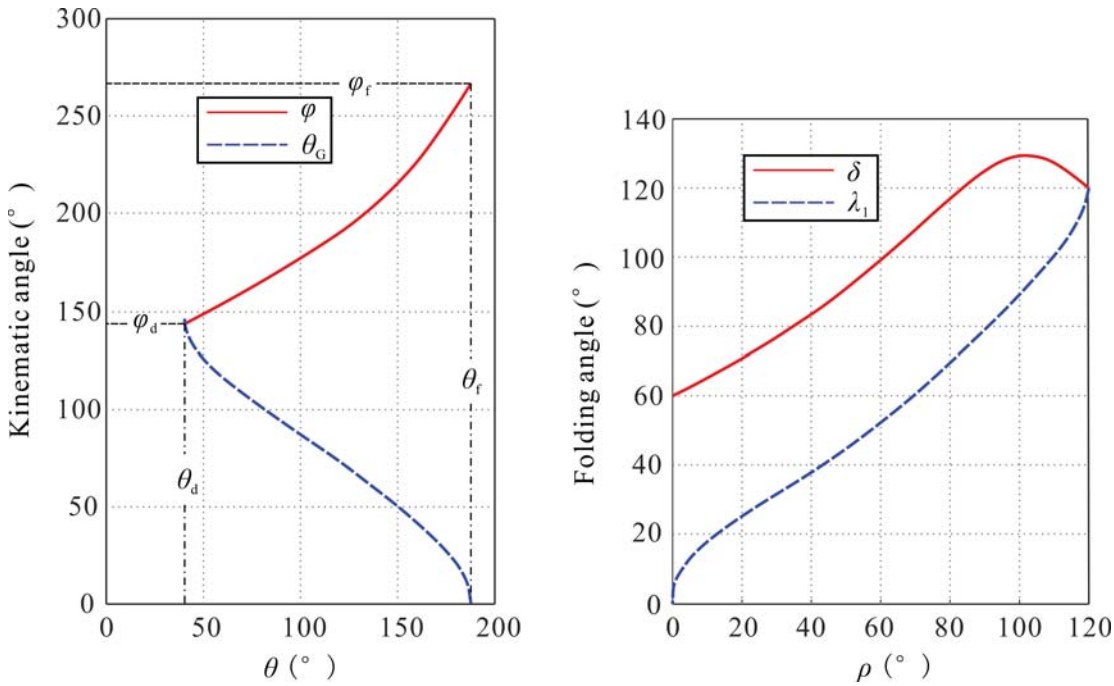

(a) (b)

Fig. 6-4. Kinematic curves in the scheme I transformation by the relationships among (a) joint kinematic angles, (b) link folding angles.

6.4 Kinematics of Scheme II

6.4.1 Coordinates of Vertices during the Transformation Process

In scheme II, as *R* joints at K, L, M are not connected to the Bricard linkage directly, see Fig. 6-5(a), the analytical calculation of its kinematics is more complicated. Here, a numerical method combing the truss method [140] and the SVD method [43] is adopted. First, based on the truss method, the truss form of polyhedron in Fig. 6-5(a) is shown in Fig. 6-5(b), in which each *R* joint is replaced by two pins connected by a rigid bar. To maintain the kinematic equivalence between the polyhedral linkage and its truss form, the bar AF with two *R* joints are replaced by the tetrahedron AaFf, the bar MJ with one *S* joint and one *R* joint becomes triangular piece JMm, the rigid triangular link KLM with three *R* joints is now a combination of three tetrahedrons mKLM, kKLM, lKLM. Following the similar rule, all the rest links are replaced by the truss form as shown in Fig. 6-5(b). Totally, there are $j = 21$ joints and $b = 57$ bars.

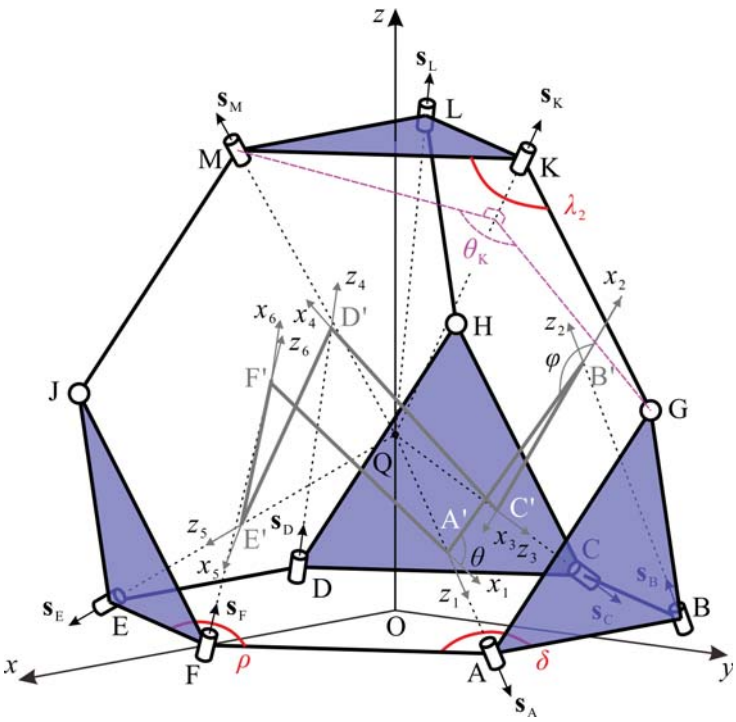

(a)

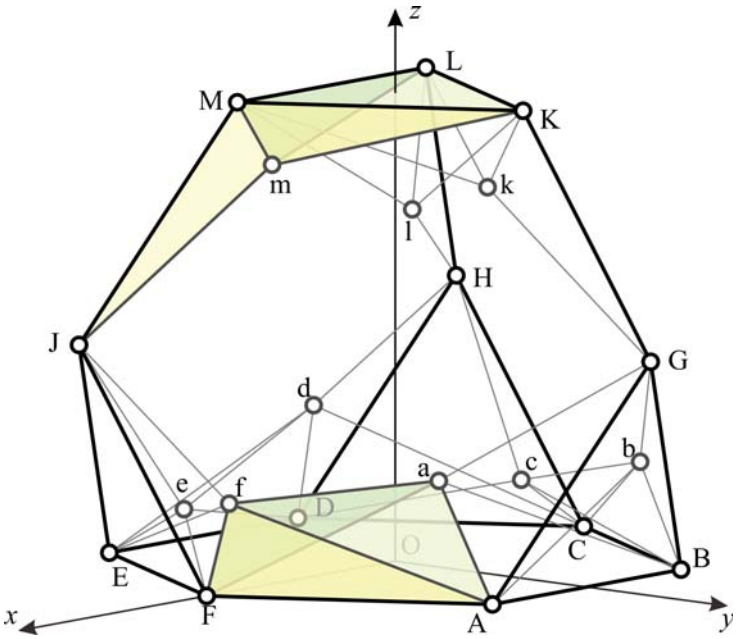

(b)

Fig. 6-5. Construction of Scheme II, (a) the joint arrangement and (b) its equivalent truss form.

Its compatibility equations can be established

$$\boldsymbol{Cd} = \boldsymbol{e}, \tag{6-53}$$

where $\boldsymbol{C}$ is the compatibility matrix with dimensions b by $3j$, $\boldsymbol{d}$ is the vector of nodal displacements with dimensions $3j$ by 1, and **e** is the vector of bar extensions with dimensions b by 1 [39]. For the polyhedral linkage, all bars are all rigid, then **e**=**0**, the rank of the compatibility matrix $\boldsymbol{C}$, $r = 56$. According to the Maxwell's rule, the mobility is

$$m = 3j - r - 6 = 3 \times 21 - 56 - 6 = 1. \tag{6-54}$$

And the number of self-stress is

$$s = b - r = 1. \tag{6-55}$$

Obviously, the null space of the compatibility matrix $\boldsymbol{C}'$, which has filtered joints and bars on the fixed frame, is the solution of the nodal displacements vector $\boldsymbol{d}$ when $\boldsymbol{e} = \boldsymbol{0}$. As $m = 1$, the motion path is always determined in the null space.

The SVD, which can be performed with mathematical tools, of its compatibility matrix $\boldsymbol{C}'$ consists of a set of left singular vectors $\boldsymbol{U}$, a set of right singular vectors $\boldsymbol{W}$ and a set of non-zero singular values $\boldsymbol{V}$.

$$\boldsymbol{C}' = \boldsymbol{U}\boldsymbol{V}\boldsymbol{W}^{\mathrm{T}}, \tag{6-56}$$

where $\boldsymbol{U} = [\boldsymbol{u}_1, \cdots, \boldsymbol{u}_r, \boldsymbol{u}_{r+1}, \cdots, \boldsymbol{u}_{r+s}]$, $\boldsymbol{V} = \begin{bmatrix} \mathrm{diag}(v_1, \cdots, v_r) & 0 \\ 0 & 0 \end{bmatrix}$, and $\boldsymbol{W} = [\boldsymbol{w}_1, \cdots, \boldsymbol{w}_r, \boldsymbol{w}_{r+1}]$. $\boldsymbol{w}_{r+1}$ contains the mode of mechanism [134]. Therefore, the motion process can be predicted by the iteration of Eq. (2-17) numerically.

6.4.2 Analysis of the Folding Process

Figures 6-6(a) and 6-6(b) show both relationships among kinematic angles and among folding angles to observe the folding performance. The result indicates that the curves are of the similar trends with those corresponding to scheme I. Meanwhile, singular values are recorded during the transformation process in Fig. 6-6(c). The smallest value is always equal to zero and the second smallest one never approaches zero. This means that the linkage is always with one DOF and no bifurcation.

6.5 Discussion

As mentioned in Section 6-2, for the construction of scheme I, the revolute axis of joint G could be in any direction on the bisection plane of $\angle \mathrm{BGK}$. The kinematic analysis in Section 6-3 was focused on the special case, the axis $\mathbf{S}_{\mathrm{G}}$ is along QG at the deployed truncated tetrahedron. Here we extend our discussion to the general directions of axis $\boldsymbol{s}_{\mathrm{G}}$, which is represented by angle δ_1 as shown in Fig. 6-7(a). The angle is between QG and axis $\boldsymbol{s}_{\mathrm{G}}$, whose positive direction is defined by the right-hand rule with the thumb directing along the normal $\boldsymbol{n}_{\mathrm{G}}$ of the bisecting plane.

With the same method proposed in Section 6-3, the relationships between linear displacements, angular displacements of triangle KLM about z axis and the folding angle ρ under different δ_1 are plotted in Figs. 6-8(a) and 6-8(b), respectively.

For $\delta_1 \geqslant 0$, the polyhedral linkage can realise the transformation without any interference as linear displacement is varying from $2\sqrt{6}/3$ to 0 and its angular

displacement is varying from 0° to 30° during the folding process.

For $\delta_1 < 0°$, linear and angular displacements of the top triangle, KLM, do not approach zero and 30°, respectively, when $\rho = 0°$. Thus, the completed physical folding can not be realised. At the last folding stage for $\rho = 0°$, linear displacement of triangle KLM generates large variation for little input angle, i.e., large sway occurs due to the large output/input ratio.

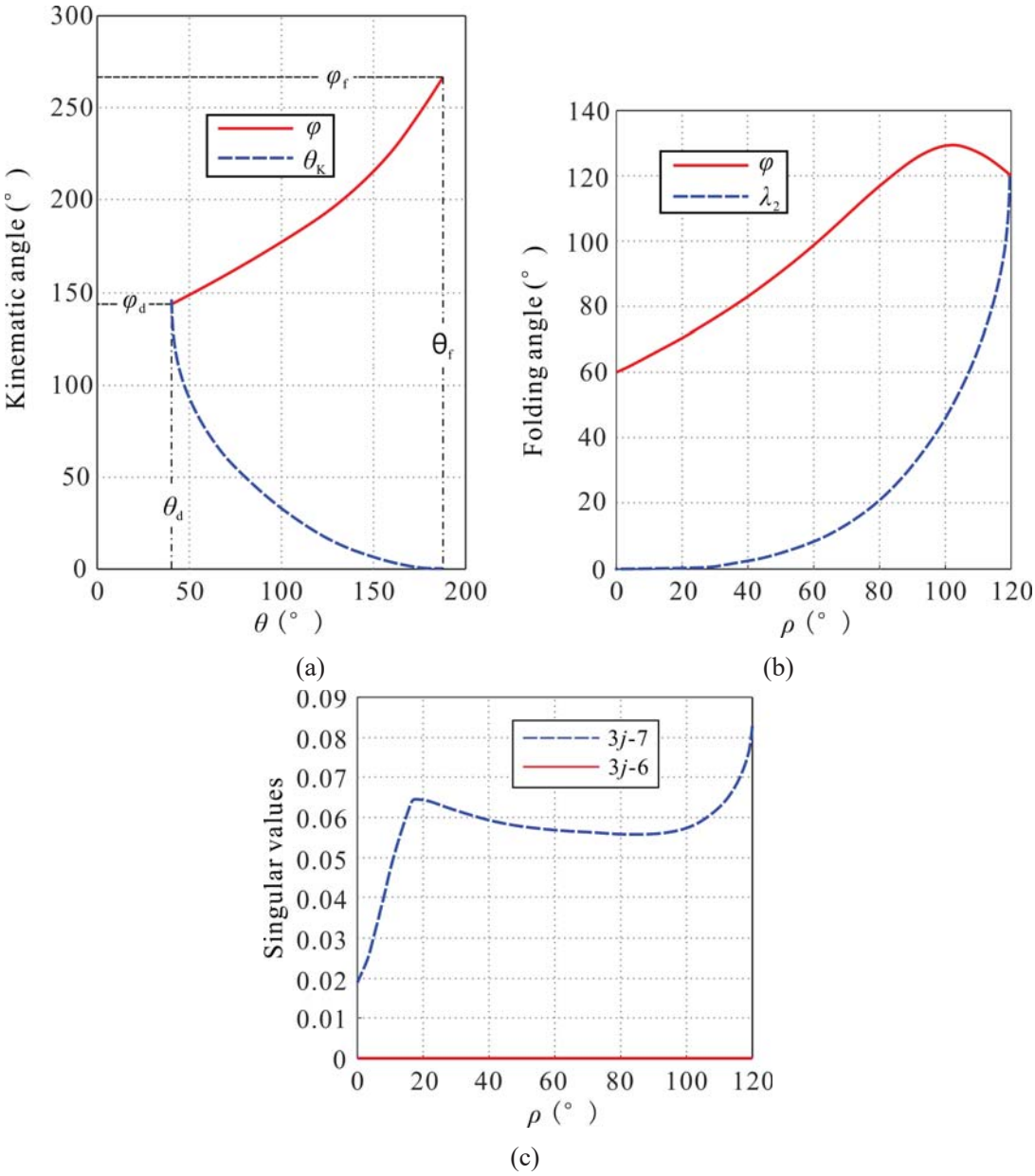

Fig. 6-6. Kinematic behaviours. (a) Input-output curves; (b) the relationship among folding angles; and (c) singular values where 3*j*-6 represents the smallest value.

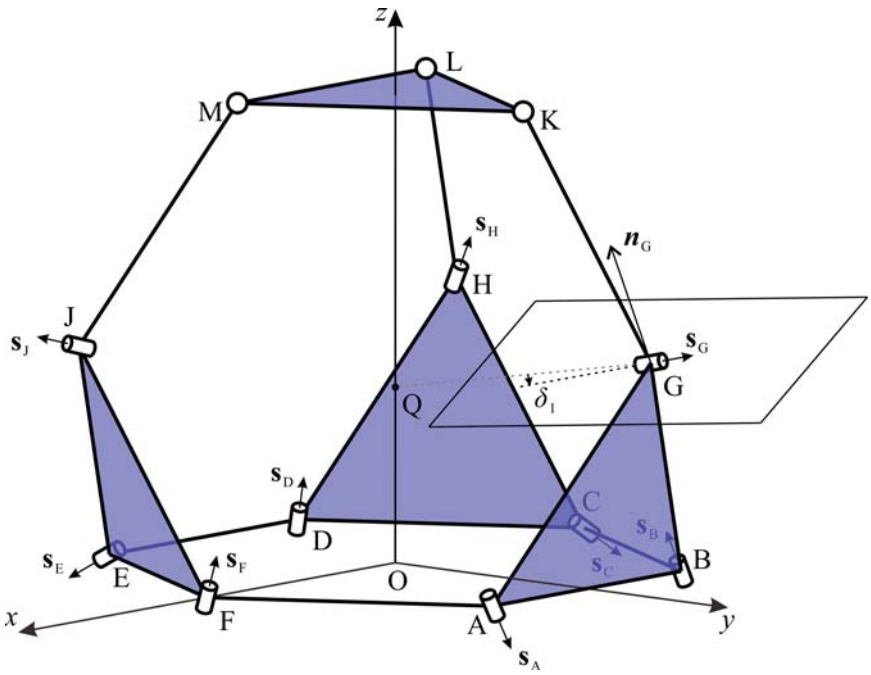

(a)

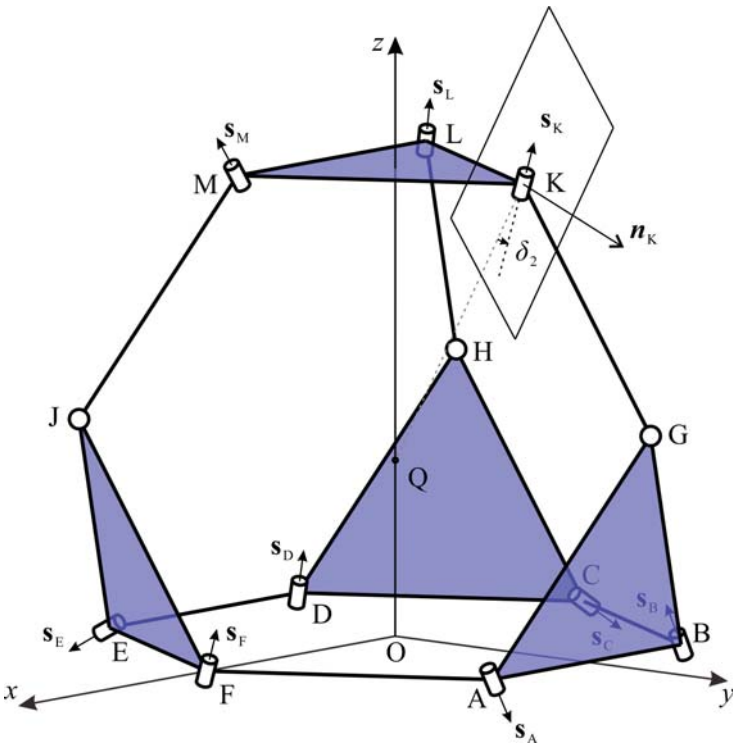

(b)

Fig. 6-7. Variable directions of the revolute axes (a) at G, H, J for scheme I and (b) at K, L, M for scheme II.

In the construction of scheme II, to generalise the directions of revolute axes at K, L, M, δ_2 is introduced in Fig. 6-7(b). Based on the numerical method in Section 6-4, the kinematics of this transformation can be analysed. Plotted in Figs. 6-8(c) and 6-8(d) are the displacements of rigid triangle KLM about *z* axis via folding angle ρ.

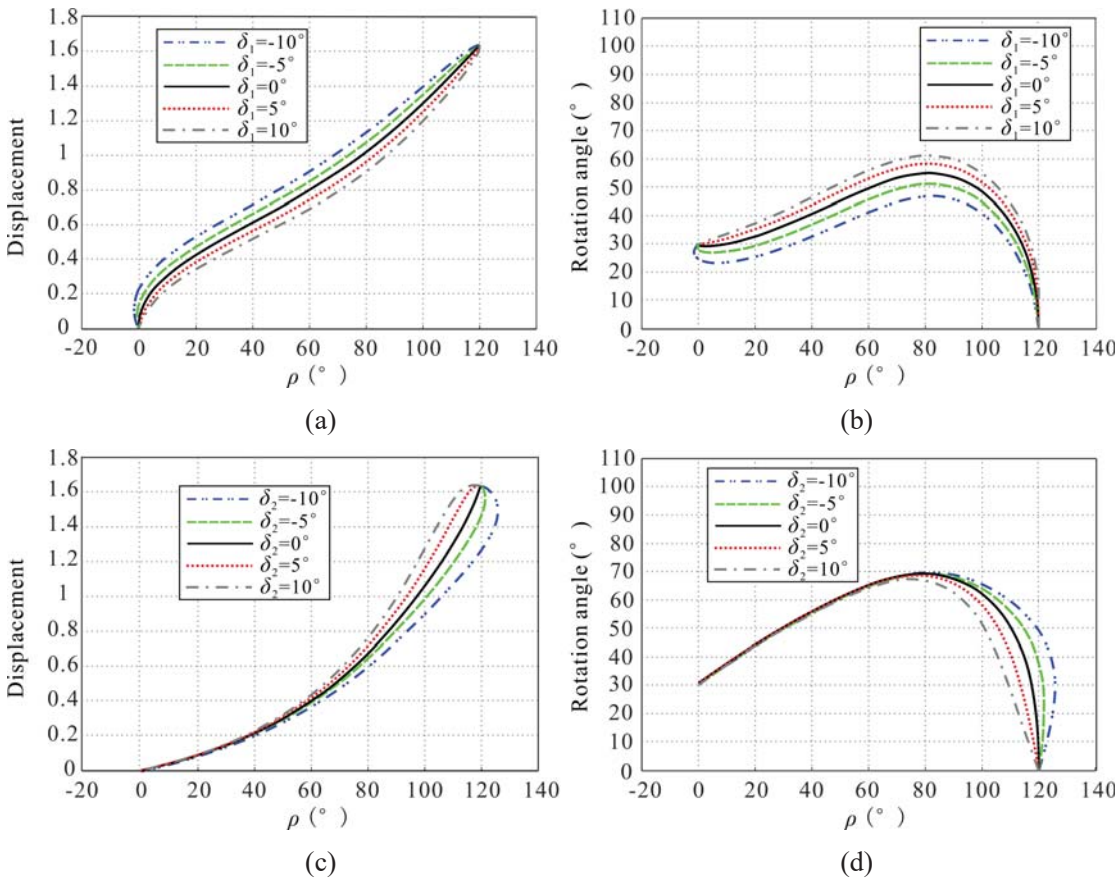

Fig. 6-8. Relationship between (a and c) linear displacements, (b and d) angular displacements of triangle KLM and the input angle ρ in scheme I and scheme II, respectively.

At the beginning movement in scheme II ($\rho = 120°$), negative δ_2 renders the Bricard linkage to move along the contrary direction at first. Hence the driver can not be setup at any joint of the Bricard linkage in the future applications. Meanwhile it is interesting to find that the folding processes at the last folding part of scheme II are always similar, which is not effected by the δ_2 significantly, see Figs. 6-8(c) and 6-8(d). So $\delta_2 \geq 0°$ are favorite for the physical implement of the transformation.

One prototype of scheme I was fabricated with the origami technique, where *S* joints at K, L, M were represented by three intersected *R* joints as shown in Fig. 6-9 with joint M as an example. And all *R* joints are realised by the polypropylene panels which possesses good folding endurance property. Motion process of the prototype in Fig. 6-10 validates the kinematic design.

6.6 Conclusions

In this chapter, we proposed a one-DOF transformation between tetrahedron and truncated tetrahedron, which have been realised by two schemes of joint arrangement. Mobility calculation and kinematic analysis of two constructions show that they are both able to realise the transformation with single DOF and no bifurcation.

Through the discussion on the folding performance under different joint directions for both constructions, possible ranges to realise the transformation without physical interference has been found. The final prototype, fabricated with the origami technique, validates the designed results. The transformation possesses great potential of application in engineering as the expansion/packing ratio in volume is up to 23.

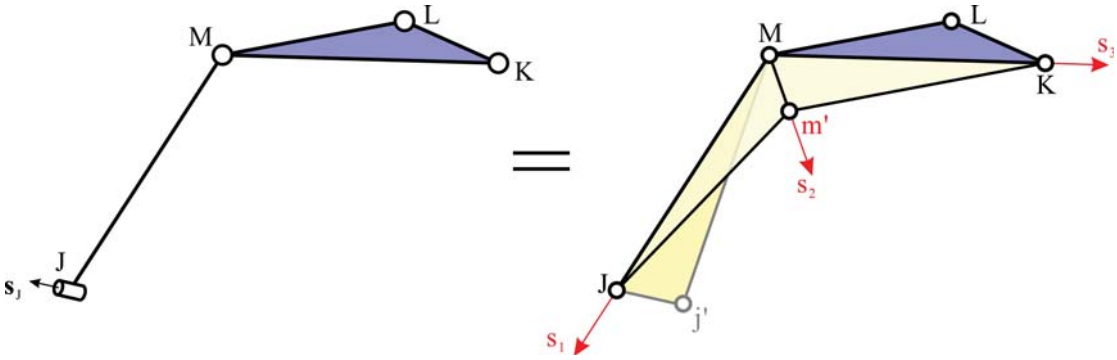

Fig. 6-9. Design and fabricate the prototype by replacing *S* joint with three folding creases.

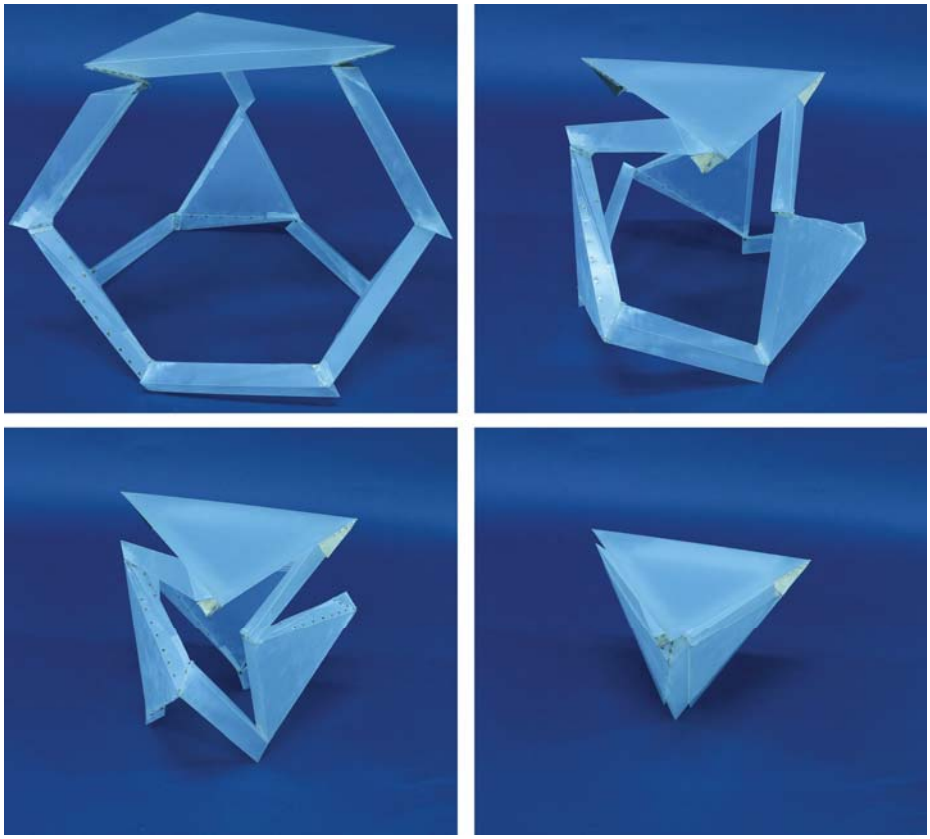

Fig. 6-10. Four folding sequences of the prototype fabricated with the origami technique.

Chapter 7 Final Remarks

The aim of this dissertation was set to develop a method to transform 3D linkages to their equivalent truss forms, and to apply this method to analyse overconstrained linkages as well as design transformable polyhedrons. In this chapter, we summarise the main achievements and highlight future works needed.

7.1 Main Achievements

- **Truss method**

First, we have established a method to transform 3D linkages to their equivalent truss forms. 3D linkages' kinematics including mobility calculation, motion path generation, and bifurcation detection are capable being performed by transforming into their truss forms, which has been certified by analysing a threefold-symmetric Bricard linkage.

The equivalence between Jacobian matrix of linkage and equilibrium matrix of its truss form has been verified by taking a planar 4*R* and a spherical 4*R* linkages as examples. And the relationship between angular and linear displacements has been derived for other spatial linkages.

- **Non-overconstrained forms of 3D overconstrained linkages**

Second, a novel approach to seek non-overconstrained forms of overconstrained linkages has been presented. It was achieved by detecting and removing redundant bars based on the truss method.

We have found that non-overconstrained forms of Bennett 4*R* linkages and Myard 5*R* linkages are *RSSR* and *RSRRR*, respectively. Meanwhile, non-overconstrained forms possessing the same kinematic properties as the original overconstrained linkages have been demonstrated in Chapter 3 with screw theory, and the non-overconstrained forms are also with great fault-tolerance capability.

This work will widen the engineering application of 3D overconstrained linkages as their strict overconstrained geometric conditions have been eliminated.

- **Transformation between cuboctahedron and octahedron**

Third, we have found that two Bennett linkages, connected with four *S* joints, are capable to construct a deployable solid. Determining directions of their *R* joints, the deployable structure can realise the transformation between cuboctahedron and octahedron. Kinematics has been studied with the truss method, which shows that the linkage can realise the polyhedral transformation with no bifurcation.

A metal prototype has been fabricated and assembled to validate the proposed transformation sequences presented in Chapter 4.

- **Transformation between truncated octahedron and cube**

Forth, we have proposed a method to realise the transformation between truncated octahedron and cube by setting each vertex with one movable joint, *R* joint or *S* joint.

We have found that a threefold-symmetric Bricard 6*R* linkage with certain parameters can fold one hexagonal face into three edges, which are perpendicular to each other, intersecting at one common vertex. And the parameters have been obtained by geometric and kinematic analysis.

The one-DOF polyhedral transformation has been realised by a multi-loop linkage constructed with two of these Bricard linkages and three *RSSSRR* as well as three *RSRSSR* linkages, where mobility and kinematics have been studied by employing the truss method. The folding process has been verified by a 3D printed prototype, shown in Chapter 5.

- **Transformation between truncated tetrahedron and tetrahedron**

Finally, the transformation between truncated tetrahedron and tetrahedron has also been realised by employing a threefold-symmetric Bricard linkage, and two schemes of joint arrangements, with one variable parameter in each scheme, have been obtained in Chapter 6.

By analytical and numerical analysis, kinematics of these two constructions has been investigated, which shows that both schemes are with one DOF and with no bifurcation. Possible range of the variable parameter to realise the transformation without physical interference has been found by parameter study for each scheme. The final prototype with the volume expansion/packing ratio up to 23 has been fabricated, which has revealed the validation of the method.

7.2 Future Works

The research reported in this dissertation is likely to have further developments in theoretical study or with the aim to be utilised in practical applications.

First, the fundamental relationship between the Jacobian matrix of linkage and equilibrium matrix of truss has yet to be found. The compatibility matrix, which is the transpose of equilibrium matrix, can be considered of Jacobian matrix of displacement equations. How to obtain the Jacobian matrix of linkage directly from the equilibrium matrix is the remaining challenge, with which the dynamic property of the linkage in truss form can be solved directly. Meanwhile, equilibrium matrix of truss can be derived as the Jacobian matrix of constrained functions for bars, with which a quadratic form can be established to judge the type of mobility, finite or infinitesimal, in structural engineering. Therefore, the issue on the difference between singularity configuration and motion bifurcation can be studied through the relationship between those two matrices.

Second, in the research of obtaining non-overconstrained forms from overconstrained linkage, it should be pointed out that for the overconstrained 6*R* linkage, there is only one redundant bar in its equivalent truss. Simply removing one bar from the truss form with the method in dealing with the Bennett linkage or Myard linkage will result in a 7*R* linkage. How to address this problem is our future research focus. Furthermore, we only explore the non-overconstrained forms of the overconstrained linkages with kinematic equivalence in this dissertation. Future effort should be broadened to the non-overconstrained new linkages by relaxing the bar removing rules to other possibilities.

Third, in the work on polyhedral transformations, we adopted one-DOF elemental linkages, Bennett 4*R* linkage or Bricard 6*R* linkage in square or hexagonal faces in order to realise transformable polyhedrons. We envisage that our method could be applied to other paired polyhedrons. For instance, a 1-DOF transformation may be realised for transformation between truncated cube and octahedron by folding those hollows in the octagon with 8*R* spatial linkages. 8*R* linkage in general would have more than one DOF. Whether a number of such interlinked linkages could lead to a single DOF spatial tiling is a challenge remains to be tackled. On the other hand, if other types of joints, such as 2-DOF universal joint, are considered, other solutions for one-DOF polyhedral transformation may exist, which requires further investigations. Meanwhile, some polyhedrons are able to be tessellated in 3D space without any gaps. It is certainly an interesting future work to obtain 3D tessellation of deployable polyhedrons with low DOF.

Last, in this dissertation, truss method was borrowed from structure to solve the difficult kinematic problem in mechanism. It is essential to study how to drive these linkages to get the optimised performance for the engineering application in the future. Meanwhile, whether other structure tools can be applied to mechanism is still a question. Moreover, the possibility to apply the mechanism theory for the challenge structural problem is an untouched area waiting us to explore.

References

[1] Ionescu TG. Terminology for mechanisms and machine science [J]. Mechanism and Machine Theory, 2003, 38(7-10): 597-1112.

[2] Gogu G. Mobility of mechanisms: a critical review [J]. Mechanism and Machine Theory, 2005, 40(9): 1068-1097.

[3] Chebychev PA. Théorie des mécanismes connus sous le nom de parallélogrammes [J]. Mém Acad Sci Pétersb, 1854, 7: 539-568.

[4] Sylvester JJ. On recent discoveries in mechanical conversion of motion [J]. Royal Institution of Great Britain, 1874, 7: 179-198.

[5] Grubler M. Allgemeine Eigenschaften der Zwanglaufigen ebenen kinematischen Ketten, Part I [J]. Zivilingenieur, 1883, 29: 167-200.

[6] Grubler M. Allgemeine Eigenschaften der Zwanglaufigen ebenen kinematischen Ketten, Part II [J]. Verh Ver Bef Gew, 1885, 64: 179-223.

[7] Hunt KH. Kinematic Geometry of Mechanisms [M]. London: Oxford University Press, 1978.

[8] Denavit J, Hartenberg RS. A kinematic notation for lower-pair mechanisms based on matrices [J]. Journal of Applied Mechanics, 1955, 22: 215-221.

[9] Dai JS. Finite displacement screw operators with embedded chasles' motion [J]. Journal of Mechanisms and Robotics-Transactions of the ASME, 2012, 4(4): 041002.

[10] Ball RS. A Treatise on the Theory of Screws [M]. Cambridge: Cambridge University Press, 1900.

[11] Huang C, Chen CM. The linear representation of the screw triangle—a unification of finite and infinitesimal kinematics [J]. Journal of Mechanical Design, 1995, 117(4): 554-560.

[12] Sun T, Yang S, Huang T, et al. A way of relating instantaneous and finite screws based on the screw triangle product [J]. Mechanism and Machine Theory, 2017, 108: 75-82.

[13] Yang S, Sun T, Huang T, et al. A finite screw approach to type synthesis of three-DOF translational parallel mechanisms [J]. Mechanism and Machine Theory, 2016, 104: 405-419.

[14] Hawkins T. Emergence of the Theory of Lie Groups [M]. Berlin, New York: Springer-Verlag, 2000.

[15] Murray RM, Li ZX, Sastry SS. A Mathematical Introduction to Robotic Manipulation [M]. Boca Raton: CRC Press, 1994.

[16] Hervé JM. The Lie group of rigid body displacements, a fundamental tool for mechanism design [J]. Mechanism and Machine Theory, 1999, 34(5): 719-730.

[17] McCarthy JM. Introduction to Theoretical Kinematics [M]. MIT Press, 1990.

[18] Perez A, McCarthy JM. Dual quaternion synthesis of constrained robotic systems [J]. Journal of Mechanical Design, 2003, 126(3): 425-435.

[19] Leclercq G, Lefèvre P, Blohm G. 3D kinematics using dual quaternions: theory and applications in neuroscience [J]. Frontiers in Behavioral Neuroscience, 2013, 7: 7.

[20] Hegedüs G, Schicho J, Schröcker H-P. Bond Theory and Closed 5*R* Linkages [M]//Jadran Lenarcic M H. Latest Advances in Robot Kinematics. Springer. 2012: 221-228.

[21] Hegedüs G, Schicho J, Schröcker H-P. Construction of Overconstrained Linkages by Factorization of Rational Motions [M]//Lenarcic J, Husty M. Latest Advances in Robot Kinematics. Springer. 2012: 213-220.

[22] Hegedüs G, Schicho J, Schröcker H-P. The theory of bonds: A new method for the analysis of linkages [J]. Mechanism and Machine Theory, 2013, 70: 407-424.

[23] Nawratil G. Introducing the theory of bonds for Stewart Gough platforms with self-motions [J]. Journal of Mechanisms and Robotics, 2013, 6(1): 011004.

[24] Hegedüs G, Li Z, Schicho J, et al. The theory of bonds II: Closed 6*R* linkages with maximal genus [J]. Journal of Symbolic Computation, 2015, 68: 167-180.

[25] Selig JM. Geometrical Methods in Robotics [M]. Springer-Verlag New York, Inc., 1996.

[26] Gosselin C, Angeles J. Singularity analysis of closed-loop kinematic chains [J]. Robotics and Automation, IEEE Transactions on, 1990, 6(3): 281-290.

[27] Di Gregorio R, Parenti-Castelli V. Mobility Analysis of the 3-UPU Parallel Mechanism Assembled for a Pure Translational Motion [C]. Proceedings of the 1999 IEEE/ASME, International Conference on Advanced Intelligent Mechatronics, Atlanta, USA, 1999: 520-525.

[28] Zlatanov D, Bonev IA, Gosselin CM. Constraint Sigularities of Parallel Mechanisms [C]. Proceedings of the 2002 IEEE International Conference on Robotics & Automation, Washington, DC, 2002.

[29] Joshi SA, Tsai L-W. Jacobian analysis of limited-DOF parallel manipulators [J]. Journal of Mechanical Design, 2002, 124(2): 254-258.

[30] Kanaan D, Wenger P, Caro S, et al. Singularity analysis of lower mobility parallel manipulators using Grassmann-Cayley algebra [J]. Ieee Transactions on Robotics, 2009, 25(5): 995-1004.

[31] Merlet J-P. Singular configurations of parallel manipulators and Grassmann geometry [J]. International Journal of Robotics Research, 1989, 8(5): 45-56.

[32] St-Onge BM, Gosselin CM. Singularity analysis and representation of the general Gough-Stewart platform [J]. International Journal of Robotics Research, 2000, 19(3): 271-288.

[33] Chai X, Li Q. Analytical mobility analysis of Bennett linkage using geometric algebra [J]. Advances in Applied Clifford Algebras, 2017, 27(3): 2083-2095.

[34] Chen Y, Chai WH. Bifurcation of a special line and plane symmetric Bricard linkage [J]. Mechanism and Machine Theory, 2011, 46(4): 515-533.

[35] Maxwell JC. On the calculation of the equilibrium and stiffness of frames [J]. Philosophical Magazine, 1864, XXVII: 599.

[36] Sugimoto K, Duffy J. Application of linear algebra to screw systems [J]. Mechanism and Machine Theory, 1982, 17(1): 73-83.

[37] Calladine CR. Buckminster Fuller's “Tensegrity” structures and Clerk Maxwell's rules for the construction of stiff frames [J]. International Journal of Solids and Structures, 1978, 14(2): 161-172.

[38] Tarnai T. Problems concerning spherical polyhedra and structural rigidity [J]. Structural topology, 1980, 4: 61-66.

[39] Pellegrino S, Calladine CR. Matrix analysis of statically and kinematically indeterminate frameworks [J]. International Journal of Solids and Structures, 1986, 22(4): 409-428.

[40] Kuznetsov EN. On immobile kinematic chains and a fallacious matrix analysis [J]. Journal of Applied Mechanics, 1989, 56(1): 222-224.

[41] Tarnai T, Szabó J. Rigidity and Stability of Prestressed Infinitesimal Mechanisms [M]//Drew H R, Pellegrino S. New Approaches to Structural Mechanics, Shells and Biological Structures. Springer Netherlands. 2002: 245-256.

[42] Tarnai T, Szabo J. On the exact equation of inextensional, kinematically indeterminate assemblies [J]. Computers & Structures, 2000, 75(2): 145-155.

[43] Kumar P, Pellegrino S. Computation of kinematic paths and bifurcation points [J]. International Journal of Solids and Structures, 2000, 37(46-47): 7003-7027.

[44] Gan W, Pellegrino S. Closed-Loop Deployable Structures [C]. 44th AIAA/ASME/ASCE/AHS/ASC Structures, Structural Dynamics, and Materials Conference: American Institute of Aeronautics and Astronautics, 2003.

[45] Gan WW, Pellegrino S. Numerical approach to the kinematic analysis of deployable structures forming a closed loop [J]. Proceedings of the Institution

of Mechanical Engineers, Part C: Journal of Mechanical Engineering Science, 2006, 220(7): 1045-1056.

[46] Chen Y, You Z. Two-fold symmetrical 6*R* foldable frame and its bifurcations [J]. International Journal of Solids and Structures, 2009, 46(25-26): 4504-4514.

[47] Tanaka M. Truss-type mechanism [J]. Advanced Robotics, 1993, 8(6): 599-599.

[48] Shai O. The duality relation between mechanisms and trusses [J]. Mechanism and Machine Theory, 2001, 36(3): 343-369.

[49] Shai O. Utilization of the dualism between determinate trusses and mechanisms [J]. Mechanism and Machine Theory, 2002, 37(11): 1307-1323.

[50] Waldron KJ. Overconstrained Linkages [J]. Environment and Planning B: Planning and Design, 1979, 6(4): 393-402.

[51] Sarrus PF. Note sur la transformation des mouvements rectilignes alternatifs, en mouvements circulaires, et reciproquement [J]. Académie des Sciences, 1853, 36: 1036-1038.

[52] Bennett GT. A new mechanism [J]. Engineering, 1903, 76: 777-778.

[53] Bennett GT. The skew isogram mechanism [J]. Proceedings of the London Mathmatical Society Series 2, 1914, 13: 151-173.

[54] Delassus E. Les chaînes articulées fermées et déformables à quatre membres [J]. Bulletin des Sciences Mathématiques, 2nd series, 1922, 46: 283-304.

[55] Bricard R. Mémoire sur la théorie de l'octaèdre articulé [J]. J Math Pures Appl, 1897, 3: 113-150. (English translation by E. A. Coutsias, 2010, e-print, http://arxiv.org/abs/1203.1286)

[56] Bricard R. Leçons de cinématique Tome II Cinématique appliquée [M]. Paris: Gauthier-Villars, 1927.

[57] Myard FE. Contribution à la géométrie des systèmes articulés [J]. Bulletin de la Société Mathématique de France, 1931, 59: 183-210.

[58] Goldberg M. New five-bar and six-bar linkages in three dimensions [J]. Transactions of the ASME, 1943, 65: 649-663.

[59] Waldron KJ. A family of overconstrained linkages [J]. Journal of Mechanisms, 1967, 2(2): 201-211.

[60] Waldron KJ. Hybrid overconstrained linkages [J]. Journal of Mechanisms, 1968, 3(2): 73-78.

[61] Waldron KJ. Symmetric overconstrained linkages [J]. Journal of Engineering for Industry, 1969, 91(1): 158-162.

[62] Wohlhart K. A New 6*R* Space Mechanism [C]. Proceedings of the 7th World

Congress on the Theory of Machines and Mechanisms, Spain: Sevilla, 1987: 193-198.

[63] Wohlhart K. Merging two general Goldberg 5*R* linkages to obtain a new 6*R* space mechanism [J]. Mechanism and Machine Theory, 1991, 26(7): 659-668.

[64] Wohlhart K. The two types of the orthogonal bricard linkage [J]. Mechanism and Machine Theory, 1993, 28(6): 809-817.

[65] Song CY, Chen Y. A family of mixed double-Goldberg 6*R* linkages [J]. Proceedings of the Royal Society A: Mathematical, Physical and Engineering Science, 2012, 468(2139): 871-890.

[66] Wang Q, Chen Y, Tang H. Mechanism Design for Aircraft Morphing Wing [C]. 53rd AIAA/ASME/ASCE/AHS/ASC Structures, Structural Dynamics and Materials Conference: American Institute of Aeronautics and Astronautics, 2012.

[67] Gao B, Kang R, Chen Y. Deployable Mechanism Design for Span Morphing Wing Aircraft [C]. Mechanism and Machine Science: Proceedings of ASIAN MMS 2016 & CCMMS 2016, Singapore: Springer Singapore, 2017: 801-813.

[68] Baker JE. The Bennett, Goldberg and Myard linkages—in perspective [J]. Mechanism and Machine Theory, 1979, 14(4): 239-253.

[69] Baker JE. The Bennett linkage and its associated quadric surfaces [J]. Mechanism and Machine Theory, 1988, 23(2): 147-156.

[70] Baker JE. The composition of Bennett's hyperboloids from the loop itself [J]. Journal of Mechanical Design, 2004, 126(5): 875-880.

[71] Chen Y, You Z. Spatial 6*R* linkages based on the combination of two Goldberg 5*R* linkages [J]. Mechanism and Machine Theory, 2007, 42(11): 1484-1498.

[72] Chen Y, You Z. An extended Myard linkage and its derived 6*R* linkage [J]. Journal of Mechanical Design, 2008, 130(5): 052301.

[73] Chen Y. Design of Structural Mechanisms [D]. PhD thesis, London; University of Oxford, 2003.

[74] Baker JE. An analysis of the Bricard linkages [J]. Mechanism and Machine Theory, 1980, 15(4): 267-286.

[75] Chen Y, You Z, Tarnai T. Threefold-symmetric Bricard linkages for deployable structures [J]. International Journal of Solids and Structures, 2005, 42(8): 2287-2301.

[76] Shang H, Wei D, Kang R, et al. A Deployable Robot Based on the Bricard Linkage [C]. Mechanism and Machine Science: Proceedings of ASIAN MMS 2016 & CCMMS 2016, Singapore: Springer Singapore, 2017: 737-747.

[77] Chai WH, Chen Y. The line-symmetric octahedral Bricard linkage and its structural closure [J]. Mechanism and Machine Theory, 2010, 45(5): 772-779.

[78] Song CY, Chen Y, Chen IM. Kinematic study of the original and revised general line-symmetric Bricard 6*R* linkages [J]. Journal of Mechanisms and Robotics-Transactions of the Asme, 2014, 6(3): 031002.

[79] Feng H, Chen Y, Dai JS, et al. Kinematic study of the general plane-symmetric Bricard linkage and its bifurcation variations [J]. Mechanism and Machine Theory, 2017, 116: 89-104.

[80] Pellegrino S. Deployable Structures [M]. Wien, New York: Springer, 2001.

[81] Baker JE, Yu HC. Re-examination of a kempe linkage [J]. Mechanism and Machine Theory, 1983, 18(1): 7-22.

[82] Baker JE, Yu HC. On spatial analogues of Kempe's linkages and some generalisations [J]. Mechanism and Machine Theory, 1983, 18(6): 457-466.

[83] Baker JE, Hu M. On spatial networks of overconstrained linkages [J]. Mechanism and Machine Theory, 1986, 21(5): 427-437.

[84] Chen Y, You Z. Mobile assemblies based on the Bennett linkage [J]. Proceedings of the Royal Society a-Mathematical Physical and Engineering Sciences, 2005, 461(2056): 1229-1245.

[85] Chen Y, You Z. On mobile assemblies of Bennett linkages [J]. Proceedings of the Royal Society a-Mathematical Physical and Engineering Sciences, 2008, 464(2093): 1275-1293.

[86] Chen Y, Baker JE. Using a Bennett linkage as a connector between other Bennett loops [J]. Proceedings of the Institution of Mechanical Engineers, Part K: Journal of Multi-body Dynamics, 2005, 219(2): 177-185.

[87] Chen Y, You Z. Square deployable frames for space applications. Part 1: theory [J]. Proceedings of the Institution of Mechanical Engineers Part G-Journal of Aerospace Engineering, 2006, 220(G4): 347-354.

[88] Chen Y, You Z. Square deployable frames for space applications. Part 2: realization [J]. Proceedings of the Institution of Mechanical Engineers Part G-Journal of Aerospace Engineering, 2007, 221(G1): 37-45.

[89] Yu Y, Luo Y, Li L. Deployable membrane structure based on the Bennett linkage [J]. Proceedings of the Institution of Mechanical Engineers, Part G: Journal of Aerospace Engineering, 2007, 221(5): 775-783.

[90] Guo H, You Z. Deployable Masts Based on the Bennett Linkage [M]//Dai JS, Zoppi M, Kong X. Advances in Reconfigurable Mechanisms and Robots I. Springer London. 2012: 739-747.

[91] Baker JE. A collapsible network of similar pairs of nested Bennett linkages [J]. Mechanism and Machine Theory, 2013, 59: 119-124.

[92] Yang F, Li J, Chen Y, et al. A Deployable Bennett Network in Saddle Surface [C]. The 14th IFToMM World Congress, Taipei, Taiwan, 2015.

[93] Lu S, Zlatanov D, Ding X. Approximation of cylindrical surfaces with deployable Bennett networks [J]. Journal of Mechanisms and Robotics, 2017, 9(2): 021001.

[94] Liu SY, Chen Y. Myard linkage and its mobile assemblies [J]. Mechanism and Machine Theory, 2009, 44(10): 1950-1963.

[95] Qi X, Huang H, Miao Z, et al. Design and mobility analysis of large deployable mechanisms based on plane-symmetric Bricard linkage [J]. Journal of Mechanical Design, 2016, 139(2): 022302.

[96] Huang H, Li B, Zhu J, et al. A new family of Bricard-derived deployable mechanisms [J]. Journal of Mechanisms and Robotics, 2016, 8(3): 034503.

[97] Song X, Guo H, Li B, et al. Large deployable network constructed by Altmann linkages [J]. Proceedings of the Institution of Mechanical Engineers, Part C: Journal of Mechanical Engineering Science, 2016, 231(2): 341-355.

[98] Atarer F, Korkmaz K, Kiper G. Design alternatives of network of Altmann linkages [J]. International Journal of Computational Methods and Experimental Measurements, 2017, 5(4): 495-503.

[99] Baker JE, Duclong T, Khoo PSH. On attempting to reduce undesirable inertial characteristics of the Schatz mechanism [J]. Journal of Mechanical Design, 1982, 104(1): 192-205.

[100] Milenkovic P, Brown MV. Properties of the Bennett mechanism derived from the *RRRS* closure ellipse [J]. Journal of Mechanisms and Robotics-Transactions of the Asme, 2011, 3(2).

[101] Lee C-C, Hervé JM. Oblique circular torus, Villarceau circles and four types of Bennett linkages [J]. Proceedings of the Institution of Mechanical Engineers, Part C: Journal of Mechanical Engineering Science, 2013.

[102] Cromwell PR. Polyhedra [M]. Cambridge: Cambridge University Press, 1997.

[103] Wikipedia. Platonic solid [OL]. 2016.

[104] Wikipedia. Archimedean solid [OL]. 2017.

[105] Coxeter HSM. Regular Polytopes [M]. London: Methuen Publishing Ltd, 1948.

[106] Fuller RB. No More Secondhand God and Other Writings [M]. Carbondale, Illinois: Southern Illinois University Press, 1963.

[107] Clinton JD. Advanced Structural Geometry Studies, Part II. A Geometric Transformation Concept for Expanding Rigid Structures [R]. Washington D. C.: Southern Illinois University, NASA Report CR-1735, 1971.

[108] Fuller RB. Synergetics: Explorations in the Geometry of Thinking [M]. New York: MacMillan, 1997.

[109] Stachel H. Zwei bemerkenswerte bewegliche Strukturen [J]. Journal of Geometry, 1992, 43(1-2): 14-21.

[110] Schwabe C. Eureka and Serendipity: The Rudolf von Laban Icosahedron and Buckminster Fuller's Jitterbug [C]. Bridges 2010: Mathematics, Music, Art, Architecture, Culture, Pécs, Hungary, 2010.

[111] Verheyen HF. Expandable Polyhedral Structures Based on Dipolygonids [C]. Proceedings of 3rd International Conference on Space Structures, London: Elsevier, 1984: 88-93.

[112] Verheyen HF. The complete set of Jitterbug transformers and the analysis of their motion [J]. Computers & Mathematics with Applications, 1989, 17(1–3): 203-250.

[113] Agrawal SK, Kumar S, Yim M. Polyhedral single degree-of-freedom expanding structures: design and prototypes [J]. Journal of Mechanical Design, 2002, 124(3): 473-478.

[114] Hoberman C. Geared expanding structures [P/OL]: United States of America, US20040134157A1. 2004-07-15. http://pdfpiw.uspto.gov/.piw?docid=07464503&PageNum=1&IDKey=E656F1763890&HomeUrl=http://patft.uspto.gov/netacgi/nph-Parser?Sect1=PTO2%2526Sect2=HITOFF%2526p=1%2526u=%25252Fnetahtml%25252FPTO%25252Fsearch-bool.html%2526r=1%2526f=G%2526l=50%2526co1=AND%2526d=PTXT%2526s1=%252522Geared%252Bexpanding%252Bstructures%252522%2526OS=%2526RS=.

[115] Wohlhart K. Kinematics and dynamics of the Fulleroid [J]. Multibody System Dynamics, 1997, 1(2): 241-258.

[116] Kiper G. Fulleroid-Like Linkages [M]//Ceccarelli M. Proceedings of EUCOMES 08: The Second European Conference on Mechanism Science. Dordrecht; Springer Netherlands. 2009: 423-430.

[117] Roschel O. Overconstrained Mechanisms Based on Trapezohedra [C]. Proceedings of the 15th International Conference on Geometry and Graphics (ICGG), Montreal, Canada, 2012: 629-637.

[118] Roschel O. A Fulleroid-like mechanism based on the cube [J]. Journal for Geometry and Graphics, 2012, 16(1): 19-27.

[119] Li R, Yao Y-a, Kong X. Reconfigurable deployable polyhedral mechanism based on extended parallelogram mechanism [J]. Mechanism and Machine Theory, 2017, 116(Supplement C): 467-480.

[120] Wohlhart K. Heureka Octahedron and Brussels Folding Cube as Special Cases of the Turning Tower [C]. Proceedings of the 6th IFToMM International Symposium on Linkages and Computer Aided Design Methods, Bucharest,

Romania, 1993.

[121] Wohlhart K. New Overconstrained Spheroidal Linkages [C]. Proceedings the 9th World Congress on the Theory of Machines and Mechanisms, Milano, Italy, 1995: 149-154.

[122] Wohlhart K. Deformable Cages [C]. 10th World Congress on the Theory of Machines and Mechanisms, Oulu, Finland, 1999: 683-688.

[123] Gosselin CM, Gagnon-Lachance D. Expandable polyhedral mechanisms based on polygonal one-degree-of-freedom faces [J]. Proceedings of the Institution of Mechanical Engineers, Part C: Journal of Mechanical Engineering Science, 2006, 220(7): 1011-1018.

[124] Laliberté T, Gosselin CM. Polyhedra with Articulated Faces [C]. Proceedings of the 12th IFToMM World Congress, Besançon, June, 2007: 18-21.

[125] Wei G, Dai JS. Synthesis and Construction of a Family of One-DOF Highly Overconstrained Deployable Polyhedral Mechanisms (DPMs) [C]. ASME 2012 International Design Engineering Technical Conferences and Computers and Information in Engineering Conference, Chicago, 2012.

[126] Wei G, Dai JS. A spatial eight-bar linkage and its association with the deployable platonic mechanisms [J]. Journal of Mechanisms and Robotics, 2014, 6(2): 021010.

[127] Wei G, Chen Y, Dai JS. Synthesis, mobility, and multifurcation of deployable polyhedral mechanisms with radially reciprocating motion [J]. Journal of Mechanical Design, 2014, 136(9): 091003-091003-091012.

[128] Kiper G, Söylemez E. Regular Polygonal and Regular Spherical Polyhedral Linkages Comprising Bennett Loops [M]//Kecskeméthy A, Müller A. Computational Kinematics. Springer Berlin Heidelberg. 2009: 249-256.

[129] Kiper G. Design methods for planar and spatial deployable structures [D]. PhD thesis, Ankara: Middle East Technical University, 2011.

[130] Shim J, Perdigou C, Chen ER, et al. Buckling-induced encapsulation of structured elastic shells under pressure [J]. Proceedings of the National Academy of Sciences, 2012, 109(16): 5978-5983.

[131] Skelton R. Tensegrity Approaches to in-space construction of a 1g growable habitat [C]. The NASA Innovative Advanced Concepts (NIAC) Program's 2016 Symposium, Raleigh, NC, 2016.

[132] Ames Research Center. Small spacecraft technology state of the art, NASA/TP-2015-216648/REV1 [R], 2015.

[133] Pellegrino S. Analysis of prestressed mechanisms [J]. International Journal of Solids and Structures, 1990, 26(12): 1329-1350.

[134] Pellegrino S. Structural computations with the singular value decomposition of

the equilibrium matrix [J]. International Journal of Solids and Structures, 1993, 30(21): 3025-3035.

[135] Tarnai T. Infinitesimal and Finite Mechanisms [M]//Pellegrino S. Deployable Structures. Wien, New York; Springer. 2001: 113-142.

[136] Huang Z, Xia P, Ding H. Analysis of DOF Bennett mechanism using screw theory [J]. Journal of Yanshan University, 2004, 28(3): 189-191. (in Chinese)

[137] Hartenberg RS, Denavit J. Synthesis of Spatial Linkages [M]. Kinematic Synthesis of Linkages. New York; Mcgraw-Hill Book Company. 1964.

[138] Rajagopalan S, Cutkosky M. Error analysis for the In-Situ fabrication of mechanisms [J]. Journal of Mechanical Design, 2004, 125(4): 809-822.

[139] ISO 2768-1:1989, General tolerances-Tolerances for linear and angular dimensions without individual tolerance indications [S].

[140] Yang F, Chen Y, Kang R, et al. Truss transformation method to obtain the non-overconstrained forms of 3D overconstrained linkages [J]. Mechanism and Machine Theory, 2016, 102: 149-166.

[141] Koks D. Explorations in Mathematical Physics [M]. New York: Springer, 2006.

[142] Beggs JS. Advanced Mechanism [M]. New York: Macmillan, 1966.

List of Publications during this PhD Study

Papers：

[1] Yang F, Chen Y, Kang R, et al. Truss transformation method to obtain the non-overconstrained forms of 3D overconstrained linkages [J]. Mechanism and Machine Theory, 2016, 102(149-166).

[2] Chen Y, Yang F, You Z. Transformation of polyhedrons [J]. International Journal of Solids and Structures, Under revision review.

[3] Yang F, Chen Y. One-DOF transformation between truncated tetrahedron and tetrahedron [J]. Mechanism and Machine Theory, 2018, 121(169-183).

[4] Yang F, Chen Y. Polyhedral transformation inspired by a new mobile assembly of two Bennett linkages. Ready to submit.

[5] Yang F, Chen Y. Foldable hexagon structures based on threefold-symmetric Bricard linkage. Ready to submit.

[6] Yang F, Li J, Chen Y, et al. A Deployable Bennett Network in Saddle Surface [C]. The 14th IFToMM World Congress. Taipei, Taiwan. 2015. (YDP Grant)

[7] 杨富富, 陈焱. 可展开多面体结构，第二届可展开空间结构学术会议（中国航天科技集团公司、中国力学学会、中国振动工程学会、中国宇航学会和空间微波技术重点实验室主办）, 2016 年 10 月 24 日至 10 月 25 日, 北京.（会议优秀论文）

Patents:

[1] 陈焱，杨富富，李建民，马家耀. 可折叠多面体结构，授权号：ZL201510997199.4, 发明专利, 授权公告日：2017.6.16.

[2] 陈焱, 杨富富, 康荣杰, 马家耀. 可折展六面体结构, 申请号：2016211459542，发明专利, 2016.10.21.

[3] 陈焱, 杨富富, 康荣杰, 马家耀. 可折展四面体结构, 申请号：2016109195540，发明专利, 2016.10.21.

Research Projects Participated in:

[1] 国家自然科学基金优青项目：机构运动学与可动结构（项目编号：51422506），主要参与人

[2] 国家自然科学基金面上项目：可重构机器人中折展结构基础设计理论研究（项目编号：51275334），主要完成人

Acknowledgements

First and foremost I would like to express the deepest appreciation to my supervisor, Prof. Yan Chen, for her encouraging support and patient guidance throughout this research. Her constructive suggestions and guiding discussion throughout this research work have been a driving force to fulfill the goals of this work. Furthermore, her patience, motivation, enthusiasm, immense knowledge, and scholarly attitude will continually effect on my future work. Also I greatly appreciate Prof. Yong Chang at Jimei University for frequent encouragement in my PhD study.

I wish to express my gratitude to Prof. Zhong You at the University of Oxford for discussion on detailed problems and suggestion for my thesis proposal; to Prof. Tibor Tarnai at the Budapest University of Technology and Economics of Hungary for greatly valuable comments and suggestions to solve detailed issues; to Prof. Jian S Dai at King's College London and Prof. Grigore Gogu at French Institute of Advanced Mechanics for discussion and suggestion; and to Prof. Tian Huang at Tianjin University for his recommendation in application of IFToMM YDP grant.

I would like to thank Prof. Jiayao Ma for his suggestions on model fabrication, Prof. Rongjie Kang, Prof. Jianmin Li, Prof. Zhibin Song, and Ms. Yunyan Wang at Tianjin University as well as Dr. Joe Gattas at the University of Queensland for their kind help. Meanwhile, I also would like to thank Dr. Yang Li at California Institute of Technology for the indelible discussion about the numerical simulation, and Mr. Jeff Lee at the University of Queensland for teaching me software.

I would like to thank all members in Motion Structure Laboratory, in particular Miss Huijuan Feng, Mr. Rui Peng, Mr. Xiao Zhang, Mr. Zufeng Shang, Mr. Weilin Lv, Mr. Jichao Song, Mr. Junjie Gao, Miss Mengyan Shi, Mr. Linfeng Zhang, Mr. Binbin Gao, Mr. Yong Guo, Mr. Xiaolei Guo, Mr. Haiyang Liu, Miss Xiaochen Yang, Mr. Xuesong Chen, Mr. Zhiyao Cheng, Mr. Cheng Ji for their help and contribution to many memorable and enjoyable occasions. Also I would like to thank my friends, in particular Mr. Liheng Wu, Mr. Jiawei Zang, Mr. Ruilin Yang, Mr. Shihui Zhang, Mr. Xiaoqiang Wu, Mr. Jianmin Xu, for enjoying wonderful study life together.

Financial support by the National Natural Science Foundation of China (Projects 51275334, 51290293, 51422506 and 51575377), by the Ministry of Science and Technology of China (Project 2014DFA70710), by the graduate scholarship from Tianjin University, by Weichai power scholarship, and by the YDP grant from the 14th IFToMM World Congress are also gratefully acknowledged.

Finally I would like to thank my parents and my elder brother for their supporting and confidence in me, and give special thanks to my dear wife Xiaolin Cheng for her love, patience, and encouragement.